Université de Montréal

Emerging electrocatalytic strategies for small molecule electrosynthesis

Par
Yuxuan Zhang

Départment de chimie
Faculté des arts et des sciences

Mémoire présentée à la Faculté des études supérieures et
postdoctorales en vue de l'obtention du grade de Maîtrise ès sciences
(M.Sc.) en chimie

Août, 2022

Université de Montréal

Département de chimie, Faculté des arts et des sciences

Ce mémoire intitulé

Emerging electrocatalytic strategies for small molecule electrosynthesis

Présenté par

Yuxuan Zhang

A été évalué par un jury composé des personnes suivantes

Garry Hanan
Président-rapporteur

Nikolay Kornienko

Directeur de recherche

Audrey Laventure

Membre du jury

Résumé

À la lumière du changement climatique et de l'épuisement des réserves de combustibles fossiles, l'innovation dans les technologies énergétiques vertes et durables devient un défi crucial. La fabrication de produits chimiques consomme de grandes quantités d'énergie et est responsable d'une part importante des émissions mondiales de carbone. Dans ce contexte, l'électrosynthèse, alimentée par de l'électricité renouvelable, peut remplacer de nombreux procédés thermochimiques industriels pour générer des carburants, des produits chimiques et des engrais. Plutôt que de nous concentrer sur des domaines qui ont reçu beaucoup d'attention ces dernières années (par exemple, l'électrolyse de l'eau et la réduction du CO_2), nous avons exploré les domaines émergents de l'électrosynthèse hétérogène pour lesquels il existe un besoin substantiel.

Dans **le chapitre 3**, nous soulignons l'importance de concevoir des électrocatalyseurs avec des sites actifs bien définis. Nous rapportons l'utilisation de la chimie réticulaire pour concevoir un système de modèle électrocatalytique à base d'organo-métallique conducteur avec des sites actifs moléculaires M-O4 pour l'oxydation électrochimique du 5-hydroxyméthylfurfural (HMFOR). L'activité des MOF portant des sites actifs Ni-O4 (Ni-CAT) et Co-O4 (Co-CAT) a été analysée avec des techniques spectroscopiques électrochimiques et operando pour élucider le mécanisme de réaction se produisant à la surface. Les expériences électrochimiques révèlent que le Co-CAT a un potentiel d'apparition plus précoce pour activer le HMFOR, par rapport à la plupart des catalyseurs établis, tandis que le Ni-CAT présente une cinétique plus rapide pour la conversion du 5-hydroxyméthylfurfural (HMF) en acide 2,5-furandicarboxylique (FDCA). Nous avons déterminé que Ni-CAT atteignait des rendements de FDCA (notre molécule cible) de 98,7 %. L'efficacité faradique peut atteindre 86,8% d'efficacité faradique. La spectroscopie infrarouge indique le HMF avec un groupe aldéhyde lié à la surface comme intermédiaire clé dans le cycle catalytique, qui se forme une fois que l'oxydation M (II \III) se produit. Ce travail illustre l'avantage d'utiliser des sites actifs moléculairement définis couplés à la spectroscopie operando pour fournir des informations fondamentales sur une variété de réactions électrosynthétiques et ouvrir la voie à la conception future de catalyseurs.

Suite à ce projet, nous nous sommes tournés vers l'utilisation d'un réacteur à membrane sélective pour l'hydrogène afin d'explorer de nouveaux concepts de réaction et de catalyseurs. La clé ici était d'utiliser une feuille de Pd comme matériau qui réduisait les protons en *H dans un compartiment aqueux et transférait l'hydrogène dans un compartiment organique où il hydrogénait le réactif de choix. À l'aide d'un réacteur à membrane, nous avons pu séparer physiquement la réduction électrochimique de l'hydrogène et la chimie de l'hydrogénation d'une manière qui contournait l'utilisation du gaz H_2 qui serait autrement nécessaire. Nous choisissons comme point de départ un produit chimique produit industriellement en excès, l'acétonitrile. Le réacteur à membrane Pd est appliqué pour hydrogéner complètement la liaison C≡N de l'acétonitrile. Avec succès, nous avons obtenu de l'ammoniac et de l'acétaldéhyde comme produits de réaction à un potentiel de début record de 0.4 V vs Ag/AgCl. Enfin, en concevant soigneusement une cellule spectroélectrochimique unique, nous avons pu effectuer des mesures spectroscopiques infrarouges pour visualiser le processus de réaction dans la membrane Pd et par conséquent proposé un mécanisme unique de réaction d'hydrolyse de l'imine (**Chapitre 4**).

Dans **le chapitre 5**, nous choisissons d'innover dans un domaine émergent: la formation de liaisons électrochimiques C-N à partir de réactifs de petites molécules (par exemple CO_2, NH_3). Le mécanisme conventionnel de formation de liaisons électrochimiques C-N est basé sur le CO2RR électrochimique. Dans ce chapitre, nous proposons une stratégie orthogonale pour activer simultanément le CO_2 et les N-réactifs en appliquant respectivement des impulsions de potentiel négatives et positives. Les nanoparticules de Cu sont utilisées comme catalyseur modèle, le CO_2 agit comme réactif C et le NH3 agit comme réactif N pour le couplage C-N. Dans des conditions optimisées dans lesquelles la couverture $*NH_2$ est maintenue à l'état stable tandis que Cu reste métallique, l'électrolyse pulsée augmente à la fois le taux de formation et la sélectivité des produits C-N urée, formamide et acétamide de 3 à 20 fois. En étendant le champ d'application à des réactifs C et N supplémentaires, ainsi qu'au couplage C-S, cette nouvelle approche démontre davantage sa valeur générale en électrosynthèse.

Mots-clés: Électrosynthèse; électrocatalyseur ; Oxydation de la biomasse ; clivage de la liaison C-N ; Réacteur à membrane Pd ; Formation de liaison C-N.

Abstract

In light of climate change and depleting fossil fuel reserves, innovating green and sustainable energy technologies becomes a critical challenge. Chemical manufacturing consumes large amounts of energy and is responsible for a substantial portion of global carbon emissions. Against this backdrop, electrosynthesis, powered by renewable electricity, can replace many industrial thermochemical processes to generate fuels, chemicals, and fertilizers. Rather than focusing on areas that have received much attention in recent years (e.g. water electrolysis and CO_2 reduction), we explored emerging areas within heterogeneous electrosynthesis for which there is a substantial need.

In **chapter 3**, we highlight the importance of designing electrocatalysts with well defined active sites. We report the use of reticular chemistry to design a conductive metal organic framework-based electrocatalytic model system with molecular M-O_4 active sites for electrochemical oxidation of 5-hydroxymethylfurfural (HMFOR). The activity of MOFs bearing Ni-O_4 (Ni-CAT) and Co-O_4 (Co-CAT) active sites were analyzed with electrochemical and *operando* spectroscopic techniques to elucidate the reaction mechanism occurring on the surface. Electrochemical experiments reveal that Co-CAT has an earlier onset potential for enabling HMFOR, relative to most established catalysts, while the Ni-CAT shows faster kinetics for the conversion of 5-hydroxymethylfurfural (HMF) to 2,5-furandicarboxylic acid (FDCA). We determined that Ni-CAT achieved FDCA (our target molecule) yields of 98.7% yield. The faradic efficiency can reach out to 86.8% faradic efficiency. Infrared spectroscopy points to HMF with a surface-bound aldehyde group as the key intermediate in the catalytic cycle, which forms once the M(II\III) oxidation occurs. This work illustrates the advantage of utilizing molecularly defined active sites coupled with *operando* spectroscopy to provide fundamental insights into a variety of electrosynthetic reactions and pave the way for future catalyst design.

Following this project, we turned to the use of a hydrogen-selective membrane reactor to explore more new reaction and catalysts concepts. The key here was using a Pd foil as a material that reduced protons to *H at an aqueous compartment and transferred the hydrogen through to an organic compartment where it hydrogenated the reactant of choice. Using a membrane reactor, we

could physically separate electrochemical hydrogen reduction and hydrogenation chemistry in a manner that circumvented the use of H_2 gas as would otherwise be necessary. We choose a chemical that is industrially produced in excess, acetonitrile, as a starting point. The Pd membrane reactor is applied to fully hydrogenate the C≡N bond of acetonitrile. Successfully, we obtained ammonia and acetaldehyde as reaction products at a record onset potential of 0.4 V vs Ag/AgCl. Finally, by carefully designing a unique spectroelectrochemical cell, we were able to carry out infrared spectroscopic measurements to visualize the reaction process in Pd-membrane and consequently proposed a unique imine-hydrolysis reaction mechanism (**Chapter 4**).

In **Chapter 5**, we choose to innovate in an emerging area: electrochemical C-N bond formation from small molecule reactants (e.g. CO_2, NH_3). The conventional electrochemical C-N bond formation mechanism is based on electrochemical CO_2RR. In this chapter, we propose an orthogonal strategy to simultaneously activate CO_2 and N-reactants by applying negative and positive potential pulses, respectively. Cu nanoparticles are used as a model catalyst, CO_2 acts as the C-reactant, and NH_3 acts as the N-reactant for C-N coupling. Under optimized conditions in which $*NH_2$ coverage is maintained at steady state while Cu remains metallic, pulsed electrolysis increases both the rate of formation and the selectivity of the C-N products urea, formamide and acetamide by 3-20 times. By extending the scope to additional C- and N-reactants, as well as C-S coupling, this new approach further demonstrates its general value in electrosynthesis.

Key words: Electrosynthesis; Electrocatalyst; Biomass oxidation; C-N bond cleavage; Pd-membrane reactor; C-N bond formation.

Table of Contents

List of Figures

CHAPTER 1

CHAPTER 3

CHAPTER 3 SI

CHAPTER 4

CHAPTER 4 SI

CHAPTER 5

CHAPTER 5 SI

List of tables

CHAPTER 3 SI

CHAPTER 5 SI

List of Abbreviations

E_{an}: Anodic Potential

E_{ca}: Cathodic Potential

i_x: Partial Current Density for x

υ_x: volume concentration of x based on the calibration of the GC

A: Surface Area of the Electrode

ACN: Acetonitrile

ATR: Attenuated Total Reflectance

$C_6H_{15}N_3 \cdot 3H_2O$: Acetaldehyde Ammonia Trimer

CA: Chronoamperometry

C_{dl}: Double Layer Capacitance

CE: Counter Electrode

CH_2O: Formaldehyde

CO_2RR: Electrochemical Carbon Dioxide reduction reaction

CV: Cyclic Voltammetry / Cyclic Voltammogram

DFF: 2,5-Diformylfuran

DFT: Density Functional Theory

DMSO: Dimethyl Sulfoxide

EA: Ethyl Acetate

ECSA: Electrochemical Active Surface Area

EDS: Energy-Dispersive X-ray Spectroscopy

F: Faradaic constant, 96485.3499 C mol^{-1}

FDCA: 2,5-Furandicarboxylic Acid

FE: Faradaic Efficiency

$FeCl_3 \cdot 6H_2O$: Iron Chloride Hexahydrate

FFCA: 5-Formyl-2-furancarboxylic Acid

FID: Flame Ionization Detector

FR: Formation Rate

FTIR: Fourier Transform Infrared Spectroscopy

FTO: Fluorine-doped Tin Oxide

GC: Gas Chromatography

GC-MS: Gas Chromatography – Mass Spectrometry

GDE: Gas Diffusion Electrode

H_2SO_4: Sulfuric Acid

HAADF: High Angular Annular Dark-field Imaging

HCl: Hydrochloric Acid

HER: Hydrogen Evolution Reaction

HER: Hydrogen Evolution Reaction

HHTP: 2,3,6,7,10,11-Hexahydroxytriphenylene Hydrate

HMF: 5-(Hydroxymethyl) Furfural

HMFCA: 5-Hydroxymethyl-2-furancarboxylic Acid

HMFOR: Electrochemical 5-(Hydroxymethyl) Furfural Oxidation Reaction

HPLC: High Performance Liquid Chromatography

HSQC: Heteronuclear Single-Quantum Correlation

IR: Infrared Spectroscopy

LSV: Linear Sweep Voltammetry

M-CAT: Metal-catecholates

MOF: Metal Organic Framework

NMR: Nuclear Magnetic Resonance

Pd: Palladium Foil

$PdCl_2$: Palladium Chloride

Q: Total Charge Passed During Electrochemical Reaction

RE: Reference Electrode

RHE: Reversible Hydrogen Electrode

SEM: Scanning Electron Microscopy

SERS: Surface Enhanced Raman Spectroscopy

TCD: Thermal Conductivity Detector

TEM: Transmission Electron Microscopy

TOF: Turnover Frequency

TON: Turnover Number

V: Cell voltage

WE: Working Electrode

XPS: X-ray Photoelectron Spectroscopy

XRD: X-ray Diffractometry

ZIR: Ohmic Drop Correction

Acknowledgement

After finishing my bachelor of Materials Physics degree at the University of Jinan in July 2017, and after several years of exploring, I made a very important decision on relocating from Zibo, China to the beautiful city of Montreal to pursue a Master of Science degree at the University of Montreal. Completing the master's thesis requires a lot of effort in chemistry and this cannot be done successfully without the generous support from my supervisor, my family, and all friend I made in Montreal.

First of all, I would like to express my deep gratitude to my supervisor, Dr. Nikolay Kornienko. Prior to entering graduate school, I always hoped to have a friendly and supportive supervisor, so joining Nick's research group has been one of my best decisions ever! I am grateful to you, Nick, for the valuable advice, patience, and technical support you provided whenever I encountered challenges during my research and experiments. Additionally, the care, kindness, and understanding you showed me when I encountered hardships warmed my heart and helped me overcome the difficulties of living abroad. Although I didn't do well, Nick taught me a lot, such as reading, writing, and summarizing regularly, preparing to learn new techniques, and finding time to support others in the lab. Basically, my professor's help and support motivated me to come to the lab.

Secondly, many thanks to the supportive and inclusive environment that the department of chemistry and my colleagues provided. Working with all the technicians is both pleasant and fun! Without the suggestions and advice from Dr. Loic Mangin, Dr. Pedro Aguiar, Dr. Alexandra Furtos, Dr. Cédric Malveau, Prof Davit Zargarian, and Dr. Daniel Chartrand, I think I can't make it possible to incarnate my research and submit it for publication. They both taught me a lot of technical skills from a varied field of chemistry and willing to share opinions about my research. Special thanks to Jean-Francois Myre, who always wears a smile, is willing to adjust my reaction cell according to my need, and even shows patience whenever I want to find some small tools from the workshop.

Thirdly, I had the pleasure of working with our group members and the students in the inorganic group who provide a welcoming and enjoyable environment: Morgan, Hossein, Junnan, Rajib, Arefh, Jiayi, Matteo, Chris, Kiran, Naser, Romane, Alex, Yanyu. It was really fun and happy to work with them. I would like to thank Aida Mikhno and Marie-Claude Turmel for their responsive and helpful emails in addressing all my questions.

Finally, my biggest thank you to my family and friends who support me wholeheartedly during my graduate study and research at UdeM. Thanks, Shaun, Qingqing, May, Siqi, Shiyu, Emily, Marie, and Martyna, for the various extracurricular activities we had together—it is great fun to explore different restaurants in the city, hiking, and road trips with you guys! They are awesome friends who have an open ear and are willing to share gossip during our spare time. Thanks to Shuang for constantly pushing and accompanying me to go to the gym regularly otherwise my belly would be worse. Last but not least, I'm grateful to my parents and grandparents, and little

brother. It is amazing how supportive they are of whatever decision I make and how well they care for my dogs, even though I complain I am not the only kid in the family.

Chapter 1 Introduction

1.1. Energy consumption overview and outlook

In addition to spurring explosive population growth, fossil fuel-powered chemical industries emit significant levels of greenhouse gases[1]. Greenhouse gas emission from the increasing population contributes to climate change, particularly via the greenhouse effect. Carbon dioxide (CO_2) makes up the vast majority of greenhouse gas emission, approx. 79%. The anthropogenic emission of carbon dioxide is due to the burning of fossil fuels, including coal, oil, and natural gas to manufacture chemicals and daily necessities. Compared to pre-industrial levels, human-caused emissions have increased atmospheric carbon dioxide by about 50%. To mediate climate warming and meet the energy demand of the ever-increasing human population, sustainable technologies must be developed to reduce greenhouse gas emissions and overhaul our energy systems.

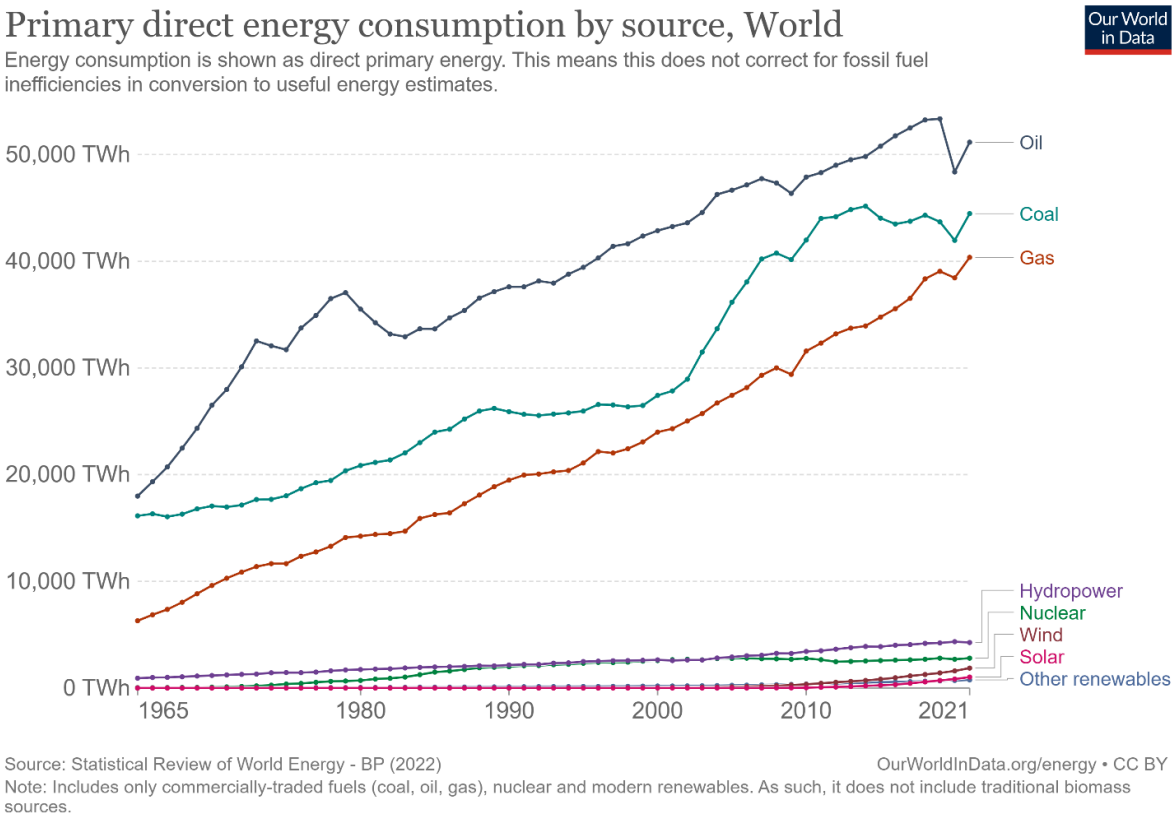

Figure 1-1. Primary direct energy consumption by source, World. The definition of primary energy supply is energy production plus energy input. It is classified into two groups: non-renewable (oil, coal, gas) or renewable (hydropower, nuclear, wind, solar, and others) on the basis of whether they are limited supplies. Figure sourced from Statistical Review of World Energy[2].

Globally, 85.4% of the global energy demand comes from fossil fuels, such as oil, coal, and gas, whereas renewable energy such as hydropower and nuclear power constitute less than 15% of the total. The use of clean, renewable energy and energy-efficient technologies can be a good solution to reduce global CO_2 emissions, and by doing so we can slash fossil fuel production, consumption, and pollution. It is possible to replace fossil fuel energy with renewable energy using "cap and invest" programs, carbon pricing, and carbon capture, storage, and utilization technologies (the process of permanently burying carbon dioxide underground or converting it to produce other useful chemicals after it is captured from emissions sources such as power plants or from the atmosphere).

1.2. Electrolysis as a sustainable route to generate fuels and chemicals

Chemistry can, without a doubt, help reduce greenhouse gas emissions and CO_2 levels in the atmosphere by supplying a variety of solutions. The chemical industry requires large amount of energy supply and features a large quantity of carbon emissions from processes such as production of plastic products (e.g., poly(ethylene-terephthalate) (PET) plastics), and commodity chemicals products (e.g., H_2, CH_4, NH_3). For example, a well- known chemical process - the Haber-Bosch process, is responsible for about 1.4% of the annual CO_2 emissions, as the supplied H_2 is derived from steam reforming of methane. Almost 50% of hydrogen is produced via stream reforming and used to feed ammonia production, consisting of 180 million tons in 2022. Both the Haber-Bosch process and steam reforming need to break stable chemical bonds, which often means those processes require high temperature and high pressure to achieve these transformations. Fossil fuel combustion is usually responsible for providing energy for those harsh reaction conditions. Therefore, to achieve carbon neutrality, chemistry can contribute by modifying the process of chemical manufacturing to make it more sustainable.

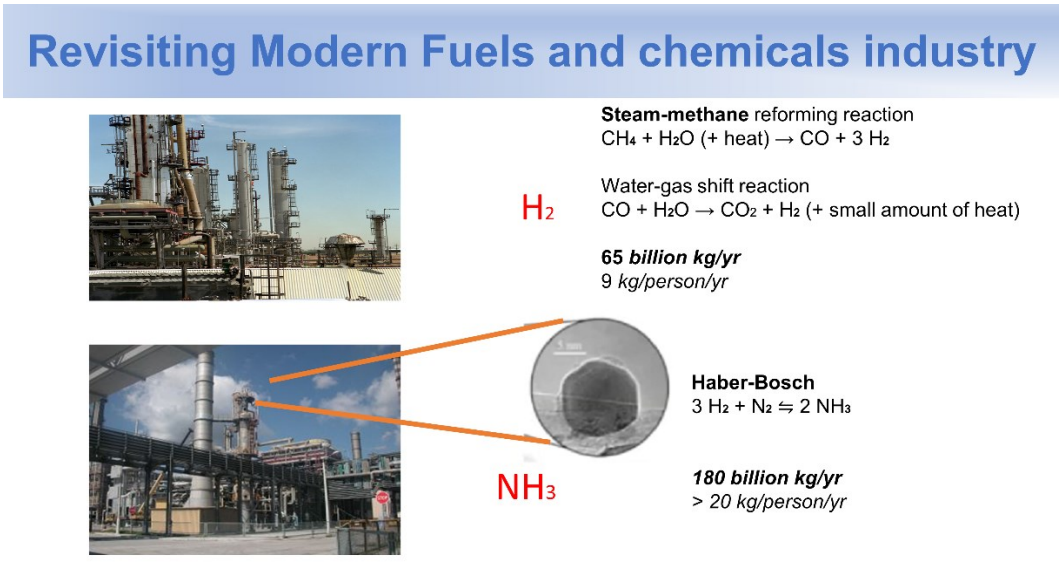

Figure 1-2. Revisiting the modern fuels and chemistry industry. Examples of chemistry process responsible for majority of carbon dioxide emission such as Haber-Bosch Process.

A future scenario is to turn waste, CO2, and air into precious resources to achieve a solar-powered carbon-neutral economy and society using the chemistry method. As a promising method, electrification of the traditional fossil fuel-driven chemical process to synthesize chemicals would be an ideal solution for minimizing the emission of greenhouse gases and providing necessary chemicals and energy to the society. This could be explained in two reasons: 1) the cost of renewable energy continues to decline, replenished energy such as solar, wind and so on, become more and more cost-competitive with the marginal cost of selected existing conventional generation technologies (Figure 1-3); 2) electrochemistry entails accurate control of a chemical reaction by simply tuning the applied potential and is capable to transfer energies more efficiently than traditional technologies, thus avoiding numerous waste product such as CO_2 emission. For example, the electrochemical water splitting as a replacement for steam reforming to produce H_2 will not produce any CO_2.

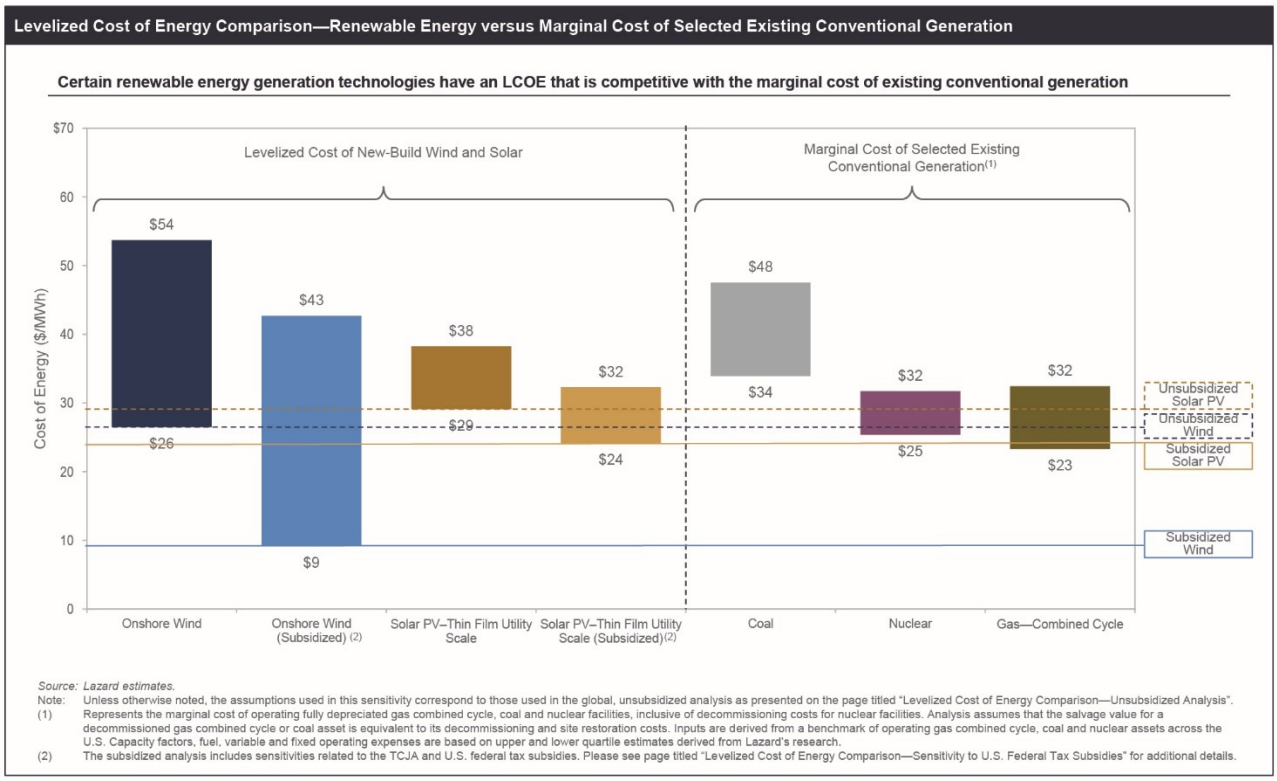

Figure 1-3. Levelized cost of energy comparison – Renewable energy versus marginal cost of selected existing conventional generation. The cost of wind and solar is competitive with the marginal cost of coal, nuclear and combined cycle gas generation. Figure sourced from Lazard Estimate[3].

With its invention at the beginning of the 18th century, electrolysis has gradually become a mature technology in fields like energy storage and chemical synthesis (e.g. batteries and the chloro-alkali process). Electrochemistry's success can be attributed to the precise control of the

potential applied to electrodes to modulate the selectivity of target reactions. By applying an external potential, chemicals could be driven far from thermodynamic equilibrium, leading to reaction pathways that otherwise would not occur spontaneously. In addition, electrolysis is often more energy efficient than traditionally used fossil fuel-powered harsh conditions reactions, making it a potentially sustainable alternative to fossil fuels for chemical synthesis. As an example, Haber-Bosch nitrogen fixation releases CO_2 by producing ammonia under high pressure (200 atmospheres) and high temperatures (400 °C), while electrochemistry reduces N_2 bonds to produce ammonia at room temperature. In addition to benefiting agriculture and the environment with less greenhouse gas emissions, this technology could serve as a hydrogen storage method to store energy.

1.3. Emerging directions and techniques in electrolysis

With a growing emphasis on renewable energy, electrosynthesis technologies have the potential to power our modern society in a clean and renewable way. Although electrosynthesis has been extensively researched in the last decade in directions such as water electrolysis and CO_2, its scope can be greatly expanded to encompass a broad range of chemical targets that can be used as building blocks for materials, pharmaceuticals, fertilizers, and so on. The knowledge and insights we get from the electrochemical water splitting and CO_2RR can be a good reference to translate to emerging fields. Particularly, HMF oxidation and CO_2 based C-N bond coupling, and cleavage represent two under-developed areas that are becoming more popular. It is therefore essential to develop novel reaction routes and catalytic systems that circumvent conventional electrocatalysis limitations.

Electrochemical reduction of CO_2 (CO_2RR) using renewable sources of electrical energy holds promises for both converting CO_2 to fuels and feedstocks and closing the carbon cycle. The general key insights get from the CO_2RR reaction transfer into other emerging new field like C-N bond formation and C-S bond formation via electrochemically activating small molecule.

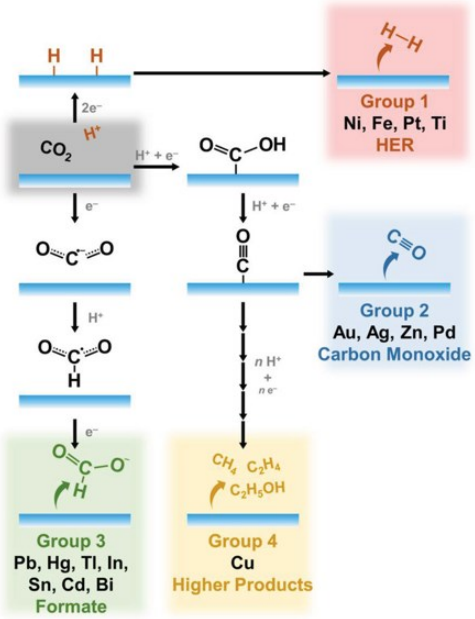

Figure 1-4. Overall reaction mechanism of electrochemical CO_2 reduction reaction and HER on metal electrodes in aqueous solution[4]. Reproduced with permission from 2020 Advanced Materials.

Given that the CO_2R is a multielectron and multiproduct process, an ideal electrocatalyst should be capable of transferring CO_2 with high current density as well as high selectivity. Based on the analysis of the selectivity toward specific products, we can classify the heterogenous metal catalysts into four categories: Pb, Hg, In, Sn, Cd, Bi are mainly producing formate ($HCCO^-$); Au, Ag, Zn, and Ga show selectivity towards carbon monoxide (CO); Ni, Fe, Pt, Ti exhibit better selectivity for the competing reaction for CO2RR-more favorable to H_2[5]. Copper presents a unique ability to catalyze the formation of multi-carbon containing fuels and chemicals, such as ethylene and ethanol, which is valuable both as a clean fuel and feedstock of chemical industry[4]. However, designing active sites on Cu with significant selectivity for a single high-value product while reducing the energy requirements (overpotential) remain as challenges.

CO_2RR on Cu is highly complex as it involves multiple competing reaction pathways: transferring multiple protons and electrons. For achieving the commercial goal of this green technology, we need to understand the mechanisms of the CO_2RR further and based on this mechanism design a high-energy current density catalysis with optimized selectivity and reactivity. Even though the catalyst's discovery can significantly be accelerated using the emerging technology of computational catalyst design, its applicability to CO_2RR has been hampered mostly by explaining experiment trends, rather than predicting novel materials. This situation origins from a limited mechanistic understanding of this kind of reaction as multiple factors could influence product distribution.

1.3.1. Electrochemical biomass upgrading

Aside from relatively well-established water electrolysis and CO_2 reduction reactions, electrochemical upgrading of biomass platforms into new fuels and components of polymers and pharmaceuticals is an emerging but poorly understood area. 5-Hydroxymethylfurfural (HMF) is a highly valuable platform chemical that obtains from waste lignocellulose biomass. Oxidizing HMF (HMF oxidation reaction, HMFOR) electrochemically to 2,5-furan dicarboxylic acid (FDCA) can be achieved in ambient pressure and aqueous conditions[6]. Compared with conventional poly (ethylene terephthalate), FDCA is a superior building block to produce plastics due to its better chemical and gas barrier properties. This HMFOR can offer a promising way of transferring the established wind or solar electricity due to its value of the derived product is >10X higher than simple products from water electrolysis (H_2) and CO_2 reduction, and this technology can replace the anodic water oxidation in the aforementioned system to simultaneously co-generate value-added products on the anodic and cathodic sides (Figure. 1-5)[7].

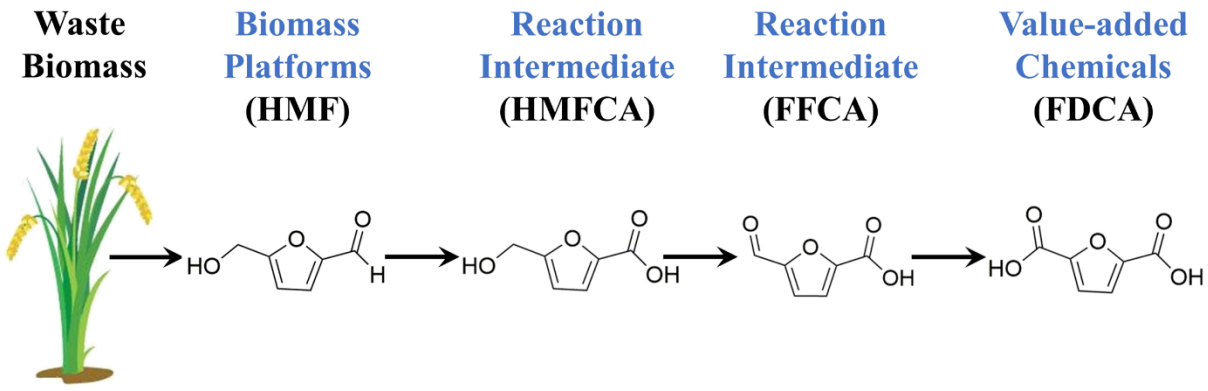

Figure 1-5. The overall scheme of renewable energy used for biomass valorization.

To make the technology economically viable, a proper mechanistic understanding of the reaction pathways and identification of reactive sites are critical. However, the clear identification of the catalytic active sites on state-of-the-art transition metal oxide catalysts and the elucidation of the reaction mechanisms in HMFOR remain elusive. Therefore, in **Chapter 3**, we wish to develop a tunable electrocatalyst model system that has well-defined active sites to obtain mechanistic understanding towards electrochemical biomass valorization.

1.3.2. C-N bond formation via electrocatalysis.

There are exciting achievements in CO_2RR both experimentally and computationally, leading to both enhanced understanding and improvement of performance. Based on the gradually maturation of CO_2RR technologies, fine chemical synthesis is drawing attention. These routes often involve coupling of CO_2 with other intermediates[8] or further reacting with downstream products[9,10] High-demand chemicals such as urea, amine, and amide, for example, could be

produced via the electrochemical CO_2 with NH_3[11], nitrite, nitrate[12], even N_2[13], which endowed CO_2RR with new potential in the synthetic community.

To reach the goal of CO_2 industrial utilization, many efforts have been made to increase selectivity for a specific reaction product. The outcome of CO and HCOOH has realized pilot plant scale because of its faradic efficiency (~100%) at an industrial current density (0.5 A cm^{-2}) and easy storage/transportation process[14,15]. CO_2 derived CO or HCOOH can be converted into high-value chemicals, which expands the scope of high-valued products available CO_2RR. Electrochemically reducing CO with NH_3 capable of producing acetamide with nearly 40% Faradic efficiency[9]. The reaction mechanism involves nucleophilic addition of NH_3 to a surface-bound ketene intermediate supported by full-solvent quantum mechanical calculations. Chengying Guo et al report an electrochemical process to transform HCOOH and nitrite into high-valued formamide over a copper catalyst. The selectivity to formamide can reach 90 % and illustrate the key C-N bond formation through coupling *CHO and *NH_2 intermediates[16].

We published a review paper to summarize some new achievement in this emerging field and point out several key strategies for improve the selectivity by lend insights from the conventional C-N bond formation ways: both in the field of biology and organic chemistry[17]. For now, most of the work is center in catalyst design, such as oxygen vacancy engineering and the selection of suitable materials[18,19]. In spite the above-mentioned pioneering works, the products derived from C-N coupling are still limited and most of the current reactions are heavily rely on the nucleophilic attack of the chosen nitrogenous small molecules. In **Chapter 5**, we would introduce a simple way to facilitate the C-N bond formation via the application of a pulsed potential. The pulsed electrolysis method presented here has previously been applied to CO_2RR, along with altering the local reaction static field, affecting the catalyst structure and oxidation status, and modulating the relative surface coverage of key intermediates. The purpose of our research, however, is to introduce a fundamentally different strategy to overcome the limitations of the nucleophilicity of chosen N-species. By precisely tuning the electrochemical potential, NH_3 is activated to produce higher nucleophilicity chemicals-NH_2 (Figure 1-6), facilitating the reaction pathway towards C-N bond products, as opposed to CO_2.

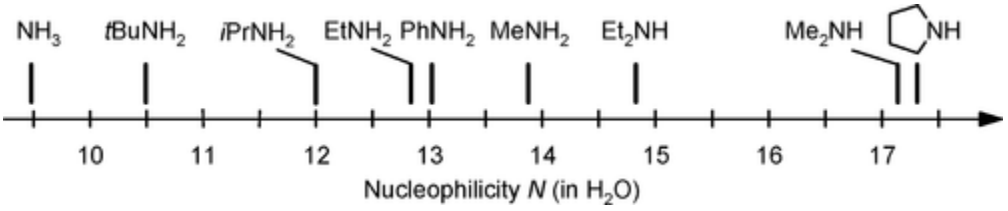

Figure 1-6. As the principal step in heterogeneous electrocatalytic C-N formation typically involves the nucleophilic attack of a nitrogen species at an electrophilic carbon centre, the nucleophilicity of the nitrogenous reactant or intermediates can have a determining role in the reaction selectivity[20]. Reproduced with permission from 2007, American Chemical Society.

1.3.3. C-N bond cleavage

Similar to the formation of C-N bonds, the breaking of C-N bonds is also a central topic in organic chemistry, organometallic chemistry, and biochemistry. For example, both the process of forming proteins from amino acids through C-N bonds and the reverse process of cleavage from amino acids to proteins through amide C-N bonds in the presence of enzymes are essential to life. Understanding how to break C-N is essential for designing the corresponding reactions to explore efficiently carbon and/or nitrogen sources with a synthetic purpose. Cleavage of the C-N bond remains a challenge due to the high bond dissociation energy and considerable molecular stability for chemical transformation, in particular, the C≡N bond in nitrile. Although the activation of the C-N bond has attracted increasing attention in the field of organometallic chemistry, the difficulties in activating unstrained nitriles are still evident and two approaches should be considered: 1) more powerful reaction systems are required for the activation of thermodynamically stable nitriles in ambient conditions; 2) Mechanistic understanding of C-N bond cleavage is still unclear. This content emphasizes the recent electrochemical method of upgrading nitrile since electrochemical potential provides the driving force in breaking C-N bond under ambient conditions in an efficient, simple, and eco-friendly way.

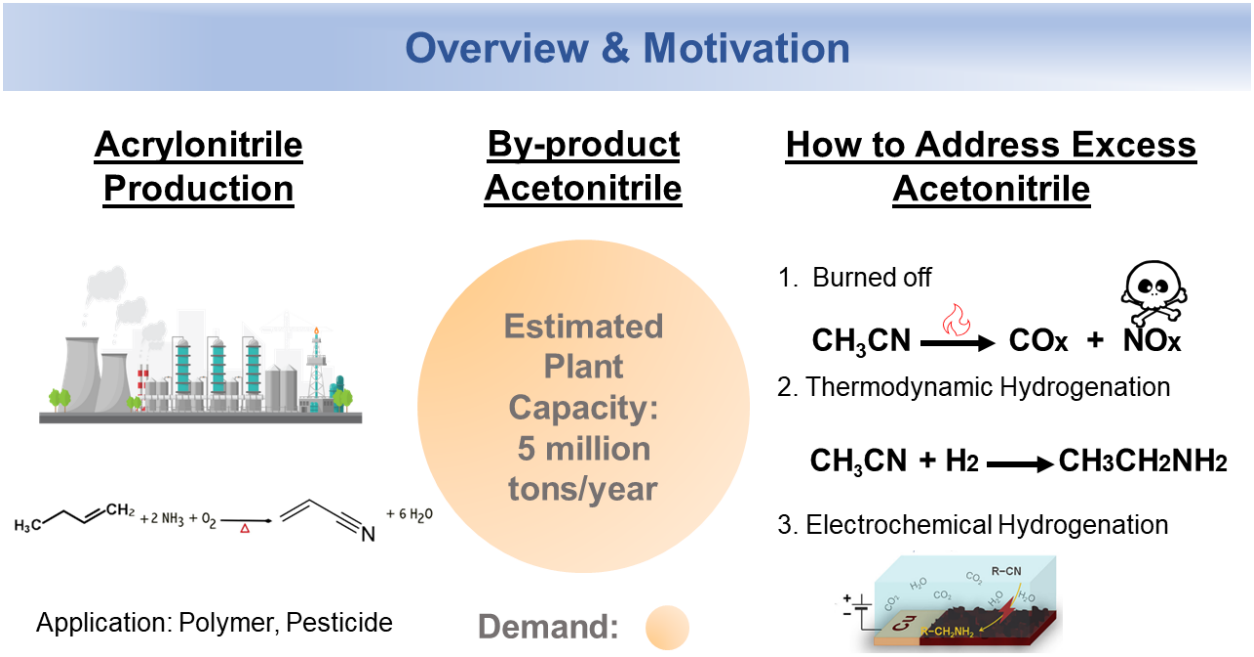

Figure 1-7. The overall motivation of addressing the by-product in acrylonitrile production.

Amines may also be produced by direct hydrogenation of nitrile. This route provides a sustainable and environmentally friendly method for converting excess acetonitrile production capacity, as well as a convenient way of storing hydrogen. Acetonitrile is often generated in huge excess from acrylonitrile synthesis and primarily burned off, with massive toxic NO_x species

release (Figure.1-7). More recently, homogenous cobalt-based molecular catalysts (Figure. 1-8) were adapted to electrochemically reduce acetonitrile to ethylamine using acetic acid as a hydrogen source in organic electrolytes[21]. This work presents an interesting perspective that catalysts designed for hydrogen evolution reaction are potentially suitable for electrocatalytic hydrogenation for the C≡N bond. However, electrochemical reduction of nitrile suffers from low faradic efficiency and selectivity. Inspired by metallic catalysts which exhibit enhanced amine selectivity in thermocatalytic C≡N bond cleavage, several metal catalysts are initially screened in a flow cell electrolyzer to determine the optimal catalysts for the electrochemical approach for acetonitrile reduction. The maximum FE of ~95% for ethylamine is achieved at −0.29 V_{RHE} on Cu nanoparticle catalysts. The reaction mechanism is investigated by computational study, which suggests the high ethylamine selectivity on Cu is due to the moderate binding affinity for the reaction intermediates. This work illustrates a moderate adsorption of MeCN on the surface via the C ≡ N group is necessary to enhance the hydrogenation process and preserve the hydrogenated C-N bond[22].

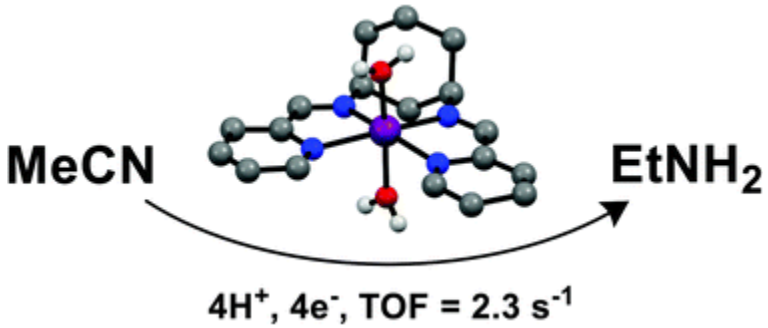

Figure 1-8. New cobalt bis-iminopyridines, [Co(DDP)(H2O)2](NO3)2 (1, DDP = **cis**-[1,3-bis(2-pyridinylenamine)] cyclohexane) electrocatalysis the 4-proton, 4-electron reduction of acetonitrile to ethylamine. Reproduced with permission from the 2019 Royal Society of Chemistry.

To break the C ≡ N bond and obtain high selectivity for useful products like $EtNH_2$, another aspect needs to be considered: preventing the condensation reaction between the imine intermediates and the generated primary amine during the reaction. A proof-of-concept work introduced CO_2 into the electrolyte to protect the initially formed $EtNH_2$ on the surface by forming carbamic acids, contributing a further improvement in the amine selectivity. The synergy of the Cu catalyst and the CO_2 saturated in aqueous successfully obtain a selectivity of 99% for $EtNH_2$, with a total Faradaic efficiency (FE) up to 94%[23].

Instead of primary amines[24], the electrochemical cleavage of C ≡ N also terminate at ammonia, which represents a more challenging reaction pathway. Since amines belong to unreactive classes of organic compounds which preserve high C–N bond dissociation energy. We will discuss a strategy of utilizing a Pd-membrane reactor in **Chapter 4**, and thus enable the hydrogenation to be carried out in a predominantly organic environment. In the Pd-membrane

reactor, protons from acidic electrolytes were reduced to hydrogen species on the surface of Pd, and the hydrogen atoms migrated through the Pd to reach the acetonitrile solution, at which point they subsequently hydrogenated acetonitrile to terminate at ammonia and acetaldehyde products in a newly discovered reaction pathway. An innovative infrared spectroelectrochemical setup was further utilized to probe the catalytic system as it functioned to extract out key mechanistic insights dictating the reaction process. It was determined that the reaction proceeds rapidly through an imine hydrolysis like pathway and the hydrogenation of the latent NH_x species on the Pd surface is the slowest step in the reaction cycle. Overall, this work opens up new avenues in electrochemical cleavage the $C \equiv N$.

1.4. Reference

1 Perera, F. Pollution from Fossil-Fuel Combustion is the Leading Environmental Threat to Global Pediatric Health and Equity: Solutions Exist. *Int J Env Res Pub He* **15** (2018).

2 Dale, S. *bp Statistical Review of World Energy*, <https://www.bp.com/en/global/corporate/energy-economics/statistical-review-of-world-energy.html> (2022).

3 Estimate, L. *Levelized Cost Of Energy, Levelized Cost Of Storage, and Levelized Cost Of Hydrogen*, <https://www.lazard.com/perspective/levelized-cost-of-energy-levelized-cost-of-storage-and-levelized-cost-of-hydrogen/> (2023).

4 Tomboc, G. M., Choi, S., Kwon, T., Hwang, Y. J. & Lee, K. Y. Potential Link between Cu Surface and Selective CO2 Electroreduction: Perspective on Future Electrocatalyst Designs. *Adv Mater* **32** (2020).

5 Zhi, X., Jiao, Y., Zheng, Y., Vasileff, A. & Qiao, S. Z. Selectivity roadmap for electrochemical CO2 reduction on copper-based alloy catalysts. *Nano Energy* **71** (2020).

6 Barwe, S. *et al.* Electrocatalytic Oxidation of 5-(Hydroxymethyl)furfural Using High-Surface-Area Nickel Boride. *Angew Chem Int Ed Engl* **57**, 11460-11464 (2018).

7 You, B., Liu, X., Jiang, N. & Sun, Y. J. A General Strategy for Decoupled Hydrogen Production from Water Splitting by Integrating Oxidative Biomass Valorization. *J Am Chem Soc* **138**, 13639-13646 (2016).

8 Li, J. Y., Song, Q. W., Zhang, K. & Liu, P. Catalytic Conversion of Carbon Dioxide through C-N Bond Formation. *Molecules* **24** (2019).

9 Jouny, M. *et al.* Formation of carbon-nitrogen bonds in carbon monoxide electrolysis. *Nature Chemistry* **11**, 846-851 (2019).

10 Guo, C. Y. *et al.* Electrochemical Upgrading of Formic Acid to Formamide via Coupling Nitrite Co-Reduction. *J Am Chem Soc* (2022).

11 Li, J. N. & Kornienko, N. Electrochemically driven C-N bond formation from CO2 and ammonia at the triple-phase boundary. *Chem Sci* **13**, 3957-3964 (2022).

12 Lv, C. D. *et al.* Selective electrocatalytic synthesis of urea with nitrate and carbon dioxide. *Nat Sustain* (2021).

13 Chen, C. *et al.* Coupling N2 and CO2 in H2O to synthesize urea under ambient conditions. *Nature Chemistry* **12**, 717-724 (2020).

14 Shi, Y. M. *et al.* Unveiling hydrocerussite as an electrochemically stable active phase for efficient carbon dioxide electroreduction to formate. *Nat Commun* **11** (2020).

15 Shi, Y. *et al.* Unveiling hydrocerussite as an electrochemically stable active phase for efficient carbon dioxide electroreduction to formate. *Nat Commun* **11**, 3415 (2020).

16 Guo, C. *et al.* Electrochemical Upgrading of Formic Acid to Formamide via Coupling Nitrite Co-Reduction. *J Am Chem Soc* **144**, 16006-16011 (2022).

17 Li, J. N., Zhang, Y. X., Kuruvinashetti, K. & Kornienko, N. Construction of C-N bonds from small-molecule precursors through heterogeneous electrocatalysis. *Nat Rev Chem* **6**, 303-319 (2022).

18 Lv, C. D. *et al.* A Defect Engineered Electrocatalyst that Promotes High-Efficiency Urea Synthesis under Ambient Conditions. *Acs Nano* **16**, 8213-8222 (2022).

19 Wei, X. X. *et al.* Oxygen Vacancy-Mediated Selective C-N Coupling toward Electrocatalytic Urea Synthesis. *J Am Chem Soc* (2022).

20 Brotzel, F., Chu, Y. C. & Mayr, H. Nucleophilicities of primary and secondary amines in water. *J Org Chem* **72**, 3679-3688 (2007).

21 Child, S. N. *et al.* Cobalt-based molecular electrocatalysis of nitrile reduction: evolving sustainability beyond hydrogen. *Dalton Trans* **48**, 9576-9580 (2019).
22 Xia, R. *et al.* Electrochemical reduction of acetonitrile to ethylamine. *Nat Commun* **12** (2021).
23 Zhang, D. *et al.* Highly efficient electrochemical hydrogenation of acetonitrile to ethylamine for primary amine synthesis and promising hydrogen storage. *Chem Catalysis* **1**, 393-406 (2021).
24 Bian, X. Q. *et al.* Single-atom transition metals supported on defective graphene for electrochemical reduction of acetonitrile to ethylamine. *Appl Surf Sci* **599** (2022).

Chapter 2 Methodologies for pioneer new electrosynthesis reaction systems

In many emerging avenues of electrolysis, the catalysts for converting reactants into desired products are not yet selective and efficient enough to make it economically competitive with fossil fuel-based methods. For example, heterogeneous catalysts typically used in CO_2R have multiple active sites on their surfaces that bind CO_2 and/or H^+ from water with different affinities. Depending on the energy landscape of the reaction on the surface of the material, the various reaction steps (*electron* transfer, hydrogenation, C-C coupling) may occur and their precise rates and order will dictate the product distribution[1]. Controlling multi-step reactions, is rather difficult, and consequently most catalytic materials produce a wide array of products. Furthermore, while it would be ideal to have independent control over the free energy and binding strength of each intermediate in the reaction pathway, most intermediates share a similar metal-carbon or metal-oxygen bond and therefore their free energies scale linearly with respect to one another as the catalyst surface is altered according to so-called scaling relationships. Thus, multiple catalysts design strategies and materials characterization method are in development to enhance understanding and consequently increase selectivity to desired products. In this chapter, we introduce key aspects that go into the design of active sites, cell engineering, and reaction modulation.

Research strategies to address challenges in electrosynthesis have concentrate on the increasing the catalysts selectivity through the design of catalysts structure[2] and morphology (nanostructure or facet effect)[3], composition (bimetallic catalysts)[4,5], modifying electrolyte composition (pH, different cation)[6], or the cell design (fuel cell, membrane cell)[7]. Those design strategies could modify absorbate coverage, promoting mass transport, or turning the electronic structure by oxidation or defect engineering[8].

2.1. Catalyst design and material characterization

Electrolysis was an ideal strategy to deal with resource depletion issues and close the carbon cycle. However, designing rational catalysts with both high efficiency and selectivity to achieve commercial purpose remains a giant challenge. Facet effects[9], oxidation states tuning[10], and secondary coordination sphere effects could be effective strategies to modulate electrocatalysts electronic structure, therefore promote its catalytic behavior. However, underpinning the future success of electrolysis in the fundamental understanding of the catalysts. Many catalyst systems have rather poorly defined surfaces that may also contain a range of distinct active sites and coordination motifs[11]. Materials, whether amorphous or crystalline, may feature flaws, undercoordinated sites, surface-exposed crystalline facets, and other heterogeneities. Key insights are difficult to draw from fundamental as a result. Particularly, in such materials, electrocatalytic activity cannot be attributed to a particularly active site or surface motif. Without pinpointing the active site, it is more challenging to detect intermediates using spectroscopy. Additionally, when

there are a variety of different active site types, modeling attempts are less obviously tied to experimental results.

To this end, many efforts towards designing and implementing atomically precise active sites, combined with electrochemical analysis, in situ spectroscopic, and theory investigation to decipher individual actives sites' function[12]. In such a study, active sites could be investigated one by one in order to gain a deeper understanding of electrode/electrolyte reactions, thereby laying the groundwork for their eventual application. In **Chapter 3**, we introduced a work developing a metal-organic framework (MOF)-based electrocatalyst as a model system for electrochemical biomass valorization[13]. We used this MOF to oxidize 5-Hydroxymethylfurfural (HMF), a platform chemical derived from waste lignocellulose biomass to obtain 2,5-furan dicarboxylic acid (FDCA), a green polymer precursor. We first engineered the coordinatively unsaturated transition metal active sites into conductive MOF to explore its electrochemical behavior to HMF. This system was successful in converting HMF to FDCA with Faradaic efficiencies above 90%. Subsequently, we applied *operando* infrared spectroscopy to precisely analyze how the active sites interacted with reactants through the reaction cycle and identified the rate-limiting steps in the process. This work stands to elevate the community's understanding of MOF electrochemistry, biomass valorization, and the translation of *operando* vibrational spectroscopic techniques to electrochemical systems.

XRD, SEM, and high-resolution TEM, could be employed to observe the crystal structure, morphology, and the surface facets exposed to reactants under operating conditions. Standard electrochemical techniques would be used to evaluate the catalysts' performance (cyclic voltammetry, chronoamperometry). Further, binding motifs to catalytic sites, distributions of reaction intermediates, and rate-limiting steps in the catalytic cycle can all be elucidated. Finally, we apply XPS and XRD to characterize the electronic and physical structure of the catalysts after extended reaction times to probe any catalysis induced changes.

2.2. Cell engineering: H-membrane reactor

Instead of focusing on the catalysts, there are numerous work focus on engineering cell structure to change the mass transport of the electrochemical reaction. Among the cell engineering, the membrane reactor is promising innovative technology as it could integrate a chemical conversion process with a membrane separation process to separate reactants and products.

The use of intercalation materials for reactant delivery such as Pd-hydride membrane delivering hydrogen for electrochemical hydrogenation of organic species[14]. Curtis Berlinguette's group report the use of an electrolytic palladium membrane reactor to pair a hydrogenation reaction at a palladium membrane with an electrochemical oxidation reaction[15]. The use of a dense palladium membrane as an alternative to performing paired electrolysis reactions enables the integration of two otherwise incompatible reactions. The architecture of the reactor consists of a chemical compartment and two electrochemical compartments. The electrochemical membrane reactor architecture places the hydrogen content of Pd under electrochemical control to enable facile tuning of interstitial hydrogen content, thereby offering a means of controlling reaction rate and selectivity over the degree of chemical hydrogenation. They selected the oxidation of 4-methoxybenzyl alcohol (anisyl alcohol) to 4-methoxy benzaldehyde (anisaldehyde) in tandem with

the hydrogenation of 1-hexyne to 1-hexene as proof-of-concept reactions. The starting materials in both chambers react quantitatively over 5 hours of electrolysis, and selectivity $\geqslant$ 95% can be achieved for 4-methoxy benzaldehyde and 1-hexene with control of reaction conditions. This reactor assembly offers the opportunity to utilize electricity to drive hydrogenation reactions without the complications associated with handling hydrogen gas. The tunable selectivity of the hydrogenation reaction by altering current and electrolyte may also enable the ability to change product selectivity under *operando* conditions without having to modify the catalyst or the system.

The introduction of Pd membrane reactor is versatile and can work with chemicals that are not soluble in aqueous electrolyte. The key here was using a Pd foil as a material that reduced protons to *H radicals at an aqueous compartment and transferred the hydrogen to an organic compartment where it hydrogenated the reactant of choice. Because the aqueous and organic part are separate, the product separation is much easier than the conventional electrochemical way.

2.3. Pulsed electrolysis

The application of voltage pulses stands as a simple yet elegant method to enhance the efficiency of electrolysis[16]. By varying the profile of the applied potential (time duration, symmetry, anodic potential, and cathodic potential), the pulse impacts reactant concentration at the electrode surface, catalyst surface oxidation, and the electrical double layer. Most work for now are focused on the CO_2RR and the most common catalysts is copper, although silver and Pd have also been investigated. While the pulsed potential is versatile, its underlying mechanism and the control method is still in the development as it involves several processes that occur simultaneously.

Compared to potential static electrolysis conditions, the product selectivity has a major shift eg with applied voltage pulses in the millisecond time regime, syngas ($CO+H_2$) has a pulse-time-dependent molar ratio[17]. By controlling the pulse duration and suppressing the competing reaction of water electrolysis, selectivity increases for CH_4 and CO have also been reported[18]. Also, this method has been shown to improve the stability of catalysts in some cases[19]. The effect of turning oxidation state of copper also been illustrated by *in situ* X-ray adsorption near-edge spectroscopy (XANES)[20,21]. The selectivity changes to multi-carbon products have been attributed to the proton rearrangement and accumulation of surface OH^- absorption promote the CO* absorption[22]. The adaption of gas diffusion cell and pulsed electrolysis is also interesting and applied different potential might have different mechanism of selectivity changes[21,23].

2.4. Developing *operando* spectroscopic techniques to extract key reaction mechanisms

Most materials and devices typically operate under specific environmental conditions, many of them highly reactive[24]. Heterogeneous catalysts, for example, work under different atmosphere or in acidic/ basic solutions. The relationship between surface structure and composition of materials during operation and their chemical properties needs to be established in order to understand the mechanisms at work and to enable the design of new and better materials[25]. Although studies of the structure, composition, chemical state, and phase transformation under working conditions are challenging, progress has been made in recent years in the development of new techniques that

operate under a variety of realistic environments[26]. With them, new chemistry and new structures of materials that are only present under reaction conditions have been uncovered[27].

Electrolysis can analysis in parallel with in situ spectroscopy to determine reaction intermediates adsorbed on electrode surfaces as well as evolution of electrode surface. The main techniques involved in this thesis are vibrational (Raman Spectroscopy and FTIR spectroscopy), electronic spectroscopies and XRD.

As research into novel electrocatalytically system has expanded, it is clearly of great scientific interest to visualize the electrodes of electrochemical cells at all stages in their developmental lifecycle to extract performance gains and maximize their stability, selectivity, and performance. Through *in-situ* and operando spectroscopy, both catalysts microstructures and reaction intermediates can be visualized as a function of variables such as state of charge and time and conditions such as high pka or temperature difference. We believe that in-situ and operando spectroscopy has continually growth potential in the design and engineering of new electrocatalytically system.

In addition to qualitative observations on electrode structure and reaction intermediates, techniques such as in situ Raman can be used to track pH gradient and quantify the CO_2 utilization within the electrodes. With a better understanding of the fundamental processes occurring at the electrodes and how cell conditions and configurations affect these processes, electrode materials can be optimized to improve their stability and performance. Furthermore, we can extract the understanding of electrochemical reaction to instruct the reaction parameter selections, and thus optimize the catalyst reaction outcome.

In this work, the construction of different spectroscopic cells to adapt differently in situ observation condition is another focus. Through the use of conventional electrochemical cells (**Chapter 3**) or Pd hydrogen membrane reactors (**Chapter 4**) or gas diffusion electrode-based cells (**Chapter 5**), we modify and design different systems to adapt to different reaction configurations. The goal in here is to overcome the conventional characterization techniques to capture the transient evolutions of reaction intermediates on the catalyst's surfaces. With the help of *in situ* techniques, we could explore the fascinating chemistry inside that transformation like structural and electronic changes occurring within or on the surface of catalysts and propose an electrosynthesis mechanism behind resultant the small molecule transformations.

2.5. Reference

1 Ross, M. B. *et al.* Designing materials for electrochemical carbon dioxide recycling. *Nature Catalysis* **2**, 648-658 (2019).

2 Nazemi, M., Panikkanvalappil, S. R. & El-Sayed, M. A. Enhancing the rate of electrochemical nitrogen reduction reaction for ammonia synthesis under ambient conditions using hollow gold nanocages. *Nano Energy* **49**, 316-323 (2018).

3 Jung, H. *et al.* Electrochemical Fragmentation of Cu2O Nanoparticles Enhancing Selective C-C Coupling from CO2 Reduction Reaction. *J Am Chem Soc* **141**, 4624-4633 (2019).

4 Ji, Y. L. *et al.* Selective CO-to-acetate electroreduction via intermediate adsorption tuning on ordered Cu-Pd sites. *Nature Catalysis* **5**, 251-258 (2022).

5 Chen, C. *et al.* Coupling N2 and CO2 in H2O to synthesize urea under ambient conditions. *Nat Chem* **12**, 717-724 (2020).

6 Monteiro, M. C. O. *et al.* Absence of CO2 electroreduction on copper, gold and silver electrodes without metal cations in solution. *Nature Catalysis* (2021).

7 Lazouski, N., Chung, M. J., Williams, K., Gala, M. L. & Manthiram, K. Non-aqueous gas diffusion electrodes for rapid ammonia synthesis from nitrogen and water-splitting-derived hydrogen. *Nature Catalysis* **3**, 463-+ (2020).

8 Wei, X. X. *et al.* Oxygen Vacancy-Mediated Selective C-N Coupling toward Electrocatalytic Urea Synthesis. *J Am Chem Soc* (2022).

9 Feng, X., Jiang, K., Fan, S. & Kanan, M. W. A Direct Grain-Boundary-Activity Correlation for CO Electroreduction on Cu Nanoparticles. *ACS Cent Sci* **2**, 169-174 (2016).

10 Li, C. W. & Kanan, M. W. CO2 Reduction at Low Overpotential on Cu Electrodes Resulting from the Reduction of Thick Cu2O Films. *J Am Chem Soc* **134**, 7231-7234 (2012).

11 Taitt, B. J., Nam, D. H. & Choi, K. S. A Comparative Study of Nickel, Cobalt, and Iron Oxyhydroxide Anodes for the Electrochemical Oxidation of 5-Hydroxymethylfurfural to 2,5-Furandicarboxylic Acid. *Acs Catal* **9**, 660-670 (2019).

12 Zhang, Y., Li, J. & Kornienko, N. Towards atomic precision in HMF and methane oxidation electrocatalysts. *Chem Commun (Camb)* **57**, 4230-4238 (2021).

13 Zhang, Y. & Kornienko, N. Conductive Metal-Organic Frameworks Bearing M-O4 Active Sites as Highly Active Biomass Valorization Electrocatalysts. *ChemSusChem* (2021).

14 Delima, R. S., Sherbo, R. S., Dvorak, D. J., Kurimoto, A. & Berlinguette, C. P. Supported palladium membrane reactor architecture for electrocatalytic hydrogenation. *J Mater Chem A* **7**, 26586-26595 (2019).

15 Sherbo, R. S., Delima, R. S., Chiykowski, V. A., MacLeod, B. P. & Berlinguette, C. P. Complete electron economy by pairing electrolysis with hydrogenation. *Nature Catalysis* **1**, 501-507 (2018).

16 Casebolt, R., Levine, K., Suntivich, J. & Hanrath, T. Pulse check: Potential opportunities in pulsed electrochemical CO2 reduction. *Joule* **5**, 1987-2026 (2021).

17 Kumar, B. *et al.* Controlling the Product Syngas H-2:CO Ratio through Pulsed-Bias Electrochemical Reduction of CO2 on Copper. *Acs Catal* **6**, 4739-4745 (2016).

18 Kimura, K. W. *et al.* Controlled Selectivity of CO2 Reduction on Copper by Pulsing the Electrochemical Potential. *Chemsuschem* **11**, 1781-1786 (2018).

19 Jannsch, Y. *et al.* Pulsed potential electrochemical CO2 reduction for enhanced stability and catalyst reactivation of copper electrodes. *Electrochem Commun* **121** (2020).
20 Kimura, K. W. *et al.* Selective Electrochemical CO2 Reduction during Pulsed Potential Stems from Dynamic Interface. *Acs Catal* **10**, 8632-8639 (2020).
21 Timoshenko, J. *et al.* Steering the structure and selectivity of CO2 electroreduction catalysts by potential pulses. *Nat Catal* **5**, 259-267 (2022).
22 Jiang, K. *et al.* Metal ion cycling of Cu foil for selective C-C coupling in electrochemical CO2 reduction. *Nature Catalysis* **1**, 111-119 (2018).
23 Jeon, H. S. *et al.* Selectivity Control of Cu Nanocrystals in a Gas-Fed Flow Cell through CO2 Pulsed Electroreduction. *J Am Chem Soc* **143**, 7578-7587 (2021).
24 Tao, F. & Salmeron, M. In Situ Studies of Chemistry and Structure of Materials in Reactive Environments. *Science* **331**, 171-174 (2011).
25 Tao, F. *et al.* Reaction-Driven Restructuring of Rh-Pd and Pt-Pd Core-Shell Nanoparticles. *Science* **322**, 932-934 (2008).
26 Jeon, H. S. *et al.* Operando Insight into the Correlation between the Structure and Composition of CuZn Nanoparticles and Their Selectivity for the Electrochemical CO2 Reduction. *J Am Chem Soc* **141**, 19879-19887 (2019).
27 Favaro, M. *et al.* Subsurface oxide plays a critical role in CO2 activation by Cu(111) surfaces to form chemisorbed CO2, the first step in reduction of CO2. *P Natl Acad Sci USA* **114**, 6706-6711 (2017).

Chapter 3 Conductive metal-organic frameworks bearing M-O_4 active sites as highly active biomass valorization electrocatalysts

3.1. Abstract

The electrochemical oxidation of the biomass platform 5-hydroxymethyl furfural (HMF) to 2,5-furandicarboxylic acid (FDCA), is an important reaction in the emerging area of renewable energy-powered biomass valorization. A key limitation in this field is the ill-defined nature of the catalytic sites of the highest-performing materials that limits the fundamental insights that can be extracted. To this end, we report the development of a conductive metal organic framework-based electrocatalytic model system with well-defined M-O_4 active sites for electrochemical HMF oxidation. These materials were found to be highly active towards FDCA generation, with product yields of over 95%. In parallel, infrared spectroscopy was employed to capture a surface-bound aldehyde group as the key intermediate in the catalytic cycle, which forms once M(II/III) oxidation occurs. This work illustrates the advantage of utilizing molecularly defined active sites coupled with *operando* spectroscopy to provide fundamental insights into a variety of electrosynthetic reactions and thus paves the way for future catalyst design.

3.1.2. Keywords

Electrocatalysis, biomass valorization, *operando* spectroscopy, HMF oxidation, metal-organic frameworks.

Contribution:

Yuxuan Zhang: designed the project, carried out experiments, processed data, contributed intellectual insights, and wrote the manuscript.

Nikolay Kornienko: supervision, designed the project, carried out experiments, processed data, contributed intellectual insights, and wrote the manuscript.

Conductive metal-organic frameworks bearing M-O_4 active sites as highly active biomass valorization electrocatalysts

Yuxuan Zhang[1] and Prof. Nikolay Kornienko[1]*

[1]Department of Chemistry, Université de Montréal, 1375 Avenue Thérèse-Lavoie-Roux, Montréal, QC H2V 0B3, Canada.

*E-mail: nikolay.kornienko@umontreal.ca

Full Paper

Manuscript received: July 27, 2021; Accepted manuscript online: August 20, 2021

DOI: doi.org/10.1002/cssc.202101587

Reproduced with permission from *ChemSusChem* **2022**,15, e202101587 (7 of 7)

3.1.3. Table of content graphic

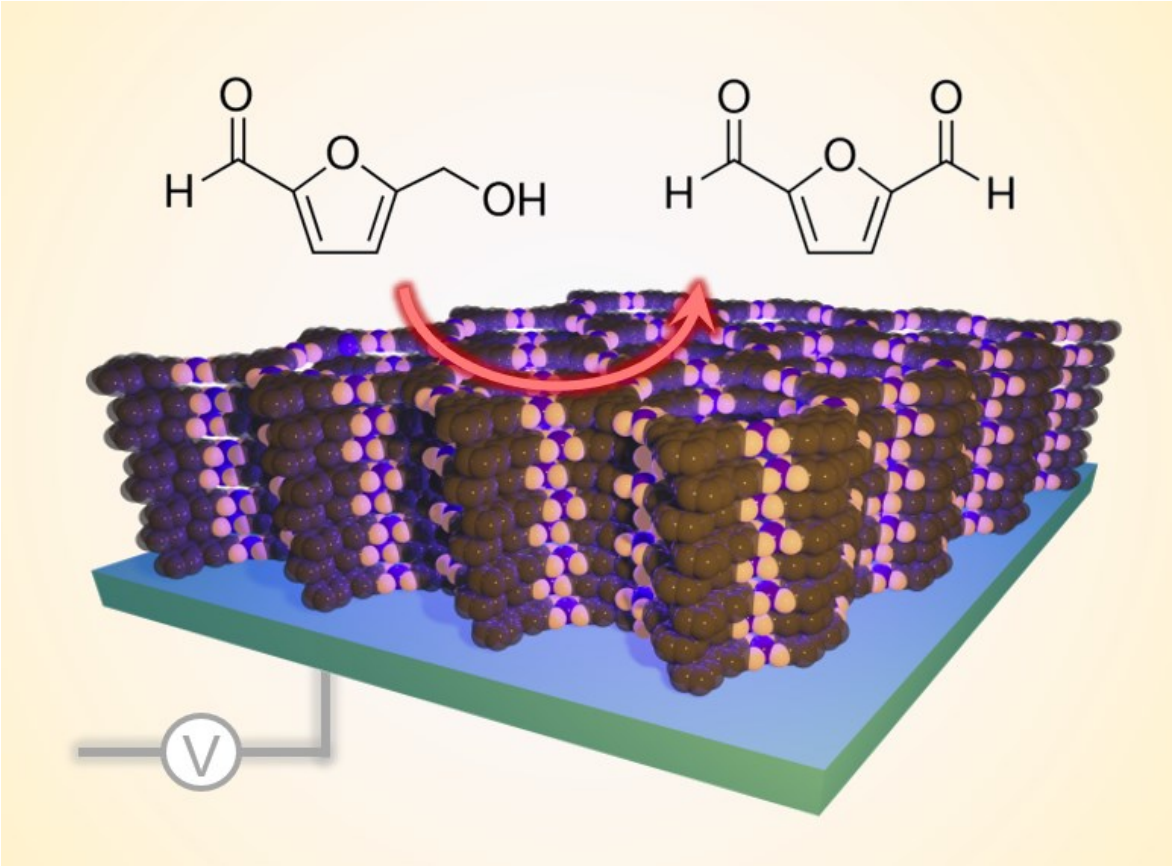

Conductive Framework Electrocatalysts: Conductive MOFs are studied with a combination of electrochemical and spectroscopic techniques. The results indicate that their unsaturated transition metal sites are highly active for the oxidation of biomass platforms (HMF) into value-added chemical products.

3.2. Introduction

The transition to a sustainable society requires developing alternative approaches towards energy conversation and storage technologies.[1] To this end, efforts in generating fuels and value-added chemicals from abundant feedstocks and renewable electricity has significantly grown in recent years.[2,3] While much focus lies in the development of electrocatalytic systems for water electrolysis and CO_2 reduction, there are many other abundant sources that can be harnessed, including methane and biomass. In this work, we focus on the electrochemical upgrading of biomass platforms, chemical derived from waste biomass that can be electrochemically converted into valuable fuels, monomers and fine chemicals.[4-6] While the payoff can be high, considering the value of the products, this set of reactions is much less understood, impeding the rational design of next-generation systems.

Within the context of biomass valorization, our work concentrates on the oxidation of 5-hydroxymethylfurfural (HMF), a biomass platform chemical obtained from hexose and pentose sugars that can be upgraded to useful products.[7,8] Notably, 2,5-furan dicarboxylic acid (FDCA), generated from the oxidation of HMF, is an emerging building block to used produce plastics and possible alternative to polyethylene terephthalate (PET)-based materials.[9,10] In the context of sustainability, it is particularly attractive to generate FDCA electrochemically, as opposed to currently used thermochemical routes employing high pressures and elevated temperatures.[11,12]A significant challenge is that state-of-the-art HMFOR catalysts still exhibit large overpotentials and thus, decreasing this metric is necessary to bring HMFOR systems closer to economic practicality. This is coupled to an incomplete mechanistic picture within the community of the precise reaction mechanism and unfortunately, most reported materials to date do not feature well-defined active sites.

Transition metal-based catalysts are the most heavily studied class of materials for HMFOR to date and show initial promise for widespread use as they are relatively cost-effective and scalable.[13-20] While high selectivity for FDCA production has been attained, the onset potential for most materials is still above 1.3V vs. RHE (Table S1). Ideally this would be decreased to 1.0V or even lower. Coupled to the positive onset potentials, another limitation associated with many of the systems mentioned above is their relatively poor-defined surface which may feature a large variety of different active sites and coordination motifs. The materials are either amorphous or crystalline with a plethora of possible surface-exposed crystalline facets, defects, undercoordinated sites and more which may all have differing catalytic activities. This hampers fundamental investigations into their intrinsic activities and consequently the extraction of key insights from which to build upon. Specifically, with such materials it is difficult to assign electrocatalytic activity to any one active site or surface motif. Further spectroscopic detection of intermediates is less clear without precise active site determination. Finally, modelling efforts have a less clear connection to the experimental data when many different types of active sites may be present.

Towards well-defined catalytic systems, metal organic frameworks (MOFs) are intriguing candidate materials as they exhibit high porosities and precisely distributed, molecularly defined active sites, thus enabling them to serve as ideal model systems for designing and understanding catalysis.[21-24] In the direction of MOFs applied as HMFOR catalysts, Cobalt-doped two-dimensional (2D) MOF nanosheets have been found to promote the formation of the high valence of Ni species as active sites for HMFOR.[25] In addition, Nickel(II)-modified covalent-organic framework (COF) films have been employed for HMFOR, though with limited FDCA yields and Faradaic efficiencies.[26] Defect sites within Ni-MOF-74 have also been identified as being active for HMFOR by enabling *OH to function as a H-acceptor.[27] Building on these initial advances, there is still much room to improve the HMFOR catalytic efficiency and elucidate the reaction mechanism with MOF-based platforms. Despite their aforementioned strengths, an drawback is that many MOFs are insulating in nature, and therefore their application requires the integration of small particles with conductive electrodes, further placing constraints on their use. Thus, as described below, we moved to study conductive MOFs whose activity was not hindered by charge transfer through them.

In parallel to material design, spectroscopic methods are beginning to be employed to elucidate the reaction mechanism on their surfaces.[28] For example, high-surface-area nickel boride (NiB) was studied to uncover the preferred HMFOR reaction pathway with infrared spectroscopy which helped reveal that the reaction proceeds through aldehyde oxidation first.[29] Another study utilized sum frequency generation (SFG) spectroscopy to investigate a carbon-coupled nickel nitride nanosheet (Ni_3N@C) electrode to similarly extract the HMFOR reaction pathway.[30] Gold nanoparticles[31] and thin films of transition metal oxides that covered them were also investigated with surface-enhanced Raman spectroscopy to unveil a correlation between electrolyte alkalinity, reactant binding, and overall reaction kinetics.[32] These studies serve as an inspiration from which to build upon in determining reaction pathways in the well-defined catalytic systems detailed below.

In light of the challenges above, we chose to construct a conductive metal-catecholate (M-CATs, M=Co, Ni, Cu, etc.) framework based-electrocatalytic system with molecularly defined active sites. The M-CATs consist of two dimensional (2D) layers with coordination between transition metal species and hexahydroxytriphenylene organic ligands.[33] Beneficial to catalysis, the triphenylene units and thus the resultant MOFs are electrically conductive and the M-O_4 units are well-defined, coordinatively-unsaturated catalytic sites.

Following its synthesis, we moved to investigate its electrochemical HMFOR activity with a combination of electroanalytical and *operando* spectroscopic techniques. We first systematically investigated and compared the intrinsic catalytic properties of Ni-O_4 and the Co-O_4 active sites within the framework (see comparison to state-of-the-art in table S1). Through the application of *operando* infrared spectroscopy, we show that the HMFOR reaction is initiated by the generation of the M(III) species and subsequent adsorption of HMF via its aldehyde group. The rate limiting step is reactant adsorption in the case of Co-CAT and intermediate desorption for Ni-CAT. The results stand to provide key insights on HMFOR on transition metal active sites embedded within MOFs underpinning the design next generation electrocatalytic systems.

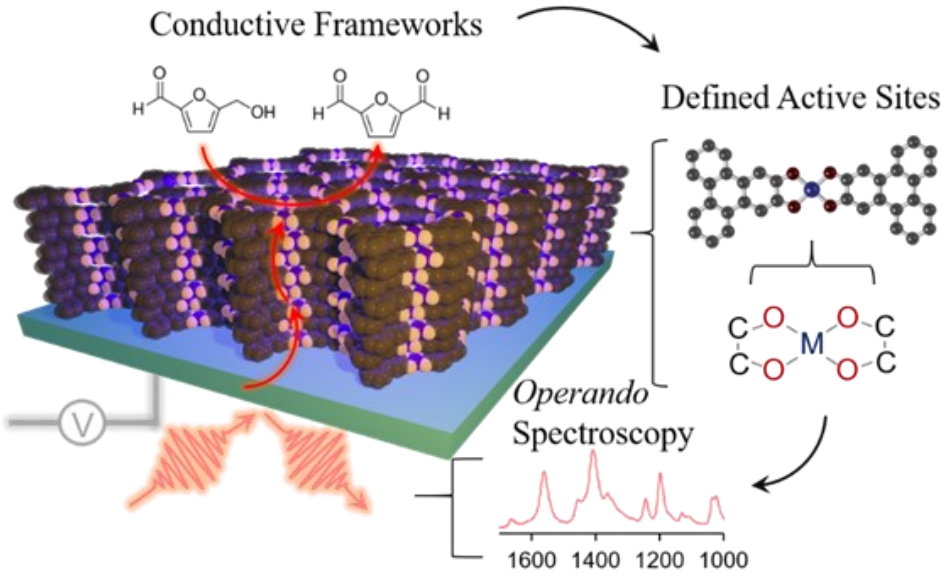

Figure 3-1. M-CAT, employed in this work, is conductive framework containing well-defined undercoordinated active sites for HMFOR. We investigate these active sites with a combination of electrochemical and operando spectroscopic techniques.

3.3. Results and discussion

The synthetic procedure for M-CATs (M= Ni^{2+} and Co^{2} is adapted from previous reports[33,34] and described in detail in the SI. Briefly, the M-CATs were synthesized under simple solvothermal conditions from a stoichiometric precursor solution comprising 2,3,6,7,10,11-hexahydroxytriphenylene hydrate (HHTP), and the Ni or Co acetate dissolved in a solvent mixture (1:1 v/v) of water and 1-propanol (Figure 2a). The resultant material's crystal structure was confirmed through X-ray diffraction (XRD). Figure 2b shows the XRD pattern of M-CATs powder, M-CAT grow on carbon paper substrates in the scanning range of $2\theta=5\sim20^{0}$. Two main peaks at 9.2° and 13.9° correspond to the (200) and (3-11) crystallographic planes were observed. The detected diffraction peaks in the four samples match well with their calculated patterns. The XRD patterns for the materials on carbon paper substrates is shown because this system featured more material deposited on the surface and hence, larger signals from the M-CATs. Top-view SEM and cross-section micrographs of the Ni-CAT-FTO (Figure 2c) and Co-CAT-FTO (Figure S1b) indicate the surface is covered with MOF crystals. Similar morphologies are evidenced for the M-CATS on carbon paper (Fig. S1e, f). The cross-section SEM images illustrates that the Ni-CAT-FTO films have a thickness of about 220 nm (Figure 2c insert). The rod-like crystallites are densely packed, forming a continuous film along with the surface of FTO. TEM analysis of Ni-CAT (Figure 2d) and Co-CAT (Figure S1d) particles removed from the FTO surface reveals the hexagonal pores within the samples.

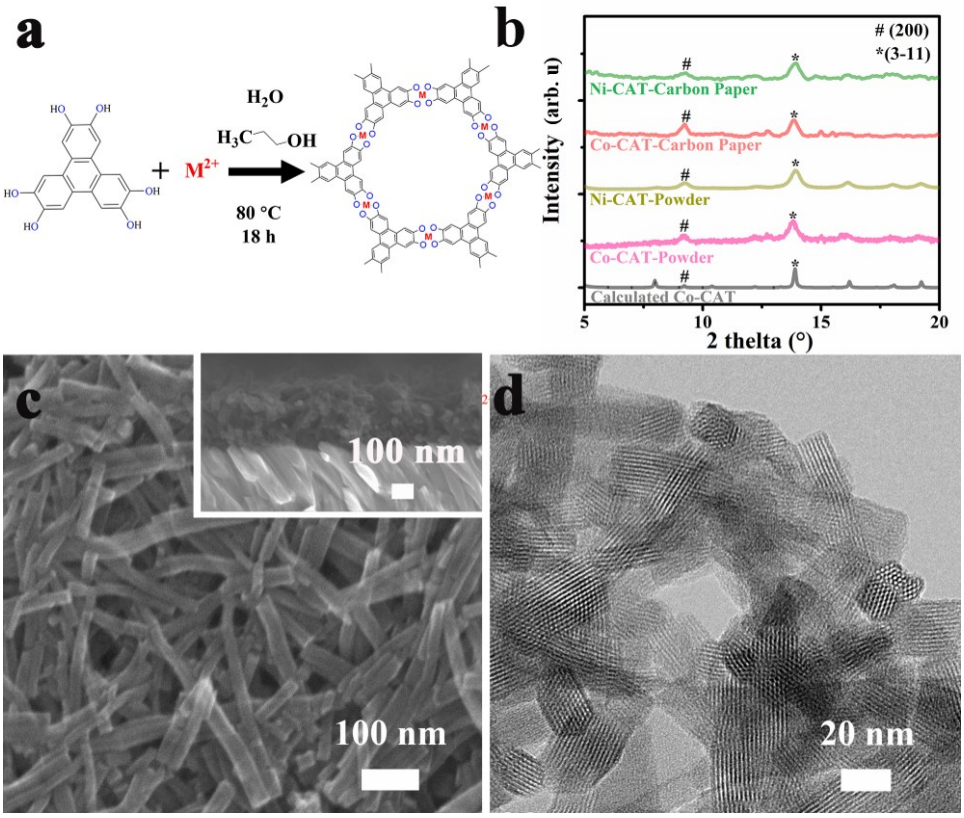

Figure 3-2. Synthetic scheme of M-CAT (M=Ni^{2+}, Co^{2+}) (a). X-ray diffraction patterns of the Ni-, Co-CAT powder, Ni-, Co-CAT-Carbon Paper and the calculated patterns of the Co-CAT (b). Top-view SEM micrographs of the Ni-CAT-FTO (c) with the insert showing side review of the Ni-CAT-FTO. TEM micrographs of the Ni-CAT particles (d).

The electrocatalytic performance of M-CATs electrodes for HMFOR was next evaluated in a three-electrode setup. The CV measurements of the electrodes were first measured in 1 M KOH, then again with 10 mM HMF added to the electrolyte for Co-CAT-FTO (Figure 3a) and Ni-CAT-FTO (Figure 3b). Two electrochemical features can be seen in Figure 3a: the first redox wave is noted at 1.0 V vs RHE, is attributed to the Co(II/III) redox couple. Upon HMF addition, irreversible oxidizing current initiates immediately after the Co(II/III) redox transition. We take this as Co(III) as being the first active species for HMFOR. For Ni-CAT-FTO, the Ni(II/III) couple is situated at 1.35V. The catalytic current onset also coincides with this redox potential. However, the current increases much more rapidly as compared to Co-CAT, initially indicating faster kinetics. Scan rate dependence studies of the Co-CAT-FTO were conducted to see if the conductivity of the MOF was limiting. The experiments reveal a conductive regime of charge transfer to the Co active sites at slower scan rates (< 300 mV s^{-1}) and diffusion-limited behavior at higher scan rate (Figure S2 a-d). In contrast, plots of the peak current versus scan rate on Ni-CAT electrode illustrate solely a linear relationship (Figure S2 e, f), indicating conductive behavior throughout. While conductivity

is likely not significantly limiting our experiment parameters, Ni-CAT seems more conductive in this electrochemical context.

We next extended M-CAT growth to a high surface area carbon paper electrode as a more practical electrolytic system (Figure 2 c,d). Similarly, the CV indicates both Co-CAT and Ni-CAT electrode suggest the presence of the M(II/III) redox waves at the same potentials as with the M-CAT-FTO. We noted that the current density of M-CAT-Carbon Paper is almost ten times higher than M-CAT-FTO substrate. Integrating the current under the redox peak indicates the quantity of redox-active of Co-CAT on carbon paper is 14.7 times greater than that on FTO. An equivalent measurement of Ni-CAT on carbon paper shows an increased active site loading of 2.7 greater compared to the FTO.

We performed bulk electrolysis at 1.42 V in 10 mM HMF in 1 M KOH with both catalysts grown on carbon paper (Fig. 3e). We illustrate the first 5 hrs of the reaction for the sake of comparison because the Ni-Cat reaction was finished within this timeframe. This potential was chosen because it was sufficiently more positive than both of the Co (II/III) and Ni(II/III) redox potentials. NMR analysis of the electrolytes revealed that FDCA and HMFCA were the only detectable products. After the full reaction process (20 hrs, Fig. S5) Co-CAT reached a turnover number (TON) as a function of FDCA molecules of 953 and as function of electrons transferred of 5,718 (turnover frequencies of 48 and 286 hr^{-1}, respectively). The yield of FDCA (after 20 hrs) was 99.3 % and the Faradaic efficiency was calculated to be 97.6 %. We further probed Co-CAT reactivity at 1.12 V, just past the Co(II/III) redox potential and found that the catalyst still exhibits measurable activity (yield for FDCA of 25% after 5 days of electrolysis, Faradaic efficiency of 31.13 %, Figure S6). To the best of our knowledge, this is the most positive potential that has been reported for HMFOR on transition metal catalysts (see table S1).

Conversely, after 5 hours at 1.42 V for Ni-CAT-electrode, all the of HMF was consumed and FDCA was generated with a final Faradaic efficiency of 86.8 % and a yield of 98.7 % (Figure 3e). The comparatively smaller Faradaic efficiency of Ni-CAT likely stems from a portion of current going towards the OER at 1.42 V as Ni-CAT is a more active OER catalyst. After 5 hrs of electrolysis at 1.42 V vs. RHE, Ni-CAT exhibited a TON as a function of FDCA molecules of 5,411 and TON as a function of electron transferred of 32,466 (turnover frequencies of 1082 and 6493 hr^{-1}, respectively). This further supports the notion that Ni-CAT features intrinsically faster reaction kinetics but only at relatively positive potentials. We note that by performing electrolysis at a less positive potential of 1.38V, a Faradaic Efficiency of 97.4% could be attained.

The retention of the M-CATs on the electrode surface was confirmed by XPS analysis (Figure S7). XPS measurements revealed a slight shift towards lower binding energy of both Co 2p and Ni 2p signals after 6h electrolysis, indicating changes in the metal coordination environment during the electrocatalysis (e.g. residual solvent leaving or water/hydroxide molecule attachment), but the retained Co 2p and Ni 2p peaks nonetheless suggest the retention of the transition metal species. O 1s peaks similarly showed a slight shift to lower binding energies. SEM after electrolysis showed the retention of the MOF structures on the surface (Fig. S8). Furthermore, a recyclability test of the Ni-CAT revealed that the performance and FDCA conversion remains throughout several electrolytic runs.

We next sought to use a rotating disk electrode setup to further probe reaction kinetics of the above-studied Ni-CAT and Co-CAT electrocatalysts. To do so, we deposited M-CAT powders directly on a glassy carbon disk and performed a slow voltametric measurement under 1600 rpm rotation to efficiently transport the HMF to the catalyst. The Tafel plot of the Co-CAT electrode shows a larger Tafel slope of 141.16 mV/dec (Figure 3f) while the Tafel slope of 42 mV/dec observed on Ni-CAT, indicating a higher catalytic performance.

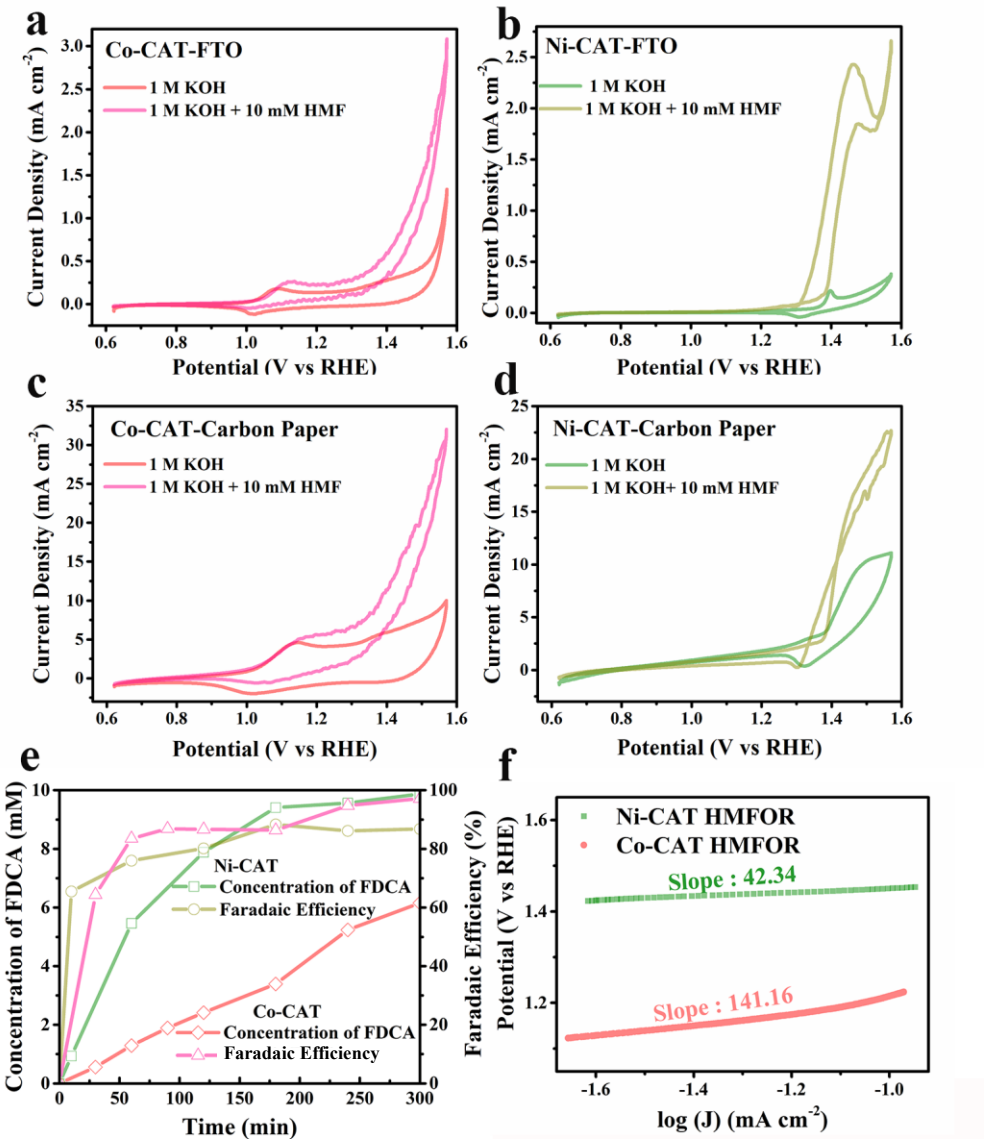

Figure 3-3. **Electrochemical analysis.** Cyclic voltammetry (CV) measurements show the catalytic current onset at the same potential as the Co(II/III) (a) and Ni(II/III) (b) redox peaks for catalysts on FTO substrates. A similar behaviour was observed for Co-CAT (c) and Ni-CAT(d) on carbon paper substrates. Faradaic efficiency and yields of FDCA using Ni-CAT and Co-CAT for

a 5hr electrolysis at 1.42 V vs. RHE (e). Catalytic differences are also evident by differences in Tafel slopes, measured in a rotating disk configuration.

To obtain a deeper level of insights into the surface catalytic mechanism of the Ni-CAT and Co-CAT, we employed IR measurements in an ATR configuration. A carbon cloth was used as the counter electrode and an Ag/AgCl in saturated KCl solution as the reference electrode. The first measurement performed was the acquisition of the IR spectra of HMF in KOH electrolyte that was allowed to adsorb onto the surfaces of M-CAT. There may be charge transfer to key functional groups on HMF when it adsorbs on the M-CAT surface, resulting in changes in band positions and relative intensities. Thus, this measurement aims to detect how HMF interacts with our model M-CAT catalysts. Spectral features were assigned on the basis of previous spectroscopic and theoretic studies of these molecules.[29,35-37] We first measured 10 mM HMF in 1 M KOH electrolyte to obtain the spectra of HMF in an alkaline environment. Then the M-CAT electrode was immersed in the electrolyte, and after carefully subtracting out the spectra of the hydrated MOF, we extracted the new spectral features that resulted from HMF interacting with M-CAT (Figure 4a, b). At the high-frequency spectral range, both the C=O and C=C bands at 1654.7 cm^{-1} and 1515.8 cm^{-1} can be observed. When HMF absorbed onto the catalyst surfaces, the C=O bands shifted by 82.4 cm^{-1} and 88.2 cm^{-1} for the Co-CAT and Ni-CAT materials relative to the solution spectra. Hence, this indicates an absorption in with the C=O band is weakened through interaction with the Co and Ni active sites. The band at 1027 cm^{-1} corresponds to the alcohol group of HMF. For Ni-CAT, this band is also red shifted and split into two bands at 1023.4 and 1011.2 cm^{-1}. This suggests the alcohol group of HMF may have two kinds of surface interactions with Ni-CAT. Through analysis of the IR spectra, we deduce that both the aldehyde group and alcohol group of HMF can interact with our catalysts under open circuit conditions.

To bolster our understanding of the catalytic mechanism of both Ni-CAT and Co-CAT, we probed the spectral changes as a function of applied potential. IR spectra were recorded before (at open circuit, used as a background) and during the electrochemical reaction in a series of potentials (Figure 4c, d). The assignment of the IR bands and thus the correlation with different reaction intermediates was based on comparison with reference spectra (Figure S11, 12) of the pure compounds. Upon the application of positive potentials, a very intense peak at 1357.7 cm^{-1} of both Co-CAT (Figure 4c) and Ni-CAT (Figure 4d) can be assigned to FDCA due to the symmetric vibration of its carboxylate groups. HMFCA formation is indicated by its C=O band at 1560 cm^{-1}. Similarly, we can also observe this band at 1569.8 cm^{-1} in the case of Ni-CAT and the slight difference in band position is ascribed to the different electronic properties of the active site and thus the interaction with the surface intermediate. We next plotted the relationship between the relative intensities of bands at 1357.7 and 1560 and the applied potential. For Co-CAT, as the potential increased, the intensities of both peaks gradually increased (Figure 4e). This slow increase suggests that the rate-determining step might be the initial intermediate absorption. This is also reflected in the CVs of Co-CAT that feature a slowly increasing current density after the Co(II/III) transition. When we performed the equivalent analysis on Ni-CAT, we noted a rapid increase in peak intensity of the C=O band at the Ni(II/III) redox potential. This tendency indicates

that once Ni(III) forms, the active sites will immediately bind HMF. However, after reaching the peak at 1.4V, the 1569.8 peak began to slowly decrease. This phenomenon can be interpreted as the Ni-CAT electrocatalysis is limited by the desorption process of the final intermediate, which becomes more rapid at higher potentials and thus gives rise to a lower peak intensity in the spectra.

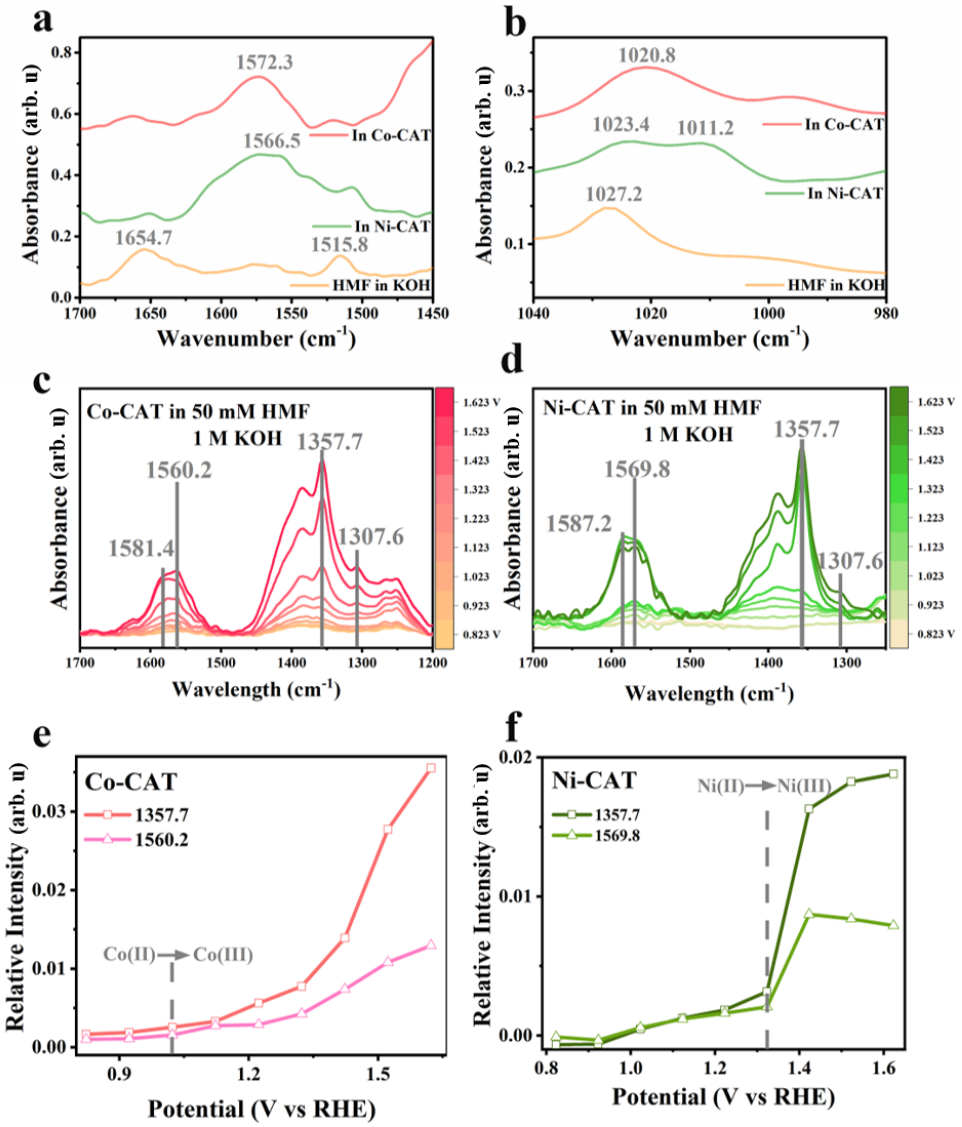

Figure 3-4. Mechanism analysis. The MOF-HMF physical absorb interactions can be observed from both high wavenumber range (a) and (1040-980 cm^{-1}) range IR spectra (b). Potential-dependent ATR-IR difference spectra of the Co-CAT (c) and Ni-CAT (d) in HMF electrolyte under applied potentials. The color scheme denotes V vs. RHE. Bands at 1357.7 and 1560.2 begin to rise just past the Co(II/III) redox potential (e). Similar results are evidenced for Ni-CAT, which features a markedly faster spectral change once the Ni(II/III) redox potential is reached.

3.4. Conclusion

We have developed a model HMFOR catalyst system with well-defined, unsaturated transition metal active site embedded within conductive frameworks. Electrochemical analysis revealed Co-CAT and Ni-CAT to be high performing materials for this reaction, with low onset potentials (Co-CAT) and Tafel slopes (Ni-CAT). By combining our electrochemical analysis with *operando* infrared spectroscopy, we unveiled a mechanistic understanding underpinning the reactivity of the materials. In all, leveraging active site control in electrocatalysts within MOF frameworks is set to provide a unique avenue in rational materials design in renewable energy driven electrosynthetic technologies.

3.5. Acknowledgements

N.K. and Y.Z. acknowledge NSERC Discovery Grant RGPIN-2019-05927.

3.6. Experimental

M-CAT and Co-CAT MOFs were fabricated through a solvothermal recipe. The entailed the mixing of HHTP, Co/Ni acetate tetrahydrate, DI water and n-propanol in a scintillation vial and heating this solution at 85 ºC for 18 hrs, washing with acetone, then drying. The surface growth of the MOFs entailed layering the solution over the desired substrates, then similarly heating in the oven. Precise details are given in the SI. Electrochemical measurements were performed in two-compartment custom built glass electrochemical cells with an Ag/AgCl reference electrode. Two CV scans were performed prior to recording data to ensure that residual organic species were removed from/within the MOFs. Products were quantified through NMR using a calibration curve and internal standard. Infrared spectroscopy was performed with custom-designed Teflon reaction cells and data processed with OPUS software. Typically, *operando* spectra were acquired in a stepped chronoamperometry mode, with approximately 4 minutes at each potential and the reference was the spectrum at open circuit.

Conductive metal-organic frameworks bearing M-O_4 active sites as highly active biomass valorization electrocatalysts.

3.6.1. Chemicals

2,3,6,7,10,11-Hexahydroxytriphenylene Hydrate (HHTP, 95.0+%, TCI America™), Nickel(II) acetate tetrahydrate (extra pure, ACROS Organics™), Cobalt(II) acetate tetrahydrate (extra pure, ACROS Organics™) were purchased from Thermo Fisher Scientific company for catalysis synthesis.

5-(Hydroxymethyl) furfural (HMF, ⩾99%, Sigma-Aldrich), 2,5-Diformylfuran (DFF, >98.0%, TCI America™), 5-Hydroxymethyl-2-furancarboxylic acid (HMFCA, ⩾98%, Cayman Chemical), 5-Formyl-2-furancarboxylic Acid (FFCA, >98.0%, TCI America™), 2,5-Furandicarboxylic Acid (FDCA, >98.0%, TCI America™) were purchased for product analysis.

3.6.2. Synthesis and characterization of M-CAT

Metal-catecholates (M-CAT) powder was prepared according to previous literature reports[61]. A mixture of HHTP (3.5 mg) and metal (nickel or cobalt) acetate tetrahydrate (5 mg) was dissolved in a solvent mixture of deionized water and n-propanol (1 ml: 1 ml) in a 5 mL culture tube. The culture tube was capped and sonicated for 5 min to form a homogenous dark blue solution. Subsequently, the reaction mixture was subjected to a preheated solvothermal oven at 85 °C for 18 h. The resulted solution was washed by three times with dry acetone and collected by centrifugation for 30 min. The obtained dark blue microcrystalline was dried in a dynamic vacuum at 50 °C prior to characterization.

M-CAT-FTO and M-CAT-Carbon Paper were prepared by the same recipe mentioned above. The schematic of the synthetic process was depicted in Figure 2(a). The carbon paper or FTO function as conductive substrate was put into the dark blue solution before putting the culture tube into the oven. Similarly, after heated at 85 °C for 18h, a layer of dark blue crystalline was growing on the substrate surface. The resulting film growth on FTO or carbon paper was rinsed by water, acetone, and ethylene. The samples were scanned two cycles CV before characterization to removal the possible residual organics.

The morphology and microstructure of M-CAT were investigated transmission electron microscopy (TEM) and scanning electron microscopy (SEM). TEM and SEM images were collected at the Centre for Characterization and Microscopy of Materials at Polytechnique Montreal. TEM images were conducted on a JEOL JEM-2100F FEG-TEM, operated at 200 kV. For TEM characterizations, samples (Ni-CAT-FTO and Co-CAT-FTO) were prepared by carefully scratched off the film layer on top of the FTO substrate, dispersed in ethanol, and subsequently depositing the sample onto a copper grid supporting a thin electron transparent carbon film. SEM images were obtained after growth. The crystalline structures of samples were identified by powder X-ray diffraction (XRD, Bruker D8 Advance diffractometer) using Cu-Kα radiation source (λ=1.5418 Å).

The high-resolution X-ray photoelectron spectroscopy (XPS) analysis before and after 6h electrolysis was performed using a Vacuum Generated Escalab 220i-XL system in the Institute National de la Recherche Scientifique Centre Énergie Matériaux et communications. For this, Mg was used as an X-ray source. The data were calibrated to the C 1s peak at 284.8 eV to set the x-axis (binding energy).

3.6.3. Electrocatalytic oxidation of HMF to FDCA

Electrochemistry experiments were carried out in a two-compartment glass electrochemical cell, custom built glass cells separated with a porous glass frit. Ag/AgCl in saturated KCl solution was used as the reference electrodes and a graphite rod was used as the counter electrode. The used

Ag/AgCl reference was periodically checked against a master reference electrode for any potential drifts to ensure stability in the alkaline electrolyte. A biologic VMP200 potentiostat and EC-lab software were used for electrochemical experiments. In order to compensate for the IR drop (at 85%), the ZIR program in the EC-lab software was employed by recording the impedance between the cathode and reference electrode at open circuit at 100 KHz frequency. In all electrochemical measurements, 1.0 M KOH was used as the electrolyte. Cyclic voltammetry (CV) measurements were performed with the scan rate of 20 mV s^{-1} with and without HMF for each electrode. Chronoamperometry was conducted to conduct constant potential electrolysis of HMF.

Linear sweep voltammetry (LSV) was scanned at 0.5 mV/s and calculate the Tafel slopes in a rotating disk configuration.

For product analysis, all reactant and products were quantified with NMR (Bruker AVANCE II 400 se), using D_2O with acetate as an internal standard.

To detecting the recyclability of Ni-CAT, adding 10 mM HMF into 1 M KOH electrolyte each time when the reactant is almost exhausted and taking out 400 mL electrolyte to detect the NMR.

3.6.4. *Operando* spectroscopy

Infrared spectroscopy in an ATR configuration was performed with Thermo Fischer Nicolet 380 FTIR-ATR system. For both *operando* and ex-situ measurements, each spectrum was recorded with an accumulation of 200 scans with a resolution of 4 cm^{-1}. An atmospheric background spectrum was taken before every MOF spectrum. OPUS 7.0 software was used to carefully subtract out the air and KOH solution background. This software was used for baseline correction and peak fitting as well.

As the reference, the infrared spectra of Ni-CAT-Powder, Co-CAT-Powder, Ni-CAT-Carbon Paper, Co-CAT-Carbon Paper, and HHTP were measured. The spectra of HMF and all oxidation products were collected in the same condition as well.

Operando IR spectroscopy executed with the use of a custom-built spectroelectrochemical cell. Simultaneously, a carbon cloth was used as the counter electrode and an Ag/AgCl in saturated KCl solution as the reference electrode. The M-CATs growth on the flexible carbon cloth was selected as the working electrode. Spectra were first acquired at the most negative potential and the voltage was progressively increased in a chronoamperometric scan.

3.7. References

1 Chu, S. & Majumdar, A. Opportunities and challenges for a sustainable energy future. *Nature* **488**, 294-303 (2012).

2 Stamenkovic, V. R., Strmcnik, D., Lopes, P. P. & Markovic, N. M. Energy and fuels from electrochemical interfaces. *Nat. Mater.* **16**, 57-69 (2017).

3 Lewis, N. S. & Nocera, D. G. Powering the planet: Chemical challenges in solar energy utilization. *Proc. Natl. Acad. Sci. U.S.A.* **103**, 15729 (2006).

4 Du, L. *et al.* Electrocatalytic valorisation of biomass derived chemicals. *Catal. Sci. Technol.* **8**, 3216-3232 (2018).

5 Li, K. & Sun, Y. Electrocatalytic Upgrading of Biomass-Derived Intermediate Compounds to Value-Added Products. *Chem. Eur. J.* **24**, 18258-18270 (2018).

6 Lucas, F. W. S. *et al.* Electrochemical Routes for the Valorization of Biomass-Derived Feedstocks: From Chemistry to Application. *ACS Energy Lett.* **6**, 1205-1270 (2021).

7 van Putten, R.-J. *et al.* Hydroxymethylfurfural, A Versatile Platform Chemical Made from Renewable Resources. *Chem. Rev.* **113**, 1499-1597 (2013).

8 Wang, T., Nolte, M. W. & Shanks, B. H. Catalytic dehydration of C6 carbohydrates for the production of hydroxymethylfurfural (HMF) as a versatile platform chemical. *Green Chem.* **16**, 548-572 (2014).

9 de Jong, E., Dam, M. A., Sipos, L. & Gruter, G. J. M. in *Biobased Monomers, Polymers, and Materials* Vol. 1105 *ACS Symposium Series* Ch. 1, 1-13 (American Chemical Society, 2012).

10 Motagamwala, A. H. *et al.* Toward biomass-derived renewable plastics: Production of 2,5-furandicarboxylic acid from fructose. *Sci. Adv.* **4**, eaap9722 (2018).

11 Sajid, M., Zhao, X. & Liu, D. Production of 2,5-furandicarboxylic acid (FDCA) from 5-hydroxymethylfurfural (HMF): recent progress focusing on the chemical-catalytic routes. *Green Chem.* **20**, 5427-5453 (2018).

12 Dutta, S., De, S. & Saha, B. A Brief Summary of the Synthesis of Polyester Building-Block Chemicals and Biofuels from 5-Hydroxymethylfurfural. *ChemPlusChem* **77**, 259-272 (2012).

13 Taitt, B. J., Nam, D.-H. & Choi, K.-S. A Comparative Study of Nickel, Cobalt, and Iron Oxyhydroxide Anodes for the Electrochemical Oxidation of 5-Hydroxymethylfurfural to 2,5-Furandicarboxylic Acid. *ACS Catal.* **9**, 660-670 (2019).

14 Liu, W.-J. *et al.* Electrochemical Oxidation of 5-Hydroxymethylfurfural with NiFe Layered Double Hydroxide (LDH) Nanosheet Catalysts. *ACS Catal.* **8**, 5533-5541 (2018).

15 Kang, M. J. *et al.* Electrocatalysis of 5-hydroxymethylfurfural at cobalt based spinel catalysts with filamentous nanoarchitecture in alkaline media. *Appl. Catal., B* **242**, 85-91 (2019).

16 Huang, X. *et al.* Enhancing the electrocatalytic activity of CoO for the oxidation of 5-hydroxymethylfurfural by introducing oxygen vacancies. *Green Chem.* **22**, 843-849 (2020).

17 You, B., Jiang, N., Liu, X. & Sun, Y. Simultaneous H2 Generation and Biomass Upgrading in Water by an Efficient Noble-Metal-Free Bifunctional Electrocatalyst. *Angew. Chem. Int. Ed.* **55**, 9913-9917 (2016).

18 Nam, D.-H., Taitt, B. J. & Choi, K.-S. Copper-Based Catalytic Anodes To Produce 2,5-Furandicarboxylic Acid, a Biomass-Derived Alternative to Terephthalic Acid. *ACS Catal.* **8**, 1197-1206 (2018).
19 Deng, X. *et al.* Understanding the Roles of Electrogenerated Co3+ and Co4+ in Selectivity-Tuned 5-Hydroxymethylfurfural Oxidation. *Angew. Chem. Int. Ed.* **n/a** (2021).
20 Yang, Y. & Mu, T. Electrochemical oxidation of biomass derived 5-hydroxymethylfurfural (HMF): pathway, mechanism, catalysts and coupling reactions. *Green Chem.* **23**, 4228-4254 (2021).
21 Downes, C. A. & Marinescu, S. C. Electrocatalytic Metal–Organic Frameworks for Energy Applications. *ChemSusChem* **10**, 4374-4392 (2017).
22 Heidary, N., Harris, T. G. A. A., Ly, K. H. & Kornienko, N. Artificial photosynthesis with metal and covalent organic frameworks (MOFs and COFs): challenges and prospects in fuel-forming electrocatalysis. *Phys. Plant.* **166**, 460-471 (2019).
23 Diercks, C. S., Liu, Y., Cordova, K. E. & Yaghi, O. M. The role of reticular chemistry in the design of CO2 reduction catalysts. *Nat. Mater.* **17**, 301-307 (2018).
24 Zhang, Y., Li, J. & Kornienko, N. Towards atomic precision in HMF and methane oxidation electrocatalysts. *Chem. Commun.* **57**, 4230-4238 (2021).
25 Cai, M. *et al.* Two-dimensional metal–organic framework nanosheets for highly efficient electrocatalytic biomass 5-(hydroxymethyl)furfural (HMF) valorization. *J. Mater. Chem. A* **8**, 20386-20392 (2020).
26 Cai, M. *et al.* Nickel(ii)-modified covalent-organic framework film for electrocatalytic oxidation of 5-hydroxymethylfurfural (HMF). *Chem. Commun.* **56**, 14361-14364 (2020).
27 Heidary, N., Chartrand, D., Guiet, A. & Kornienko, N. Rational incorporation of defects within metal–organic frameworks generates highly active electrocatalytic sites. *Chem. Sci.* (2021).
28 Heidary, N. & Kornienko, N. Operando vibrational spectroscopy for electrochemical biomass valorization. *Chem. Commun.* **56**, 8726-8734 (2020).
29 Barwe, S. *et al.* Electrocatalytic Oxidation of 5-(Hydroxymethyl)furfural Using High-Surface-Area Nickel Boride. *Angew. Chem. Int. Ed.* **57**, 11460-11464 (2018).
30 Zhang, N. *et al.* Electrochemical Oxidation of 5-Hydroxymethylfurfural on Nickel Nitride/Carbon Nanosheets: Reaction Pathway Determined by In Situ Sum Frequency Generation Vibrational Spectroscopy. *Angew. Chem. Int. Ed.* **58**, 15895-15903 (2019).
31 Heidary, N. & Kornienko, N. Operando Raman probing of electrocatalytic biomass oxidation on gold nanoparticle surfaces. *Chem. Commun.* **55**, 11996-11999 (2019).
32 Heidary, N. & Kornienko, N. Electrochemical biomass valorization on gold-metal oxide nanoscale heterojunctions enables investigation of both catalyst and reaction dynamics with operando surface-enhanced Raman spectroscopy. *Chem. Sci.* **11**, 1798-1806 (2020).
33 Hmadeh, M. *et al.* New Porous Crystals of Extended Metal-Catecholates. *Chem. Mater.* **24**, 3511-3513 (2012).
34 Mähringer, A. *et al.* Oriented Thin Films of Electroactive Triphenylene Catecholate-Based Two-Dimensional Metal–Organic Frameworks. *ACS Nano* **13**, 6711-6719 (2019).
35 Kim, T., Assary, R. S., Curtiss, L. A., Marshall, C. L. & Stair, P. C. Vibrational properties of levulinic acid and furan derivatives: Raman spectroscopy and theoretical calculations. *J. Raman Spectrosc.* **42**, 2069-2076 (2011).

36 Josephson, T. R. *et al.* Solvent-Induced Frequency Shifts of 5-Hydroxymethylfurfural Deduced via Infrared Spectroscopy and ab Initio Calculations. *J. Phys. Chem. A* **118**, 12149-12160 (2014).
37 Thuriot-Roukos, J., Khadraoui, R., Paul, S. & Wojcieszak, R. Raman Spectroscopy Applied to Monitor Furfural Liquid-Phase Oxidation Catalyzed by Supported Gold Nanoparticles. *ACS Omega* **5**, 14283-14290 (2020).

3.8. Supporting information

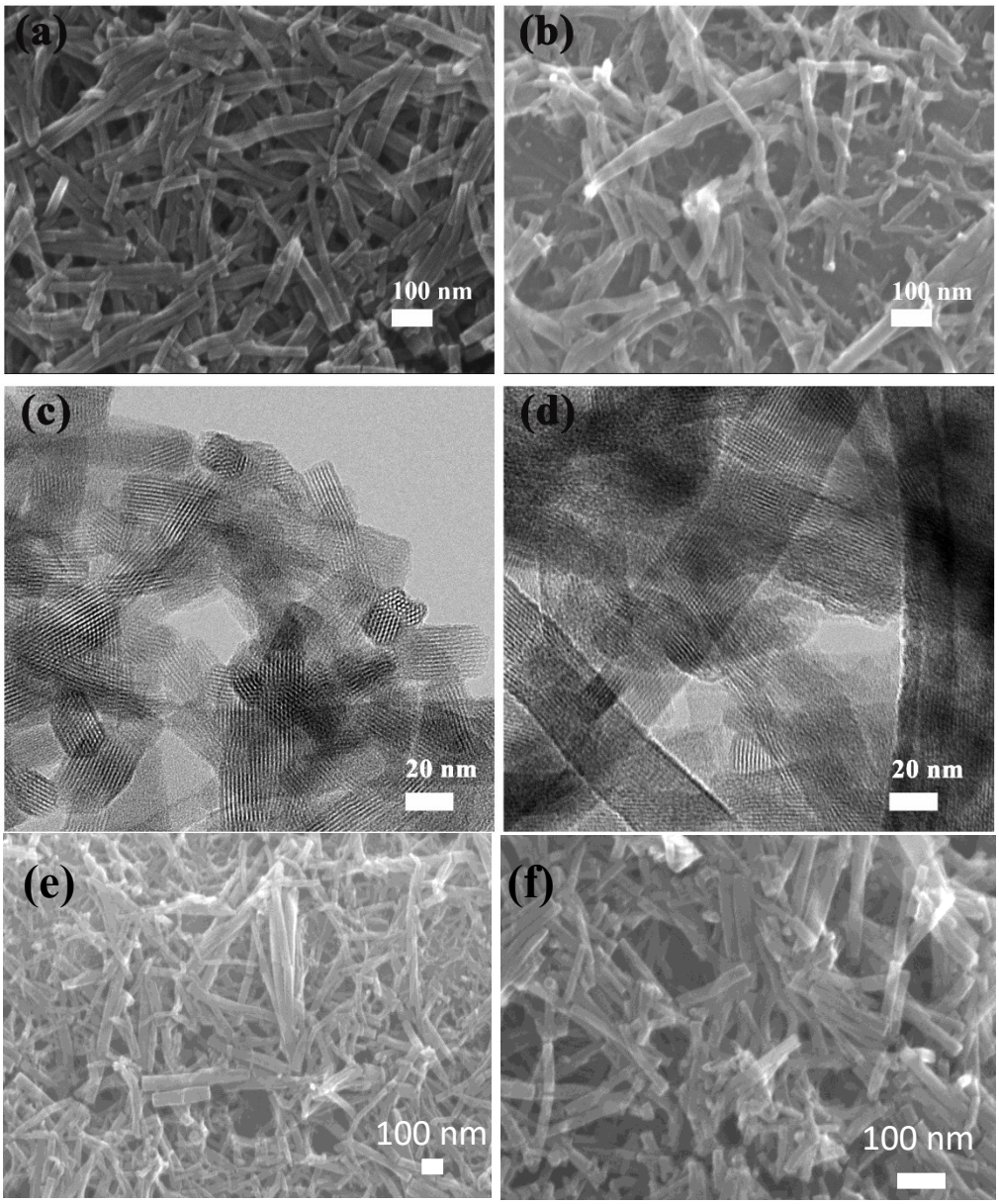

Figure 3-S1. SEM images of Ni-CAT-FTO (a) and Co-CAT-FTO (b). TEM images of Ni-CAT-FTO (c) and Co-CAT-FTO (d). SEM images of Co-CAT-Carbon paper (e) and Ni-CAT-Carbon paper (f).

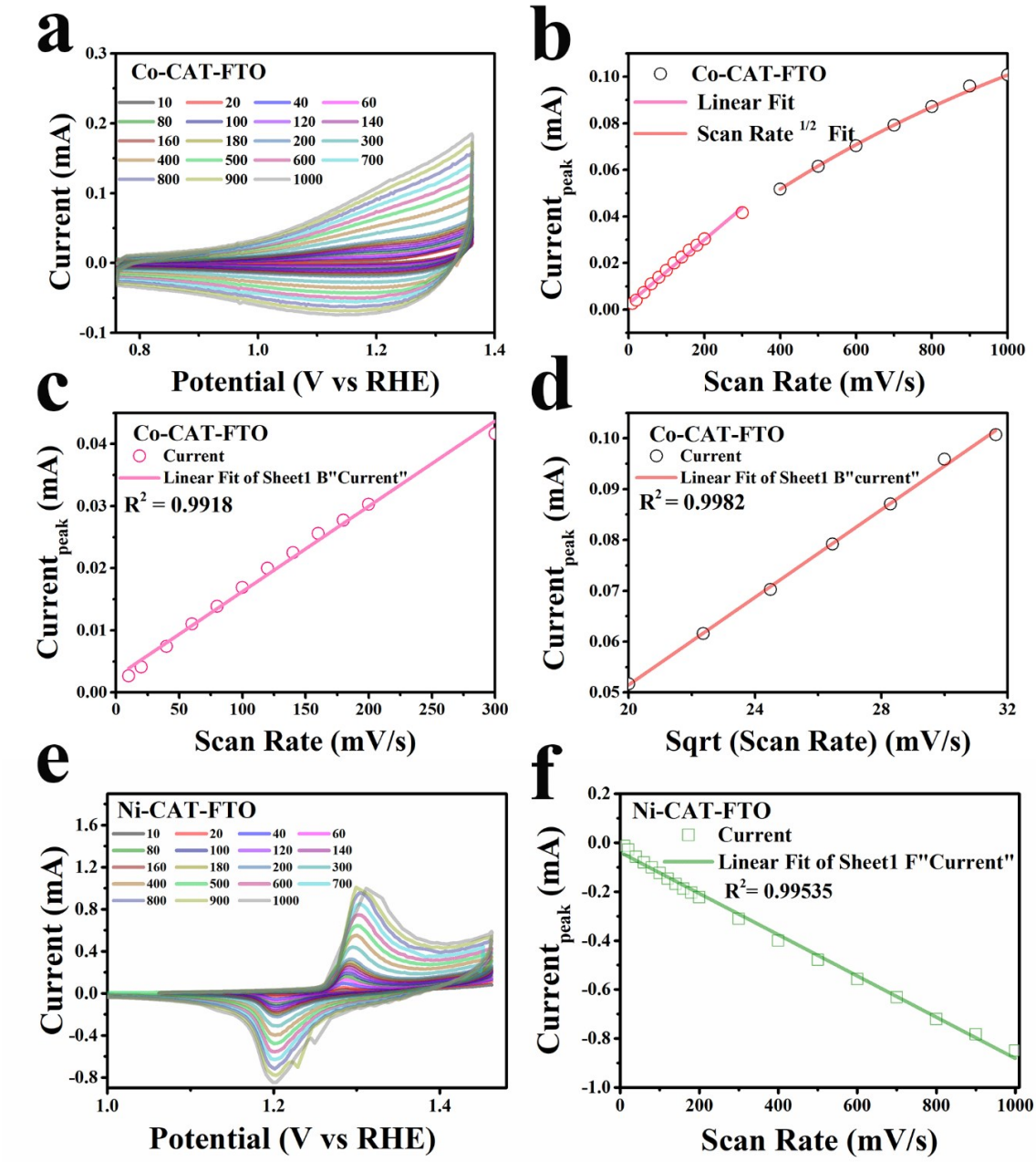

Figure 3-S2. Scan rate dependence analysis. CVs show the scan rate dependence of Co-CAT-FTO (a-d) and Ni-CAT-FTO (e,f) in 1 M KOH electrolyte at the applied potential from 0.82 V to 1.42 V vs RHE. (c) Plot of the Co(II)/ Co(III) peak current for Co-CAT-FTO versus the scan rate. (d) Plot of the Ni(II)/ Ni(III) peak current for Ni-CAT-FTO versus the square root of the scan rate. (f) Plot of the Ni(II)/ Ni(III) peak current for -Ni-CAT-FTO versus the scan rate.

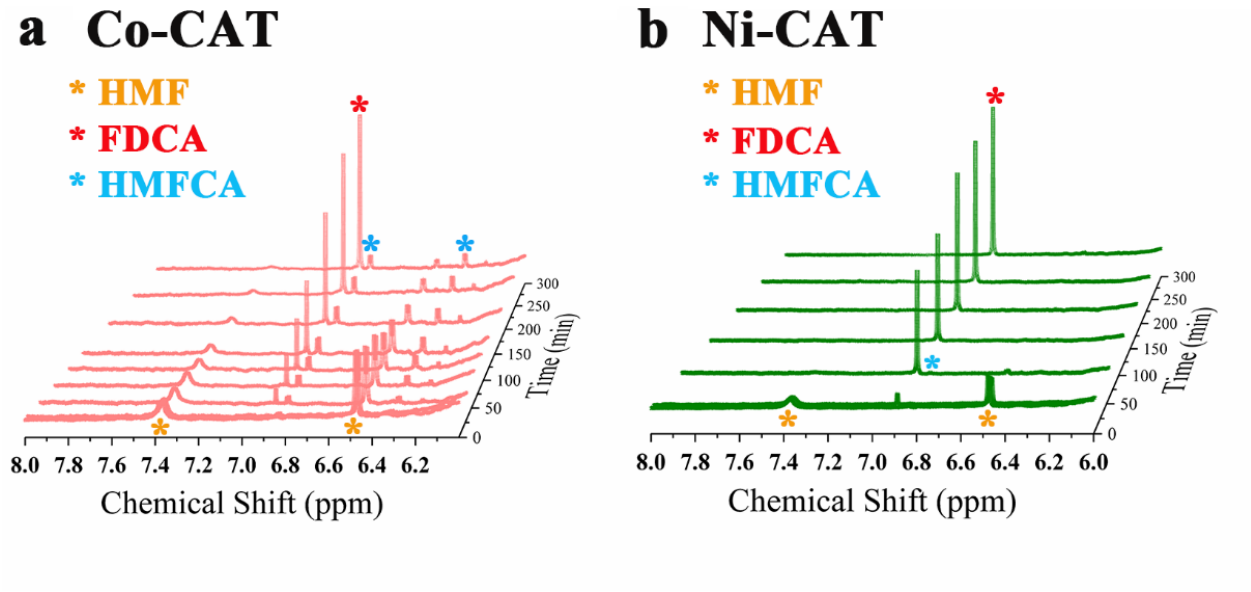

Figure 3-S3. Bulk product analysis was performed using a 10 mM HMF-containing electrolyte and periodic sampling of the solution, followed by analysis with NMR. A chronoamperometric scan at 1.42 V shows a decreasing current as HMF is depleted and converted into HMFCA and FDCA as measured with NMR at different time (a), (b).

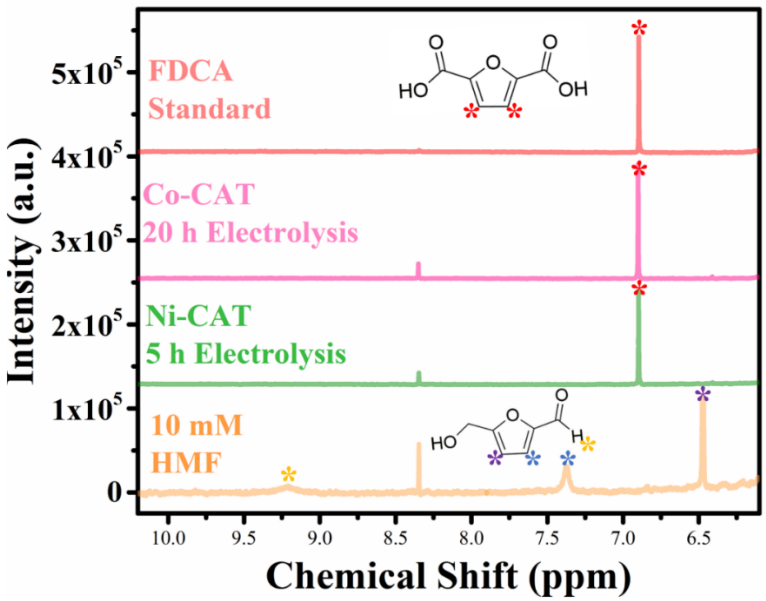

Figure 3-S4. NMR spectra of a FDCA standard, of reaction solution of Co-CAT electrolysis after 20 h, of reaction solution of Ni-CAT electrolysis after 5h and 10 mM HMF in 1 M KOH solution (from top to bottom). HMF could be completely converted to FDCA after extended electrolysis shown in this NMR spectra.

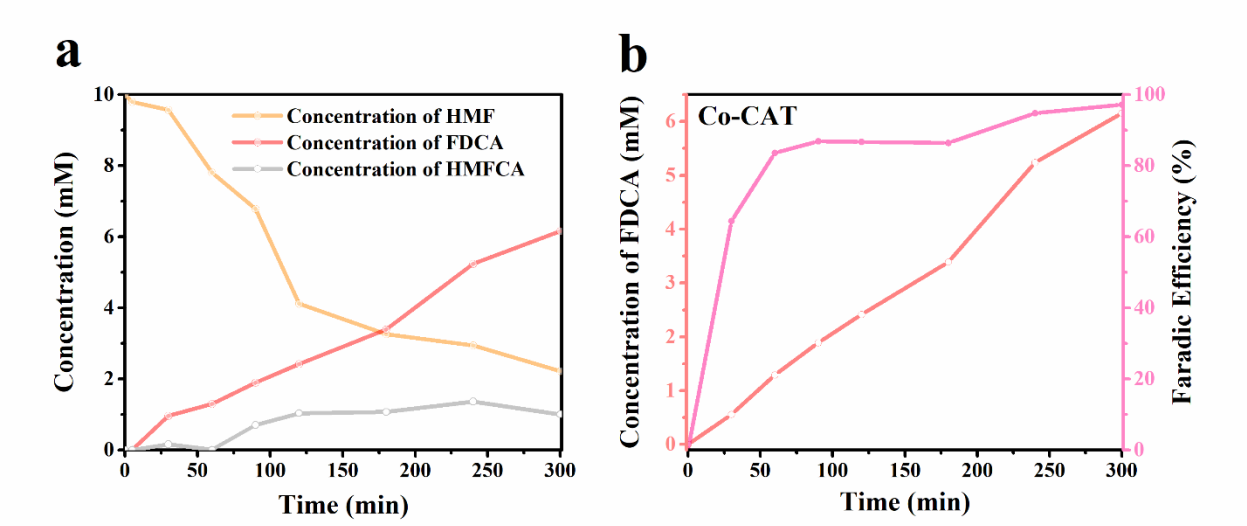

Figure 3-S5. Concentration versus time plot of HMF, FDCA, and the intermediates at various electrolysis times (a). Faradaic efficiencies (FEs) for FDCA by Co-CAT at applied potentials 1.42 V vs RHE after 5 h electrolysis (b).

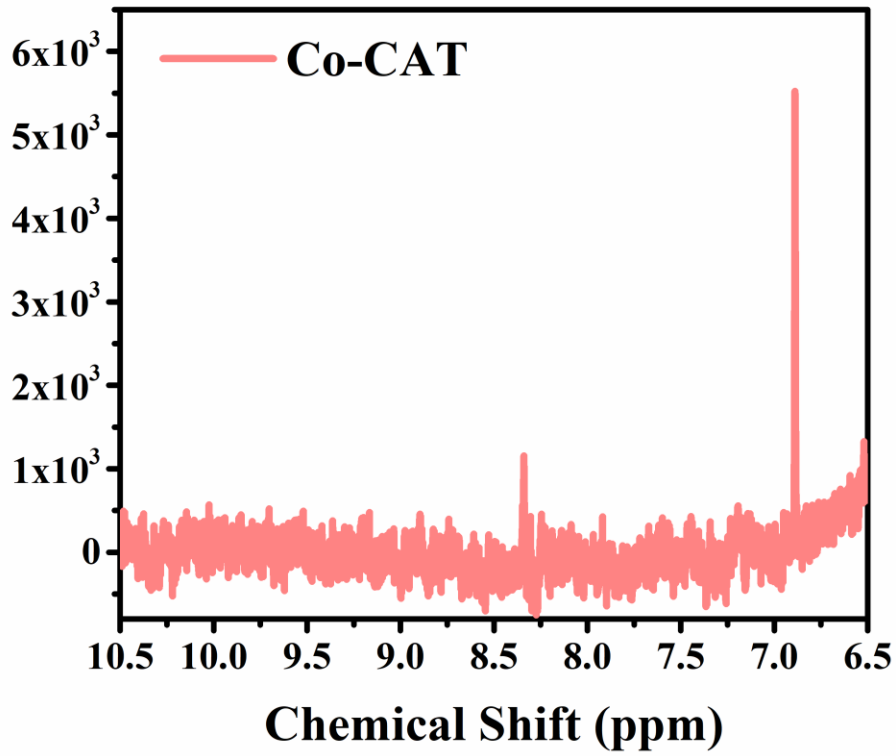

Figure 3-S6. NMR spectra of 5 mM HMF of Co-CAT after 5 days electrolysis at 1.12 V. The final product is FDCA (faradic efficiency is 31.13 %) and only trace amount of HMF been detected.

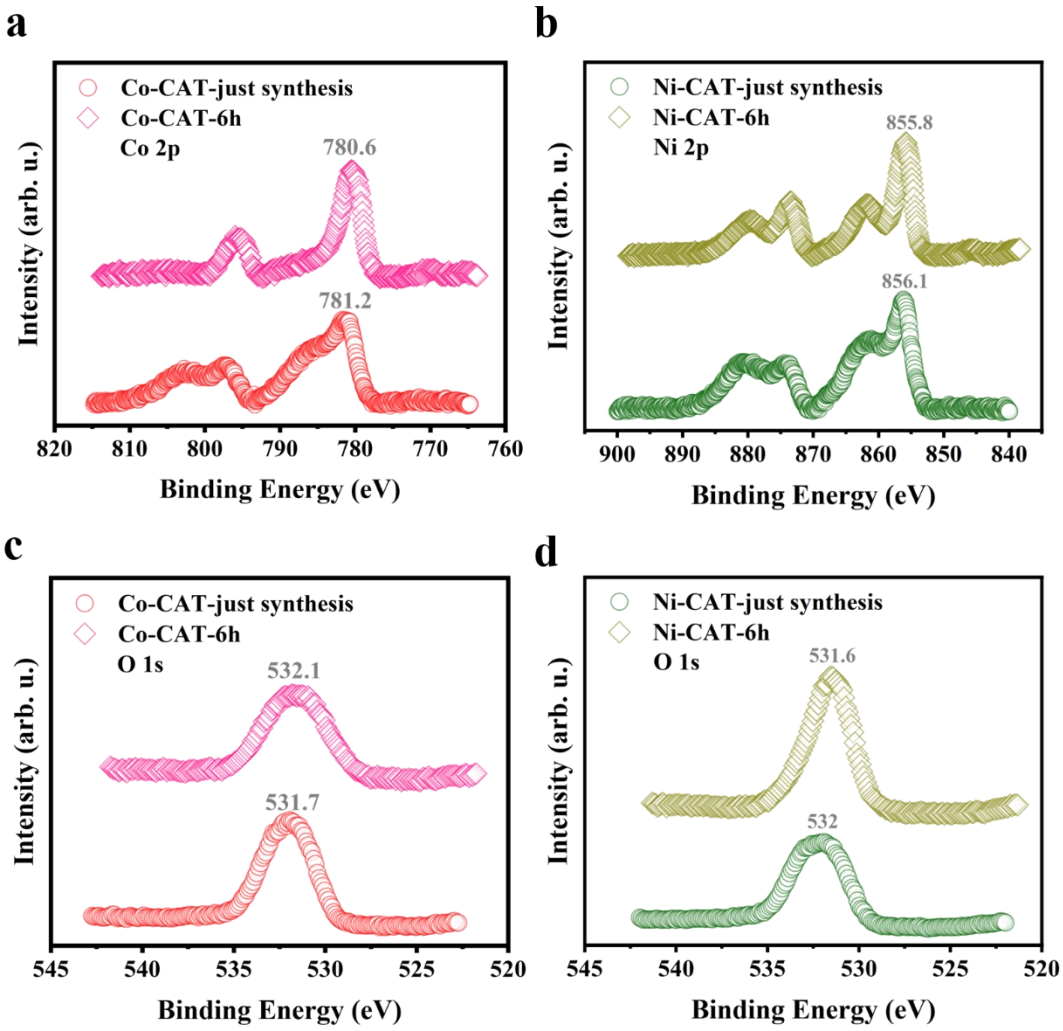

Figure 3-S7. XPS characterization of Co-CAT (a), (c) and Ni-CAT (b), (d) before and after 6h electrolysis at 1.42 V vs RHE. We attribute a small shift to lower binding energies for all peaks as due to differences in solvent infiltration or coordination within the MOFs and removal of residual organics throughout the electrocatalytic experiments.

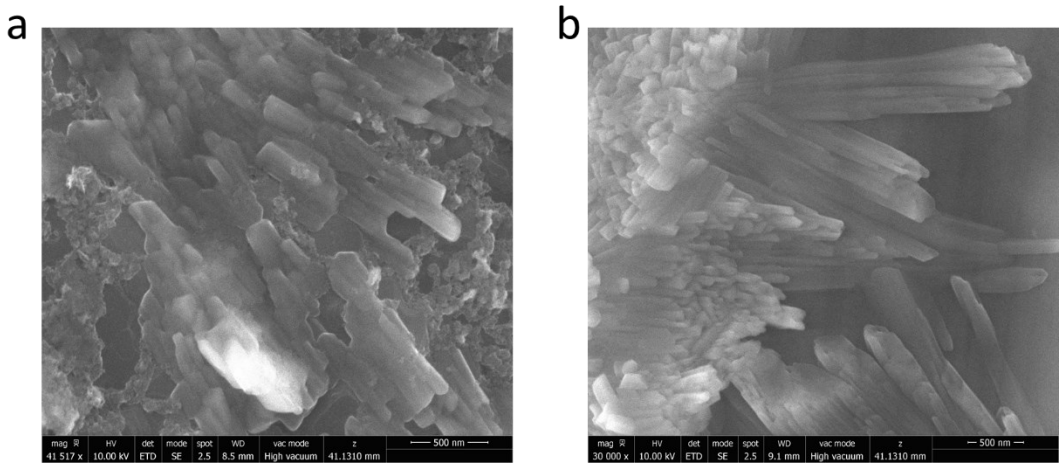

Figure 3-S8. SEM measurements of Co-CAT (a) and Ni-CAT (b) after 6 hrs of electrolysis at 1.42 V vs. RHE.

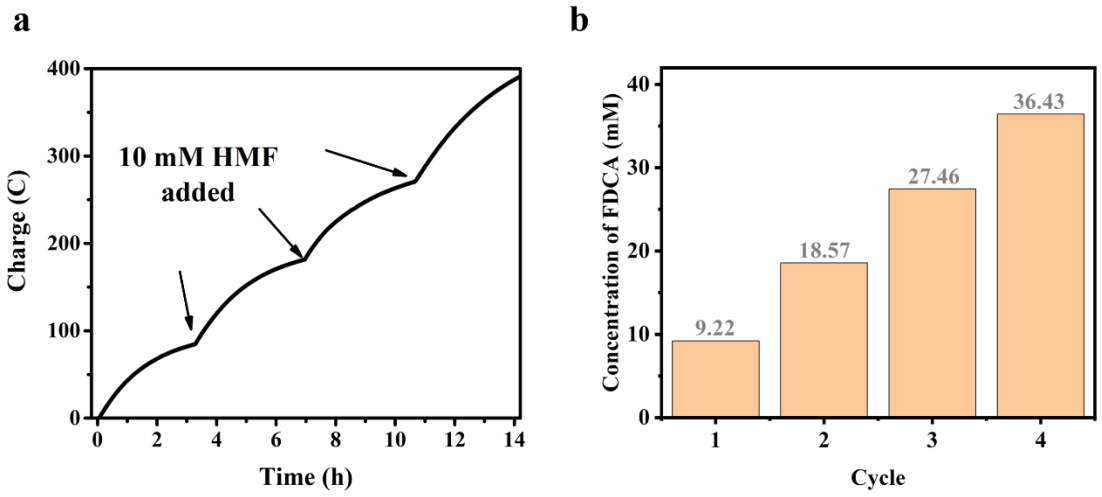

Figure 3-S9. A recyclability test was performed with the Ni-CAT. 10mM HMF was added for several cycles, which showed an increase in current (a) and continual buildup of FDCA (b) with each cycle.

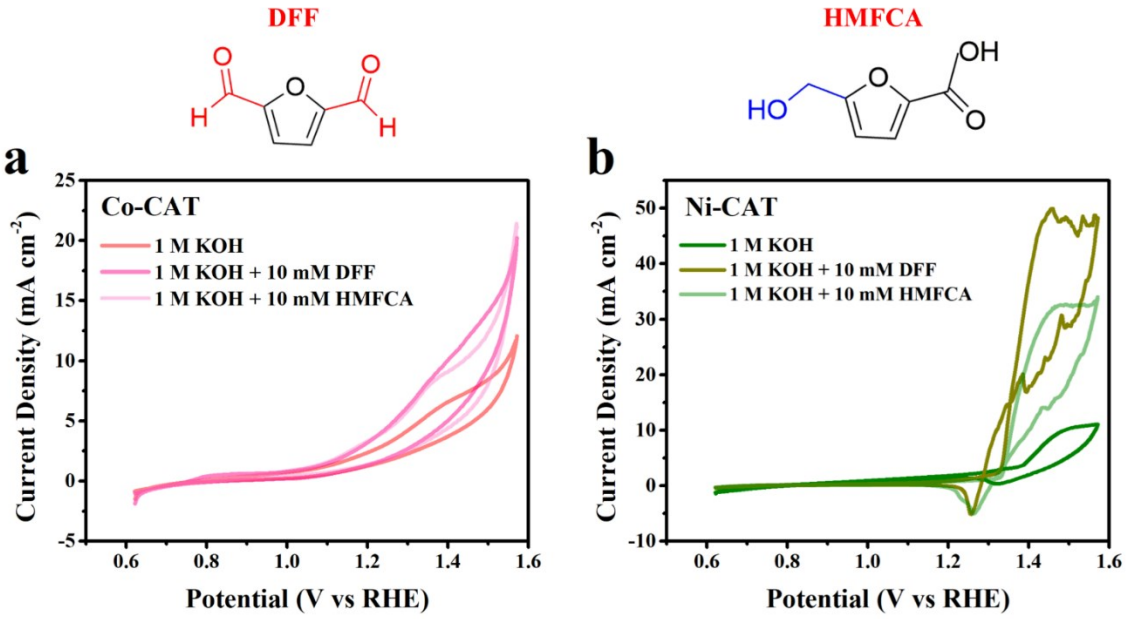

Figure 3-S10. CV measurements in the solution 10 mM DFF or HMFCA in the 1 M KOH with the same parameter setting with Figure 3-3.

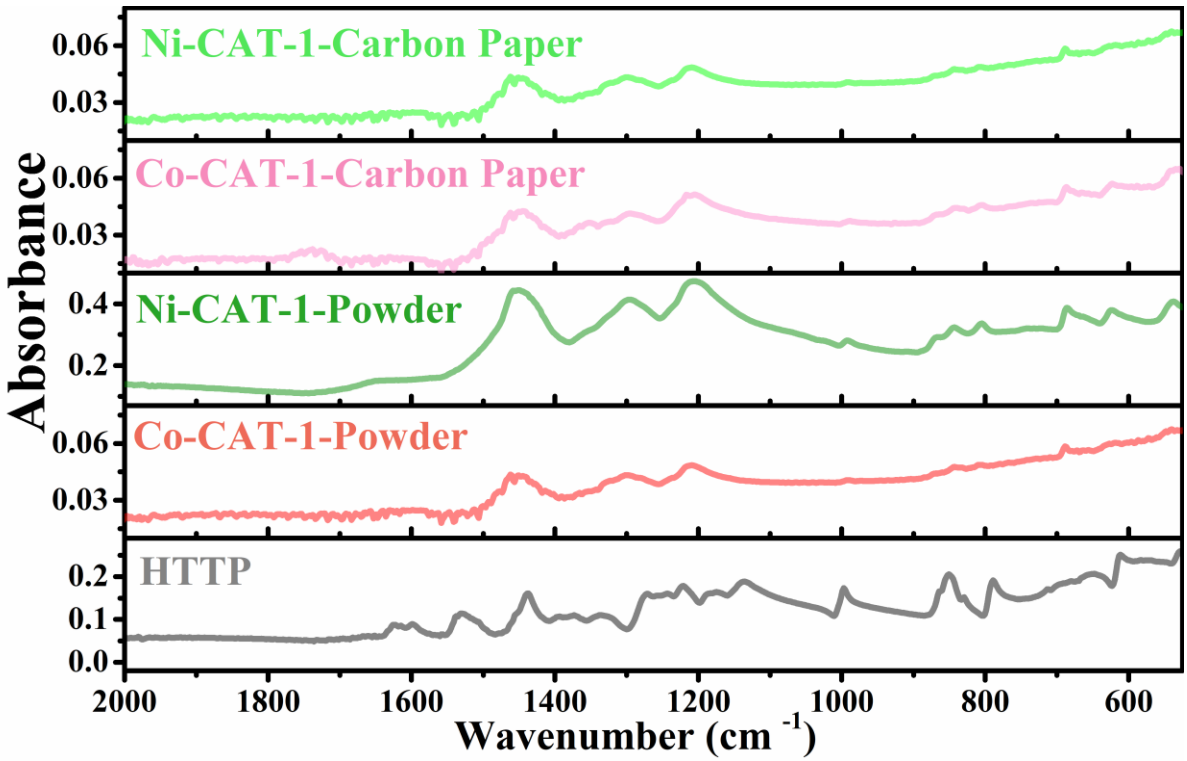

Figure 3-S11. The IR spectra of obtained Ni-CAT-Carbon Paper, Co-CAT-Carbon Paper, Ni-CAT-Powder, Co-CAT-Powder and HHTP, from top to bottom.

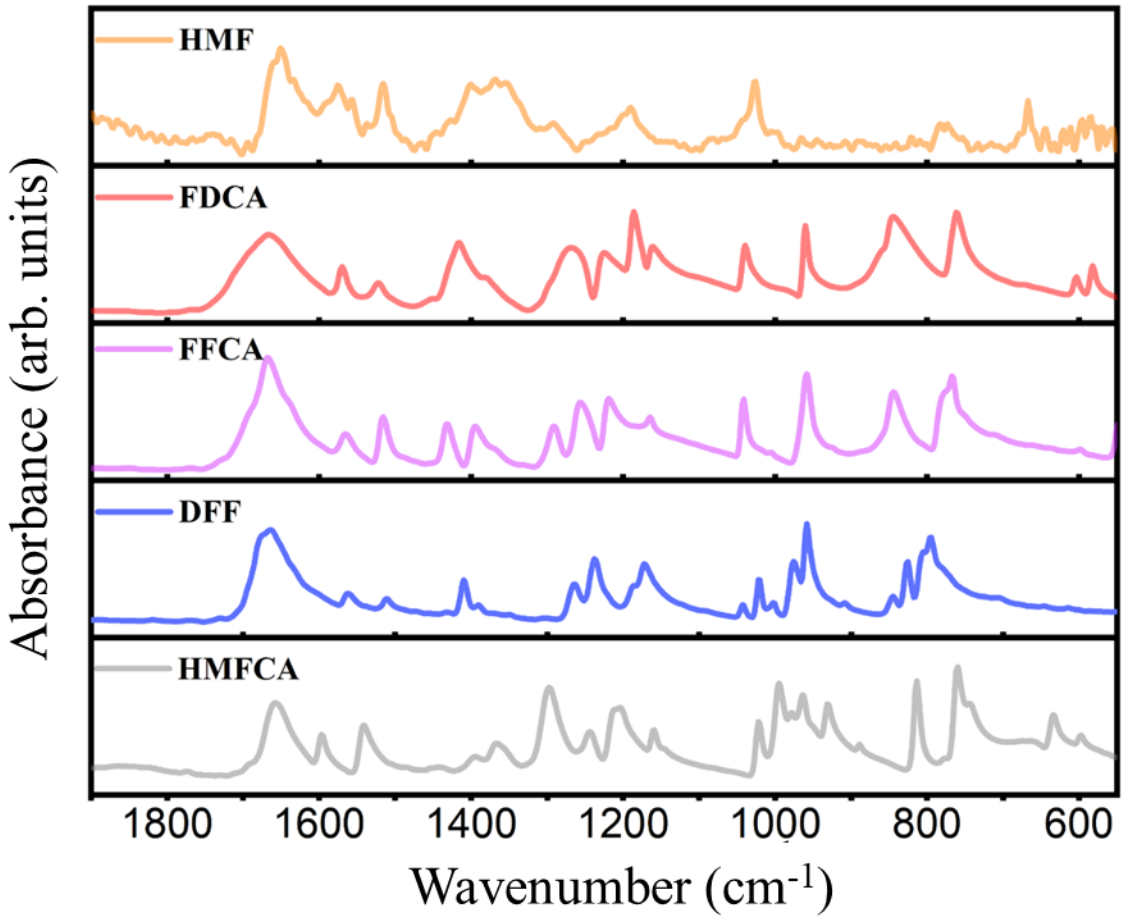

Figure 3-S12. IR spectra of HMF, FDCA, FFCA, DFF and HMFCA.

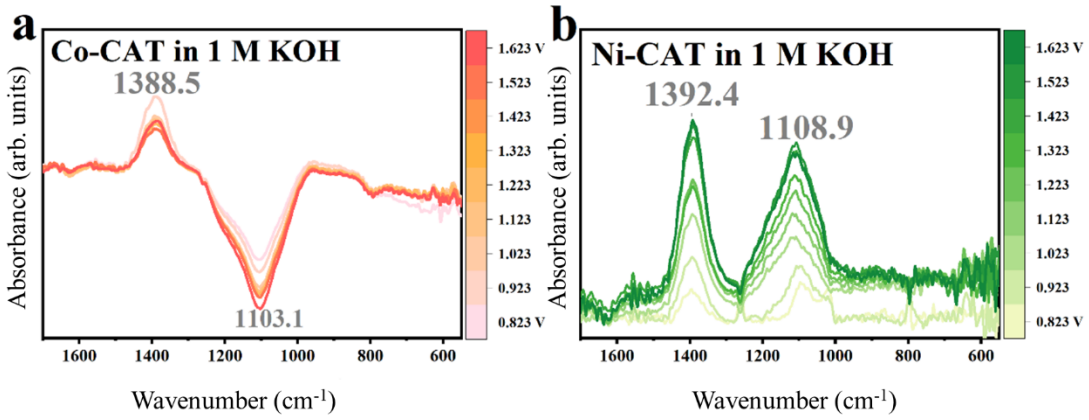

Figure 3-S13. Potential-dependent ATR-IR difference spectra of the Co-CAT and Ni-CAT in 1M KOH electrolyte under applied potentials.

Table 3-S1. Comparison of activity of M-CAT to other reported HMFOR catalysts.

Electrode Materials	Electrolyte Type	Onset Potential (V vs RHE)	Faradic Efficiency (%)	Tafel Slope mV/dec	Ref
Co-CAT	1 M KOH 10 mM HMF	1.05	97.7 % at 1.42 V	141.16	This work
Ni-CAT	1 M KOH 10 mM HMF	1.38	86.8 % at 1.42 V	42.34	This work
TpBpy-Ni@FTO	0.1 M $LiClO_4$ (pH = 13) 5 mM HMF	1.50	Not reported	Not reported	[65]
NiCoBDC	0.1 M KOH 10 mM HMF	1.50	78.8% at 1.55 V	60.8	[52]
Ir-Co_3O_4	1 M KOH 5 mM HMF	1.15	98% at 1.42 V	Not reported	[66]
$NiCo_2O_4$	1M KOH 5 mM HMF	1.20	87.5% at 1.5 V	135.7	[67]
CoP	1 M KOH 50 mM HMF	1.30	Not reported	Not reported	[68]
CoO-$CoSe_2$	1 M KOH 10 mM HMF	1.30	97.9% at 1.43 V	89.2	[69]
Branched Ni	0.1m KOH 10 mM HMF	1.39	Not reported	52.6	[70]
NiB	1M KOH 10 mM HMF	1.45	Near 100% at 1.45 V	Not reported	[71]
NiFe LDH	1M KOH 10 mM HMF	1.25	99.4% FE of HMF at 1.25 V	75	[41]
Ni_2P NPA/NF	1M KOH 10 mM HMF	1.35	Near 100% at 1.423 V	93	[72]
Ni_3S_2/Ni foam	1M KOH 10 mM HMF	1.38	98 % at 1.423 V	136	[73]
NiCoFe-LDHs	1 M NaOH 10 mM HMF	1.35	90% at 1.54 V, 55 °C	92	[74]
hp-Ni	1 M KOH 10 mM HMF	1.35	98% at 1.423 V	Not reported	[75]
Ni_3N@C	1 M KOH 10 mM HMF	1.38	99% at 1.45 V	48.9	[76]
CoB	1 M KOH 10 mM HMF	1.39	100% at 1.45 V	Not reported	[77]
NCF (Cu foam)	M KOH 5 mM HMF	1.38	96.4% at 1.62 V	Not reported	[45]

Table 3-S2. The Calculated Faradic Efficiency for electrolysis at 1.38 V.

Time (h)	Concentration of FDCA (mM)	Calculated Charge (C)	Passed Charge (C)	Faradic Efficiency (%)
2.5	7.77	67.47	73.09	92.32
3.5	9.24	80.20	82.30	97.45

3.9. Supporting Reference

1. Mähringer, A. et al. Oriented Thin Films of Electroactive Triphenylene Catecholate-Based Two-Dimensional Metal–Organic Frameworks. *ACS Nano* **13**, 6711-6719 (2019).
2. Cai, M. et al. Nickel(ii)-modified covalent-organic framework film for electrocatalytic oxidation of 5-hydroxymethylfurfural (HMF). *Chemical Communications* **56**, 14361-14364 (2020).
3. Cai, M. et al. Two-dimensional metal–organic framework nanosheets for highly efficient electrocatalytic biomass 5-(hydroxymethyl)furfural (HMF) valorization. *Journal of Materials Chemistry A* **8**, 20386-20392 (2020).
4. Lu, Y.X. et al. Tuning the Selective Adsorption Site of Biomass on Co3O4 by Ir Single Atoms for Electrosynthesis. *Advanced Materials* (2021).
5. Kang, M.J. et al. Electrocatalysis of 5-hydroxymethylfurfural at cobalt based spinel catalysts with filamentous nanoarchitecture in alkaline media. *Appl Catal B-Environ* **242**, 85-91 (2019).
6. Jiang, N., You, B., Boonstra, R., Terrero Rodriguez, I.M. & Sun, Y. Integrating Electrocatalytic 5-Hydroxymethylfurfural Oxidation and Hydrogen Production via Co–P-Derived Electrocatalysts. *ACS Energy Letters* **1**, 386-390 (2016).
7. Huang, X. et al. Enhancing the electrocatalytic activity of CoO for the oxidation of 5-hydroxymethylfurfural by introducing oxygen vacancies. *Green Chem* **22**, 843-849 (2020).
8. Poerwoprajitno, A.R. et al. Faceted Branched Nickel Nanoparticles with Tunable Branch Length for High-Activity Electrocatalytic Oxidation of Biomass. *Angew Chem Int Edit* **59**, 15487-15491 (2020).
9. Barwe, S. et al. Electrocatalytic Oxidation of 5-(Hydroxymethyl)furfural Using High-Surface-Area Nickel Boride. *Angew Chem Int Ed Engl* **57**, 11460-11464 (2018).
10. Liu, W.-J. et al. Electrochemical Oxidation of 5-Hydroxymethylfurfural with NiFe Layered Double Hydroxide (LDH) Nanosheet Catalysts. *ACS Catalysis* **8**, 5533-5541 (2018).
11. You, B., Jiang, N., Liu, X. & Sun, Y. Simultaneous H2 Generation and Biomass Upgrading in Water by an Efficient Noble-Metal-Free Bifunctional Electrocatalyst. *Angew Chem Int Ed Engl* **55**, 9913-9917 (2016).
12. You, B., Liu, X., Jiang, N. & Sun, Y. A General Strategy for Decoupled Hydrogen Production from Water Splitting by Integrating Oxidative Biomass Valorization. *Journal of the American Chemical Society* **138**, 13639-13646 (2016).
13. Zhang, M. et al. Trimetallic NiCoFe-Layered Double Hydroxides Nanosheets Efficient for Oxygen Evolution and Highly Selective Oxidation of Biomass-Derived 5-Hydroxymethylfurfural. *ACS Catalysis* **10**, 5179-5189 (2020).
14. You, B., Liu, X., Liu, X. & Sun, Y.J. Efficient H-2 Evolution Coupled with Oxidative Refining of Alcohols via A Hierarchically Porous Nickel Bifunctional Electrocatalyst. *Acs Catalysis* **7**, 4564-4570 (2017).
15. Zhang, N.N. et al. Electrochemical Oxidation of 5-Hydroxymethylfurfural on Nickel Nitride/Carbon Nanosheets: Reaction Pathway Determined by In Situ Sum Frequency Generation Vibrational Spectroscopy. *Angew Chem Int Edit* **58**, 15895-15903 (2019).
16. Weidner, J. et al. Cobalt-metalloid alloys for electrochemical oxidation of 5-hydroxymethylfurfural as an alternative anode reaction in lieu of oxygen evolution during water splitting. *Beilstein J Org Chem* **14**, 1436-1445 (2018).

17. Nam, D.-H., Taitt, B.J. & Choi, K.-S. Copper-Based Catalytic Anodes To Produce 2,5-Furandicarboxylic Acid, a Biomass-Derived Alternative to Terephthalic Acid. *ACS Catalysis* **8**, 1197-1206 (2018).

Chapter 4 C-N triple bond cleavage via trans-membrane hydrogenation

4.1. Abstract

Renewable energy powered electrosynthesis is an emerging green alternative to thermochemical routes. Against this backdrop, acetonitrile valorization is an important target as it is industrially produced in excess. In this work, we have developed a catalytic system which converts acetonitrile into acetaldehyde and NH_3 using a H-permeable Pd membrane reactor. In this system, H is abstracted from water in an aqueous electrolyte, transferred across the Pd membrane and is used to hydrogenate acetonitrile with up to 60% Faradaic efficiency (FE) for NH_3 generation. Further, we have constructed a unique infrared (IR) spectroelectrochemical cell that enabled us to probe the reaction as it occurred. This helped us deduce that the reaction proceeded through an imine hydrolysis pathway. Finally, we extended the scope of this system to 4 additional nitrile reactants. In all, this work establishes a new electrochemical route to nitrile hydrogenation and opens up promising avenues in electrosynthetic technologies.

Contribution:

Yuxuan Zhang: designed the project, carried out experiments, processed data, contributed intellectual insights, and wrote the manuscript.

Nikolay Kornienko: supervision, designed the project, carried out experiments, processed data, contributed intellectual insights, and wrote the manuscript.

C-N triple bond cleavage via trans-membrane hydrogenation

Yuxuan Zhang[1] and Nikolay Kornienko[1]*

[1]Department of Chemistry, Université de Montréal, 1375 Avenue Thérèse-Lavoie-Roux, Montréal, QC H2V 0B3, Canada.

*Email: nikolay.kornienko@umontreal.ca

Full Paper

Received: Nov 17, 2021; Accepted: Feb 5, 2022,

Available online: Feb 25, 2022; Version of Record: March 17, 2022.

DOI: 10.1016/j.checat.2022.02.005

Reproduced with permission from *Chem Catalysis*.

Volume 2, Issue 3, 17 March 2022, Pages 499-507

4.2. Graphical abstract

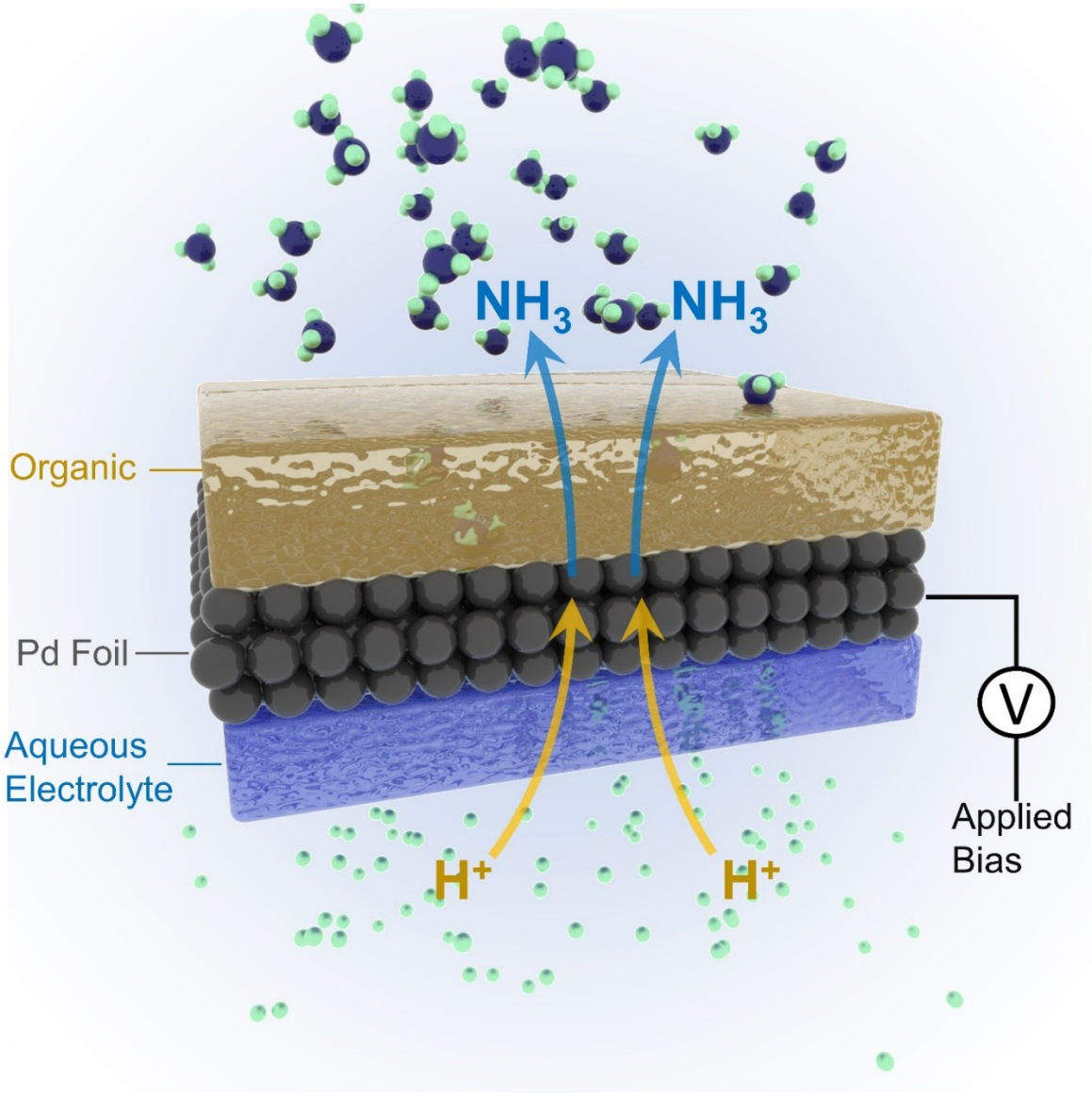

Etoc: An electrochemical method was developed to hydrogenate nitrile species en route to primary amine and ammonia production.

Highlights:

A Pd membrane reactor for electrochemical nitrile hydrogenation was developed

Operando infrared spectroscopy was used to probe the reaction mechanism

The hydrogenation of *NHx species was the limiting step in the reaction

4.3. Summary

Renewable energy powered electrosynthesis is an emerging green alternative to thermochemical routes. Against this backdrop, acetonitrile valorization is an important target as it is industrially produced in excess. In this work, we have developed a catalytic system which converts acetonitrile into acetaldehyde and NH_3 using a H-permeable Pd membrane reactor. In this system, H is abstracted from water in an aqueous electrolyte, transferred across the Pd membrane and is used to hydrogenate acetonitrile with up to 60% Faradaic efficiency (FE) for NH_3 generation. Further, we have constructed a unique infrared (IR) spectroelectrochemical cell that enabled us to probe the reaction as it occurred. This helped us deduce that the reaction proceeded through an imine hydrolysis pathway. Finally, we extended the scope of this system to 4 additional nitrile reactants. In all, this work establishes a new electrochemical route to nitrile hydrogenation and opens up promising avenues in electrosynthetic technologies.

4.4. Introduction

Developing electrosynthetic processes to produce value-added chemicals from abundant building blocks is an important direction in sustainability research.[1-3] Such reactions, driven by renewable energy, stand to take place of thermochemical pathways. While much attention has been placed on the electrocatalytic reactions of water electrolysis and CO_2 reduction, there remains much room to expand the scope of electrosynthetic technologies.[4-7] Beyond water and CO_2, additional abundant reactants of interest include methane, [8] biomass, [9,10] and chemicals like acetonitrile which are by-products of industrial processes. As such, the electrochemical conversion of acetonitrile to in-demand products is the focus of this work.

Acetonitrile is typically generated as a by-product in acrylonitrile production (produced at a scale of 5 million tons per year). Most of the acetonitrile produced is burned afterwards, generating the toxic NO_x species in the process.[11] Its uses are primarily as an organic solvent and building block in organic synthesis, but its production far outweighs its demand (~10-20 thousand tons per year). Against this backdrop, the development of electrocatalytic routes to convert acetonitrile into societally useful chemicals is an important direction in sustainability. Previously, acetonitrile conversion was mainly carried out with thermochemical processes. In particular, amines were generated as the main products using metal catalysts and H_2 as the reducing source.[12-16] However, electrochemical routes, which take hydrogen directly from water and are thus more sustainable are not yet well-established and only few reports exist. Recently, Cu has been shown to be effective in generating ethylamine as the main product in alkaline[17] or neutral[18] electrolytes. Earlier works produced ammonia and ethane with Pt electrodes.[19,20] In general, a significant challenge in electrochemical acetonitrile reduction is attaining selectivity for one particular product, minimizing the competing hydrogen evolution reaction (HER), and decreasing the overpotential necessary to carry out the reaction.

In this work, we investigated the electrochemical conversion of acetonitrile with water as the hydrogen source. Instead of carrying out the reaction in a conventional three-electrode

electrochemical setup, we used a Pd-membrane reactor[21,22] for the first time for acetonitrile conversion. In this type of reactor, a 25 μm Pd electrode served as the working electrode that reduced aqueous protons to *H. The *H diffused through the Pd from the aqueous compartment to the organic compartment where it could hydrogenate the reactant of interest. The advantage here was that the hydrogenation can take place in an organic environment which would minimize the HER. Further, through the use of the Pd-membrane reactor, we have demonstrated an improvement in onset potential of ~0.5 V over the previous state-of-the-art systems utilizing a conventional three-electrode setup.[17,18]

In our system, H^+ from an H_2SO_4 electrolyte were reduced to *H on the surface of Pd. In the organic compartment the *H reacted with acetonitrile to generate NH_3 and acetaldehyde as the two main products (Fig. 1). These two products are in high industrial demand and are currently produced through thermochemical routes. NH_3, widely used a fertilizer, is currently produced via the Haber Bosch process. Acetaldehyde, currently produced at a million ton scale through the high temperature/pressure Wacker process[23,24], is an important precursor for the production of many commodity chemicals.

To complement the electrochemical studies, we carried out an *operando* spectroscopic investigation in which the system was probed under reaction conditions. In particular, an infrared (IR) spectroelectrochemical setup was developed to enable spectra to be acquired of the reaction as a function of applied potential and/or time to identify key steps in the reaction mechanism. It was determined that the reaction proceeds rapidly through an imine hydrolysis pathway and that the hydrogenation of the latent NH_x species on the Pd surface is the slowest step in the reaction cycle. Finally, the scope of the reaction was expanded to four additional nitrile reactants. Overall, this work opens up new avenues in electrosynthesis, heterogeneous catalysis and spectroscopy all in the direction of sustainability research.

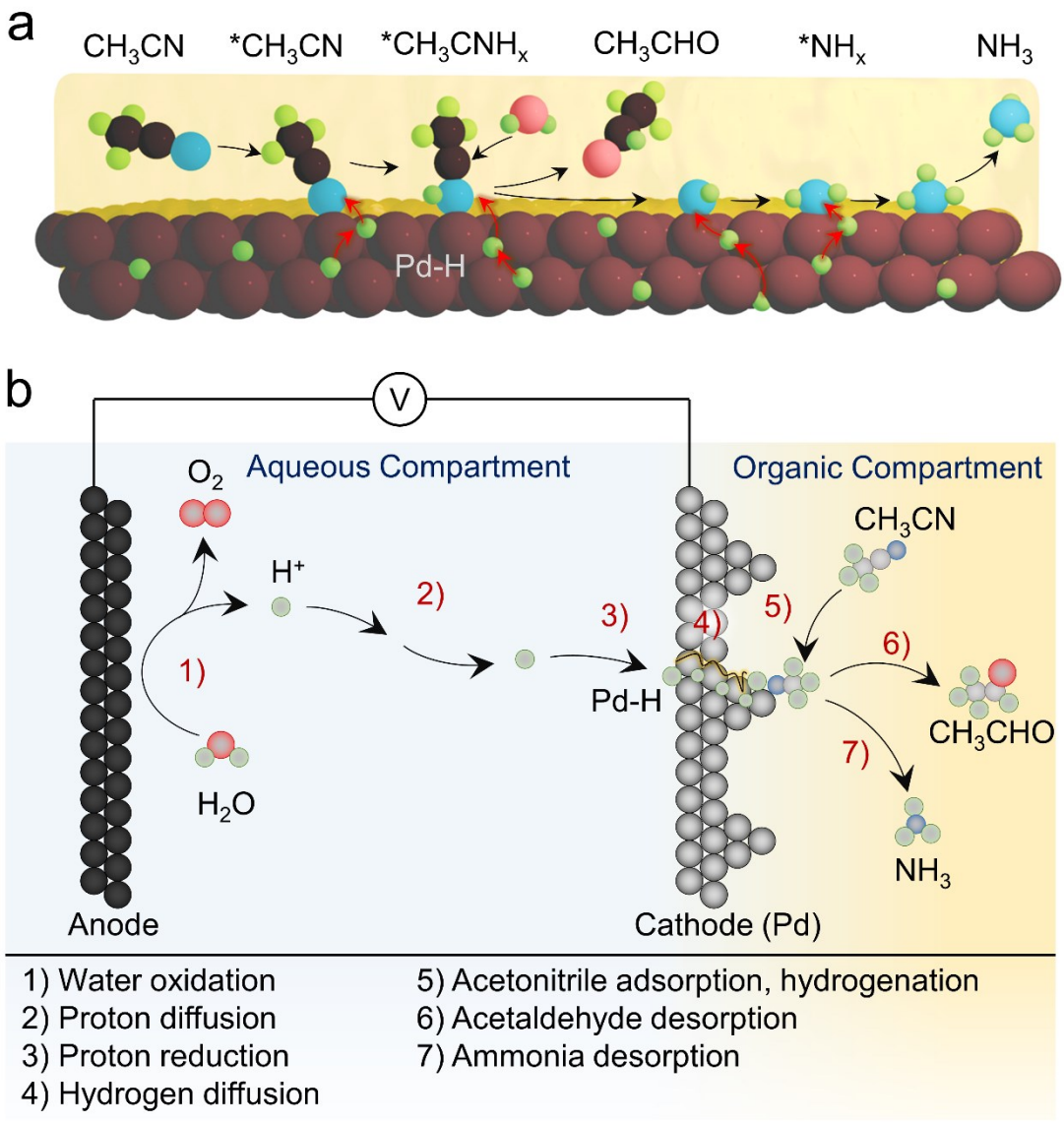

Figure 4-1. Illustration of the Pd-membrane reaction system. Schematic diagrams of acetonitrile hydrogenation to produce ammonia and acetaldehyde on the surface of Pd (a) and schematic diagrams of the device (b).

4.5. Results and Discussion

The setup for our reactor closely mirrored those previously utilized in Pd-membrane hydrogenation studies.[21] A commercially purchased 25 μm Pd foil was used as the membrane. To increase its surface area and therefore the density of catalytic sites, Pd was further electrodeposited on the side of the foil to be eventually in contact with the acetonitrile solution. The electrodeposition procedure resulted in a rough surface coverage (Fig. 2a), comprised of a Pd

spikes with ~100 nm size dimensions (Fig. 2b). The spike like morphologies result from the presence Cl^-, large overpotential applied, and faster growth kinetics in the 〈1 0 0〉 relative to the 〈1 1 1〉 growth directions.[25-28]

In our electrochemical reactor (Fig. S1, 2) 0.5M H_2SO_4 was the electrolyte in the aqueous compartment with the reference and counter electrodes also immersed in the same chamber. We first measured the cyclic voltammogram (CV) with air was on the other side (H_2SO_4 │Pd│ air). The CV shows the hydrogenation of the Pd and HER at negative potentials and a large dehydrogenation peak in the positive sweep (Fig. 2c). If the air was replaced with acetonitrile with 0.2% (V:V) acid, (H_2SO_4 │Pd│ CH_3CN), the reductive current in the CV diminished and the dehydrogenation peak also decreased.

We then tested the reaction products after electrolysis as a function of applied potential. The NMR spectra of the solution after extended electrolysis revealed that ammonia and acetaldehyde were the two main liquid phase products present (Fig. 2d, S3-5). The broad peak around 7.5 ppm stems from $NH_2CH_2CH_3$, resulting the hydrogenation of acetonitrile but not complete cleavage of the C-N bond. The products were generated through the following reactions, with 1) occurring in the aqueous compartment and 2) and 3) occurring in the organic compartment:

1) $H^+ + e^- \rightarrow *H$
2) $3*H + CH_3CN + H_2O \rightarrow NH_3 + CH_3CHO + H^+$
3) $4*H + CH_3CN \rightarrow CH_3CH_2NH_2$

While the formal redox potential for 1) is well established as 0 V_{RHE}, previous works have indicated that the formal potentials for 2) and 3) may be situated around ~0.3 – 0.6 V_{RHE}.[19,20,29] The volatility of acetaldehyde leads to its partial escape from the solution and thus its relatively lower peak area in relation to NH_3 and thus it was not included in the quantification. We tracked the partial current density of NH_3 generation (present as NH_4^+ in acidic solutions) and saw that the NH_3 production rate began to significantly increase at -0.2 $V_{Ag/AgCl}$ peaked at -0.6 $V_{Ag/AgCl}$ (Fig. 2e). The Faradaic efficiency (FE) for NH_3 reached its maximum at -0.5 $V_{Ag/AgCl}$ (Fig. 2f). HER began to dominate at potentials more negative than this.

While the maximum FE was recorded at -0.5 $V_{Ag/AgCl}$, small quantities of the reaction products (I_{NH3} < 0.1 mA/cm^2) were detected as positive as 0.4 $V_{Ag/AgCl}$, where there is still a small rate Pd hydrogenation (Fig. S6a). Though the operating currents in our work are lower, the onset potential constitutes an improvement over previously studied metal catalysts, whose onset potential was at best around ~-0.3 V_{RHE} (~-0.5 $V_{Ag/AgCl}$).[17,18] As a comparison, we also carried out the reaction with the Pd electrode in a conventional three-electrode setup. Running the reaction in one compartment with 10% (V:V) acetonitrile in 0.5 M H_2SO_4, in which *H and CH_3CN can react in a mostly aqueous environment needed applied voltages of 0V or lower (more negative) to generate any detectable NH_3 (Fig. S6b). This illustrates the H-membrane approach significantly lowers onset potentials.

At more negative potentials than the optimum -0.5 to -0.6 $V_{Ag/AgCl}$, HER was the main reaction (Fig. S7). In this regime, the hydrogenation of the nitrile group could not kinetically keep pace

with the flux of available *H. This could be improved in future studies through the use of a co-catalyst.

We next investigated the importance of having small quantities of acid in the organic compartment. The addition of DI water instead of acid into the organic compartment lead to lower performance, with a maximum FE and I_{NH3} being more than two times lower (Fig. S8). This pointed to the importance of an acidic environment. We also omitted water completely from the organic compartment. The use of dry acetonitrile resulted in no detectable NH_3 or acetaldehyde products (Fig. S9). Overall, the observation of acid-enhanced catalysis provided evidence that the reaction features a step similar to what has been observed in acid-catalyzed imine hydrolysis.[30,31] We speculated that the reaction yielded ammonia and acetaldehyde by going through a surface-bound acetonitrile-derived intermediate. We last tested the stability of the system. The reaction exhibited consistent NH_3 generation for more than 80 hrs at -0.6 $V_{Ag/AgCl}$ and electron microscopic evaluation of the Pd surface did not reveal any significant changes in its appearance (Fig. S10, 11).

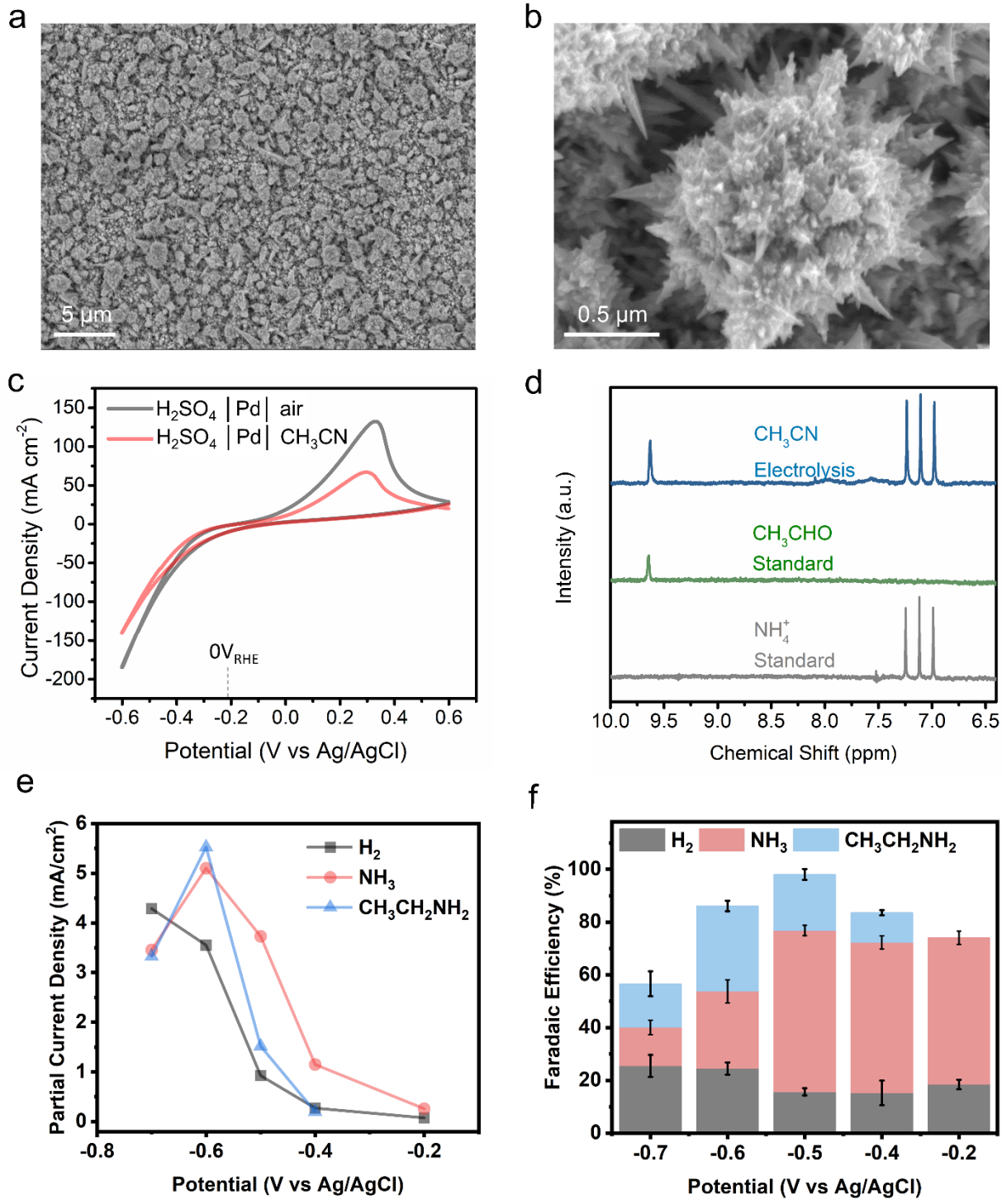

Figure 4-2. Characterization of Pd catalyst morphology and performance. Scanning electron micrographs of the rough Pd surface (a, b). CVs scans the Pd hydrogenation and dehydrogenation processes (c) and NMR spectra of the solution after electrolysis (d). The partial current density (e) and FE (f) for the reaction is plotted as a function of applied potential.

To obtain a deeper mechanistic handle on the reaction, we moved to spectroscopically investigate the process with IR techniques. To realize this, we constructed a customized cell in which a thin acetonitrile layer was sandwiched between a diamond coated ZnSe prism used for attenuated total reflection (ATR) measurements and the Pd foil (Fig. 3a). Thus, this would enable the probing of solubilized species in the acetonitrile solution and surface catalysis on the Pd. On the other side of the Pd was the aqueous compartment with the reference and counter electrodes. We note that to the best of our knowledge, this is the first time such a measurement was carried out on a Pd-membrane hydrogenation system and thus stands to open many new opportunities in the field.

We first measured the spectrum of the system at open circuit (between 0.4 and 0.5 $V_{Ag/AgCl}$) and used this as a reference against which spectral changes were recorded either as a function of potential or time. Upon moving the potential more negative than open circuit, positive bands began to appear, with the strongest located at ~2900, 1725, 1283, 1128, and 1074 cm^{-1} (Fig. 3b). The bands at 2900 and 1725 cm^{-1} match almost the bands corresponding to the C-H and C=O stretches of acetaldehyde, respectively (Fig. S12). A growing negative band at 2252 cm^{-1} matched well with the band corresponding to the C≡N bond stretch for acetonitrile and indicated its depletion. The species at 1283, 1128, and 1074 cm^{-1} were deemed to be related to hydrogenated species as those bands exhibited the expected red-shifts of 30-50 cm^{-1} if D_2O/D_2SO_4 was used in the aqueous compartment instead (Fig. 3c). Bands in this spectral region were previously noted in studies of N_2 or NO_3 reduction to ammonia[32-34] and thus, the assignment of these bands in our spectra to $*NH_x$ species is therefore reasonable.

To deepen our insights into the chemistry at play in our Pd-membrane hydrogenation process, we probed the system as a function of time immediately after jumping from open circuit to -0.6 $V_{Ag/AgCl}$ (Fig. 3d). We tracked the integrated intensity of the main bands as a function of time and individually normalized them to their intensity at the end of the measurement (at 22 min) for ease of comparison (Fig. 3e). The intensities plateaued at 10-12 minutes, so the figure is zoomed in on this time period. Immediately evident was that the acetaldehyde bands (2900 and 1725 cm^{-1}) and the 1283 cm^{-1} band rose with the same time constant. Thus, we attribute the 1283 band as a first hydrogenated species (*NH or $*NH_2$) that is remaining on the Pd surface after the imine hydrolysis step to generate acetaldehyde. In contrast, the bands at 1128 and 1075 cm^{-1} took longer to reach their maximum intensity and are thus attributed to a further hydrogenated species that remain on the Pd after acetaldehyde formation (either $*NH_2$ or $*NH_3$). The ratios between the 1128 and 1075 cm^{-1} bands and the 1283, 2900 and 1725 cm^{-1} are plotted in the inset of Fig. 3e and Fig. S13 as a complementary way to visualize the time-delay in generating this 2nd $*NH_x$ species. Thus, the spectroscopic data paints a picture in which the initial acetonitrile adsorption and hydrogenation, alongside the imine hydrolysis, occur rapidly and the final hydrogenation of the $*NH_x$ species is the slower reaction step. Further, products are observed starting from 0.4 $V_{Ag/AgCl}$, matching the initial detection of NH_3 and acetaldehyde in the NMR spectra, indicating that the thermodynamic onset is simply determined by the potential in which the Pd-hydrogenation commences.

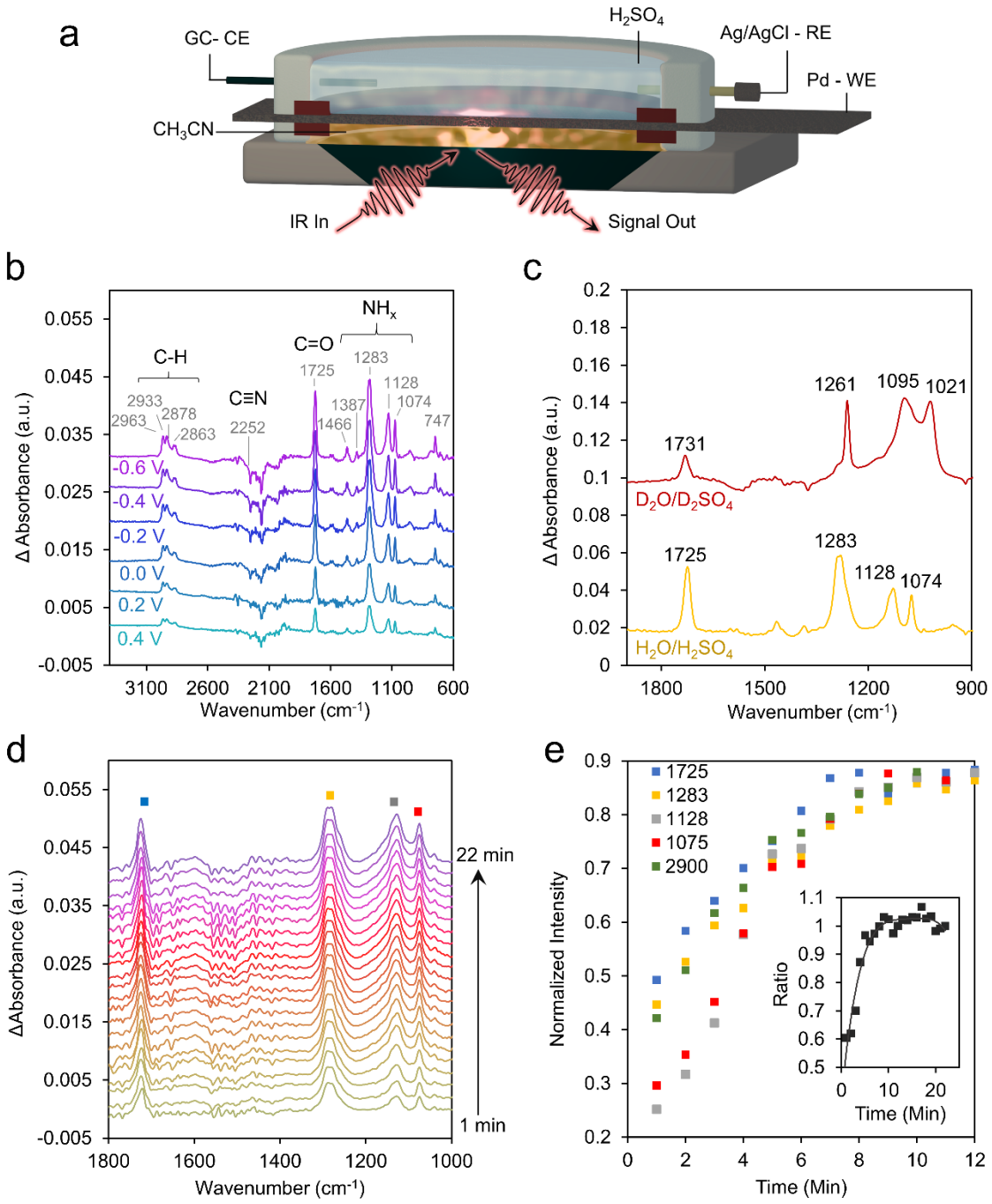

Figure 4-3. IR spectroelectrochemical testing. The spectroelectrochemical configuration employed to probe the reaction process is illustrated (a). Spectra recorded as a function of applied potential (b) and compared with those using a D_2O/D_2SO_4 electrolyte (c). Time dependent spectra (d) were used to track the evolution of individual species (e). The spectrum taken at open circuit (approx. 0.45 $V_{Ag/AgCl}$) was used as the baseline for (b-e).

Through the sum of our electrochemical and spectroscopic studies, we come to a unique reaction mechanism enabling the synthesis of acetaldehyde and ammonia from acetonitrile (Fig. 4). We believe that the initial adsorption and hydrogenation occurs rapidly, as does the imine hydrolysis step as acetaldehyde is immediately visible in the IR spectra. Instead, the downstream $*NH_x$ hydrogenation steps take longer to carry out, judging from the slow rise in the bands corresponding to latent $*NH_x$ species. Following successive hydrogenation steps, the ammonia product desorbs into the solution and is eventually protonated to give rise to the ammonium signal observed in the NMR spectra.

Instead of only terminating at ethylamine, the unique synthetic approach enables the complete cleavage of the C≡N triple bond. Further, as the reaction onset is limited by the Pd hydrogenation potential, it is possible to carry out the reaction before the thermodynamic potential for the hydrogen evolution reaction is reached. This offers a substantial advantage over a conventional electrosynthetic scheme where, for example, onset potentials for a variety of metallic catalysts were on the order of -0.3 V_{RHE},[17,18] with our work offering a significant improvement over this value.

As a final endeavor, we demonstrated the generality of our transmembrane-driven C≡N cleavage by using four additional nitrile reactants (Scheme S1, Fig. S14). Indeed, we succeeded in generating ammonia and the analogous aldehyde from propionitrile, benzonitrile, isobutyronitrile, and acrylonitrile with FEs ranging from 12 % to 21 % (Fig. S15, 16). While the performance is lower than that for the acetonitrile case and Pd dissolution must be minimized (Fig. S17), this proof-of-concept expansion of scope opens tangible opportunities for Pd membrane based conversion of nitriles.

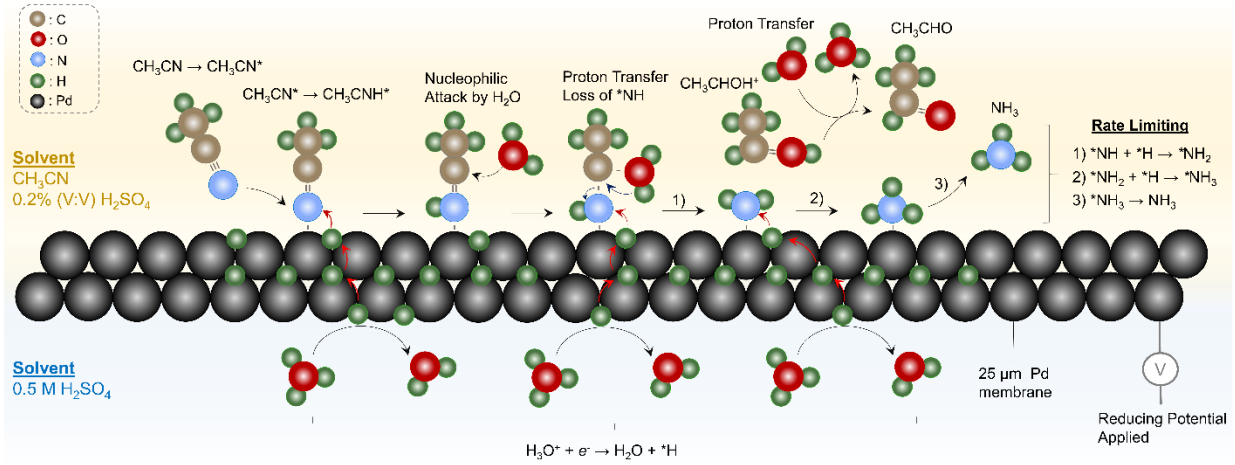

Figure 4-4. Reaction mechanism. The proposed catalytic reaction mechanism for acetonitrile conversion into ammonia and acetaldehyde is illustrated.

4.6. Concluding Remarks

Following our investigation with electrochemical and spectroscopic tools, several obvious avenues come to mind that may help improve the system's performance. Our catalytic Pd surface was not optimized beyond making it rough through an electrodeposition approach. As different facets, active sites, defects and more and known to display varying activity in heterogeneous catalysis, it would be beneficial to quantify their activity through a combination of synthesis, electrochemistry, theory and spectroscopy and maximize their abundance. Further, the deposition of a co-catalyst to aid in reactant adsorption and product desorption also stands to boost the system's activity. We identified the later hydrogenation stages of NH_x as being limiting and a co-catalyst may certainly help accelerate these steps. Further, reactor engineering may improve the throughput of the process by facilitating mass transport and translating this over to a flow cell geometry[35] could significantly boost the steady state current density. In all, this work conceptually opens many exciting routes in electrosynthesis through the discovery of complete nitrile C≡ N bond cleavage. We envision that this can readily be extended over to additional challenging reactions such as N_2 reduction or phosphorus fixation.

4.7. Experimental Procedures:

4.7.1. Chemicals

Hydrochloric acid 0.5 N (HCl), Sulfuric acid 1.0 N (H_2SO_4) were obtained from Anachemia company. Palladium foil (Pd, 0.025 mm thick, 99.9%), Acetonitrile (99.95+%), 2 propanol were purchased from Fisher Scientific company. Palladium Chloride ($PdCl_2$, 99.9%) was purchased from VWR international company. Sulfuric acid-d_2 solution (96-98 wt. % in D2O, 99.5 atom %D), Dimethyl sulfoxide-d_6 (99.9 atom % D) was get from Sigma-Aldrich Company. Ammonium Chloride (NH_4Cl, 98+ %), Iron chloride hexahydrate ($FeCl_3{\cdot}6H_2O$, 97 %) were purchased from Alfa Aesar company. Ethylamine, 70 wt. % solution in water was obtain from Elf Atochem company. Benzonitrile, 99+ %, Acrylonitrile, 99+ %, and Propionitrile, 99+ % were purchased from Acros Organics company. Maleic acid was got from Ward's Science company. Acetaldehyde ammonia trimer ($C_6H_{15}N_3{\cdot}\ 3H_2O$, >95 %) was purchased from TCI America company.

4.7.2. Catalyst Preparation and Characterization

The palladium foil was prepared by an electrodeposition method. The palladium foil substrate was clamped into the middle compartment of the H-cell as the working electrode. A 15.9 mM $PdCl_2$ electrolyte in 0.5 N HCl was used for the electrodeposition. To roughen the Pd surface, a -0.2 V versus Ag/AgCl was applied until 13 C of charge (6.5 C cm^{-2}) was passed for a estimated total of 7.17 mg of palladium on the surface. Electrochemical double-layer capacitances measurements were tested in Ar-saturated 0.5 M H_2SO_4.

An Ag/AgCl in 3M KCl solution was used as the reference electrodes and a graphite rod was used as the counter electrode. The Ag/AgCl reference was periodically checked against a master reference electrode for any potential drifts to maintain stable in alkaline electrolyte. A biologic VMP200 potentiostat and EC-lab software were used for electrochemical experiments. To compensate for the IR drop in the solution, the ZIR program was employed by recording the

impedance between the cathode and reference electrode at open circuit at 100 KHz frequency. A typical electrolysis experiment was 90 minutes in our work.

The morphology and microstructure of as prepared Pd foil were investigated by scanning electron microscopy (SEM) and transmission electron microscopy (TEM). Both the SEM and TEM images were collected at the Centre for Characterization and Microscopy of Materials at Polytechnique Montreal. SEM images were obtained using a JEOL JSM-7600F Filed Emission SEM microscope. TEM images were conducted on JEOL JEM-2100F FEG-TEM, operated at 200 kV. For TEM characterizations, samples were prepared by carefully scratched off the electrodeposition part and disperse them onto a copper grid supporting a thin electron transparent carbon film.

4.7.3. Electrochemistry Analysis and Product Quantification

Electrochemistry experiments were carried out in an H-type two-compartment glass electrochemical cell. A Pd foil was pressed between the electrochemical compartments of the cell. Each compartment contained a total of 50 ml solution volume. The electrochemical compartments obtained 1 N H_2SO_4 and the chemical compartments contained acetonitrile. Cyclic voltammetry (CV) measurements were performed with the scan rate of 20 mV s^{-1} in the H_2SO_4 solution and another compartment is filled with air or with acetonitrile. An Ag/AgCl in saturated KCl solution was used as the reference electrodes and a graphite rod was used as the counter electrode. In all cases, the surface area of the foil on the both the chemical and electrochemical sides was measured to be 0.785 cm^2. The reference (Ag/AgCl gel in 3M KCl, 25ºC) was used to calculate RHE with $\mathbf{E_{RHE} = E_{Ag/AgCl} + 0.059\ pH + E^{o}_{Ag/AgCl}}$, where $\mathbf{E^{o}_{Ag/AgCl}} = 0.206$ V**.** Ohmic losses were corrected for through electrochemical impedance measurements (at 85%) prior to electrochemical measurement through the ZIR function within the EC-lab software (impedance measured at open circuit at 100 KHz).

60 mM H_2O 2 % sulfuric acid solution (1 N) was dissolved in acetonitrile. Subsequently, the solution was bubbled with either Ar or N_2 gas for 30 min to remove the possible oxygen. Chronoamperometry was conducted at different potential to electrolysis of aqueous part (H_2SO_4 electrolyte) and the organic compartment is filled with 60 mM H_2O in acetonitrile solution. In an optimized condition, the organic compartment was filled with 0.2% (V:V) 0.5 M H_2SO_4 in acetonitrile solution while the aqueous part remains 0.5 M H_2SO_4.

The identification and quantification of all reactants and products were achieved by ^{1}H NMR (Bruker AVANCE II 400 se), using D-DMSO with 2-propanol as an internal standard. The presented data is the accumulated result of 64 scans. 400 ul of the reaction mixture, 400 ul of 10 mM 2-propanol dissolved in D-DMSO, and 100 ul of 1.0 N H_2SO_4 were used for a typical NMR sample. The same conditions were adapted to the measurements of standard solutions.

Acetonitrile was pre-dried with type 4A molecular sieves. After 1.5 hours of electrolysis of the dry acetonitrile solution, 400 ul of reactant, 400 ul of 10 mM 2-propanol dissolved in D-DMSO were used for NMR analysis. For comparison with the dry acetonitrile, we denote the acetonitrile with water or acid as the ‘wet’ acetonitrile.

Calculation of the Faradic Efficiency: The Faradaic efficiency of ammonia and is the ratio of the number of electrons transferred for the formation of ammonia to the total amount of electricity that flows through the circuit. Assuming three electrons were needed to form one ammonia, the faradaic efficiency for ammonia synthesis could be calculated as follows:

$$FE_{ammonia} = \frac{3 \times F \times C \times V}{Q} \times 100\%$$

$$i_{ammonia} = FE_{ammonia} \times i_{average\ current\ density}$$

where F is the Faradaic constant, Q is the charge passed in total during the reaction, C is the concentration of generated ammonia and V is the volume of the electrolyte.

For the ethylamine, assuming four electrons were needed to form one ethylamine, the faradaic efficiency for ethylamine synthesis could be calculated as follows:

$$FE_{ethylamine} = \frac{4 \times F \times C \times V}{Q} \times 100\%$$

$$i_{ethylamine} = FE_{ethylamine} \times i_{average\ current\ density}$$

The Faradaic Efficiency and partial current density of H_2 is calculated from gas chromatogram (GC, SRI 8610C) peak area at a given potential as follow:

$$FE_{H_2} = \upsilon_{H_2} \times V \times \frac{2F}{QV_m} \times 100\%$$

$$i_{H_2} = FE_{H_2} \times i_{average\ current\ density}$$

i_{H_2}: partial current density for H_2.

υ_{H_2}: volume concentration of H_2 based on the calibration of the GC

V: the volume of gas.

F: Faradaic constant, 96485.3499 C mol^{-1}

V_m: 22.4 L/mol

4.7.4. Infrared spectroscopy

Infrared spectroscopy in an ATR configuration was performed with ThermoFischer Nicolet 380 FTIR-ATR system with a ZnSe ATR crystal coated with a diamond surface. For ex-situ measurements, each spectrum was recorded with an accumulation of 400 scans with a resolution of 4 cm^{-1}.

For *in situ* IR spectroscopy, the experiments were executed with the use of a custom-designed spectroelectrochemical cell. The electrodeposited Pd foil was the working electrode to separate the H_2SO_4 and the acetonitrile solution. Simultaneously, Cu wire was used as the counter electrode and the Ag/AgCl was used as the reference. Each infrared absorption spectrum was acquired by averaging 200 scans and this was then subtracted from the spectra at certain potential or time values. All infrared spectral acquisitions were carried out after a constant potential was applied to the electrode for 5 min. The background spectrum of the catalyst electrode was acquired at an open-circuit voltage before each systemic measurement, and the measured potential ranges of the electrocoupling reaction were 0.4 to –0.6 $V_{Ag/AgCl}$ with an interval of 0.2 V.

For the time dependence in situ IR experiments, the background spectrum was recorded at the open circuit potential with an accumulation of 200 scans. After a constant potential was applied to the electrode for 1 min, we tracked the spectra for each min (1-22 min).

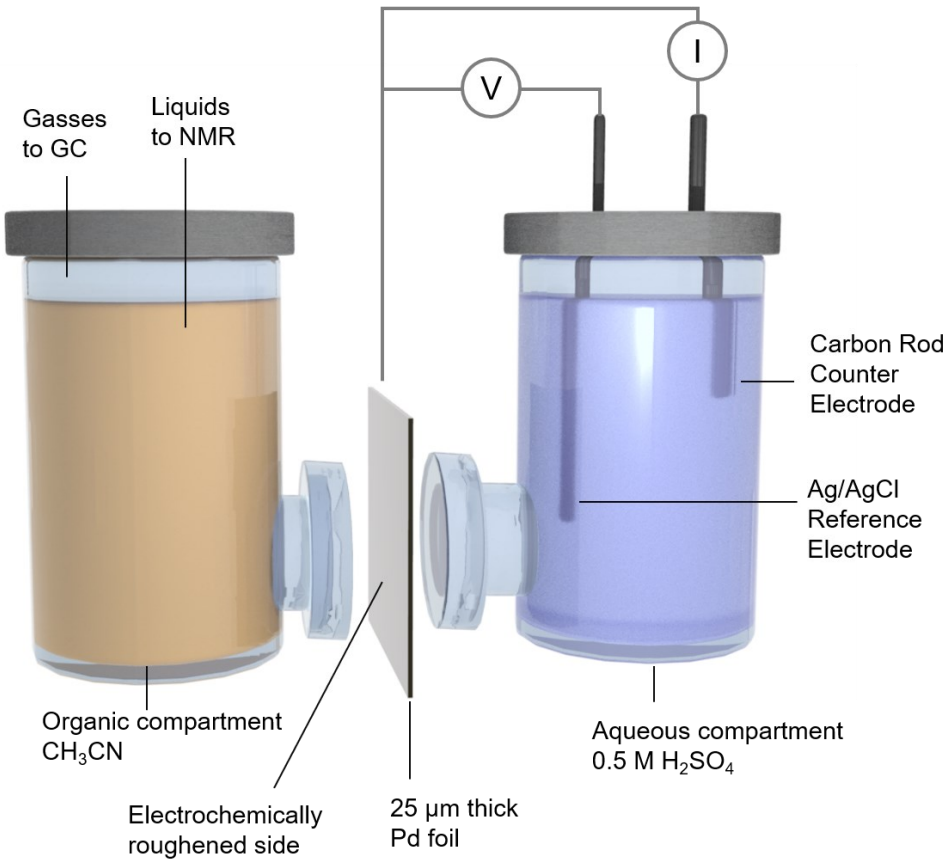

Figure 4-S1. Reactor. Simplified schematic of the electrochemical setup employed in this work.

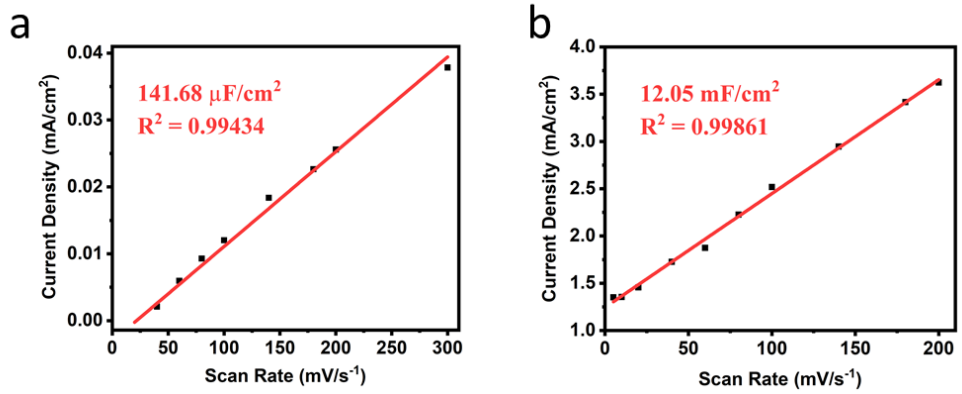

Figure 4-S2. Surface area measurements. Double-layer capacitance measurements of (a) the planar palladium electrode and (b) the electrodeposited palladium surface demonstrates an approximate 85-fold increase in surface area.

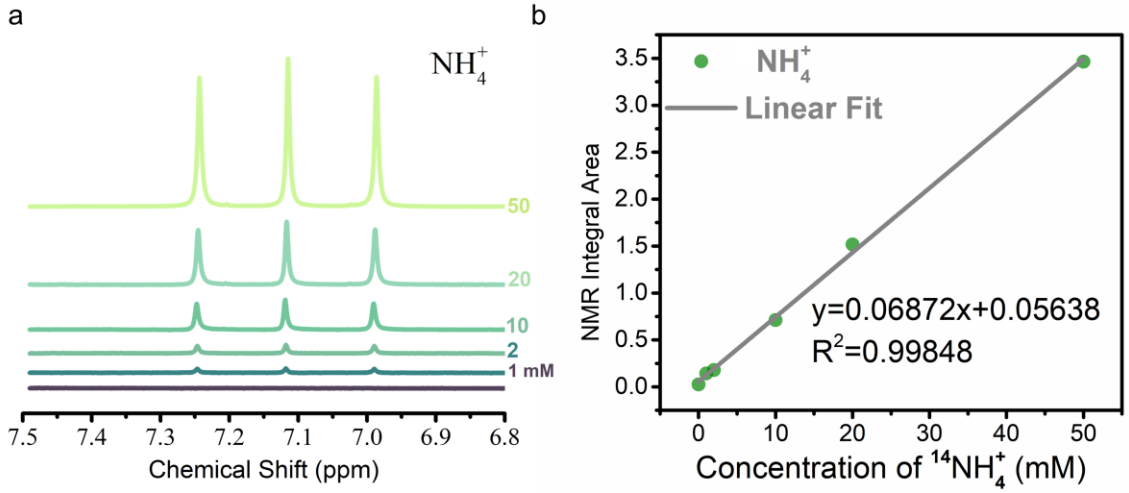

Figure 4-S3. NH_4^+ quantification. The NMR spectra (a) and calibration curve (b) of NH_4^+. The concentration of ammonia exhibits a linear relationship with the integral area of the characteristic peaks.

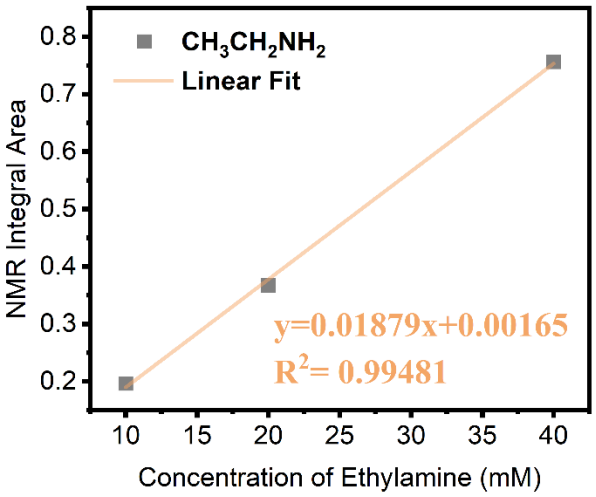

Figure 4-S4. Ethylamine quantification. Calibration curve of the ethylamine. The concentration of ethylamine exhibits a linear relationship with the integral area of the characteristic peaks.

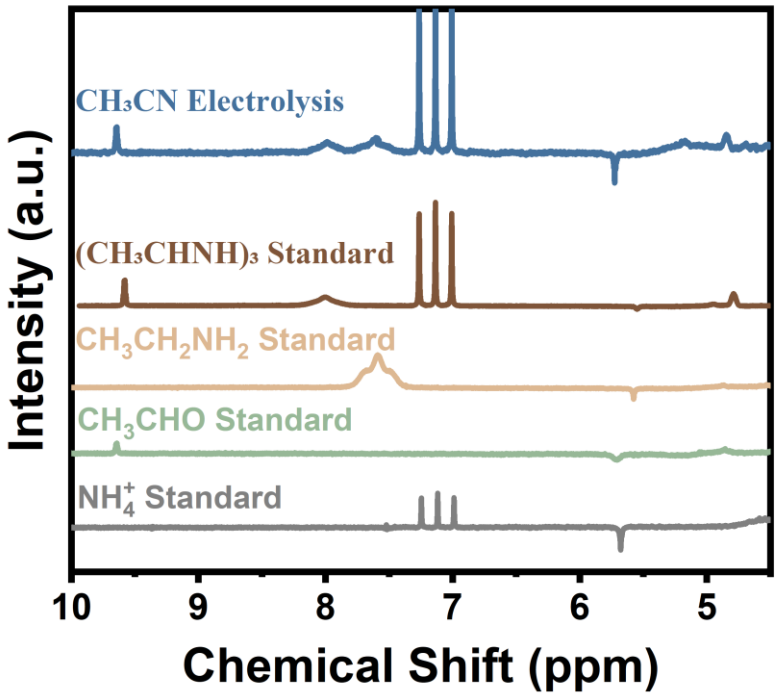

Figure 4-S5. Standards. NMR spectra of select standards and the reaction after electrolysis.

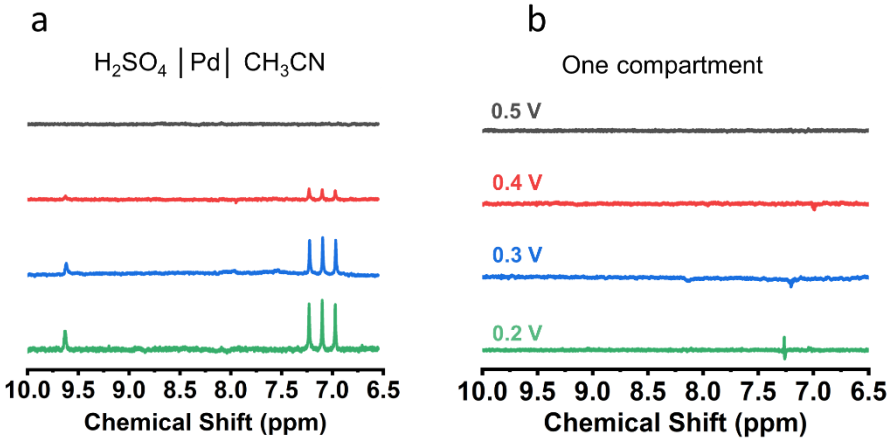

Figure 4-S6. NH_4^+ generation. Ammonia generation in a Pd-membrane reactor (a) under standard conditions as described or in a 1-compartment reactor with 10 % (V:V) CH_3CN in 0.5M H_2SO_4 with an equivalently prepared rough Pd foil used as a working electrode (b). At potentials of 0.2 $V_{Ag/AgCl}$ and higher, no detectable ammonia generation was noted.

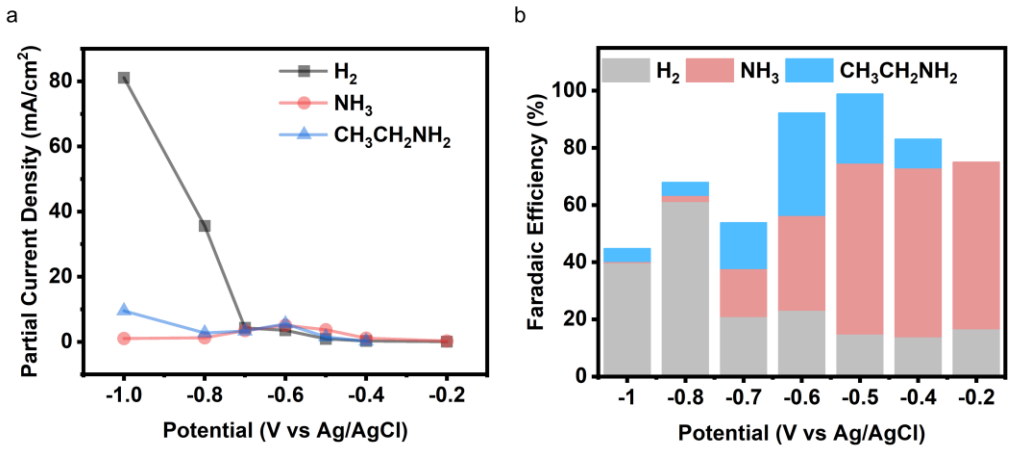

Figure 4-S7. Product generation. The partial current density (a) and Faradaic efficiency (b) of the reaction across the entire potential range tested.

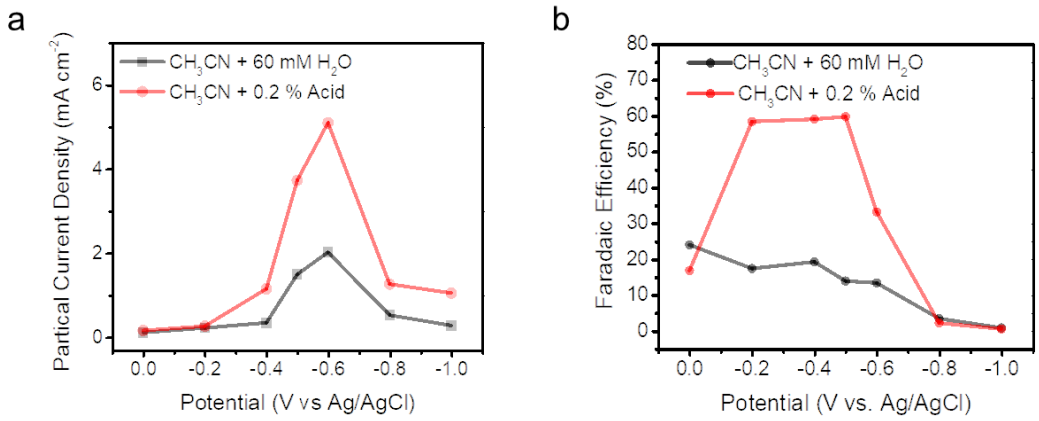

Figure 4-S8. Effect of acid. The partial current density (a) and Faradaic efficiency (b) of ammonia are both improved with 0.2 % sulfuric acid (V:V) rather than 60 mM water in the organic compartment.

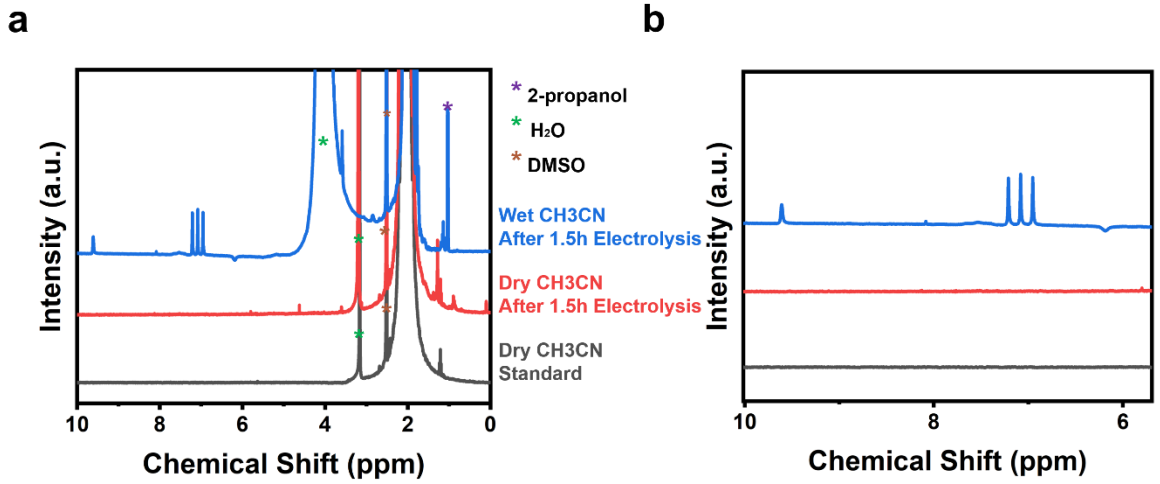

Figure 4-S9. Control experiment with dry acetonitrile. Resultant NMR spectra from running the reaction in dry and wet (0.2 % acid) acetonitrile (a). (b) shows magnified NMR spectra of the product peaks.

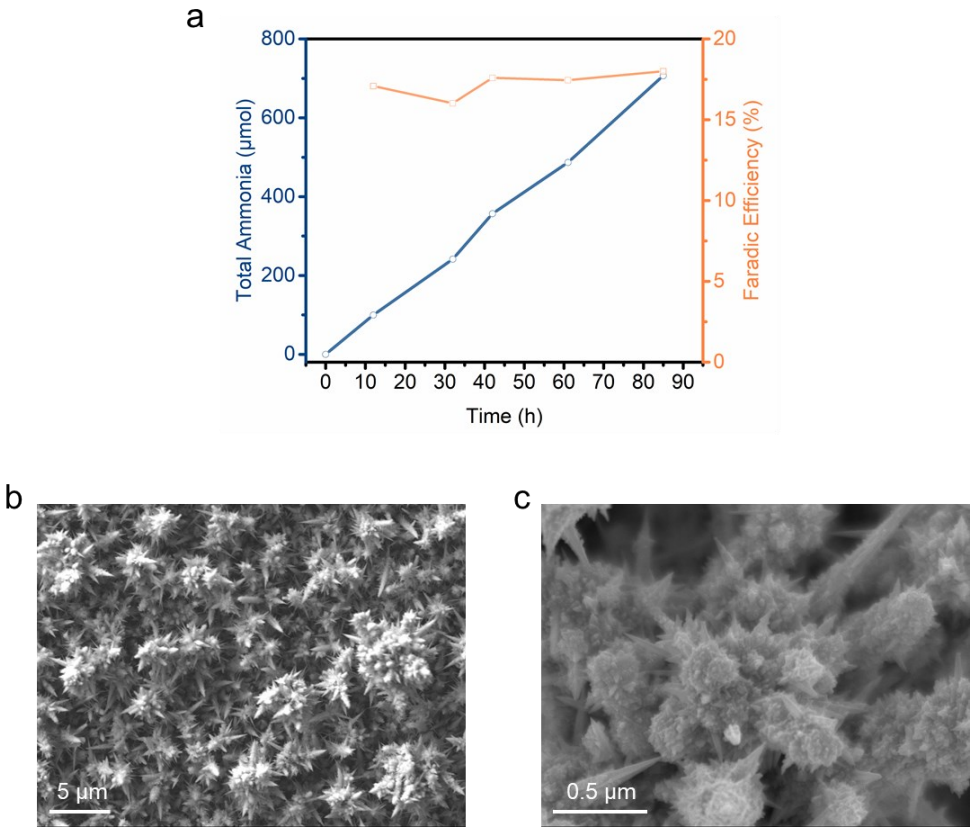

Figure 4-S10. Stability measurements. Long term operation testing at -0.6 $V_{Ag/AgCl}$ (a) and SEM images with low (b) and high (c) magnification of the Pd after a typical electrolysis experiment at -0.6 $V_{Ag/AgCl}$.

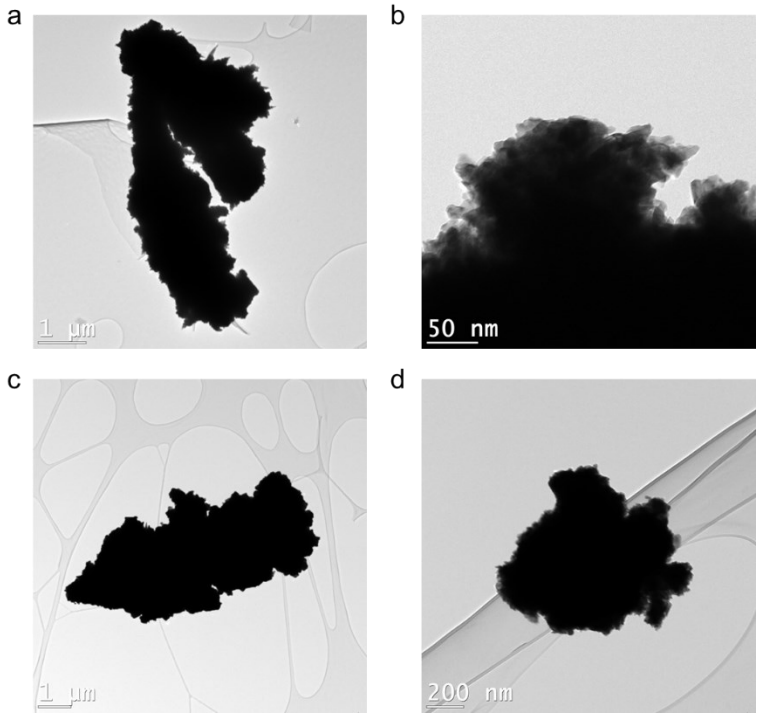

Figure 4-S11. TEM analysis. TEM images of the Pd (scratched off the electrode) before electrolysis (a, b) and after electrolysis (c, d) at -0.6 $V_{Ag/AgCl}$. Higher resolution imaging was not possible due to the instability of the Pd under high electron flux in our setup.

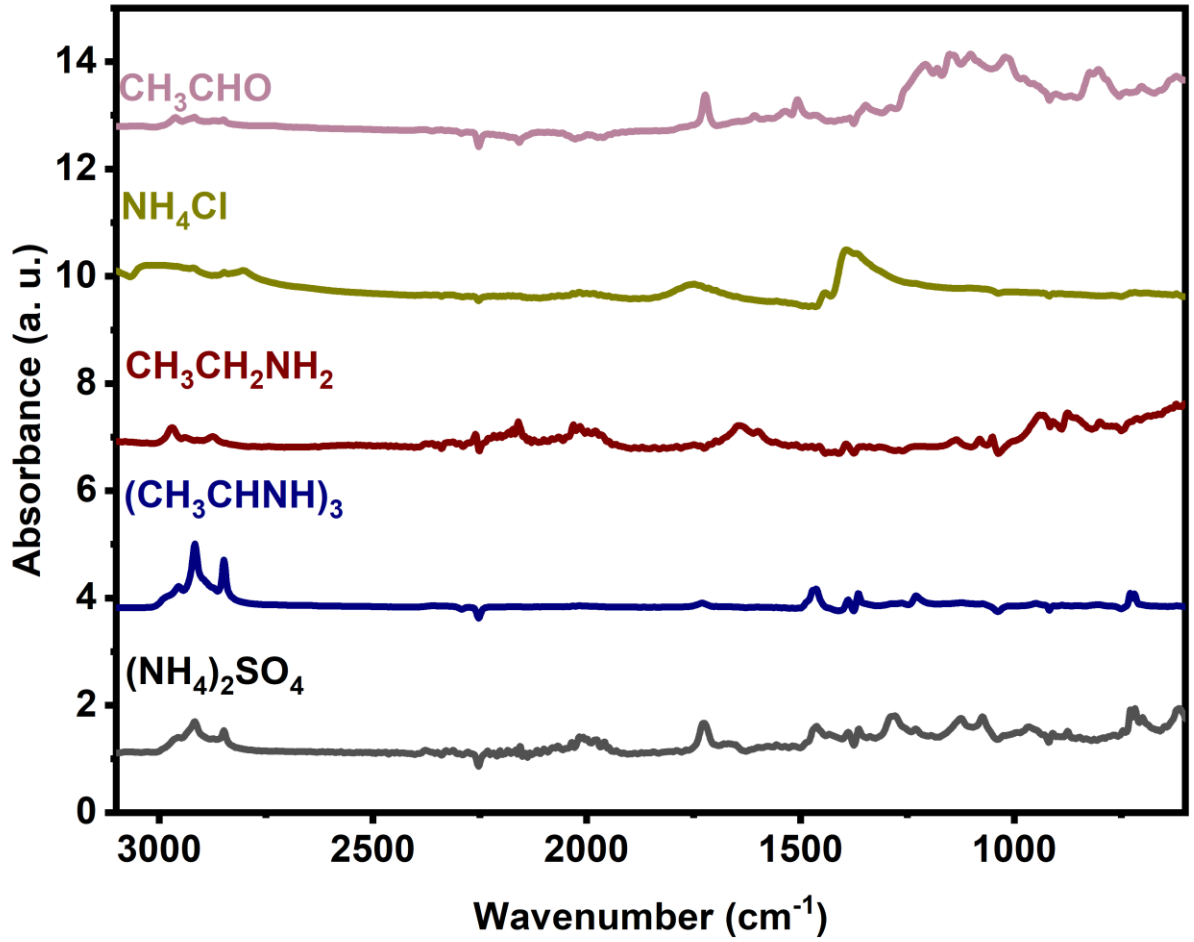

Figure 4-S12. IR Standards. Infrared spectra of several reference compounds.

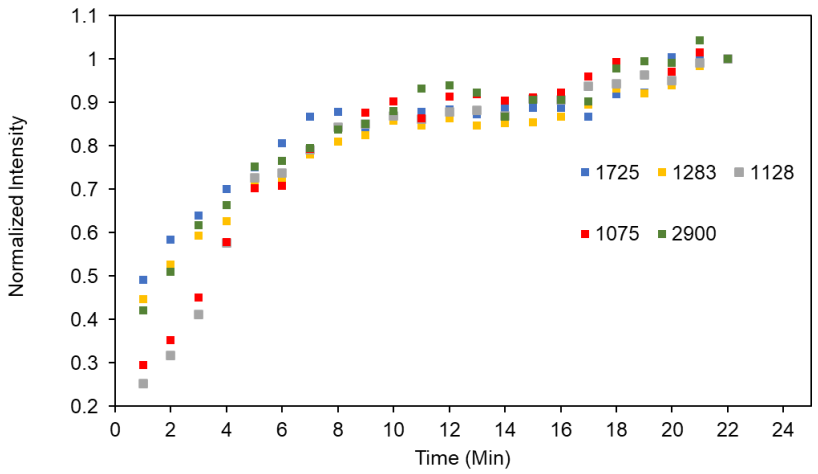

Figure 4-S13. Time-dependence. Time-dependent band changes at longer timescales at -0.6 $V_{Ag/AgCl}$, with each band normalized to its intensity at 22 minutes for ease of comparison.

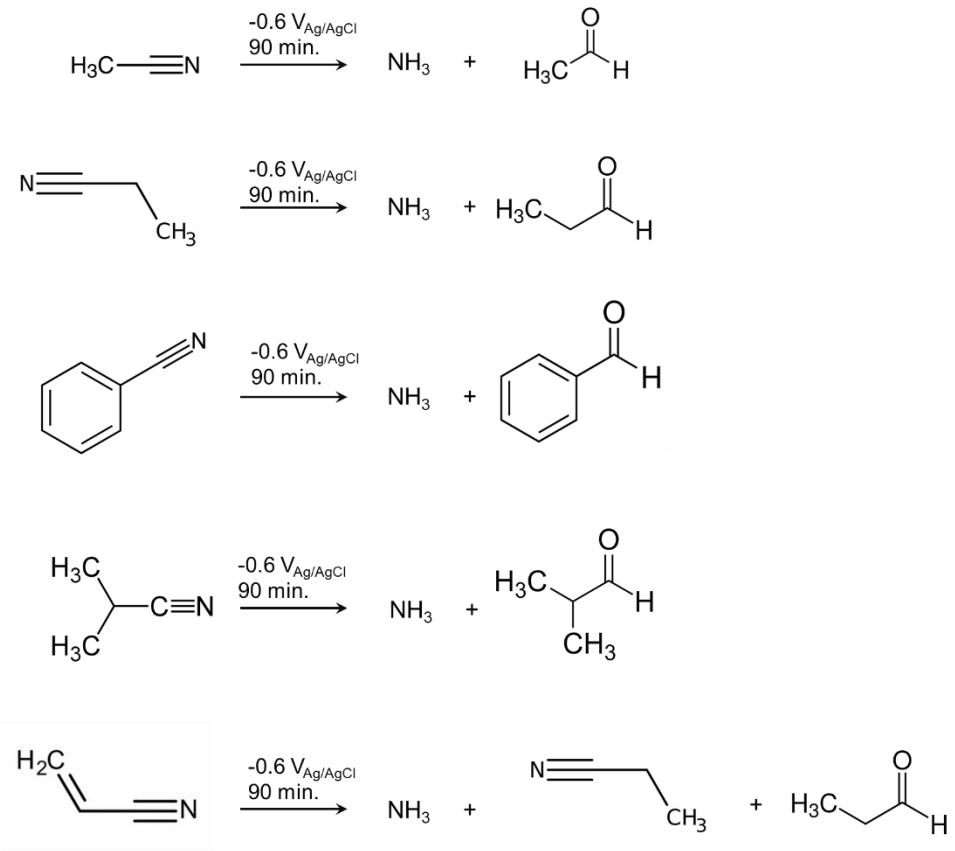

Figure 4-S14. Scheme of substrate scope. The scope of the reaction was extended beyond CH_3CN and to propionitrile, benzonitrile, isobutyronitrile, and acrylonitrile.

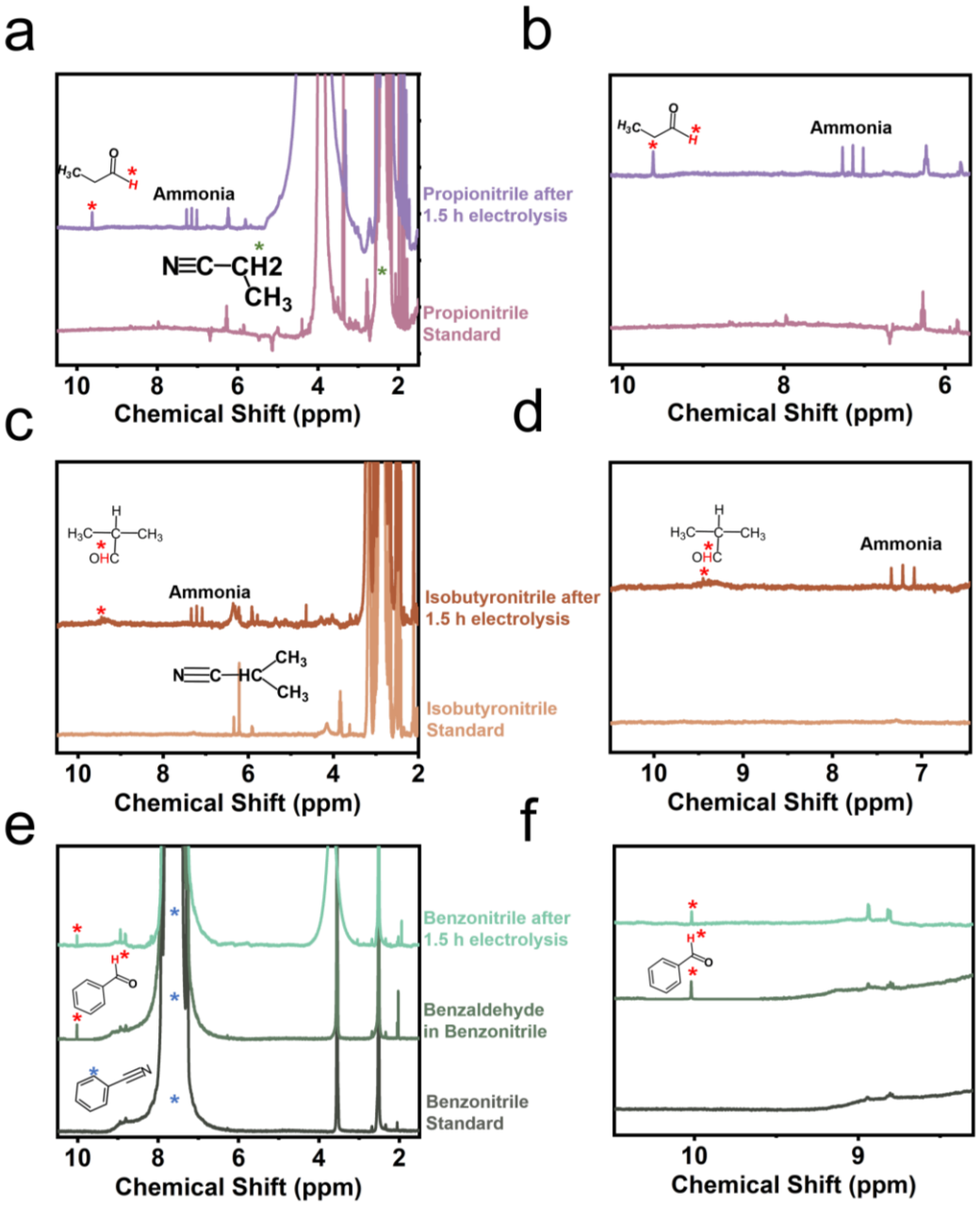

Figure 4-S15. NMR spectra of reaction products. Expansion of scope of nitrile hydrogenation: we sought to apply our hydrogenation strategy to several nitrile substrate solutions such as propionitrile (a-b), isobutyronitrile (c-d), and benzonitrile (e-f). The same conditions were used as for figure 2, with -0.6 $V_{Ag/AgCl}$ set as the applied potential. (b), (d) and (f) feature expanded views of the characteristic NMR peaks of the products. We calculated the Faradaic efficiency to be 21.54 % for propionitrile and 15.73 % for isobutyronitrile.

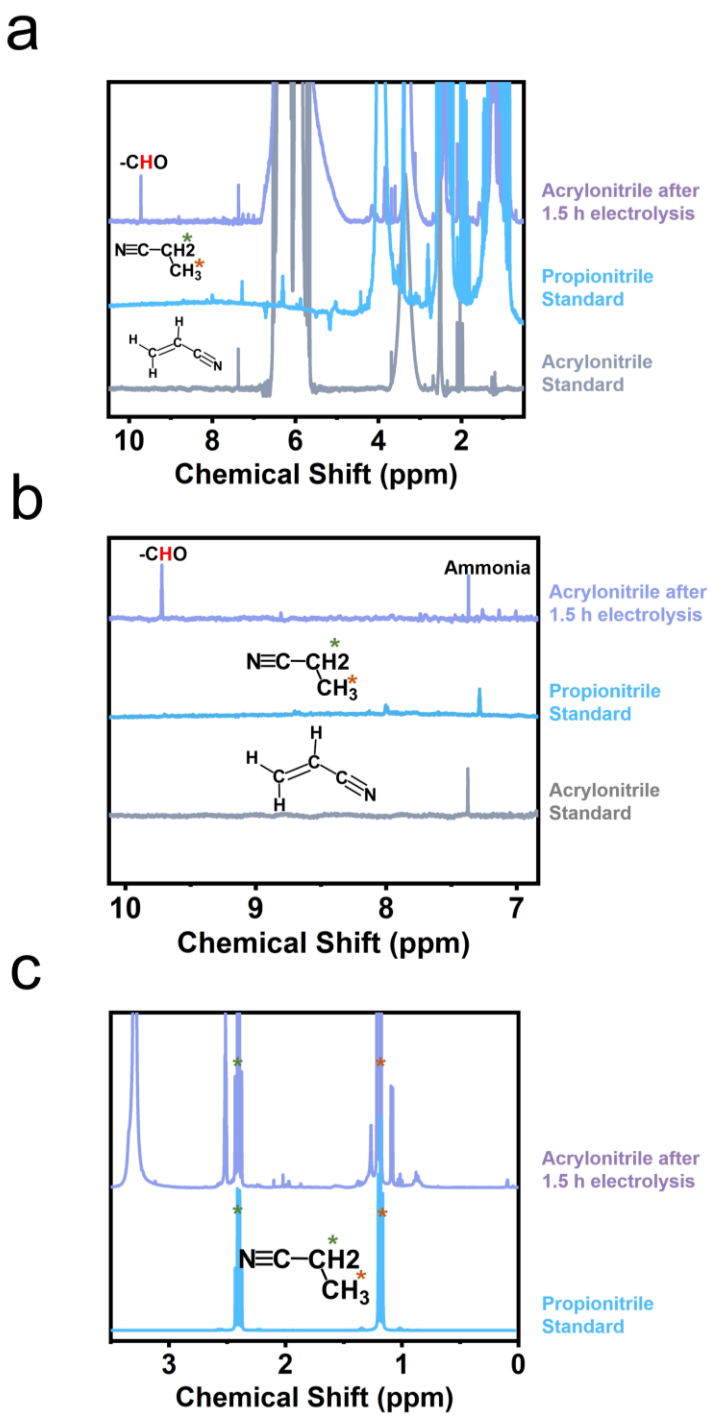

Figure 4-S16. NMR spectra of reaction products of acrylonitrile hydrogenation. NMR spectra of acrylonitrile before and after catalysis (a). The same conditions were used as for figure 2, with -0.6 VAg/AgCl set as the applied potential. (b) and (c) are magnified to show peaks of the products. The Faradaic efficiency was calculated to be 12.17 % for acrylonitrile hydrogenation.

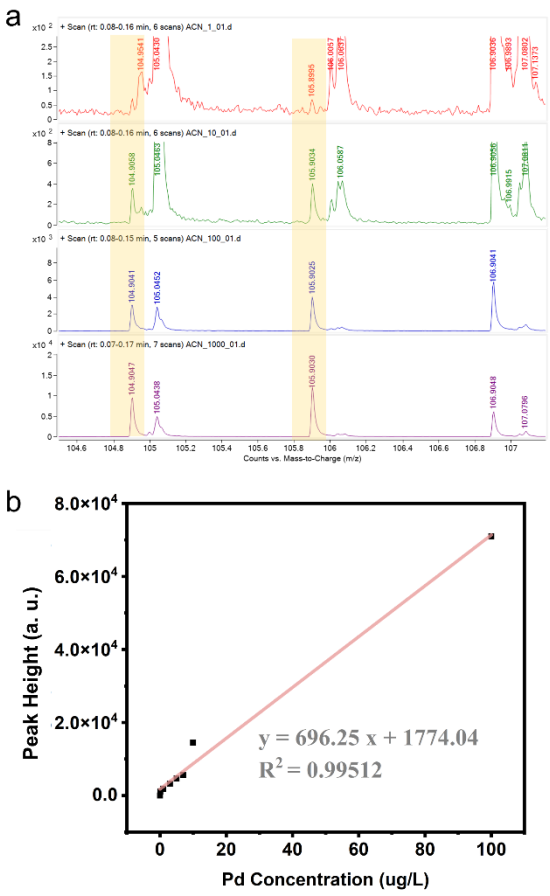

Figure 4-S17. Quantification of Pd dissolution. Mass Spectrometry measurements on the of Pd dissolution. Dissolved Pd in the acetonitrile-containing compartment was measured through its characteristic peaks at 104.9 and 105.9 mass/charge ratio (highlighted in yellow) by first quantifying a series of standards (a) and constructing a calibration curve (b). After 66 hours of operation at -0.5 $V_{Ag/AgCl}$, the dissolved Pd concentration reached 21.98 µg/L within a 50 mL solution and a Pd geometric area of 2 cm^2.

4.8. Acknowledgements

N.K. and Y.Z acknowledge NSERC Discovery Grant RGPIN-2019-05927. In addition, the authors would like to thank Loïc P. Mangin for helpful discussion and Daniel Chartrand for help with experiments.

Declaration of Interests:

A patent has been filed regarding the catalyst developed in this manuscript.

4.9. References

1 Chu, S. & Majumdar, A. Opportunities and challenges for a sustainable energy future. *Nature* **488**, 294-303 (2012).

2 Chu, S., Cui, Y. & Liu, N. The path towards sustainable energy. *Nat. Mater.* **16**, 16-22 (2017).

3 Davidson, D. J. Exnovating for a renewable energy transition. *Nat. Energy* **4**, 254-256 (2019).

4 De Luna, P. *et al.* What would it take for renewably powered electrosynthesis to displace petrochemical processes? *Science* **364**, eaav3506 (2019).

5 Paidar, M., Fateev, V. & Bouzek, K. Membrane electrolysis—History, current status and perspective. *Electrochim. Acta* **209**, 737-756 (2016).

6 Schmidt, O. *et al.* Future cost and performance of water electrolysis: An expert elicitation study. *Int. J. Hydrogen Energy* **42**, 30470-30492 (2017).

7 Jouny, M., Luc, W. & Jiao, F. General Techno-Economic Analysis of CO2 Electrolysis Systems. *Ind. Eng. Chem. Res.* **57**, 2165-2177 (2018).

8 Richard, D., Huang, Y.-C. & Morales-Guio, C. G. Recent Advances in the Electrochemical Production of Chemicals from Methane. *Curr. Opin. Electrochem.*, 100793 (2021).

9 Zhang, Y., Li, J. & Kornienko, N. Towards atomic precision in HMF and methane oxidation electrocatalysts. *Chem. Commun.* **57**, 4230-4238 (2021).

10 Du, L. *et al.* Electrocatalytic valorisation of biomass derived chemicals. *Catal. Sci. Tech.* **8**, 3216-3232 (2018).

11 Karsten, E., Erhard, H., Roland, R. & Hartmut, H. (Wiley-VCH Verlag, Weinheim, 2005).

12 Gluhoi, A. C., Mărginean, P. & Stănescu, U. Effect of supports on the activity of nickel catalysts in acetonitrile hydrogenation. *Appl. Catal., A* **294**, 208-214 (2005).

13 Iwasa, N., Yoshikawa, M. & Arai, M. Selective hydrogenation of acetonitrile to ethylamine using palladium-based alloy catalysts. *Phys. Chem. Chem. Phys.* **4**, 5414-5420 (2002).

14 Verhaak, M. J. F. M., van Dillen, A. J. & Geus, J. W. The selective hydrogenation of acetonitrile on supported nickel catalysts. *Catal. Lett.* **26**, 37-53 (1994).

15 Li, H., Wu, Y., Luo, H., Wang, M. & Xu, Y. Liquid phase hydrogenation of acetonitrile to ethylamine over the Co-B amorphous alloy catalyst. *J. Catal.* **214**, 15-25 (2003).

16 Braos-García, P., García-Sancho, C., Infantes-Molina, A., Rodríguez-Castellón, E. & Jiménez-López, A. Bimetallic Ru/Ni supported catalysts for the gas phase hydrogenation of acetonitrile. *Appl. Catal., A* **381**, 132-144 (2010).

17 Xia, R. *et al.* Electrochemical reduction of acetonitrile to ethylamine. *Nat. Commun.* **12**, 1949 (2021).

18 Zhang, D. *et al.* Highly efficient electrochemical hydrogenation of acetonitrile to ethylamine for primary amine synthesis and promising hydrogen storage. *Chem Catal.* (2021).

19 Szklarczyk, M. & Sobkowski, J. The behaviour of high polar organic solvents at platinum electrode — II. Adsorption and electrode reactions of acetonitrile. *Electrochim. Acta* **25**, 1597-1601 (1980).

20 Wasmus, S. & Vielstich, W. Electro-oxidation and electroreduction of acetonitrile in aqueous acid solution: A DEMS study. *J. Electroanal. Chem.* **345**, 323-335 (1993).

21 Sherbo, R. S., Delima, R. S., Chiykowski, V. A., MacLeod, B. P. & Berlinguette, C. P. Complete electron economy by pairing electrolysis with hydrogenation. *Nat. Catal.* **1**, 501-507 (2018).
22 Sherbo, R. S., Kurimoto, A., Brown, C. M. & Berlinguette, C. P. Efficient Electrocatalytic Hydrogenation with a Palladium Membrane Reactor. *J. Am. Chem. Soc.* **141**, 7815-7821 (2019).
23 Smidt, J. *et al.* Katalytische umsetzungen von olefinen an platinmetall-verbindungen das consortium-verfahren zur herstellung von acetaldehyd. *Angew. Chem.* **71**, 176-182 (1959).
24 Eckert, M., Fleischmann, G., Jira, R., Bolt, H. M. & Golka, K. *Acetaldehyde*. 7 edn, (2006).
25 Yang, J. *et al.* Liquid Cell Transmission Electron Microscopy Sheds Light on The Mechanism of Palladium Electrodeposition. *Langmuir* **35**, 862-869 (2019).
26 Gimeno, Y. *et al.* Electrochemical Formation of Palladium Islands on HOPG: Kinetics, Morphology, and Growth Mechanisms. *The Journal of Physical Chemistry B* **106**, 4232-4244 (2002).
27 Guo, L. & Searson, P. C. On the influence of the nucleation overpotential on island growth in electrodeposition. *Electrochim. Acta* **55**, 4086-4091 (2010).
28 Hsu, H.-H., Selvaganapathy, P. R. & Soleymani, L. Bottom-up top-down fabrication of structurally and functionally tunable hierarchical palladium materials. *Journal of The Electrochemical Society* **161**, D3078 (2014).
29 Angerstein-Kozlowska, H., Macdougall, B. & Conway, B. E. Electrochemisorption and reactivity of nitriles at platinum electrodes and the anodic H desorption effect. *Journal of Electroanalytical Chemistry and Interfacial Electrochemistry* **39**, 287-313 (1972).
30 Testa, A. C. & Reinmuth, W. H. Chronopotentiometry with Current Reversal. Application to p-Benzoquinone Imine Hydrolysis. *Anal. Chem.* **32**, 1512-1514 (1960).
31 Layer, R. W. The Chemistry of Imines. *Chem. Rev.* **63**, 489-510 (1963).
32 Wang, M. *et al.* Salting-out effect promoting highly efficient ambient ammonia synthesis. *Nat. Commun.* **12**, 3198 (2021).
33 Yao, Y., Zhu, S., Wang, H., Li, H. & Shao, M. A Spectroscopic Study on the Nitrogen Electrochemical Reduction Reaction on Gold and Platinum Surfaces. *J. Am. Chem. Soc.* **140**, 1496-1501 (2018).
34 Yao, Y., Zhu, S., Wang, H., Li, H. & Shao, M. A Spectroscopic Study of Electrochemical Nitrogen and Nitrate Reduction on Rhodium Surfaces. **59**, 10479-10483 (2020).
35 Jansonius, R. P. *et al.* Hydrogenation without H2 Using a Palladium Membrane Flow Cell. *Cell Rep. Phys. Sci.* **1**, 100105 (2020).

Chapter 5 Oxy-reductive C-N bond formation via pulsed electrolysis

5.1. Abstract

Co-electrolysis of CO_2 with simple N-species is an appealing route to sustainable fabrication of C-N bond containing products. A prominent challenge in, the area is to promote the C-N coupling step in place of the established CO_2 reduction pathways. This can be particularly difficult when relying on solution-based species (e.g., NH_3) to intercept intermediates that are continually being reduced on heterogeneous catalyst surfaces. In light of this, we introduce pulsed electrocatalysis as a tool for C-N bond formation. The reaction routes opened through this method involve both partial reduction and partial oxidation of separate reactants on the same catalyst surface in parallel to co-adsorb their activated intermediates proximal to one another. Using the CO_2 and NH_3 as model reactants, the end result is an enhancement of selectivity and formation rates for C-N bond containing products (urea, formamide, acetamide, methylamine) by factors of 3-20 as compared to static electrolysis in otherwise identical conditions. An array of *operando* measurements and computational modelling was carried out to pinpoint the key factors behind this performance enhancement. Finally, the oxy-reductive coupling strategy was extended to additional carbon and nitrogen reactants as well as applied to boost electrochemical C-S coupling.

Contribution:

Yuxuan Zhang: designed the project, carried out experiments, processed data, contributed intellectual insights, and wrote the manuscript.

Hasan Al-Mahayni: conduct calculation for the project, contributed intellectual insights.

Pedro Aguiar: build the detection method for NMR, contributed intellectual insights.

Daniel Chartrand: provided help for the *in situ* XRD detection.

Morgan McKee: carried out experiments, processed data.

Ali Seifitokaldani: supervision, contributed intellectual insights for the calculation part of this project.

Nikolay Kornienko: supervision, designed the project, carried out experiments, processed data, contributed intellectual insights, and wrote the manuscript.

Oxy-reductive C-N bond formation via pulsed electrolysis

Yuxuan Zhang[1], Hasan Al-Mahayni[2], Pedro Aguiar[1], Daniel Chartrand[1], Ali Seifitokaldani[2]* and Nikolay Kornienko[1]*

[1]Department of Chemistry, Université de Montréal, 1375 Ave. Thérèse-Lavoie-Roux, Montréal, QC H2V 0B3

[2]Department of Chemical Engineering, McGill University, 3610 University Street, Montréal, H3A 0C5 Québec, Canada

[*]Correspondence to: ali.seifitokaldani@mcgill.ca and nikolay.kornienko@umontreal.ca

*Email: nikolay.kornienko@umontreal.ca

Submitted Manuscript to *Nature Chem* on Dec 23, 2022

5.2. Introduction

Due to society's ever-increasing energy demand and resultant environmental degradation from energy consumption, developing sustainable synthetic techniques to replace the fossil-fuel-driven industry is rapidly gaining interest.[1] Among such routes is electrocatalysis, which often entails lower CO_2 emissions relative to established thermochemical routes to produce the same chemical species.[2] As a key method within chemistry's toolbox, electrochemistry offers routes to precise reaction control by adjusting applied potentials and is thus gaining popularity as a means of precisely controlling reaction pathways towards a desired product. This is particularly important for reactions involving the transformation of CO_2 into valuable products as multiple competing reactions could occur under typical reaction conditions.[3]

To date, electrosynthetic systems for water electrolysis are technologically mature and systems entailing CO_2 reduction (CO_2R) are rapidly growing as well.[4-6] However, the electrosynthetic fabrication of other classes of societally valuable chemicals are still underdeveloped.[7] As one of the most important classes of fertilizers and high-demand chemicals, products containing C-N bonds such as urea, amides, and amines play a pivotal role in society.[8] At the industrial level, the construction of C–N bonds from simple reactants is carried out under harsh thermochemical conditions and finding analogous electrosynthetic routes under mild conditions for these reactions is a challenge for the scientific community. The electrochemical formation of C-N bonds is appealing as it can direct begin with small molecules like CO_2 and nitrite,[9] nitrate,[10] ammonia,[11] and even N_2[12] to directly produce value-added C-N bond products. In this context, the C-N bond coupling reaction is primarily carried out through the reduction of CO_2 to form an activated electrophilic intermediate and subsequent attack by nucleophilic N-containing species. Consequently, the selectivity for C-N bond products reactions rely heavily on the interplay of chemical C-N coupling steps and electrochemical CO_2 reduction pathways.

So far, most efforts in the design of electrosynthetic systems, including those for C-N bond formation, have focused on either applying a constant reductive[8] or oxidative[13] potential, where the electrode polarity remains unchanged and electrons flow unidirectionally. The crossover of oxidation or reduction products to the opposite electrode here is typically undesired.[14] Although counterintuitive, we propose that the simultaneous coexistence of oxidative and reductive intermediates on a single catalyst would be an effective route promote heteroatom coupling electrosynthesis via a pulsed electrolysis.

Pulsed electrolysis, the application of alternating potentials has garnered interest in the CO_2 reduction community as this technique can afford a rational route to modulate product selectivity, stability, and activity (Fig. 1a).[15] However, the community's understanding of how pulse impacts underlying physicochemical processes in the dynamic microenvironment near the catalyst surface is being developed (Fig. 1b).[16] To this end, *operando* techniques, those performed as the reaction is occurring, help elucidate the identity of catalyst phase and reaction intermediate coverage.[17,18] In this work, we make use of synergy between pulsed electrochemistry and *operando* techniques (X-ray diffraction (XRD), Raman, infrared (IR) spectroscopy) to select conditions to modulate the reaction intermediate coverage during our electrosynthetic reaction to promote C-N coupling. We

use Cu nanoparticles as a model catalyst, CO_2 as the C-reactant and NH_3 as the N-reactant to carry out C-N coupling. We select optimized conditions in which we maintain a steady-state coverage of $*NH_2$ while maintaining Cu in the metallic state and show how pulsed electrolysis increased both the formation rate and selectivity for C-N products of urea, formamide and acetamide by factors of 3-20 (Fig. 1c). The synthetic value brought by this new approach is further demonstrated through the expansion of scope to additional C- and N- reactants and even to C-S coupling.

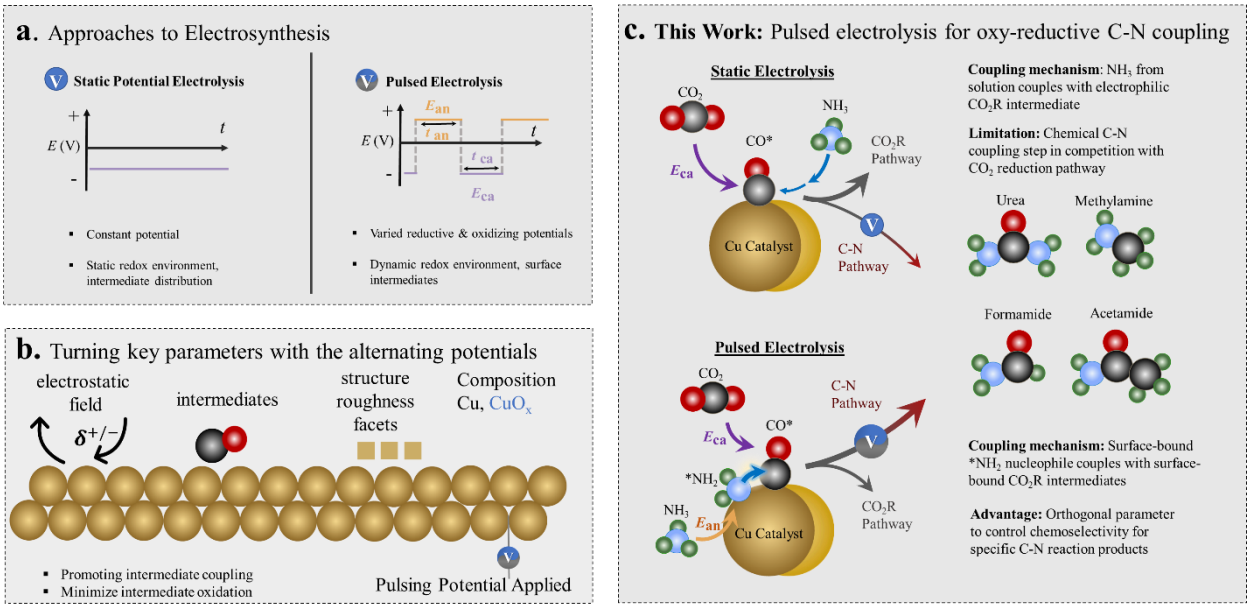

Figure 5-1. Types of waveforms in static potential and pulsed electrosynthesis (a) and brief illustration of parameters affected through electrochemical pulsing (b). Our route to C-N bond production through oxy-reductive coupling via pulsed electrolysis (c).

5.3. Results and Discussion

We carried out our measurements in a modified gas-diffusion electrode (GDE) half cell (Fig. S1), using commercial Cu nanoparticles as the catalyst and 1M KOH as the electrolyte. We first used cyclic voltammetry (CV) to identify the potentials at which various reaction steps take place (Fig. 2a). Under an N_2 environment, the CV exhibits two distinctive anodic peaks at 0.1 V and 0.6 V (vs Ag/AgCl), stemming from the oxidation of Cu. In the presence of 1.5 M NH_3, an increased current at 0 V indicates the first steps of surface adsorption and a large irreversible current at 0.5 V points to catalytic oxidation of NH_3 and its derived intermediates. In the presence of CO_2, anodic current peaking at 0.2 V likely indicates the stripping of CO_2R intermediates from the surface.

To monitor the state of the Cu species in real time during a CV (scan rate = 0.5 mV/s), we utilized *in situ* XRD as a probe of the material's crystal structure (Fig. S2, 3). After first reducing away any surface oxides, then beginning the scan in the positive direction, the XRD data shows that indeed the transformation of Cu to Cu_2O begins at -0.2 V and CuO subsequently emerges at 0 V,

through Cu_2O is still the dominant phase (Fig. 2b).[19] The catalyst is fully reduced back to Cu at -1.0 V. We next seek to get a picture of possible ammonia oxidation species during the pulsed conditions. In 1M KOH and 1.5M NH_3 conditions, we carried *in situ* IR spectroscopic measurements to detect adsorbed species on the Cu as a function of potential (Fig. S4-7). We used the spectrum at open circuit conditions (around -0.2 V) as a reference, we against which spectral changes were recorded. Under steady state conditions, ammonia was oxidized to nitrite, nitrate, and hydroxylamine, beginning at 0V as characteristic bands attributed to these species emerged in the spectra (Fig. S6). However, under pulsed electrochemical conditions (E_{ca}=1.8 V, E_{an} varied, t=1s), peaks in the 3000-3600 cm^{-1} range emerged, characteristic of N-H bands[20] that were not there under a constant potential of -1.8 V. We propose that these bands are indicative of $*NH_2$ species that arise from partial NH_3 oxidation that are neither oxidized all the way to nitrate nor fully reduced back to NH_3. Further, these species may act as an activated form of nitrogen that can couple to CO_2R intermediates via on-surface reactions as an alternative to solution-based NH_3. This route is potentially more facile to NH_3 diffusion from the electrolyte to react with the same CO_2R surface intermediates.

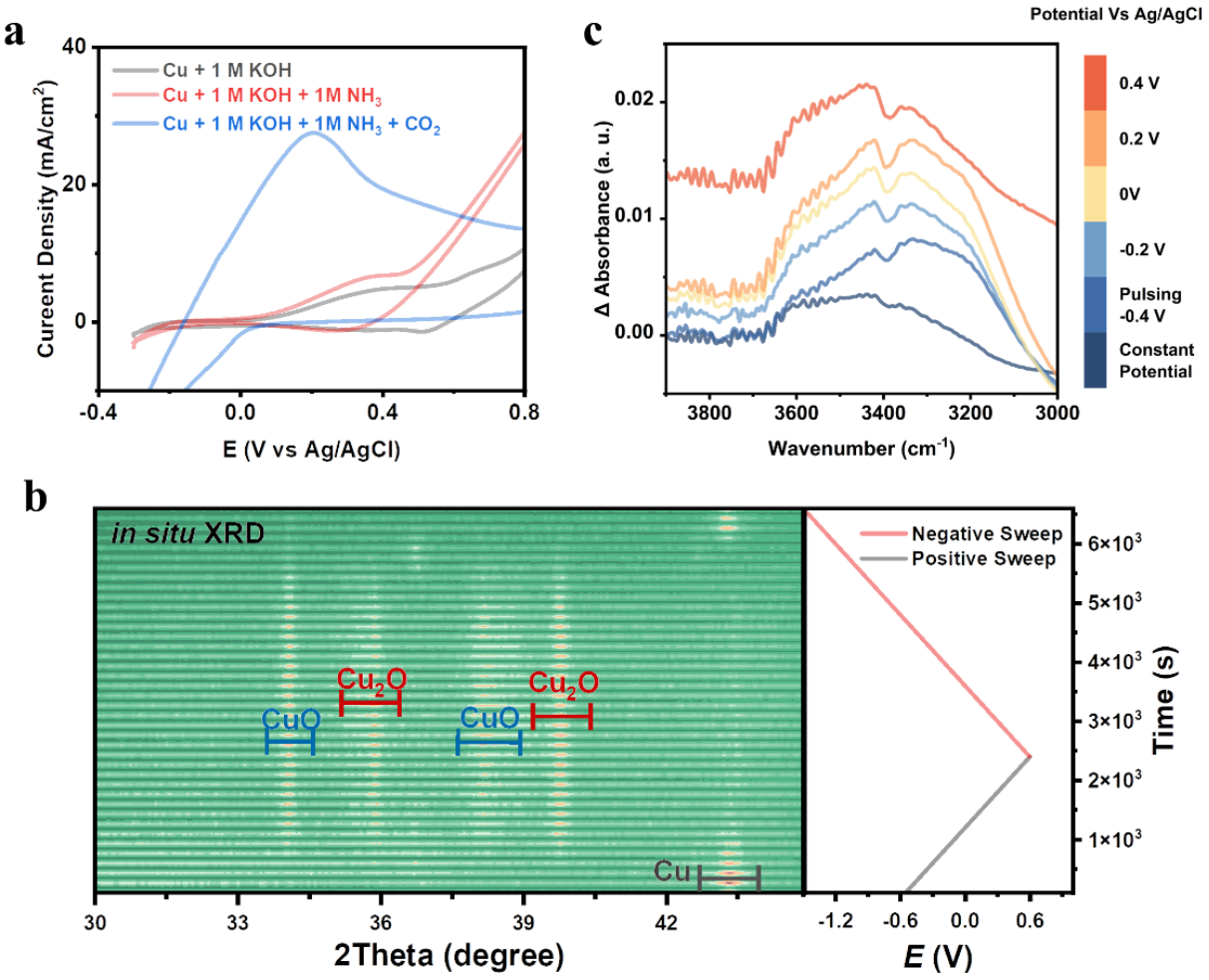

Figure 5-2. CVs of the Cu showing the oxidation of Cu, NH_3 and CO_2R intermediates (a). *In situ* XRD similarly pointed to the dominant phase of Cu as a function of potential (b) while IR measurements hinted at a steady-state coverage of $*NH_2$ during electrochemical pulsing (c).

We next investigated the effects that electrochemical pulsing would have on the performance of the system towards electrosynthetic C-N bond formation. We used static potential electrolysis with E_{ca}=1.8 V as the reference point and used systematically varied E_{an} potentials with t=1s for both E_{ca} and E_{an}. Liquid C-N products were measured through NMR and their presence was confirmed through a combination of isotope labelling, 2D NMR (Fig. S12-18). While the Faradaic efficiency (FE) for C-N products was generally below 3% for the sum of C-N products under static conditions, the application of pulsing significantly increased this by factors of approx. 3-20 up to a maximum of 33% (Fig. 3b). Notably, urea and methylamine were relatively minor products under steady state electrolysis, but their selectivity significantly increased when pulsing was applied. We found that urea selectivity was maximized in 1 M KOH and 1.5 M NH_3, while acetamide selectivity increased with 0.1 M KOH was used and decreasing the NH_3 concentration

to 1 M maximized formamide selectivity. Methylamine was present in all conditions as a minor product. Similarly, we plotted the formation rates for all C-N products and similar enhancement rates were evident. The variation of C-N product selectivity as a function of electrolyte composition and E_{an} points to the sensitivity of the electrosynthetic system's performance to $*NH_2$ and CO_2R intermediate coverage, Cu oxidation, and local pH and double layer composition at the Cu surface.

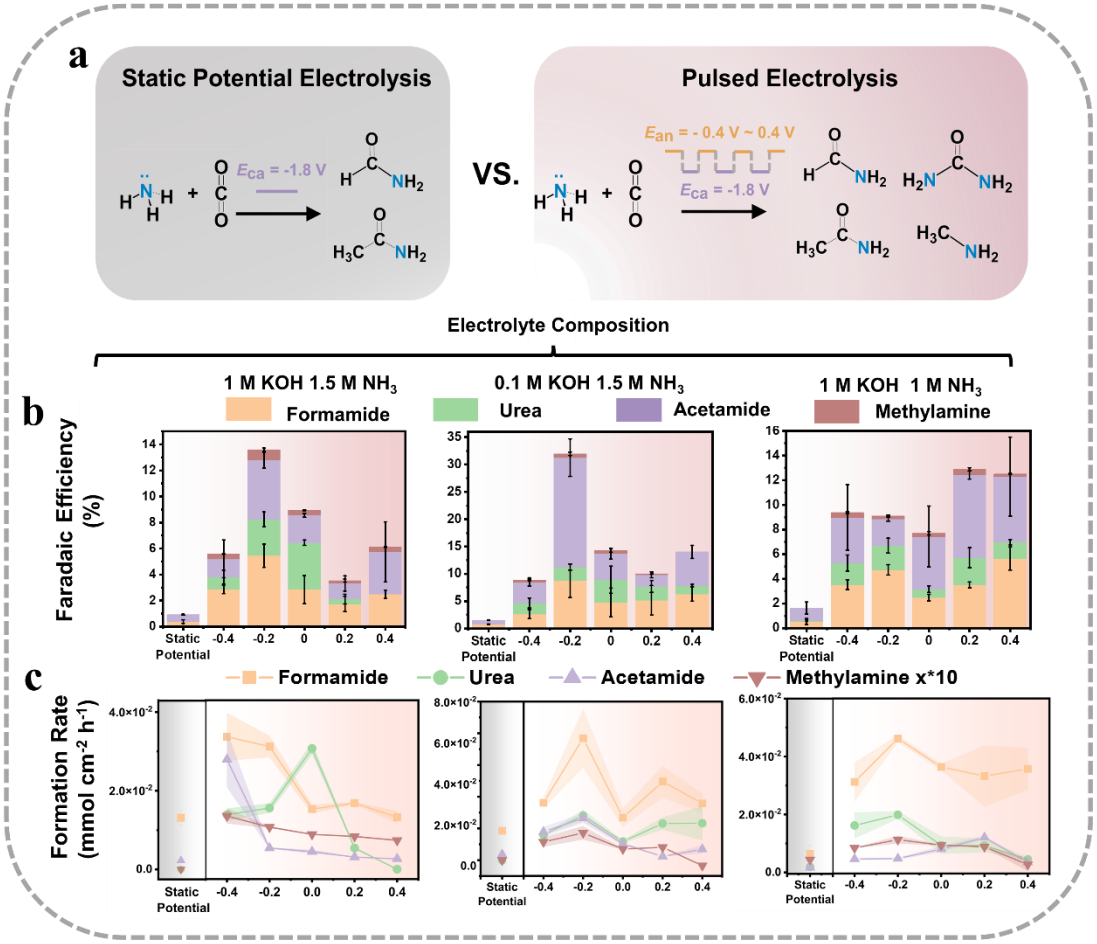

Figure 5-3. Comparison of C-N products formed through steady state and pulsed electrolysis (a). The Faradic efficiency (FE, b) and product formation rate (FR, c) for C-N products under three model conditions is significantly enhanced relative to that when using static potentials. For clarity, the FR of methylamine are multiplied by factor 10. Each electrolysis condition was repeated for more than 3 times to determine standard deviations between measurements.

Next, the system was probed under typical catalytic conditions (1M KOH, 1.5M NH_3) to visualize the interplay of catalyst phase and surface reaction intermediates potentially responsible for C-N bond formation. XRD spectra, taken at 5-minute time intervals after setting a pulsing potential, show that surface oxides are reduced away within 10 minutes at -1.8V (Fig. 4a). The only

detectable phase is metallic Cu until E_{an}=0.4 V at which Cu_2O begins to grow. This indicates that Cu is the predominant active site for this reaction. However, as a pulsed potential was applied, a tensile strain of up to 1.0% was evident as the Cu(111) peak increasingly shifted from 44.3 to 43.9° as E_{an} was set more positive, which may have a secondary effect on the Cu catalytic properties.[21]

Raman spectroscopy was next utilized to visualize reaction intermediates and near-surface species.[17] Similarly, Cu_2O was reduced away when negative potentials were applied, and bands attributed to Cu-X species were noted (320 cm^{-1}) (Fig. 4c). Cu_2O only reappeared at E_{an}=0.4, along with bands at 635 and 675 cm^{-1} attributed to Cu-OH and Cu-O_{ad}.[22,23]As E_{an} is progressively made more positive, the CO_3^{2-} signals (band at 1067 cm^{-1}) progressively diminishes and the HCO_3^- signals (bands at 1018 and 1341 cm^{-1}) grow , reflective of a pH increase at the surface.[24] Bands at 983 and 1129 cm^{-1} may indicate *CH_xO species as they have been previously assigned at these frequencies.[25] At the higher frequency region, *CO_2^- was noted (1540, 1584 and 1383)[26,27] while new bands arising at 1454 cm^{-1} could stem from COOH vibrational modes as they typically fall within this spectral range (Fig. 4d). The peak at 1547 cm^{-1} may originate from C-N bond vibrational modes, as this peak shifts to 1512 cm^{-1} when $^{15}NH_4Cl$ is used to replace the $^{14}NH_4OH$ (Fig S11).

Complementary to this, IR experiments showed new bands in the N-H region in addition to those from *NH_2 when both CO_2 and NH_3 were present, particularly when pulsed potentials were applied (Fig. 4e). These bands roughly match the N-H vibrations of the C-N products produced and thus are indicative of enhanced C-N bond formation through pulsing. In the absence of CO_2, bands relating to NO_3^- (1389 cm^{-1}) and NO_2^- (1232 cm^{-1}) are seen, stemming from the oxidation of NH_3. Similarly, once CO_2 was introduced, pulsed conditions gave rise to new bands at 1051, 1278, 1450 and 1616 cm^{-1} arising from the possible emergence of C-N products (4f). In particular, the C-N vibrational modes of the C-N reduction products fall near the 1616 cm^{-1} band observed in our experiment though we cannot yet unambiguously make this assignment as HCO_3^- also features a band in this region. Bands below 900 cm^{-1} may stem from Cu-C/N/O modes and several new bands in this region upon pulsing would be consistent with the existance of partially oxidized surface intermediates in combination with partially reduced CO_2R products.

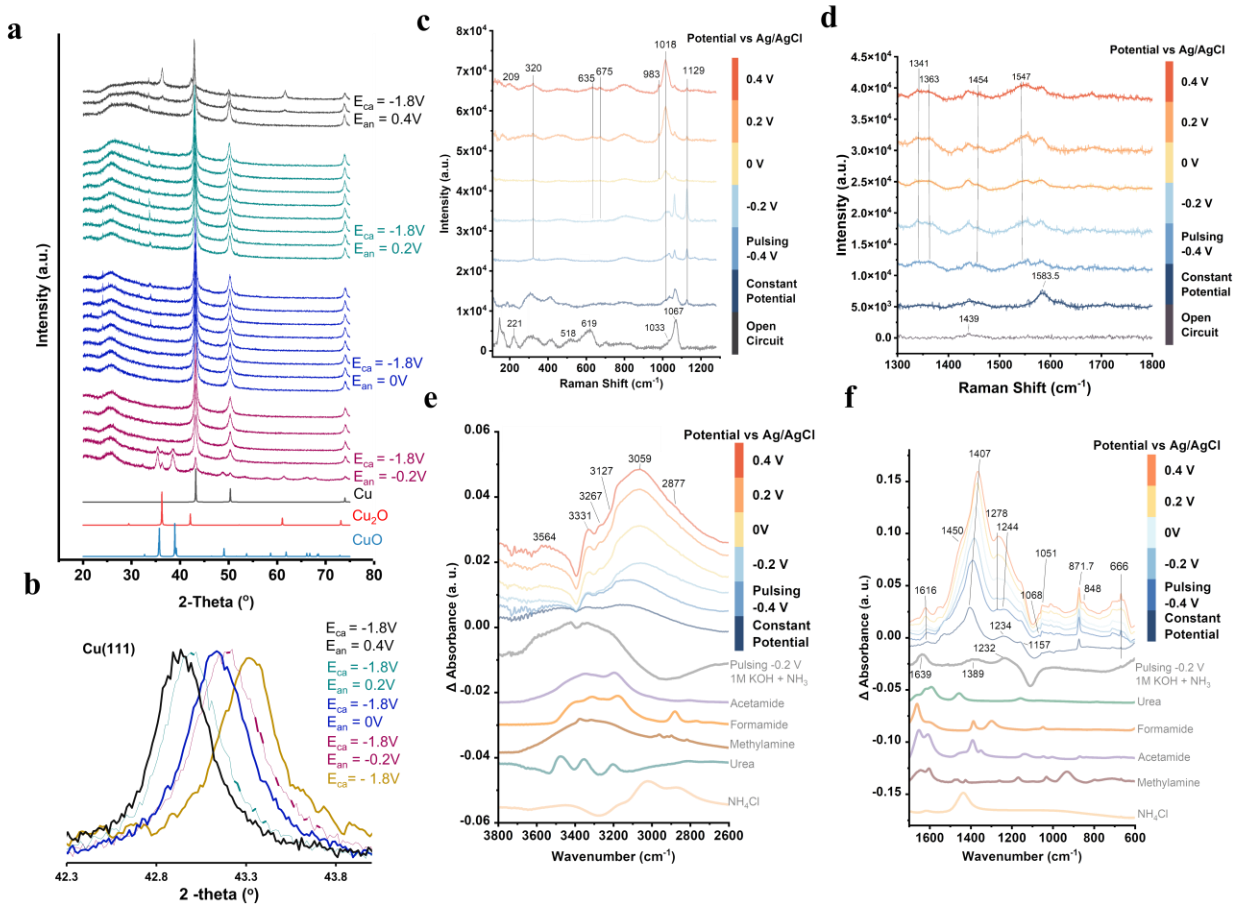

Figure 5-4. X-ray diffraction indicates Cu as the dominant phase during catalysis until E_{an}=0.4V, when Cu_2O co-exists (a). A tensile strain was evident from the shift of the Cu (111) peak to lower 2θ values (b). Raman (c,d) and IR (e,f) detect the surface bound intermediates built up under reaction conditions. All measurements conducted in 1M KOH and 1.5M NH_3 unless otherwise stated.

In order to (*i*) determine whether NH_2 or NH_3 is the key species that reacts with a CO_2 reduction reaction intermediate to create the C-N bond, (*ii*) identify the role of the anodic oxidizing potential which, as seen in experiments above, helped with the overall formation of C-N bond products, and (*iii*) discover the most favourable coupling step to form a stable C-N intermediate, we have performed density functional theory (DFT) calculations.

Experimental evidence leads to the hypothesis that NH_3 is oxidized to NH_2, which is adsorbed on the surface. This is facilitated by the anodic potential, justifying a pulsed electrolysis. To prove this on a theoretical facet, it is first important to examine the possibility of NH_3 directly reacting with a carbon intermediate. Adsorbed carbon monoxide (*CO) is considered as a key reaction intermediate coming from the CO_2 reduction, which is also a common carbonaceous group in most

of the C-N compounds observed in experiments in this work. The DFT reaction energy difference is thus calculated for the following reactions:

$NH_3^*+CO^* \rightarrow CONH_2^*+H^*$; ΔE=0.33 eV (Rx1)

$NH_2^* + CO^* \rightarrow CONH_2^*$; $\Delta E = 0.18\ eV$ (Rx2)

These reactions can be seen on Figure 5a. All optimized energies for individual reactants and products and reaction energies are summarized in Table S4 and S5, respectively. Looking at the ΔE of Rx1 and Rx2, we see that the coupling through NH_2 is more favourable than that through NH_3, further supporting the hypothesis that NH_3 first is converted into NH_2. Experimental evidence shown above (e.x. via Raman spectroscopy in Figure 4c and d), demonstrates that at E_{an} = -0.4 V and pH of approx. 9-10, there are hydroxyl ions OH^- adsorbed on the surface. It is also shown via DFT computations that the adsorption of OH^- on copper (100) is favourable by a negative adsorption energy of -0.7 eV (Figure 5b). Similarly, Figure 6b shows that NH_3 also adsorbs favourably with an adsorption energy of -0.92 eV. Therefore, it is expected to observe both NH_3 and OH^- adsorbed on the surface favorably, thereby facilitating hydrogen transfer from $*NH_3$ to *OH (Rx3):

$NH_3^* + OH^* \rightarrow NH_2^* + H_2O^*$ (Rx3)

The reaction energy barrier ΔE of Rx3 is calculated to be 0.29 eV, as can be seen in on Figure 6c. This reaction is crucial for C-N products formation; the anodic potential provides an oxidizing driving force to convert NH_3 to NH_2, which is attributed to improved C-N formation selectivity. Thus, the kinetics of Rx3 are also investigated, and are shown on Figure 5d. The activation energy barrier is found to be ~ 0.4 eV. This value is neither relatively big nor small, meaning there is a necessity for an oxidizing potential, but it does not have to be large. This fits the fact that optimal conditions were observed at -0.2 V vs Ag/AgCl.

Since multi-carbon C-N products (e.g., acetamide) is also observed among the products detected in experiment, we also considered $*NH_2$ coupling with *CCO (Rx4) in addition to with *CO (Rx2):

$NH_2^* + CCO^* \rightarrow CCONH_2^*$ (Rx4)

The calculated ΔE for Rx4 is 0.66 eV as seen on Figure 5a, making it an unfavourable coupling pathway comparatively to Rx2. Thus, from the DFT point of view, products such as acetamide with multiple carbons are first gone under C-N coupling step and then C-C coupling is carried out. Otherwise, it is expected that single-carbon C-N products to be more dominant compared to multi-carbon C-N products if a relatively low potential is applied.

Finally, Figure 5e shows the traditional rate determining step on Cu (100) for the CO_2 reduction reaction mechanism, which is the hydrogenation of CO to CHO. The energy barrier is 0.3 eV, which is comparable to 0.18 eV of the coupling step and the 0.29 eV of the NH_2 formation, meaning C-N formation and CO_2 reduction product formation should be competing, which is what the experimental results suggest.

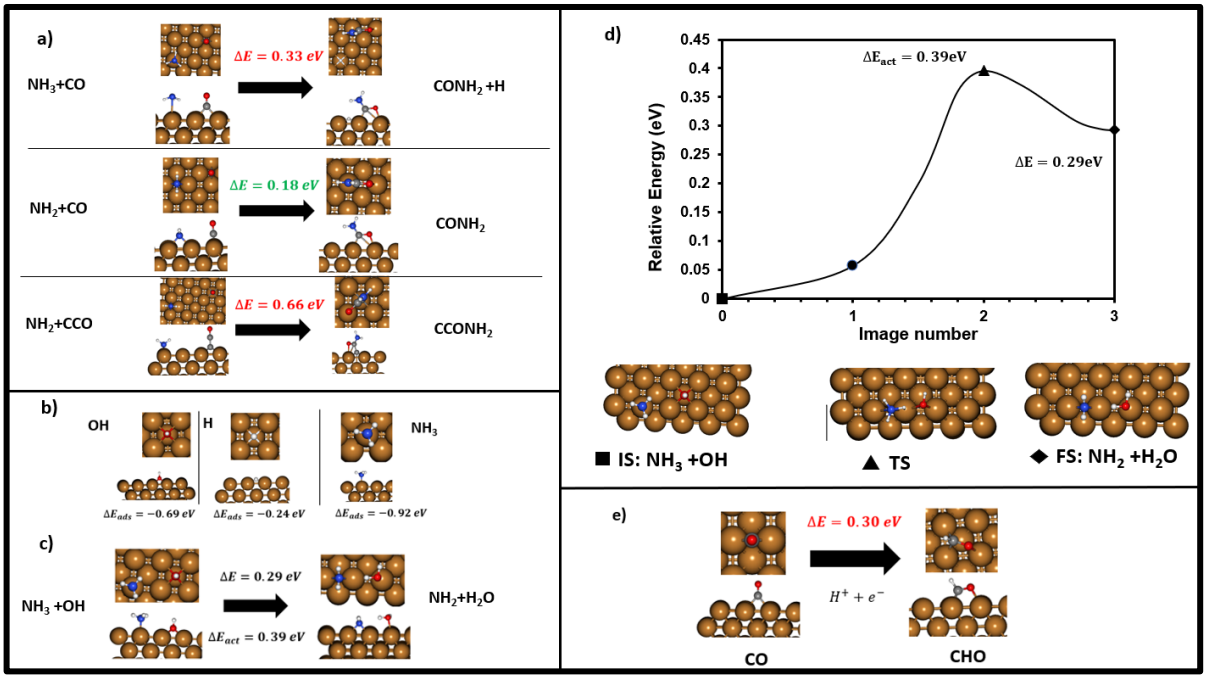

Figure 5-5. Summary of DFT results using a Cu (100) surface (a) adsorption of OH^-, $H^+$and NH_3 (b) Conversion of NH_3+OH to NH_2 +H_2O (c) Kinetics of the reaction in (b) including initial, final and transition states. (d) Coupling steps and their respective energy barriers (e) CO protonation to CHO. Green values indicate favourable pathways relative to the red values.

As a final endeavor, we moved to expand the scope of our measurements to show the broad applicability of pulsed electrosynthesis within the context of small molecule coupling. First, we modulated the E_{ca} and E_{an} durations under a typical set of reactions conditions. The formation rate of C-N bond products more than doubled when increasing E_{ca} to 2s while the FE was maintained (Fig. S24). Next, we used a series of additional reactants in place of CO_2 or NH_3 and compared the FE and formation rate (FR), given in mMol*$sec^{-1}cm^{-2}$ under static and pulsed conditions (Fig. 6a). Using formaldehyde (0.5 M), formate (0.2 M), or acetate (0.2 M) and coupling to NH_3 (1 M) in 1 M KOH led to C-N bond products with significantly enhanced FR under pulsed conditions as compared with constant potential synthesis (Fig. 6b). An advantage here is that the oxidative pulse may also activated partially reduced C-species and not just NH_3. If NO_2^- was used in place of NH_3, significantly increased FR were also noted for formamide and acetamide. As NO_3^- can also be oxidized to NO_3^-, the anodic pulse may likewise help concentrate it next to partially reduced CO_2R intermediates to promote C-N coupling. A similar route may be taking place in N_2 activation. Finally, SO_3^{2-}, 0.2 M a simple oxidizable sulfur species, was shown to couple with CO_2 to form methane sulfonate, a useful molecule in organic synthesis, with increased performance under coupling conditions (Fig. 6d). The coupling step here may similarly involve a nucleophilic attack by the S-species on an activated CO_2R intermediate.[28,29] While the initial set of results here are promising, we note that the precise operating conditions were not optimized for the each

experiment and there is therefore much room to grow in terms of performance. Finally, we cannot unambiguously rule out other effects that may be the dominant factor behind the enhanced reactivity such as changes to the catalyst structure induced by pulsing as the detailed examination of each reaction is beyond the scope of this work.

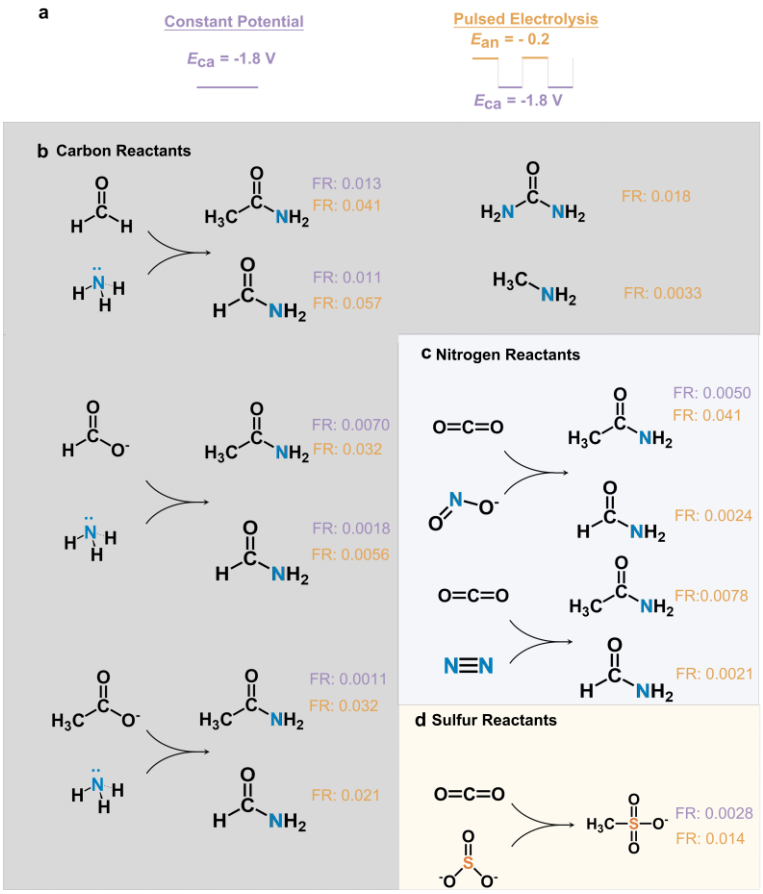

Figure 5-6. The pulsed electrochemical coupling strategy was extended to additional coupling reactions (a). Additional carbon (b) and nitrogen (c) reactants benefit from pulsed electrolysis to form C-N products. Finally, C-S bonds could be generated with enhanced rates in the formation of methanesulfonate (d). Formation rates are given in mMol*s^{-1}*cm^{-1}.

5.4. Concluding Remarks

In all, this work shows how pulsed electrolysis is a powerful tool in promoting electrocatalytic coupling reactions. In particular, the partial oxidation of NH_3 leads to a higher concentration of NH_x species on the catalyst surface and thereby facilitates their coupling to CO_2R intermediates in a new reaction mechanism and consequently greater efficiencies for C-N product generation. While CO_2 and NH_3 coupling was the model reaction in this study, we have shown that there are many avenues to explore in the use of downstream CO_2R products, additional N-species and even

C-S coupling. Finally, there is much room to explore in terms of catalyst design. Though this work used commercial Cu particles, the use of Cu with well defined facets or Cu-based alloys may be an effective strategy for precisely modulating the binding energy of key reactants and steering the reaction down a select pathway. In addition, the addition of secondary binding sites that, for example, bind N-species may stand to boost performance. In the end, with this newfound oxy-reductive coupling strategy, the electrochemical construction of a wide gamut of important chemicals from simple building blocks is closer to practicality.

5.5. Experimental Procedures

5.5.1. Chemicals:

Ammonium hydroxide solution (30-33% NH_3 in H_2O), Methylamine solution (40 wt. % in H2O), Deuterium Oxide (99.8 atom % D), Ammonium-^{15}N chloride (≥ 99.8 atom %, 15N ≥ 99 %) Sodium sulfite (⩾ 98%), sodium nitrite solution (40 wt. % in H2O) was get from Sigma-Aldrich Company. Acetamide (^{15}N, 98%+) was purchased from Cambridge Isotope Laboratories, Inc. Formamide, deionized (ultra pure) VMR Life Science. Copper nanopowder, APS 20-50 nm and Potassium hydroxide (flake, 85%) were get from Thermo Scientific. Carbon cloth (ELAT LT 1400W-40 × 40 cm) was purchased from FuelCellsEtc. Nafion D-521 dispersion (5% w/w in water and 1 propanol, ≥ 0.92 meq/g exchange capacity), Sodium formate 98 % were obtained from Alfa Aesar. Ethanol, 2 propanol, Methanol (HPLC grade) were got from Fisher chemical company. Acetic Acid were purchased from MACRON fine chemicals.

Formaldehyde solution 37% get from ward's science. Sodium methanesulfonate was get from TCI Ametica.

5.5.2. Electrode Preparation and Characterization:

The microstructure and composition of electrode after electrolysis were investigated by transmission electron microscopy (TEM) and X-ray diffraction (XRD).

Transmission Electron Microscopy and elemental mapping: TEM images were collected at The Facility for Electron Microscopy Research (FEMR) of Mcgill University. TEM characterization was performed using Thermo Scientific Talos F200X G2 (S)TEM with High visibility low-background beryllium double-tilt optimized for energy-dispersive X-ray spectroscopy (EDS). All samples were prepared by carefully scratching off from the electrode and dispersing them onto ethanol solution. After sonicating for 5 min, the solution was drop cast onto a copper grid supporting a thin electron transparent carbon film. High angular annular dark-field imaging (HAADF) performed in parallel with EDS acquisition in the collection angle of 58-200 mrad.

X-ray diffraction patterns were collected in the range of $10° \leq 2\theta \leq 80°$ on a Panalytical MPD-PRO diffractometer equipped with a linear X'celerator detector with CuKα (1.5406 Å) anode.

Detailed information about the *in situ* experiment please see the **Supplementary Note.**

5.5.3. Electrochemistry Analysis and Product Quantification:

Electrochemistry experiments were carried out in a home-made gas diffusion electrode (GDE) cell. A modified GDE half cell was used to maximize the sensitivity of the measurements through the use of lower electrolyte volumes. A carbon cloth loaded copper catalysts is sealed in the middle of a sandwiched structure. CO_2 molecules can transfer from the bulk gas phase to the gas-liquid boundary layer through the bottom layer (constant 10 mL/min). NH_3 was fed through the liquid phase (NH_4OH) with different concentrations dissolved in 1 M KOH solution. For a typical electrolysis experiment, 1 mL electrolyte was added into the hydrophobic layer of carbon cloth electrode and saturated with CO_2 for at least 5 min. The reference (Ag/AgCl gel in saturated KCl, 25°C) was used to calculate RHE with $\mathbf{E_{RHE} = E_{Ag/AgCl} + 0.059\ pH + E^{o}_{Ag/AgCl}}$, where $\mathbf{E^{o}_{Ag/AgCl}}$ = 0.206 V**.** The Ag/AgCl reference was periodically checked against a master reference electrode for any potential drifts to maintain stable in alkaline electrolyte.

Electrochemical measurements were conducted through a Biologic SP200 potentiostat and EC-lab software v11.43. A graphite rod was used as the counter electrode.

Prior to electrochemical measurements, the impedance between reference and working electrode was recorded at open circuit (100 KHz) and the ohmic drop was subsequently corrected for at 85% with the ZIR function in the EC-lab software. The area used to normalize current density in the CV plots is the geometric surface area, using a consistent mass loading of 10 mg of Cu.

The static electrolysis for typical chronoamperometric measurements is conducted at -1.8 vs Ag/AgCl (denoted as E_{an}). The reported results were obtained after 3600s under CO_2RR. For the experiments involving pulsing electrolysis, three techniques were applied: 1) one chronoamperometric run at the anodic potential (E_{an}) for 1s, 2) cathodic chronoamperometric (E_{an}) for 1s, and 3) 899 loops of 1) and 2). The pulsing anodic potential in our study was varied between -0.4 V to 0.4 V, with a 0.2 V interval. This range of potentials was selected based on our analysis, which present in the paper. Next, the cathodic reduction time and anodic time was varied to 2s, to test the influence of the anodic-cathodic time ratio.

The gas products reported were measured by gas chromatography (SRI Model 8610C GC) equipped with a thermal conductivity detector (TCD) and flame ionization detector (FID). The gas flow rate was kept constant at 10 mL/min as measured by a flow meter (Dwyer Instruments, Inc) at the exit of the GDE cell. Ultra-high purity nitrogen gas was used as the carrier gas. The electrochemical cell was directly connected to GC, therefore during reaction the CO_2 continuously flowed through the reactor and GC. The gas was sampled from the reaction vessel 30 minutes after applying the reducing potential. Calibration gases at various dilutions were used to establish a calibration curve for accurate product detection. Liquid products were measured by NMR (AV NEO 400, *Bruker BioSpin*). See Supplementary Note 1 for more details on the analysis of electrocatalytic measurement data.

5.5.4. Long term operation and GC-MS detection

In the present study, long-term electrolysis runs over 6 h are conducted in pulsed mode. Time can not be prolonged for more because of the flooding of the carbon cloth electrode. The electrolyte after electrolysis (around 4 mL) was added 1.15 ml, 2 M Phosphate buffer to turn the pH. The obtained solution was then concentrated using a rotary evaporator to get around 1 mL solution in a low-pressure mode. Next, the formamide, acetamide, urea was extracted from the concentrated electrolyte using ethyl acetate (EA). We add methanol to increase the solubility of urea in the EA. Finally, the concentrated solution was injected into the GC-MS system for analysis.

Conflicts of interest

The authors declare no competing Interests

5.6. Acknowledgements

N.K. and Y. Z. acknowledge NSERC for its Discovery Grant RGPIN-2019-05927. A.S. acknowledges NSERC for its Discovery Grant RGPIN-2020-04960 and Canada Research Chair (950-23288). Computations in this research were enabled in part by support provided by Calcul Quebec and Compute Canada.

In addition, the authors would like to thank Dr. David Liu at the Facility for Electron Microscopy Research of McGill University for help in TEM images collection. We would like to thank Dr Alexandra Furtos, the Mass spectrometry Facility Director, for helpful discussion and Jean-Francois Myre from the workshop of University of Montreal for help building the gas diffusion electrode.

5.7. References

1 Chu, S. & Majumdar, A. Opportunities and challenges for a sustainable energy future. *Nature* **488**, 294-303 (2012).

2 Schiffer, Z. J. & Manthiram, K. Electrification and Decarbonization of the Chemical Industry. *Joule* **1**, 10-14 (2017).

3 Ross, M. B. *et al.* Designing materials for electrochemical carbon dioxide recycling. *Nat. Catal.* **2**, 648-658 (2019).

4 Shin, H., Hansen, K. U. & Jiao, F. Techno-economic assessment of low-temperature carbon dioxide electrolysis. *Nat. Sustainability* **4**, 911-919 (2021).

5 Masel, R. I. *et al.* An industrial perspective on catalysts for low-temperature CO2 electrolysis. *Nat. Nanotechnol.* **16**, 118-128 (2021).

6 Lagadec, M. F. & Grimaud, A. Water electrolysers with closed and open electrochemical systems. *Nat. Mater.* **19**, 1140-1150 (2020).

7 Zhang, Y., Li, J. & Kornienko, N. Strategies for heterogeneous small-molecule electrosynthesis. *Call Rep. Phys. Sci.* **2**, 100682 (2021).

8 Li, J., Zhang, Y., Kuruvinashetti, K. & Kornienko, N. Construction of C–N bonds from small-molecule precursors through heterogeneous electrocatalysis. *Nat. Rev. Chem.* **6**, 303-319 (2022).

9 Feng, Y. *et al.* Te-Doped Pd Nanocrystal for Electrochemical Urea Production by Efficiently Coupling Carbon Dioxide Reduction with Nitrite Reduction. *Nano Lett.* **20**, 8282-8289 (2020).

10 Lv, C. *et al.* Selective electrocatalytic synthesis of urea with nitrate and carbon dioxide. *Nat. Sustainability* **4**, 868-876 (2021).

11 Li, J. & Kornienko, N. Electrochemically driven C–N bond formation from CO2 and ammonia at the triple-phase boundary. *Chem. Sci.* **13**, 3957-3964 (2022).

12 Chen, C. *et al.* Coupling N2 and CO2 in H2O to synthesize urea under ambient conditions. *Nat. Chem.* **12**, 717-724 (2020).

13 Meng, N. *et al.* Electrosynthesis of formamide from methanol and ammonia under ambient conditions. *Nat. Commun.* **13**, 5452 (2022).

14 Wang, N. *et al.* Suppressing the liquid product crossover in electrochemical CO2 reduction. *SmartMat* **2**, 12-16 (2021).

15 Casebolt, R., Levine, K., Suntivich, J. & Hanrath, T. Pulse check: Potential opportunities in pulsed electrochemical CO2 reduction. *Joule* **5**, 1987-2026 (2021).

16 Timoshenko, J. *et al.* Steering the structure and selectivity of CO2 electroreduction catalysts by potential pulses. *Nat. Catal.* **5**, 259-267 (2022).

17 Heidary, N., Ly, K. H. & Kornienko, N. Probing CO2 Conversion Chemistry on Nanostructured Surfaces with Operando Vibrational Spectroscopy. *Nano Letters* **19**, 4817-4826 (2019).

18 Handoko, A. D., Wei, F., Jenndy, Yeo, B. S. & Seh, Z. W. Understanding heterogeneous electrocatalytic carbon dioxide reduction through operando techniques. *Nat. Catal.* **1**, 922-934 (2018).

19 Scherzer, M. *et al.* Electrochemical Surface Oxidation of Copper Studied by in Situ Grazing Incidence X-ray Diffraction. *The Journal of Physical Chemistry C* **123**, 13253-13262 (2019).

20 Sokoll, R., Hobert, H. & Schmuck, I. Thermal desorption and infrared studies of amines adsorbed on SiO2 Al2O3, Fe2O3, MgO, and CaO I. Diethylamine and triethylarnine. *J. Catal.* **121**, 153-164 (1990).
21 Kim, T., Kumar, R. E., Brock, J. A., Fullerton, E. E. & Fenning, D. P. How Strain Alters CO2 Electroreduction on Model Cu(001) Surfaces. *ACS Catal.* **11**, 6662-6671 (2021).
22 Zhao, Y. *et al.* Speciation of Cu Surfaces During the Electrochemical CO Reduction Reaction. *J. Am. Chem. Soc.* **142**, 9735-9743 (2020).
23 He, M. *et al.* Oxygen induced promotion of electrochemical reduction of CO2 via co-electrolysis. *Nat. Commun.* **11**, 3844 (2020).
24 Lu, X. *et al.* In Situ Observation of the pH Gradient near the Gas Diffusion Electrode of CO2 Reduction in Alkaline Electrolyte. *J. Am. Chem. Soc.* **142**, 15438-15444 (2020).
25 Li, X. *et al.* Selective visible-light-driven photocatalytic CO2 reduction to CH4 mediated by atomically thin CuIn5S8 layers. *Nat. Energy* **4**, 690-699 (2019).
26 Chernyshova, I. V., Somasundaran, P. & Ponnurangam, S. On the origin of the elusive first intermediate of CO2 electroreduction. *Proc. Natl. Acad. Sci. U.S.A.* **115**, E9261-E9270 (2018).
27 Firet, N. J. & Smith, W. A. Probing the Reaction Mechanism of CO2 Electroreduction over Ag Films via Operando Infrared Spectroscopy. *ACS Catal.* **7**, 606-612 (2017).
28 Kornienko, N., Li, J., Al-Mahayni, H., Chartrand, D. & Seifitokaldani, A. Electrochemical Formation CS Bonds from CO2 and Small Molecule Sulfur Species. *ChemRxiv* (2022).
29 Boutin, E., Salamé, A., Merakeb, L., Chatterjee, T. & Robert, M. On the Existence and Role of Formaldehyde During Aqueous Electrochemical Reduction of Carbon Monoxide to Methanol by Cobalt Phthalocyanine. *Chem. Eur. J.* **28**, e202200697 (2022).

Supporting information for:

Oxy-reductive C-N bond formation via pulsed electrolysis

Yuxuan Zhang[1], Hasan Al-Mahayni[2], Pedro M. Aguiar[1], Daniel Chartrand[1], Morgan McKee[1], Ali Seifitokaldani[2]* and Nikolay Kornienko[1]*

[1]Department of Chemistry, Université de Montréal, 1375 Ave. Thérèse-Lavoie-Roux, Montréal, QC H2V 0B3

[2]Department of Chemical Engineering, McGill University, 3610 University Street, Montréal, H3A 0C5 Québec, Canada

*Correspondence to: ali.seifitokaldani@mcgill.ca and nikolay.kornienko@umontreal.ca

5.8. Supporting information

5.8.1. Supplementary Note 1: Using NMR to detect C-N products

The development of electrochemical C-N bond formation via activating small molecules is hampered by the lack of effective methods for quantitatively detecting the C-N bond products. Colorimetric quantification methods such as the reaction of urea with diacetyl monoxime[1,2] and enzymatic methods[3,4] are heavily relied upon for C-N bond detection, especially for urea. Those methods are well-established in aqueous media, but it is notoriously sensitive to variations in electrochemistry, multiple reaction agents, and tedious procedures in sample preparation are inevitable. The colorimetric method is significantly hindered in these media by the interference caused by temperature, pH, and ion concentration[1,4-6]. A number of advanced analytical techniques are capable of measuring urea such as Mass Spectroscopy; however, the separation of product and electrolytes is necessary due to the instrumental requirements[7,8]. Furthermore, the analysis and quantification the product requires NMR or HPLC to analyze the remainder of the CO_2-related liquid products.

Therefore, robust and general methods of C-N analysis are needed. To this end we utilised proton nuclear magnetic resonance spectroscopy (^{1}H NMR). In contrast to indirect spectrophotometric detection after derivatization, 1H NMR provides direct and highly selective analysis of ^{14}N-related species and ^{15}N-related species[9]. Moreover, NMR allows for simultaneous detection and quantification of conventional CO_2 reduction products as well as the C-N bond related products, resulting in a more efficient product analysis.

However, the detection of hydrogens directly bound to nitrogen by NMR requires care in sample preparation owing to their exchangeable nature (function of pka) and due to the intrinsic nuclear properties of the dominant isotope of nitrogen at natural aboundance, ^{14}N (N.A 99.63%). ^{14}N has spin, I > ½ (I=1) and thus, in addition to a nuclear magnetic moment (observed for all nuclei with non-zero nuclear spin, I) it has a non-zero nuclear electric quadrupolar moment (Q). This latter interaction can induce severe line-broadening to the nitrogen NMR signal itself, as well as to the signals of nuclei attached to the nitrogen. The impact of the linewidths decreases as local symmetry about the nitrogen increases and is lowest for cubic symmetry (T_d; e.g, NR_4 species). Species with higher symmetry will yield sharper ^{14}N and 1H NMR peaks. Thus, working at pH where e.g, RNH_2 is present predominantly as RNH_3^+ or NH_3 is present as NH_4^+ permits easier acquisition of 1H NMR of such species. At pHs above the pka the rate of exchange of NH hydrogens with other exchangeable hydrogens such as those of water can make these signals invisible due to exchange induced broadening.

Therefore, without turning the pH of electrolyte after reaction, sub-optimal NMR settings can result in lengthy data acquisition times[10] and underestimated quantification. In addition, formamide and urea are only stable at certain pH range. The formamide would discompose into formate either in low pH or high pH, which is typical of conditions employed in many experiments in the literature targeting C-N bond formation[11,12]. The drop of pH in alkaline conditions and the formation of buffer pairs of CO_3^{2-} /HCO_3^- during the reaction further hinders quantitative detection.

Herein, we reported a versatile method to obtain quantitative analysis of urea in high range pH electrolyte by ^{1}H NMR. The concentration of C-N bond products can be accurately determined in the range of a minimum of 1 mM and while minimizing C-N product decomposition. The method is promising for electrolysis applications, especially pulsing electrolysis, with the advantages of simplicity, high accuracy, and fast non-destructive detection.

DMSO (≥99% purity) was employed as an internal standard for quantitative ^{1}H NMR. Its distinct and intense methyl singlet does not overlap with common product peaks of CO_2 reduction, and it is miscible with a variety of solvents.

Phosphate buffer (PBS, 2.0 M) was added to each sample to adjust solution to a pH equal to 5-7 to protect the pH-sensitive C-N bond and protonated urea. If the pH of the final solution is well below the molecule's pKa, then ^{1}H NMR yields relatively sharp signals arsing from N-H hydrogen(s)[13]. However, if the electrolyte pH is higher than the molecule's pKa, protons would exchange with the water, generally prevents detection of N-H bonds.

A common practice in biochemistry is either to use a non-exchanging solvent such as DMSO-d6 or 1:9 D_2O:H_2O combined with water suppression techniques[14]. In our electrochemical reaction, DMSO-d6 is not chosen as the locker because its solubility of ions and products in the resultant solution is too low, although have a better N-H signal. D_2O and distilled water were added so that the final D_2O concentration was 10% (v/v; presence of small amount of deuterium in the solution has minimal impact to the urea quantitation as deuterium is distributed in urea and water in the same isotopic ratio).

All NMR samples were prepared so as to have a final H_2O : D_2O ratio of 9:1 by mixing appropriate volumes of electrolyte, PBS, and D_2O in 7:2:1 ratio. The method presented here detects both formamide, acetamide, and urea N-H bonds, but does not detect ammonium N-H bonds. This is because the pH of showing hydrogen attached to different nitrogen is different. The beneficial characteristic rules out the interference of the NH_3 and false positives from this species. All ^{1}H NMR experiments are the sum of 32 co-added scans with a 60s relaxation delay between scans to ensure all spins had relaxed to equilibrium (NB: the long relaxation time necessary was due primarily to the slow relaxation of the aldehydic hydrogen of formate/formamide).

5.8.2 Supplementary Note 2: Using $^{15}NH_4Cl$ to prove the formation of C-N bond

Both Isotope labelling and ^{1}H-^{15}N heteronuclear single-quantum correlation (HSQC) experiment were conducted to prove the C-N bond product formation. The results for the aqueous solutions are in good agreement with those reported previously[9].

Table 5-S1. Proton chemical shifts of Acetamide-15N in D2O/Buffer solution/ 0.1 M KOH = 1:2:7. All the chemical shift has been calibrate based on DMSO in our solution recipe as 2.71 to get rid of the effect of pH.

Acetamide	Acetamide - ^{14}N	Acetamide -^{15}N
δ_{CH_3}(ppm)	1.98	1.98
δ_{H_3} (ppm)	7.54	7.54
δ_{H_b} (ppm)	6.78	6.78
$\Delta\delta_{ab}$(ppm)	0.76	0.76

Table 5-S2. A comparison of coupling constant (Hz) in the amide groups of Formamide-15N and Acetamide-15N.

	Formamide - ^{15}N in water	Acetamide - ^{15}N in water
$\mathcal{J}(H_a - H_b)$ (Hz)	2.3	2.2
$\mathcal{J}(15N - H_a)$ (Hz)	91.3	90.9
$\mathcal{J}(15N - H_b)$ (Hz)	86.93	88.4
$\Delta\delta_{ab}$ (Hz)	0.37	0.756

5.8.3. Supporting Note 3: Identification of the oxidation potentials for Cu nanoparticles in the GDE cell.

Electrolytes were saturated with CO_2 for at least 15 min prior to applying voltage and conducting *in situ* experiments. See the **Figure S2. S3** for detailed set up of the operando XRD set up and cell.

Both *ex situ* XRD patterns and *in situ* XRD were collected with a Malvern PanAlytical Empyrean 3 diffractometer with a Cu Kα radiation source ($\lambda = 1.5418$ Å) and a PIXcel^{3D}detector in 1D mode operated in Bragg Brentano ($\theta - \theta$) geometry. For a typical ex situ measurement, a range of $5° \leq 2\theta \leq 80°$ measured with a PIXcel3Ddetector in 1D mode configuration with iCore and dCore optics with automatic slits set at 10 mm irradiated length and a collection time of 1h.

To monitor the copper oxidation state, we tracked the crystallinity of the catalysts by means of time-dependent XRD conducted simultaneously with CV measurements. We first apply a constant potential at -1.8 V for 30 minutes under CO_2-saturated 1 M KOH with 1.5 M NH_3 electrolyte to completely remove any surface oxide species. During the CV, the potential applied to the sample was changed from -0. 6 V and + 0.6 V, and then from +0.6 V to sweeping back to -1.3 V vs. Ag/AgCl, with a rate of 0.5 mV/s. The XRD detection system used a GaliPIX3D detector in 1D mode configuration with BBHD optics with a range of $30° \leq 2\theta \leq 45°$, leading to each spectrum for 160s in total.

To mimic the real operation condition when each pulsing electrolysis operates, we track the copper nanoparticle in real time when applied to the pulsing condition. Each pulsing condition would track around 30 min as the electrolysis time we keep normally is 30 mins. The pattern was collected between $20° \leq 2\theta \leq 75°$ for each spectrum of 5 min.

5.8.4. Supplementary Note 4: Calculation of the Faradaic Efficiency and formation rate of each product.

For accurately and reasonably comparing the two different electrolysis methods, we introduce the formation rate as a reasonable parameter since both static electrolysis and pulsed electrolysis share the same formula to calculate.

$$Formation\ Rate_x(mmol * cm^{-2} * h^{-1}) = \frac{n_x \times F \times C_x \times V}{A \times t_{total}}$$

Here C_x (mol/L) is the concentration of liquid phase C-N bond products obtain based on previous calibration curve obtained from the NMR (, V (L) is the volume of the electrolyte. n_x is the number of transferred electrons for a certain product, t(h) is the electrolysis time, which is typically 0.5 h. F= 96485 (A$\times s \times mol^{-1}$), A is the geometric area of the electrode (cm2).

All the catalysis results in this study are shown in terms of Faradaic Efficiency (FE) as well. FE is important criteria to evaluate an electrolysis process, though the calculation is different between the static electrolysis and pulsed electrolysis.

The Faradaic efficiencies of liquid products in static electrolysis of the NMR as indicated below:

$$FE_x = \frac{n \times F \times C_x \times V}{Q} \times 100\%$$

where F is the Faradaic constant, Q is the charge passed in total during the reaction, C is the concentration of generated liquid product and V is the volume of the electrolyte.

The Faradaic Efficiency and partial current density of gas product is calculated from gas chromatogram (GC, SRI 8610C) peak area at a given potential as follow:

$$FE_{H_2} = Vx \times flow\ rate \times \frac{nF}{QV_m} \times 100\%$$

n: number of electron transfer to H2, CO, CH4

Vx: the volume fraction

F: Faradaic constant, 96485.3499 C mol-1

V_m: 22.4 L/mol.

For the pulsed electrolysis, the change of FE over time is determined as follows. The time basis for the calculation is one pulse loop consisting of an anodic (time interval tan) and a cathodic (time interval tca) section. All the gas product such as H2, CO, CH4 only form during the cathodic potential. Thus, only invested cathodic charge Qc needs to consider and it is determined by the integration of the current in the cathodic section over time.

The Faradaic efficiency of gas product was calculated from the areas of the GC chromatogram as indicated below:

$$FE_x = \frac{Vx \times flow\ rate \times n \times F}{Q_c \times Vm} \times \frac{t_{an} + t_{ca}}{t_c} \times 100\%$$

Here the Vx is the volume concentration of gas products obtained based on the calibration curve of GC, and the n is the number of transferred electrons for a certain product. The $\frac{t_a+t_c}{t_c}$ was introduced as correction factor because the gas outlet stream of the cell contains reaction products not only during the cathodic section of the pulses, but there is a continuous stream of reaction products.

In contrast, for liquid products Q_{total}, already contains the contribution of the pulse times by integrating the cathodic charge.

$$FE_x = \frac{Cx \times V \times n \times F}{Q_{total}} \times 100\%$$

$Q_{total} = Q_{ca} + Q_{an}$

It must be pointed out that this is a simplified approach. The C-N bond product, such as urea, formamide, and acetamide, may be calculated in a more accurate manner, depending on the exact mechanism for their formation, but for now, we keep their calculations consistent with only the electrons counted towards reducing the CO2 intermediates for consistency and easy comparison with other works. We encourage discussion and opinion of accurate calculation of the FE for this reaction mechanism. We assign 2 electrons for urea, 8 electrons for acetamide and 2 electrons formamide for ease of comparison with static electrolysis. Q_{an} is the integral of all the anodic current and Q_{ca} is the integral of cathodic current.

It should be noted the methylamine is present mostly in gas phase (boiling point: −6.6 to −6.0 °C) and liquid phase as it has high solubility in water (1008 g/L (at 20 °C), but currently the gas phase detection is out of our scope. Thus, our calculation might underestimate the FE and FR of methylamine since we only calculate the liquid phase.

A simple python software was developed to calculate all the Q for ease of calculation, the original code is listed here, and the calculation is based on the explanation in ref 15.

```
    Def convertRawDate (data):
  Idx = 0
  Result = [ ]
While (idx < len(data)):
    currNumber = [ ]
```

```
        if (idx+10 >= len(data)):
                currNumber =  data[ idx:len(data)]
        else:
                currNumber = data[ idx: idx+10]
        currNumber = list(map(lambda x:float(x. split ()[1], currNumber))
    if (len(list(filter(lambda x:x<0, currNumber))) < len(list(filter(lambda x:x>=0, currNumber)))):
        result. append(max(currNumber))
        else:
                result. append(min(currNumber))
        #print (currNumber)
        Idx += 10
Return result
```

5.8.5. Supplementary Note 5: In situ IR analysis

Infrared spectroscopy in an ATR configuration was performed with a ThermoFischer Nicolet 380 FTIR-ATR system with a ZnSe ATR crystal coated with a diamond surface. Infrared spectra were collected at room temperature over the range of 400-4000 cm^{-1}. For ex-situ measurements, each spectrum was recorded with an accumulation of 800 scans with a resolution of 4 cm^{-1}.

For *in situ* IR spectroscopy, the experiments were executed through the use of a custom-designed spectroelectrochemical cell. The carbon cloth was placed in the middle to separate the electrolyte and the gas chambers. Simultaneously, glassy carbon rod was used as the counter electrode and the Ag/AgCl was used as the reference. Each infrared absorption spectrum was acquired by averaging 800 scans and then subtracting from the spectra at open circuit potential. The background spectrum of the catalyst electrode was acquired at open-circuit voltage before each systemic set of measurements, and the measured potential ranges of the electrocoupling reaction were set to 0.4 to –0.4 $V_{Ag/AgCl}$ with an interval of 0.2 V.

In the first part of in situ IR experiments, we aim to identify the onset potential for NH_3 oxidation by combining electrochemical analysis and in situ IR spectroscopy. In open circuit conditions, we add 1.5 M NH_4OH into the solution to see the adsorption behavior of ammonia on the copper surface.

We applied a series of constant potentials to observe the intiation of ammonia oxidation on copper, namely the dehydrogenation of the NH_4OH to absorbed $*NH_2/NH*$. From Figure S18, we can observe NH_2* peak and NH* species at the very beginning of the reaction and a transition point start from 0V, as the NO band begins to rise and indicate the oxidation of $*NH_2/NH$.

The second part of our in situ IR experiments involves determining if the pulsed condition would have a constant $*NH_2/*NH$ species coverage. Based on the CV results (Figure 2a), we selected a potential range of -0.4 V to 0.4 V for the anodic pulse potentials with a gap of 0.2 V. There are two possible reactions in the pulsed electrolysis in the 1M KOH, 1.5 NH_3 solution: as in the steady state anodic potential conditions, ammonia is being oxidized[16] (equation 1). However, upon the application of a cathodic potential of -1.8 V, the formed partially oxidized species would be partially reduced back to NH_3[17,18] (equation 2). Hence, it's important to investigate if there are still any $*NH_2/*NH$ species remaining on the copper surface.

We can observe from the Figure 2c, in the constant potential electrolysis, only NH_4^+ related peak present. In contrast with the constant potential, when applying pulsed electrolysis, peaks in the range of 3000-3600 cm^{-1} emerged, we ascribe them as the NH_2*. That being said, the steady state of partial NH_3 oxidation related species remain on the catalysts surface with select a range of pulsed electrolysis conditions.

In the third part, we aimed to conduct a series of experiments to detect C-N bond products being formed.

In the final part of the IR experiments, we maintain the E_{ca}=-1.8V and E_{an} = -0.2 V with a different time duration was conducted to elucidate the change of the spectra peak with different pulsing times.

Isotope labelling using $^{15}NH_4Cl$ to replace the $^{14}NH_4OH$ was conducted to identify bands associated with C-N bond and support our analysis.

5.8.6. Supplementary Note 6: Raman measurements:

In situ and ex situ Raman spectra were recorded with a Renishaw Raman spectrometer using a 5 mW 633 nm excitation laser and 1800 mm^{-1} grating. Before each set of measurements, detector calibration was conducted by measuring an internal Si wafer (521 cm^{-1}). A laser line focus module was utilized to obtain spectra by spreading out the laser intensity with approximately 20x lower laser intensity per area.

Spectra were collected in the range of 100-1800 cm^{-1} with an exposure time of 5 min for each acquisition. The laser power was 5 mW. An immersion objective (numerical aperture of 0.8) was used with a custom gas diffusion electrode for maximum signal intensity. These spectra analyzed and processed using WiRE 4.4 and OriginPro 2022 software. The spectra were baseline-substrated using the polynomial feature of eight order, and cosmic rays were removed.

The in situ GDE cell had a liquid electrolyte reservoir in which the immersion objective was dipped, and the carbon cloth coated with copper catalysts separated the electrolyte reservoir and the gas channel. CO_2 was continuously delivered to the catalyst at a flow rate of 10 sccm. The counter electrode, a glassy carbon rod, and the reference electrode, Ag/AgCl, were dipped in the electrolyte reservoir around 0.5 cm away from the cathode. After purging the CO_2 into the electrolyte for more than 15 min, we acquired a spectrum of open circuit to observe the surface species prior to electrochemical reaction. Then, a constant potential was applied, to observe the species during the static electrolysis. In the following step, we applied pulsed electrolysis conditions one by one. Electrochemical parameters were the same as described above. 1M KOH was used as electrolyte, with the presence or absence of 1.5 M NH_4OH to identify the peaks associated with C-N bond. In addition, the different electrolysis condition (static electrolysis and pulsed electrolysis) were compared to observe the difference in surface intermediates.

In the frequency range of 1200-1800 cm^{-1}, the Raman spectra of carbon cloth overlap with some important vibration modes of the C-N bond feature, so we modified the gas diffusion layer while preserving its main function. To reduce the background spectra, carbon paper was used to support copper nanoparticles. The carbon cloth is placed on the bottom of the carbon paper catalyst support so that it maintains its hydrophobicity. As the carbon cloth is made of fibers, the interspace of the fibers can let the gas permeate, so the gas diffusion layer still serves its primary function.

In the final step, we maintain the E_{ca}=-1.8V and E_{an} = -0.2 V with a different time duration to elucidate the probe of the spectra (and surface speciation) with different pulsing times.

Isotope labelling of $^{15}NH_4Cl$ to replace the $^{14}NH_4OH$ and KOD to replace the KOH, H_2O to replace the D_2O was conducted to identify the peak associated with C-N bond, and peak associate C-H vibration mode.

To better express the features of the Raman spectra in the range of 1200-1800 cm^{-1}, we utilized OriginPro 2022 software to process the Raman spectra. The Savitsky-Golay method was conducted as a fit method and the raw data and after-processed data are plotted on the same graph.

Inspired by work using in situ Raman to observe of the pH gradient near the GDE electrode of CO_2 Reduction in alkaline electrolyte[19], we analysis the local surface pH on the surface of the copper nanoparticle. The local pH could determine by the ratio of CO_3^{2-} /HCO_3^-. During our in situ Raman experiment, the distance between the immersion objective and the catalysts remains constant. Therefore, we can use the peak intensity of CO_3^{2-} and HCO_3^- to roughly determine the surface pH in different electrolysis conditions. We can observe the peak intensity of CO_3^{2-} decreasing, while the peak intensity of HCO_3^- is increasing, which indicates that the surface pH will increase with different anodic pulsed potentials. Also, since in the oxidation process, the surface *OH could react with the NH_3 to form some NH_2 or NH[16], this means the consumption of OH^- during pulsed condition might occur faster than the without NH_3 condition. This may help explain why under 1M KOH and 1M NH_4OH electrolyte composition, the reaction has higher ethanol selectivity than the 1M KOH, 1.5 M NH_4OH. The increase of bicarbonate concentration may also increase the selectivity for CH_4[20].

5.8.7. Supplementary Note 7: Scope of the oxy-reductive C-N bond couplings.

With an initial set optimized reaction parameters (for CO_2 + NH_3) in hand, we sought to explore the scope and limitations of the proposed reaction mechanism and the unique method.

Reaction conditions: Formaldehyde (CH_2O) substrate (0.5 M), NH_3 (1 M), sodium formate and sodium acetate (0.2 M), Na_2NO_3 (1 M) in the 1M KOH electrolyte. For the C-S bond coupling step, SO_3^{2-} (0.2 M) was used as the sulfur source. The CO_2 bubbling rate remained 10 sccm. When using formaldehyde, formate and acetic acid as the carbon source, N_2 (10 sccm) flowed through the electrolyte and cell for 15 min to avoid the influence of atmosphere CO_2.

The reaction mixture was electrolyzed for 30 min both in condition of static electrolysis and an pulsed electrolysis. The pulsed electrolysis condition maintained E_{an} = -0.2 V for 1s and E_{ca}= -1.8 V for 1s. However, the optimized conditions might be different for each substrate/reaction. It is beyond the scope of this work to optimize the conditions for each of the substrates, although we believe we may attain better results through screening on different potentials, pH, reactant concentration and more. Because of the uncertain reaction routes and mechanisms, the formation rate was used as a more reasonable metric to compare the static electrolysis and pulsed electrolysis.

5.8.8. Supplementary Note 8: Using GC-MS to prove the formation of the C-N bond products.

To further verify our results for the C-N bond formation, we conduct GC-MS analysis of the electrolyte after 6h electrolysis.

1.15 ml of 2 M Phosphate buffer was added to the electrolyte after electrolysis (around 4 mL) for pH adjustment and to avoid the possible C-N discompose. The obtained solution mixture was then concentrated using a rotary evaporator to get around 1 mL solution in a low-pressure mode. Prior to GC-MS analysis, the formamide, acetamide, and urea were extracted from a liquid/liquid extraction. An aliquot of 300 mL of the sample was mixed with 600 mL ethyl acetate and 100 mL methanol, vortexed then centrifuged.

An aliquot of 1 mL of the supernatant was injected into the GC-MS system with a split ratio of 20. The GC column was a DB-624, 30m x 0.25 mm, 1.4mm, operated under a temperature gradient starting at 40°C, held for 1 min, increased to 195°C at 10 °C /min, and then to 250°C at 10 °C /min for a total run time of 22 min. The ionization mode was EI and mass spectra were acquired in scan mode from m/z 10 to 500. A database search on the NIST05a library was used for compound identification. Besides solvent-related peaks, formamide, acetamide, and urea were identified in the sample with matching scores of 98.13, 98.64, and 96.11 respectively (see Figure SI 28, as generated by the Agilent database search software).

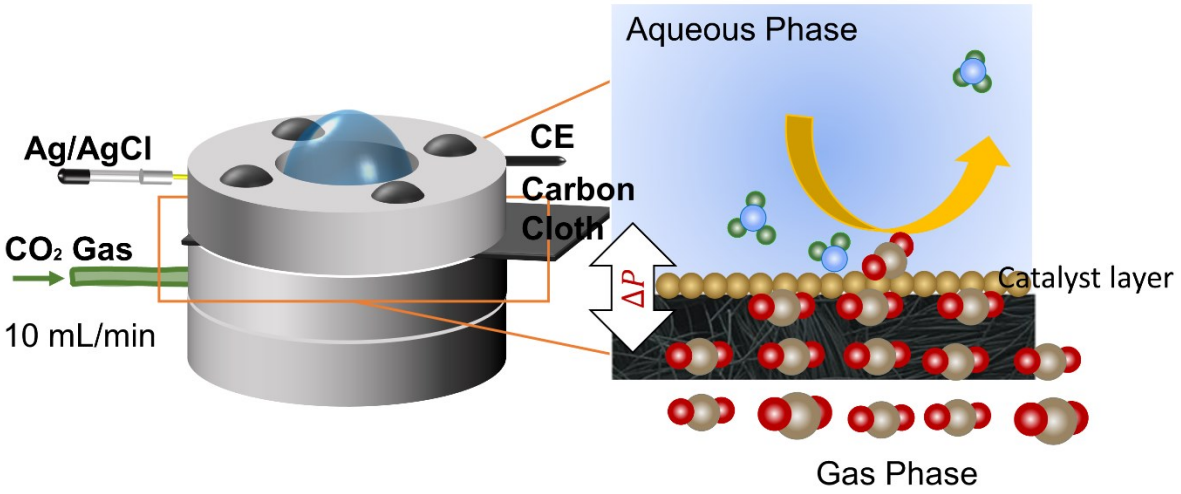

Figure 5-S1. Simplified schematic of the electrochemical GDE based setup employed in this work.

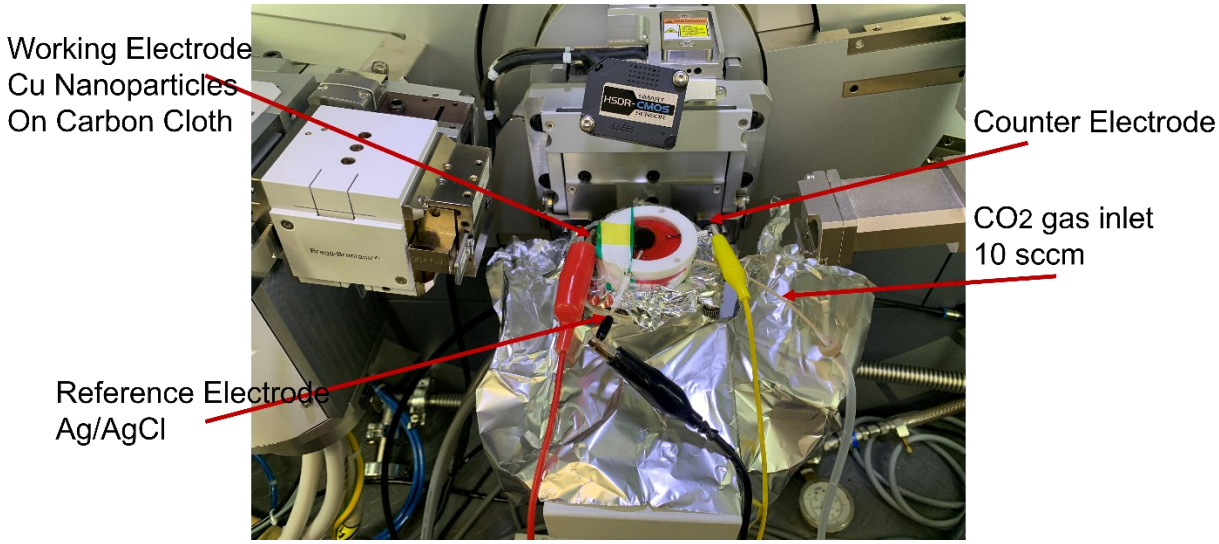

Figure 5-S2. *Operando* cell for surface X-ray diffraction measurements in an electrochemical environment. A kapton layer was cover on the working electrode surface to avoid the vaporization of the electrolyte.

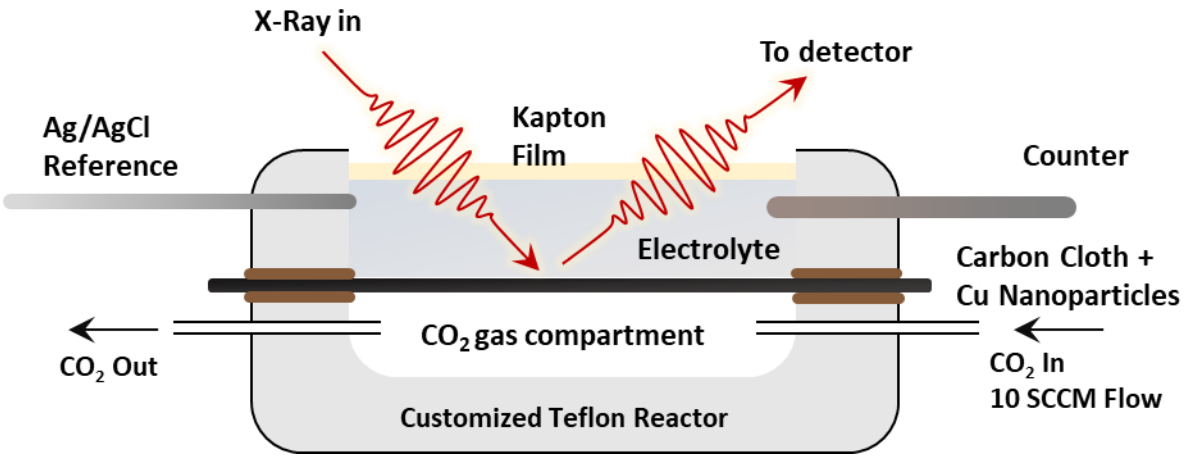

Figure 5-S3. Simplified schematic of the in situ XRD cell setup employed in this work.

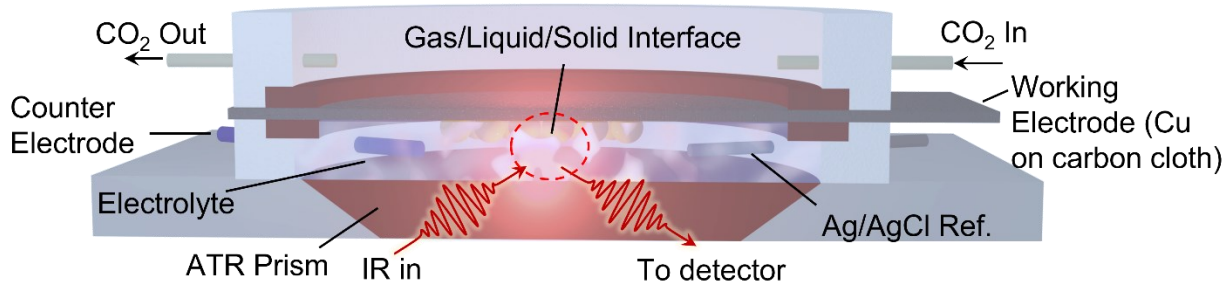

Figure 5-S4. IR spectroelectrochemical testing. The spectroelectrochemical configuration employed to probe the reaction process is illustrated.

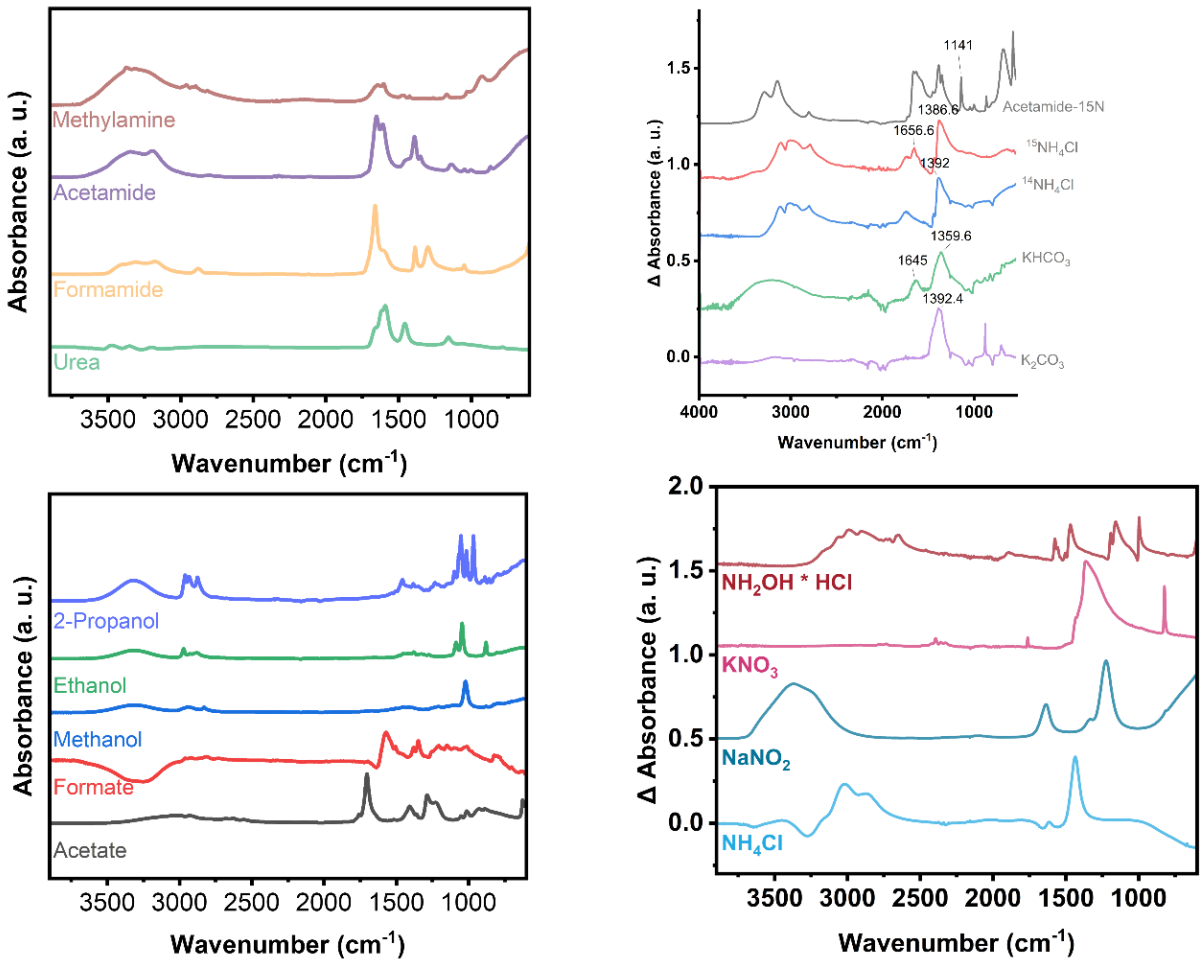

Figure 5-S5. IR spectra of standards. Infrared spectra of several reference compounds.

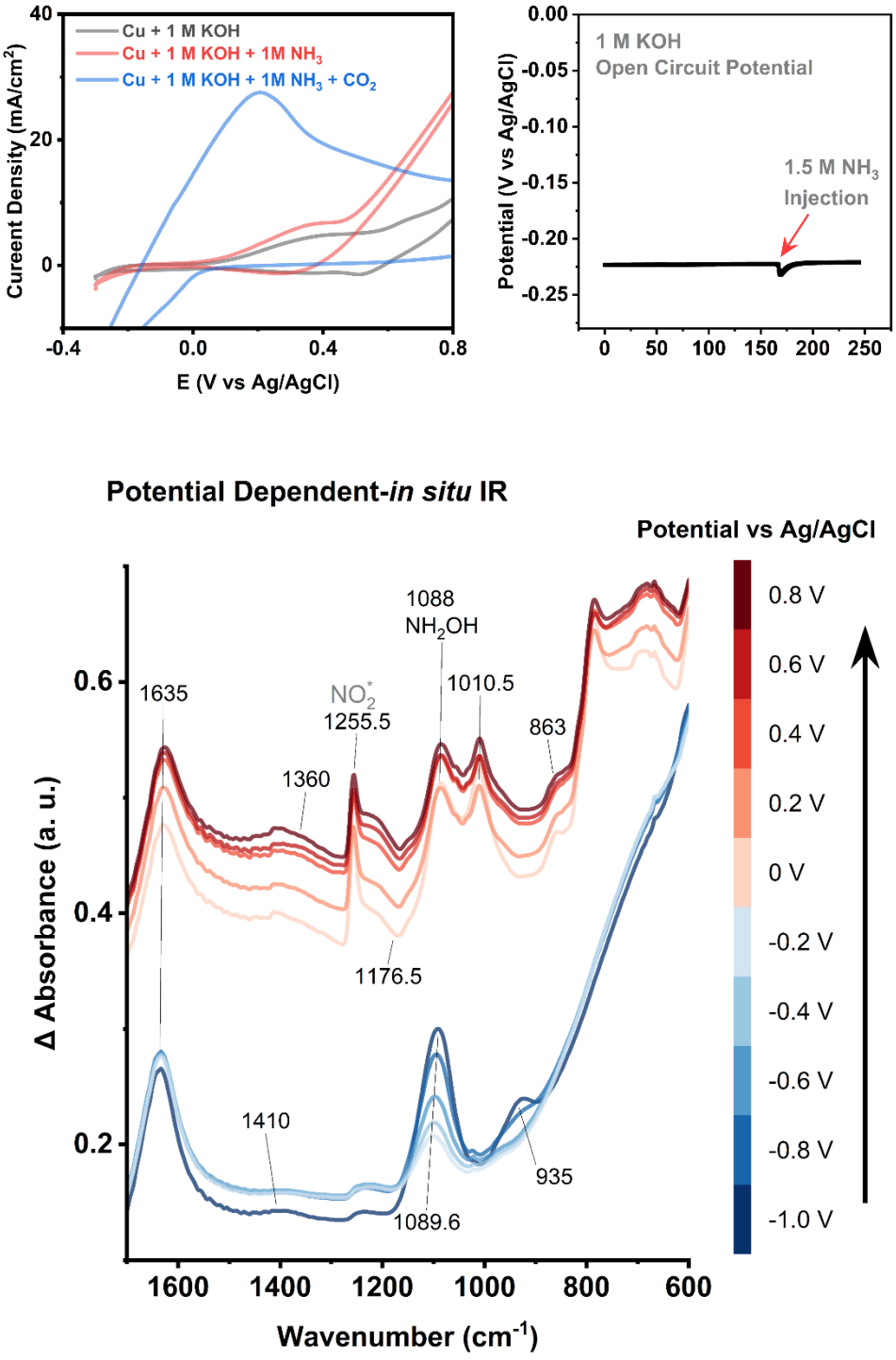

Figure 5-S6. IR spectroelectrochemical testing. CVs of the Cu showing the oxidation of Cu, NH_3 and CO_2R intermediates. Spectra recorded as a function of applied potential from (-1.0 V to 0.8 V) in the condition of 1 M KOH, 1.5M NH_3 (b).

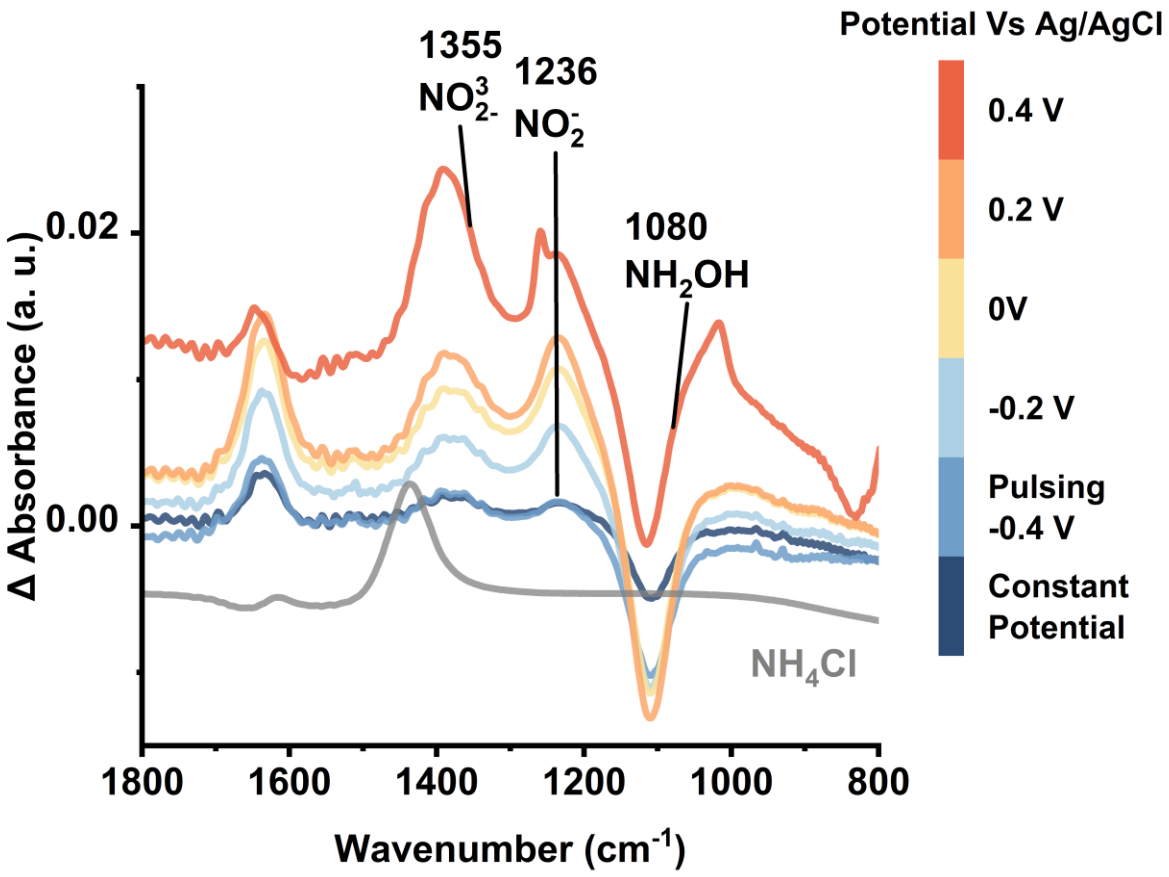

Figure 5-S7. IR spectroelectrochemical testing. With the system at open circuit used as the background, spectra were acquired at static electrolysis (E_{ca} = -1.8V vs Ag/AgCl) and Pulsed electrolysis (E_{an} = - 0.4 V ~ 0.4 V) in the presence of NH_3 only.

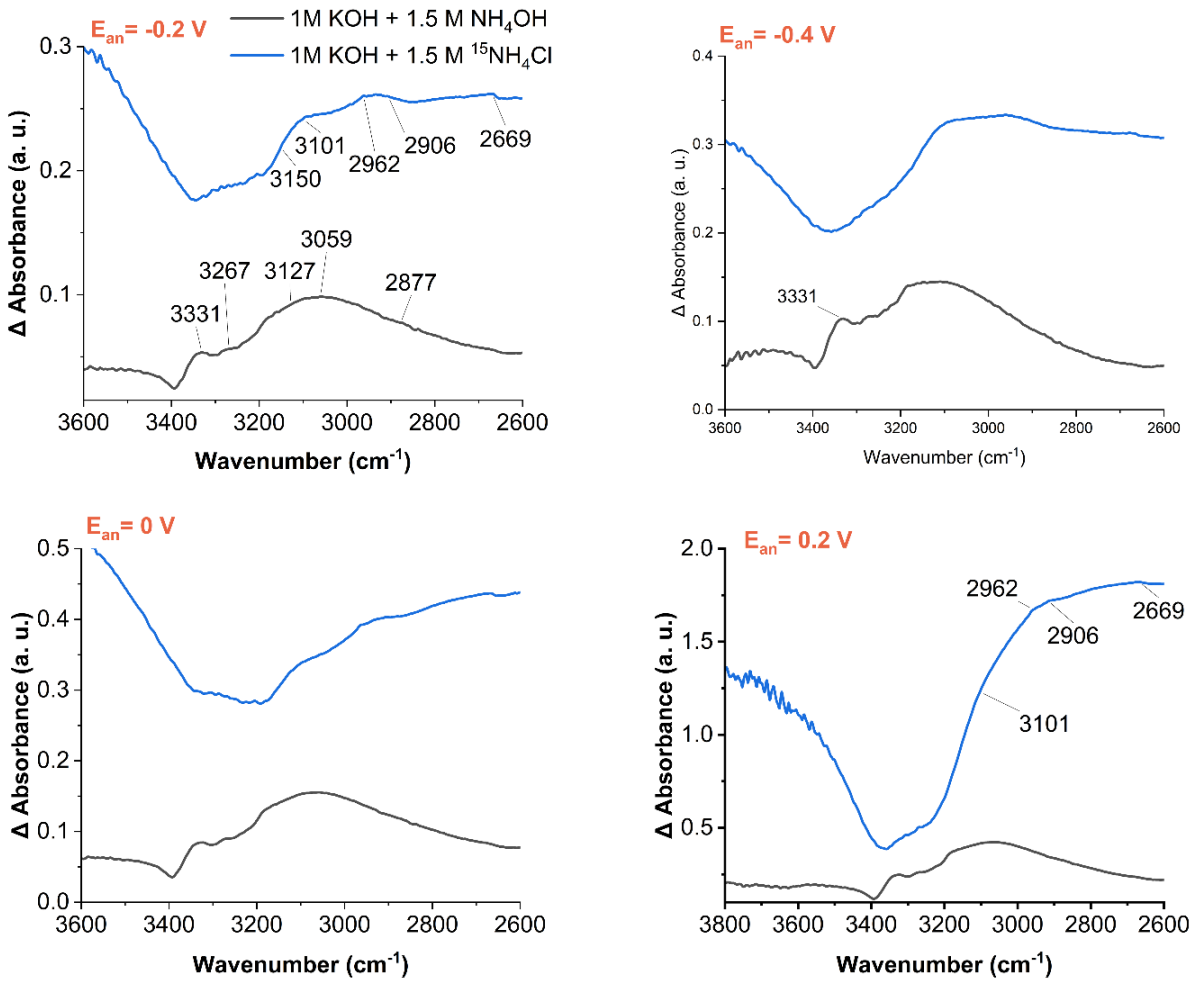

Figure 5-S8. Isotope studies. $^{15}NH_4Cl$ was used to replace the NH_4OH to identify the IR bands associate the N-H bonds or C-N bonds under several representative pulsing conditions.

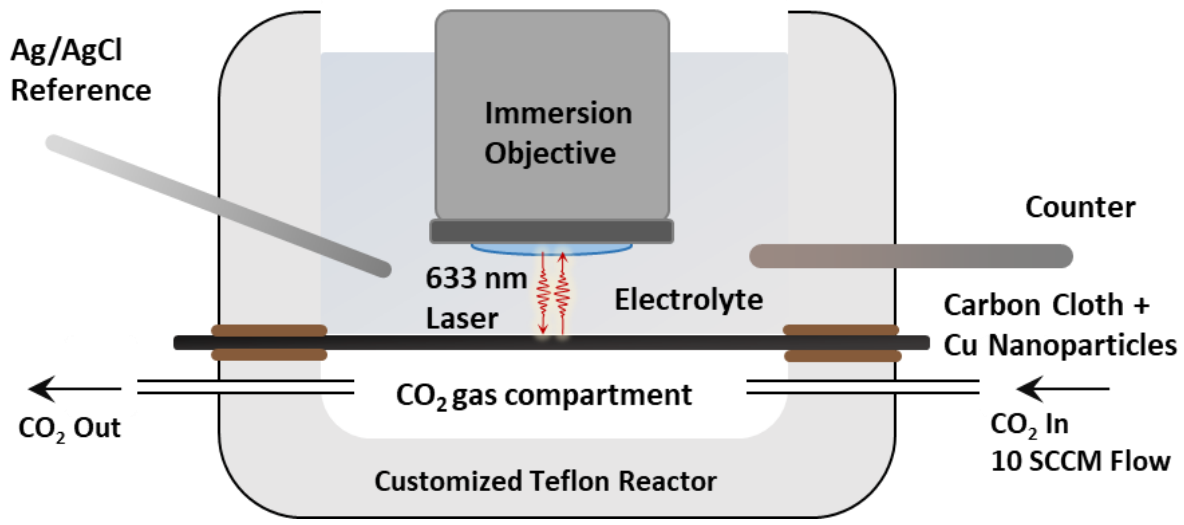

Figure 5-S9. Simplified schematic of the *in situ* Raman cell setup employed in this work.

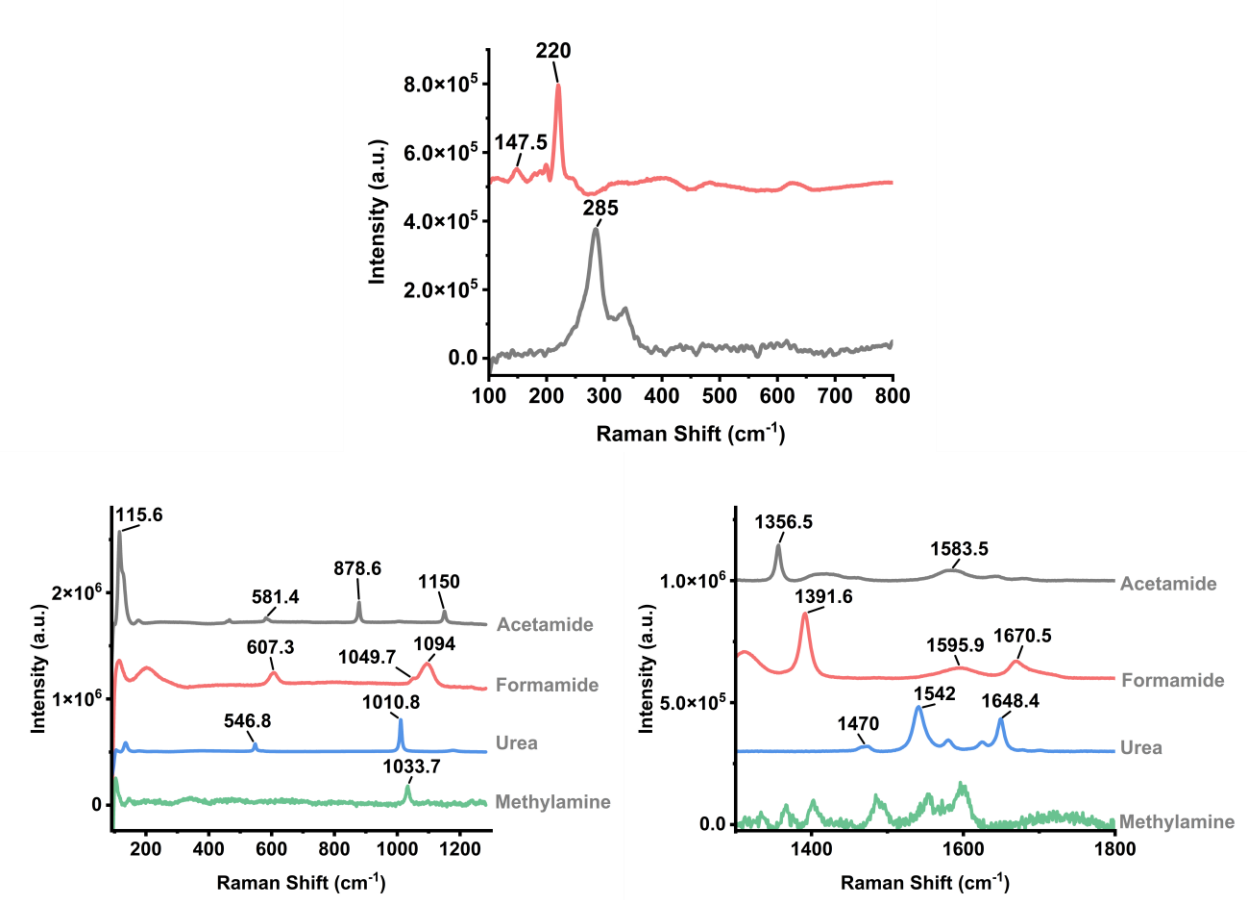

Figure 5-S10. Raman Standards. Raman spectra of several reference compounds: Cu_2O and CuO (upper), C-N bond product (bottom).

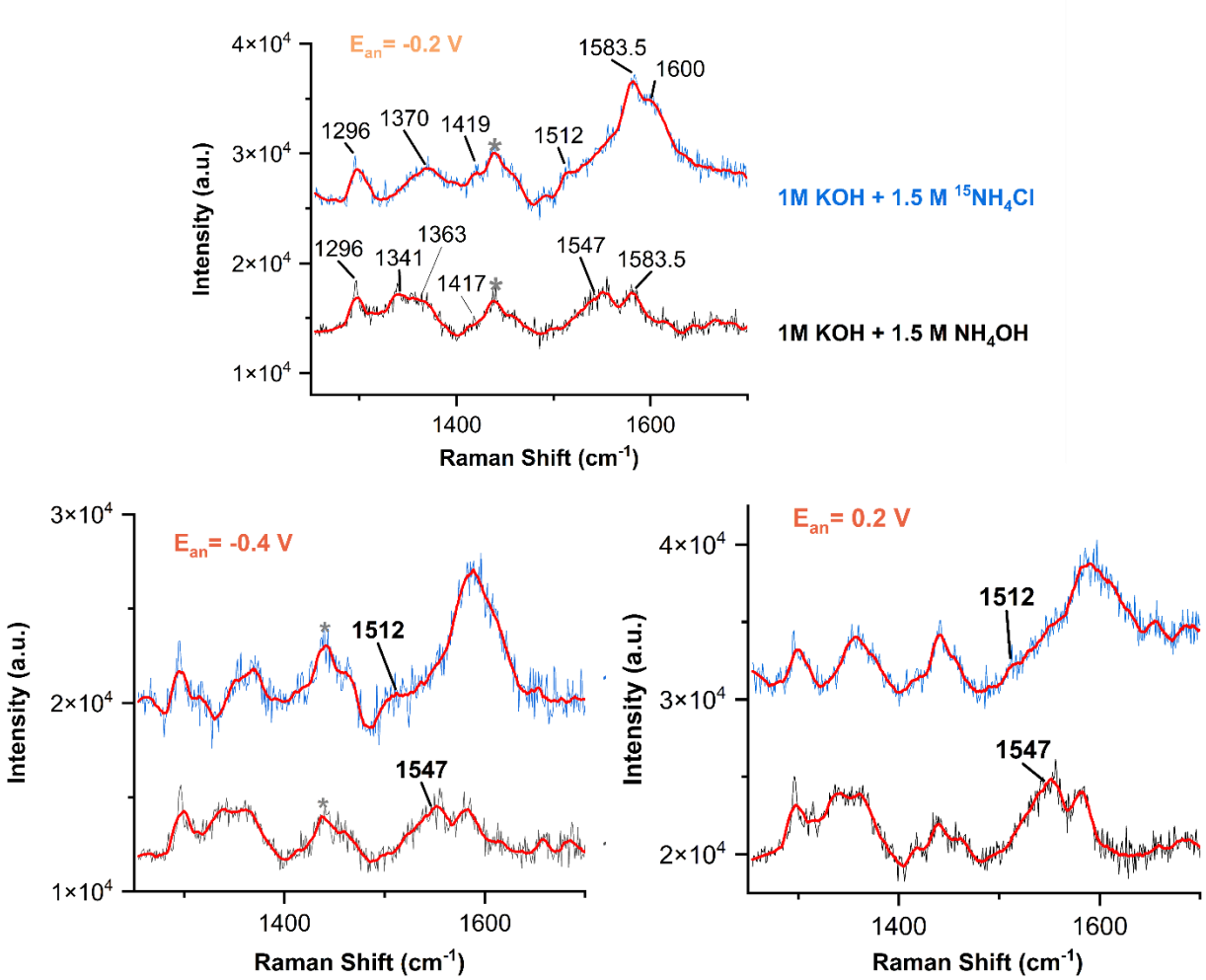

Figure 5-S11. Isotope Raman study. We used ^{15}NH4Cl to replace the NH_4OH as the nitrogen source. The peak at 1547 cm^{-1} could be originating from the C-N bond, as it shifts to 1512 cm^{-1} when ^{15}N is used. We conduct the pulsed electrolysis in varied E_{an}, and the peak shift is same in each case.

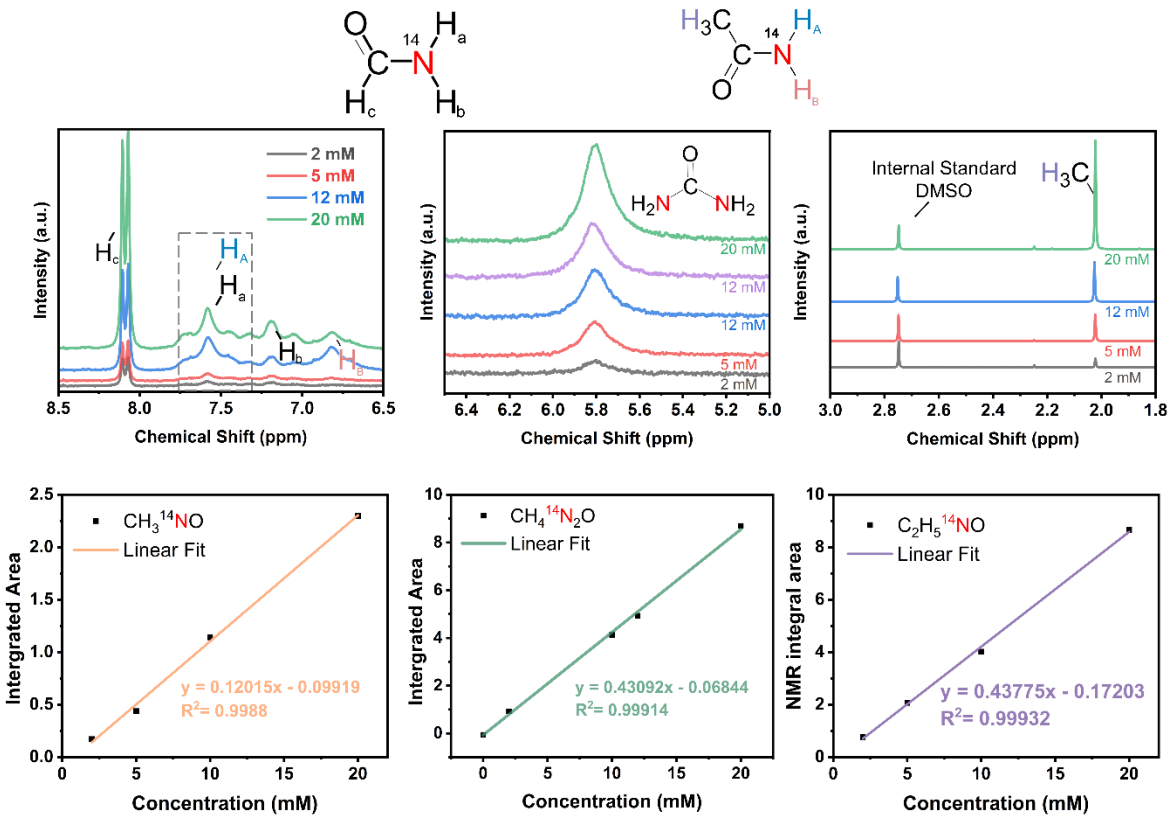

Figure 5-S12. C-N bond product quantification. ^{1}H NMR analysis of NH_4Cl standard solutions (up) and calibration curve (bottom) of formamide, urea, and acetamide, respectively. The concentration of C-N bond products exhibits a linear relationship with the integral area of the characteristic peaks.

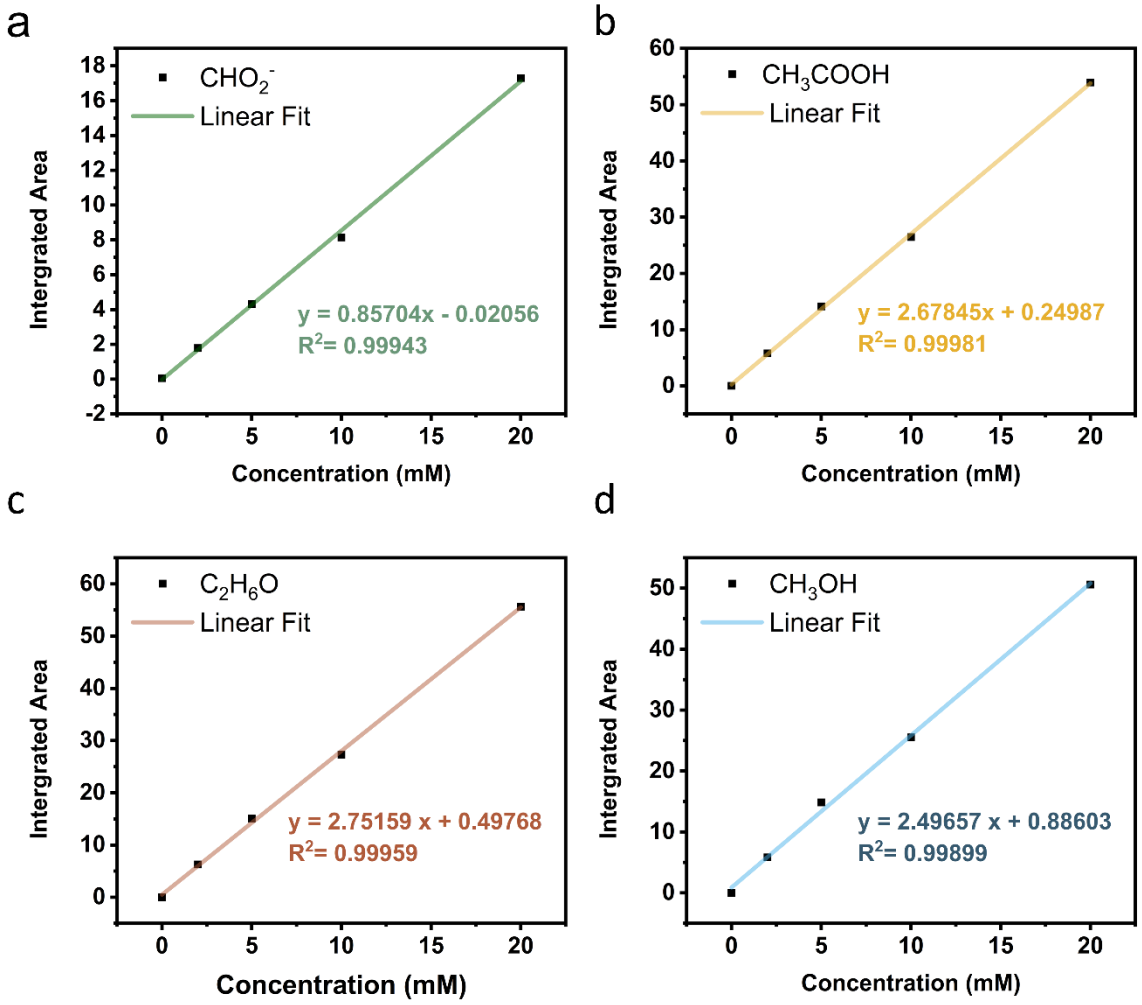

Figure 5-S13. CO_2R product quantification. The calibration curve of formate, acetic acid, ethanol, and methanol respectively. The concentration of those bond products exhibits a linear relationship with the integral area of the characteristic peaks.

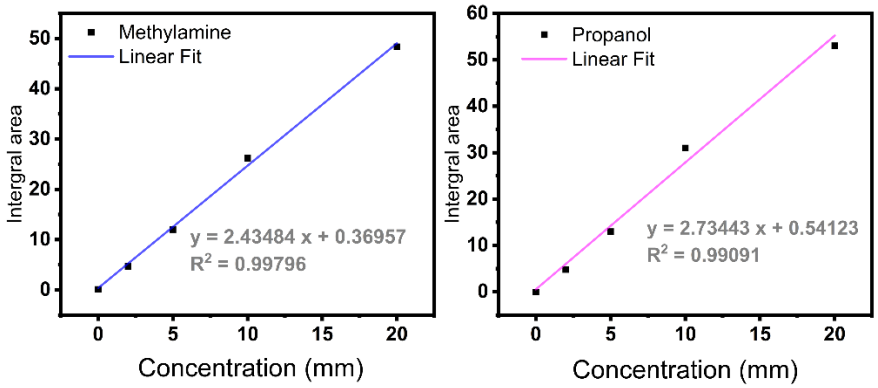

Figure 5-S14. The calibration curve of Methylamine and Propanol. The concentration of those bond products exhibits a linear relationship with the integral area of the characteristic peaks.

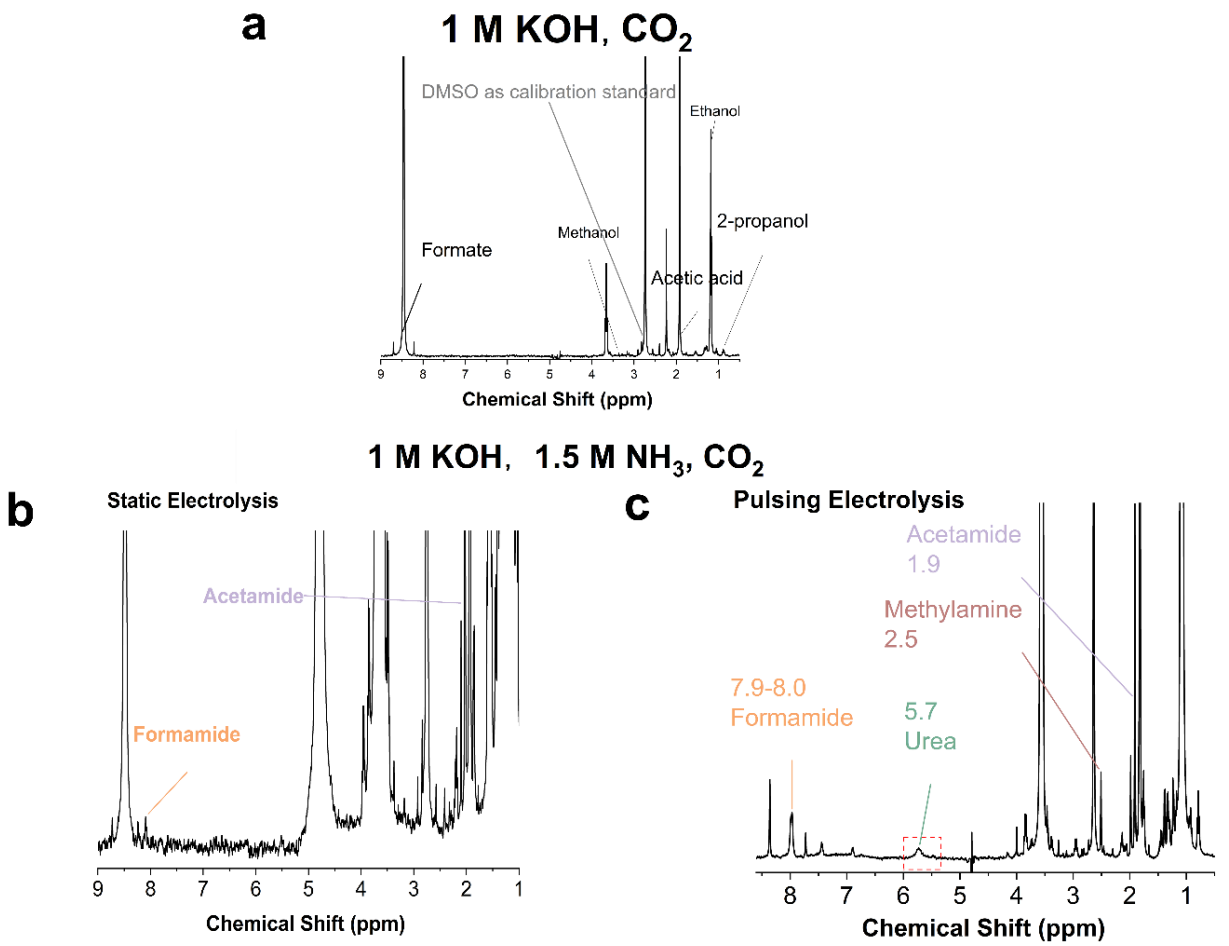

Figure 5-S15. NMR spectra of electrolyte of (a) without NH_3 after pulsing electrolysis, (b) with 1.5 M NH_3 after static electrolysis and (c) with 1.5 M NH_3 after pulsed electrolysis. No c-n bond product observed in a. No urea and methylamine could be detected in spectra b. there are four C-N bond related product could be detected in the spectra c. The signals with chemical shift between 7.8- 6.8 belong to the proton shift of N-H bond of C-N products. The pulsed electrolysis condition is 1s pulse at E_{an} = -0.2 V was followed 1s pulse at E_{ca} = -1.8 V and the loop was repeated for 30 min.

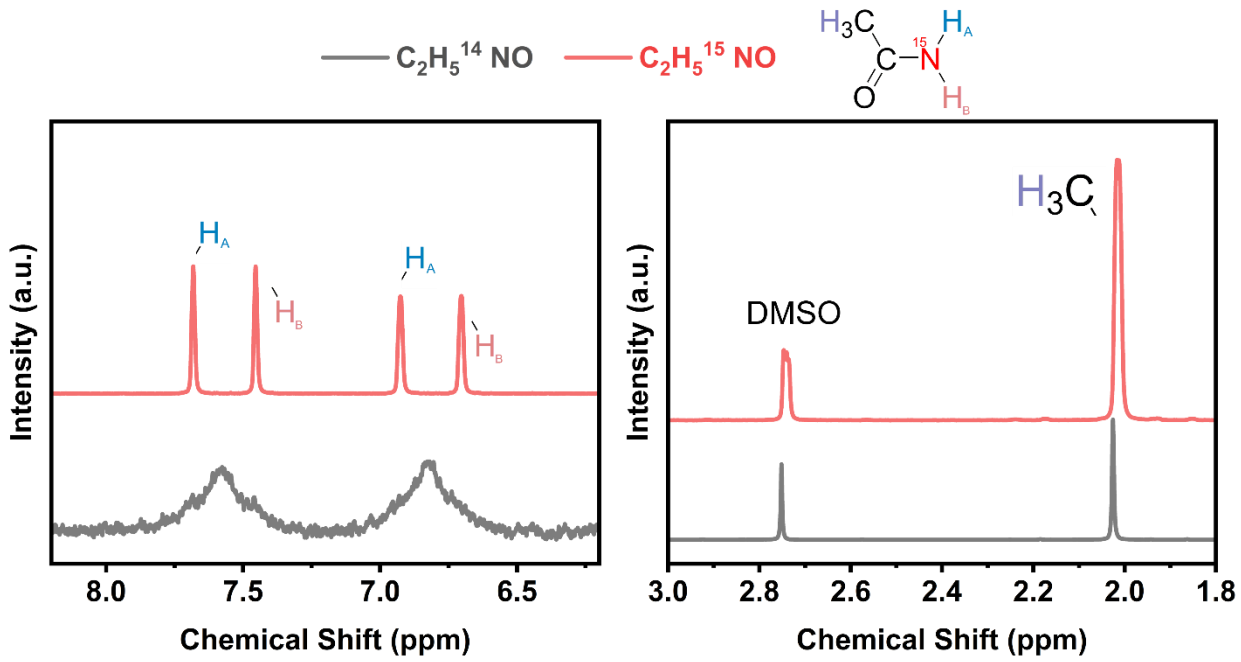

Figure 5-S16. Standard NMR spectra of ^{14}N-acetamide (gray) and ^{15}N-acetamide (red).

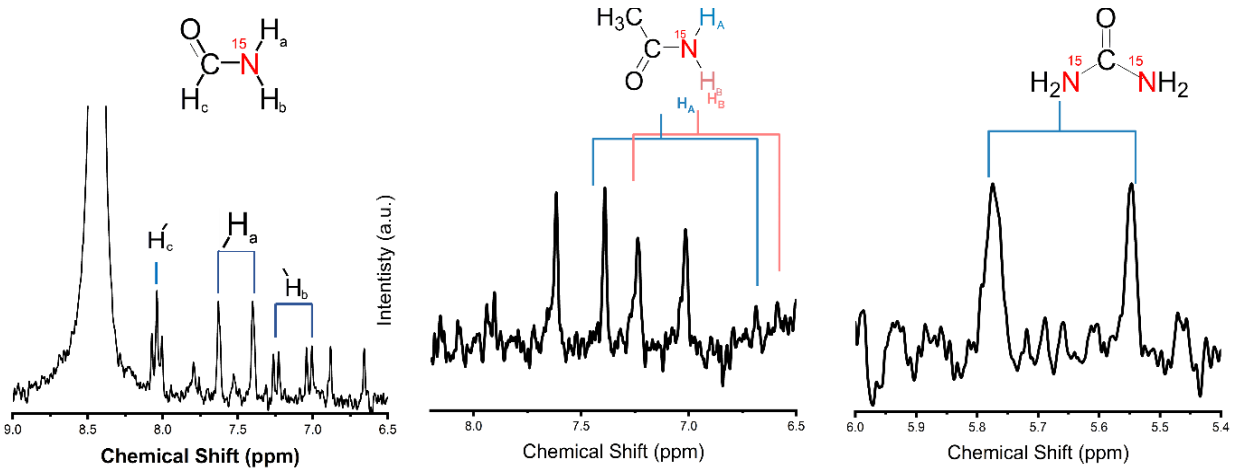

Figure 5-S17. NMR spectra of electrolyte solution after using $^{15}NH_3$ to replace the $^{14}NH_3$ to produce C-N bond products. The pulsed electrolysis condition is 1s pulse at E_{an} = -0.2 V was followed 1s pulse at E_{ca}=-1.8 V and the loop was repeated for 30 min.

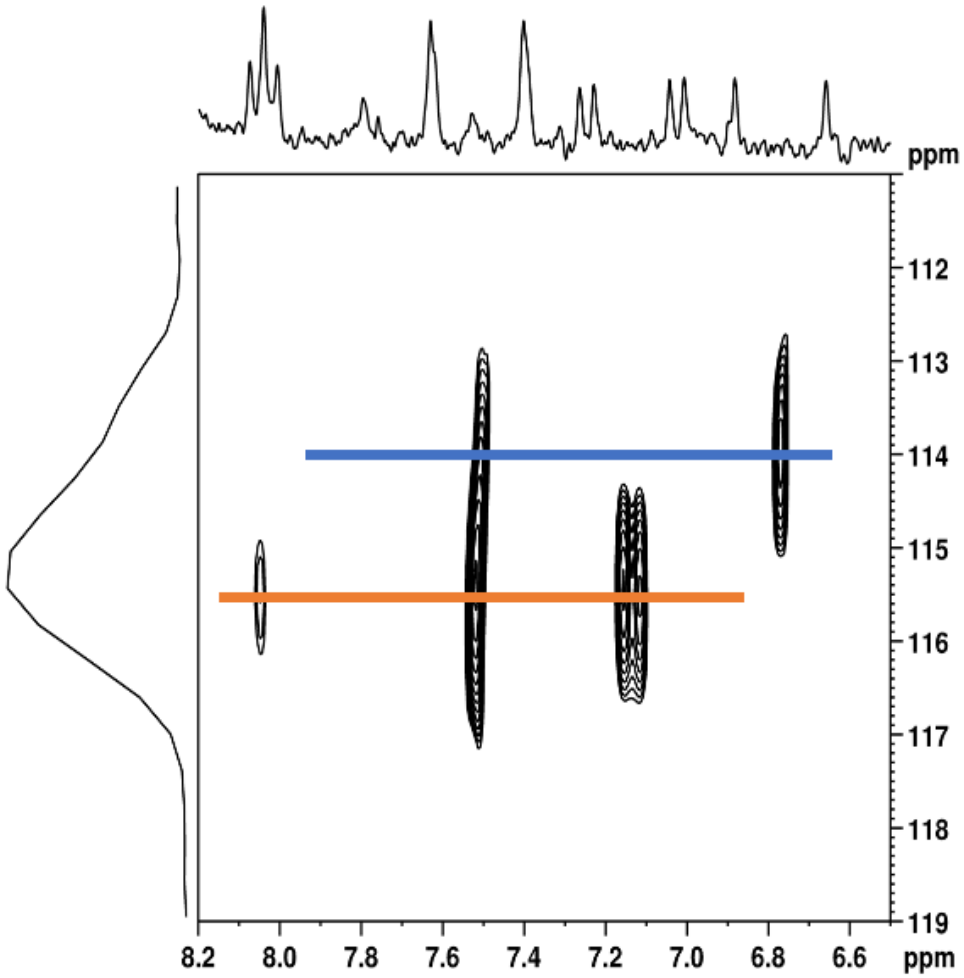

Figure 5-S18. 1H-^{15}N heteronuclear single-quantum correlation (HSQC) to prove the formation of both acetamide and formamide. Cross-peaks are observed for the two chemically distinct amide hydrogens of acetamide (blue line d_N = 114.0 ppm). For formamide cross-peaks are observed from the two chemically distinct amide hydrogens as well as the hydrogen bound to the carbonyl (orange line d_N = 115.5 ppm). The pulsed electrolysis condition is 1s pulse at E_{an} = -0.2 V was followed 1s pulse at E_{ca}= -1.8 V and the loop was repeated for 30 min.

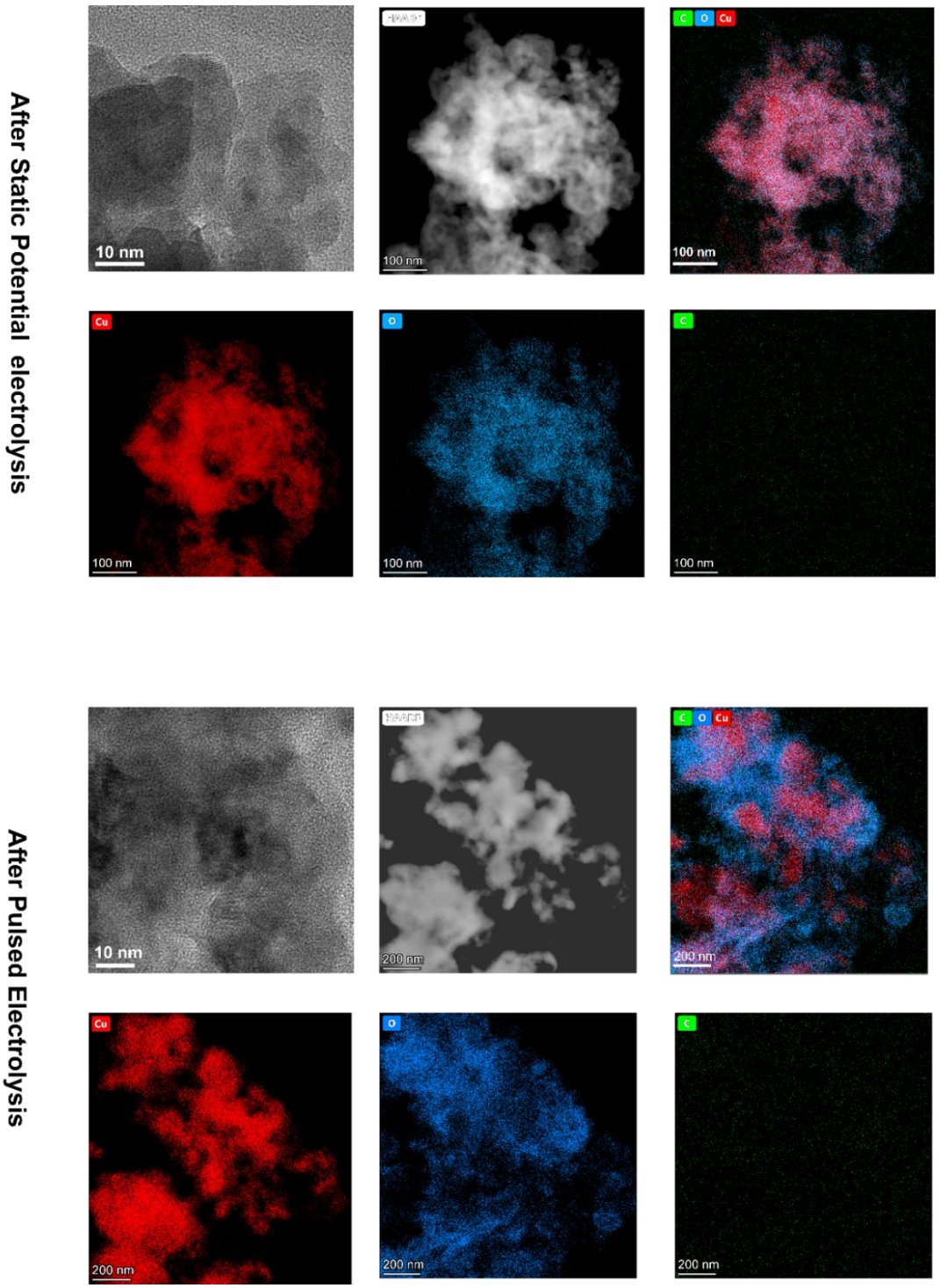

Figure 5-S19. High resolution TEM and high angle annular dark field image (HADDF) and EDS map of the catalyst particles after steady state and pulsed electrolysis. the electrolyte for both static and pulsed electrolysis is same: 1 M KOH and 1.5 M NH_4OH. For static electrolysis, the electrode applied a chronoamperometry at -1.8 V vs Ag/AgCl for 30 mins. For pulsed electrolysis, the electrode applied a cathodic potential are E_{ca} = 1.8 V for 1s then E_{an} = -0.2 V for 1s. In total, the pulsed condition is conducted 30 min.

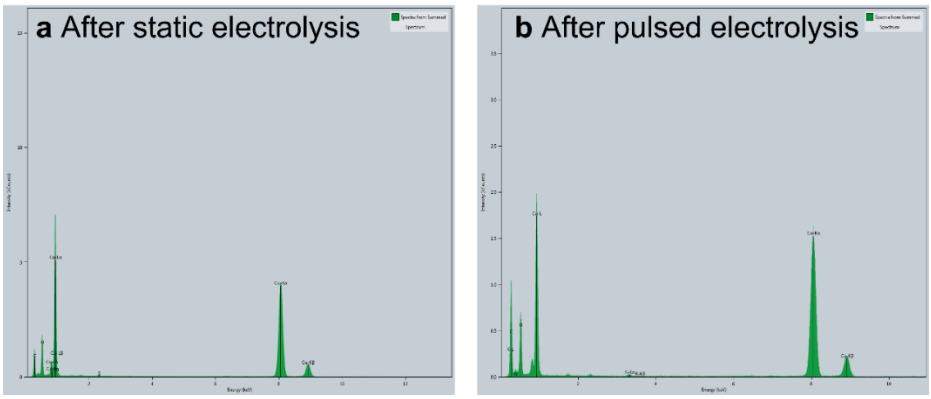

Figure 5-S20. EDS spectra of the catalyst after static electrolysis (a) and after pulsed electrolysis (b). The electrolysis condition same with Figure 5-S19.

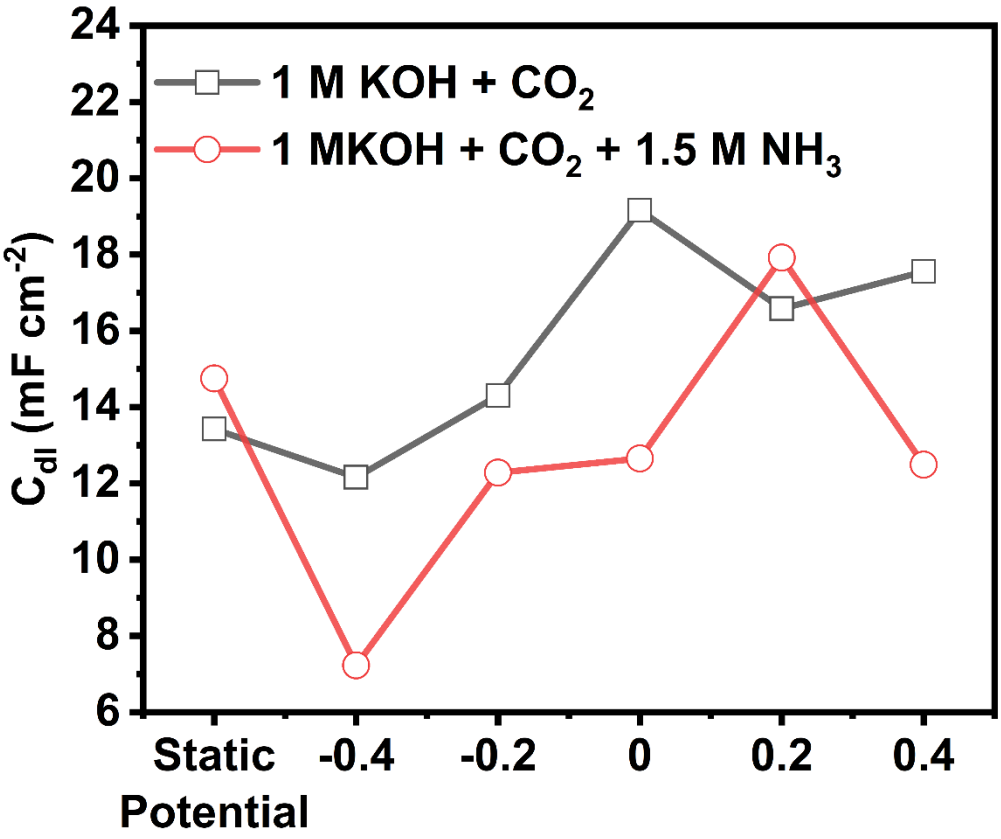

Figure 5-S21. Double-layer capacitance as determined by cyclic voltammetry. The electrochemical surface area after 0.5 h electrolysis was obtained by double layer capacitance with cyclic voltammetry (CV) in the non-Faradaic region with variable scan rates. CVs were acquired out between -0.2 to 0 V versus Ag/AgCl, with scan rate of 5, 20, 40, 60, 80, 100 and 120 mV s^{-1}.

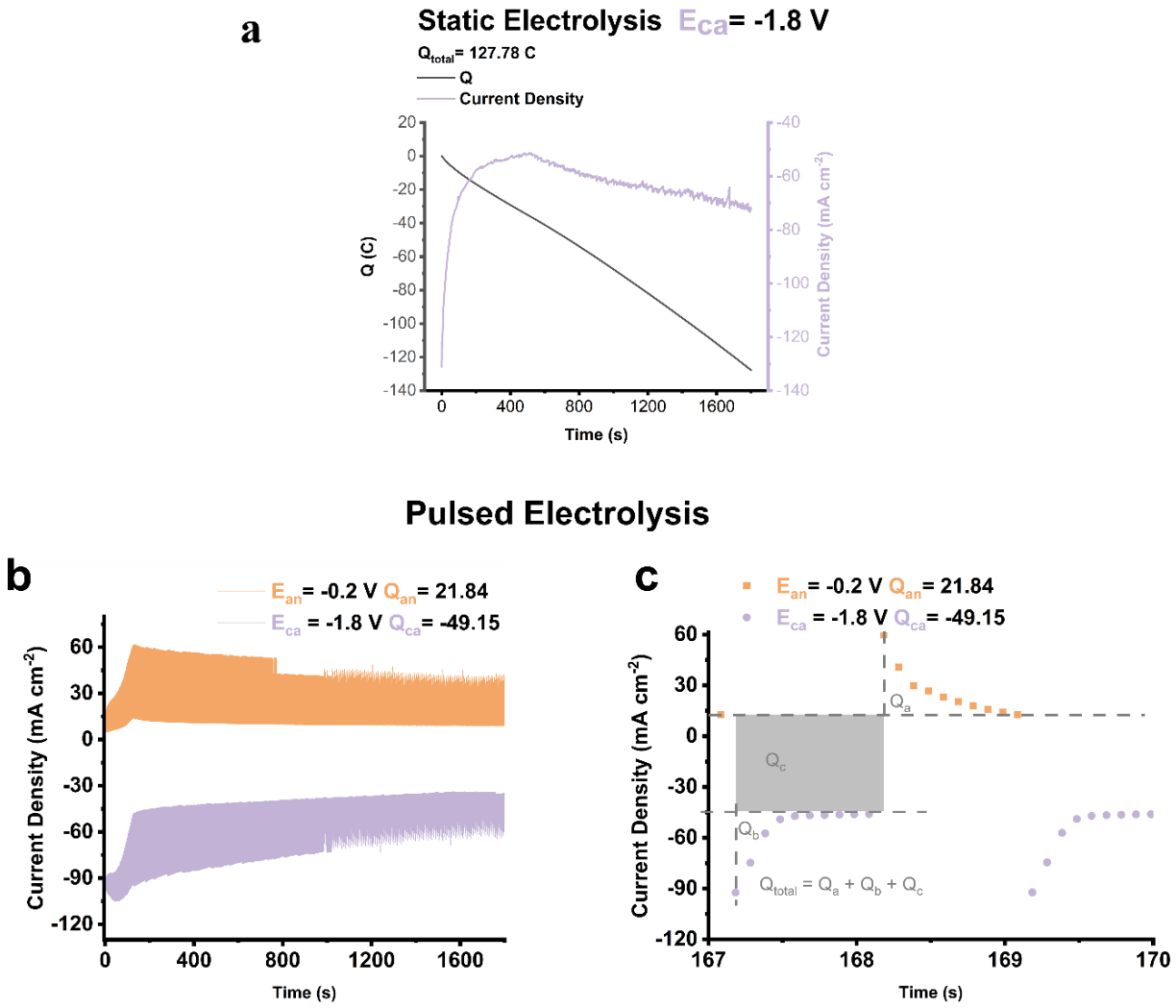

Figure 5-S22. Typical current density vs. time trace for both a steady electrolysis (a) and pulsed electrolysis (b) and zoom-in (c). The listed Q is a representative amount shown for reference. Example (c) of a current transient of pulsed electrolysis at t_{ca} = 1s and t_{an} = 1s with the corresponding oxidative (Q_a), reductive (Q_b) and total charge passed through the circuit during electrolysis ($Q_{total} = Q_a + Q_b + Q_c$).

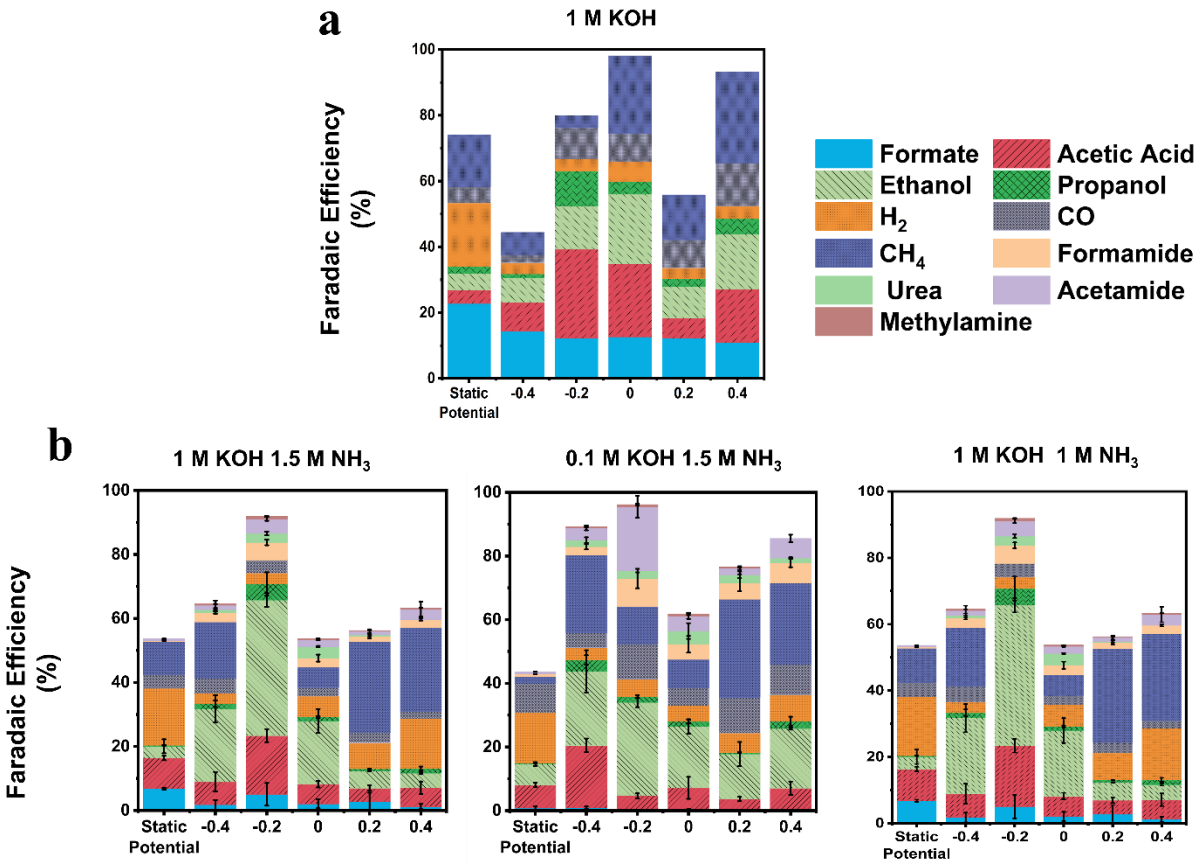

Figure 5-S23. Faradaic efficiencies for the static electrolysis and pulsed electrolysis in the absence of NH3 (a) and (b) with NH_3. For static electrolysis, the potential sets as -1.8 V. For pulsed electrolysis, the values for the cathodic time and anodic time are t_{ca} = 1s and t_{an} = 1s, and the cathodic potential are E_{ca} = 1.8 V and E_{an} = -0.4 V to 0.4 V, respectively. Each system was fed with CO_2 at a constant flow (10 sccm). The results in line with the results of the ECSA detection, which means the selectivity towards CH_4 has some relation with the surface roughness[1,2]. The highest Faradaic efficiency of CH_4 is 0 V in the absence of NH_3 and 0.2 V in the presence of the NH_3. Each electrolysis conditions were repeated for more than 3 times to determine standard deviations between measurements.

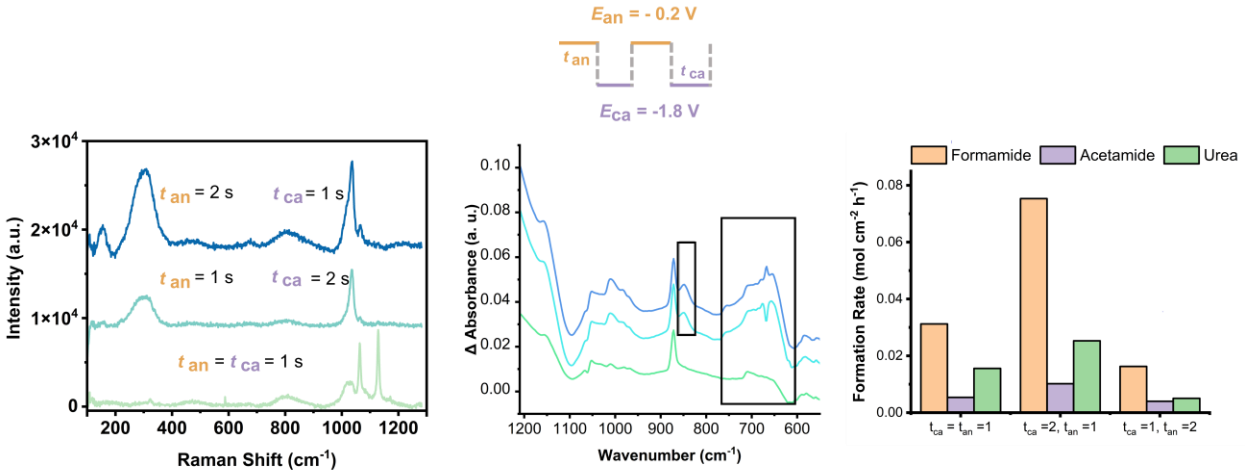

Figure 5-S24. Effects of the durations of the anodic (t_{an}) and cathodic (t_{ca}) pulses. From left to right, the graph corresponds to the *in situ* Raman Spectra, the *in situ* IR spectra and the formation rates. Doubling the anodic potential would promote the formation of oxygenated copper species, as indicated by the Raman spectra. Formation rates of formamide doubled when increasing the cathodic pulses time, and the formation rate decreases when doubling the anodic pulse duration.

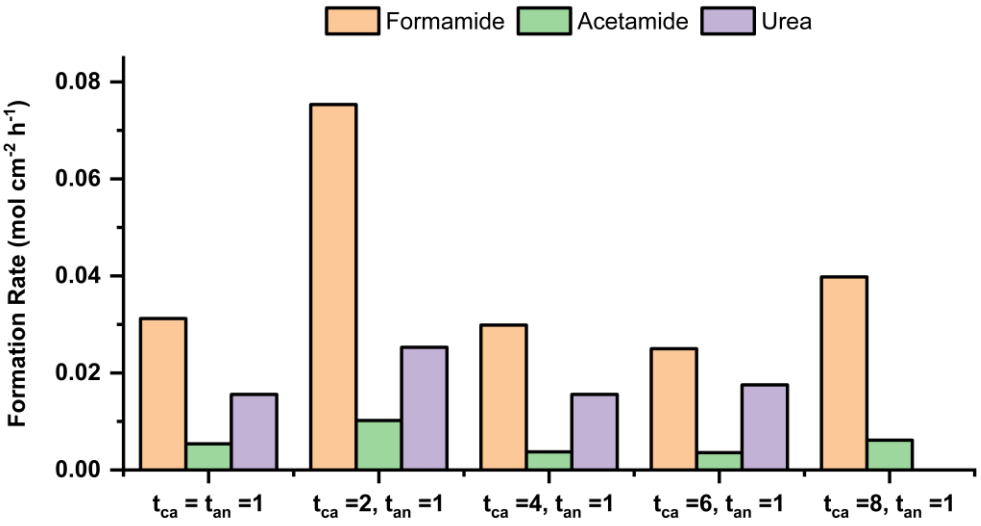

Figure 5-S25. Effect of the durations of the cathodic (t_{ca}) pulses times on product formation rates. The reaction conditions entailed 1.5 NH_3 and 1.0 M KOH, E_{ca} = -1.8 V and E_{an} = -0.2 V vs. Ag/AgCl.

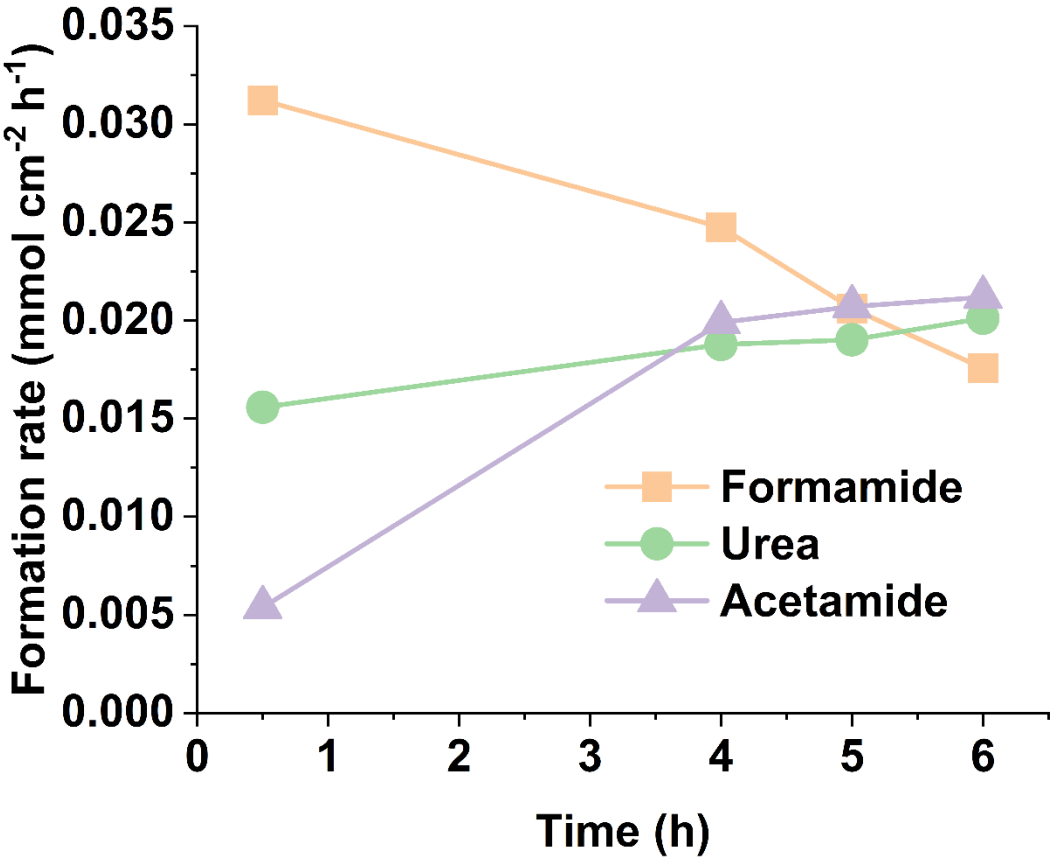

Figure 5-S26. Long term operation was tested at E_{an} = -0.2 V for 1s and E_{ca} = -1.8 V vs Ag/AgCl for 1s. The formation rate of formamide is decreasing, while the acetamide and urea formation rate is increasing might attribute to the interplay of the gradual consumption of the ammonia and the dropping of the electrolyte pH when operating.

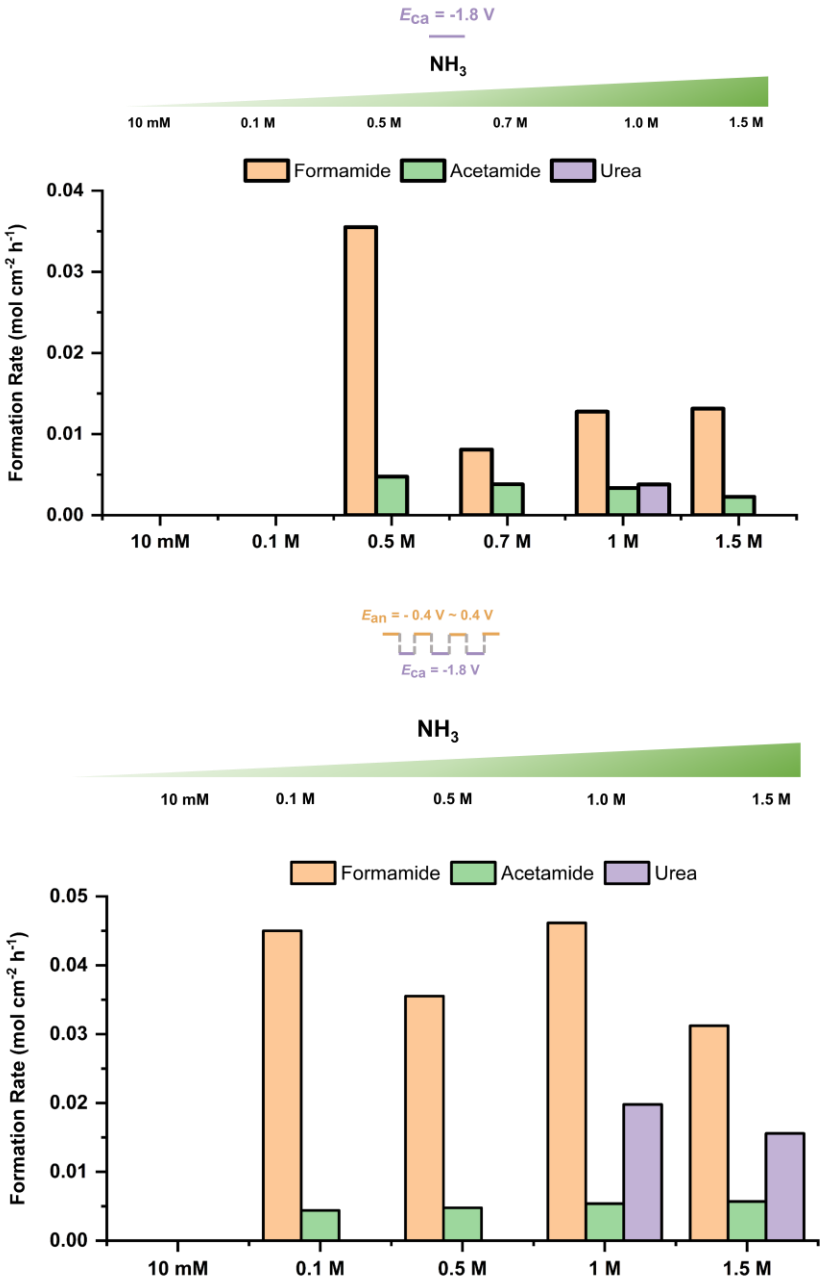

Figure 5-S27. Effects of concentration of NH_3. The reaction conditions entailed 1.5 NH_3 and 1.0 M KOH, E_{ca} = -1.8 V and E_{an} = -0.2 V vs. Ag/AgCl.

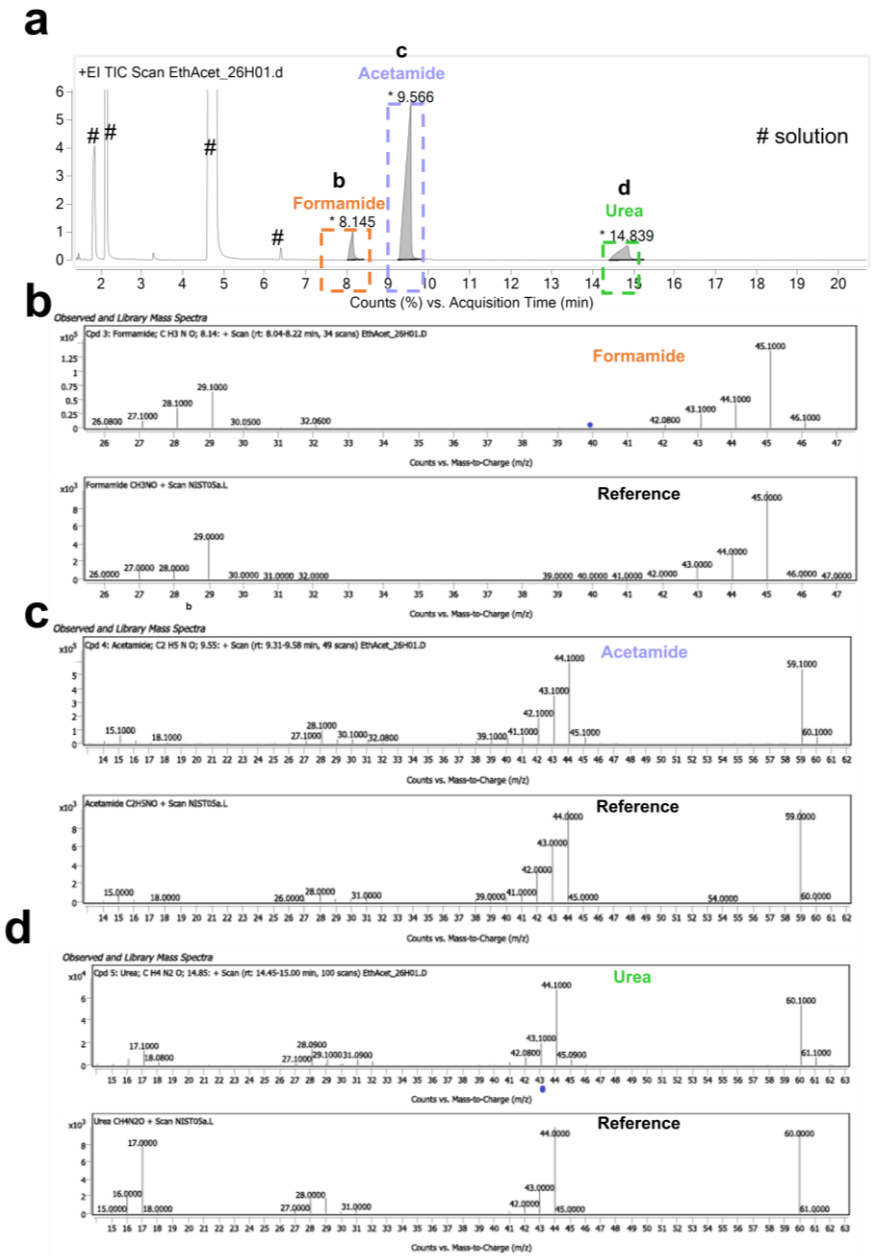

Figure 5-S28. Qualitative analysis of C-N bond formation by GC-MS. Beside solvent related peaks, formamide, acetamide and urea were identified in the sample (a) with matching scores of 98.13 (b), 98.64 (c) and 96.11 (d) respectively.

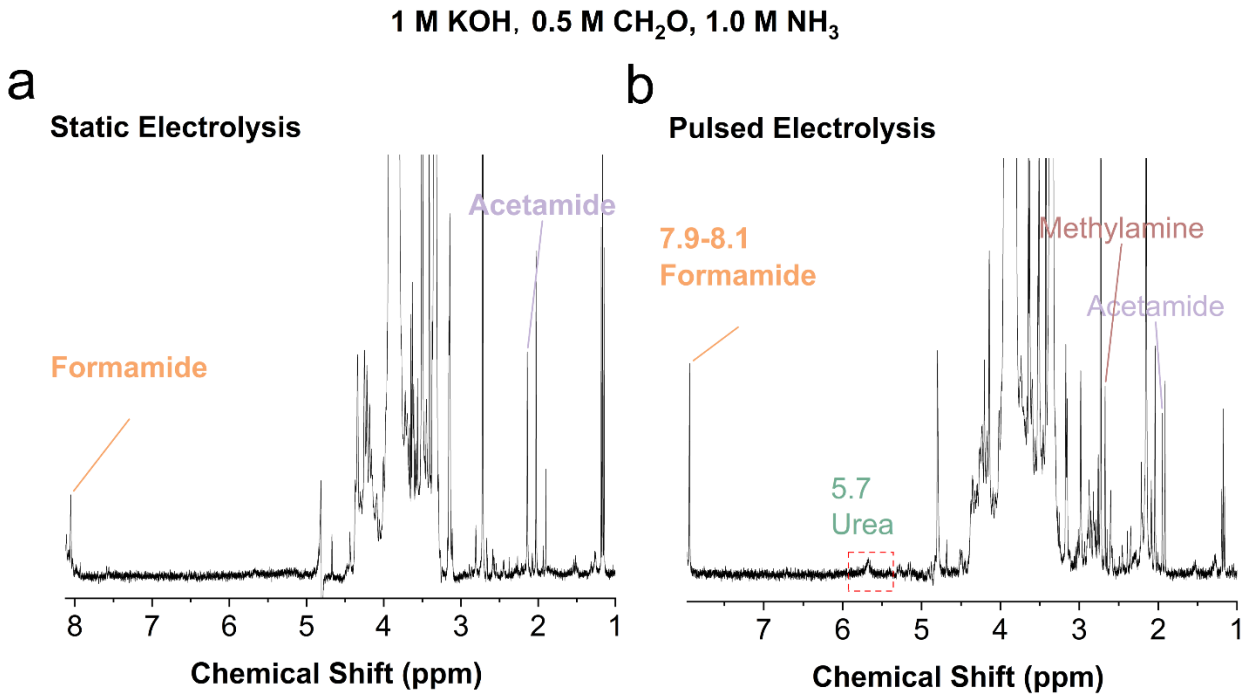

Figure 5-S29. NMR spectra of 0.5 M CH_2O used as the C-source to replace CO_2. The scale of NMR spectra of static electrolysis and pulsing electrolysis remains the same to compare the change in product concentration.

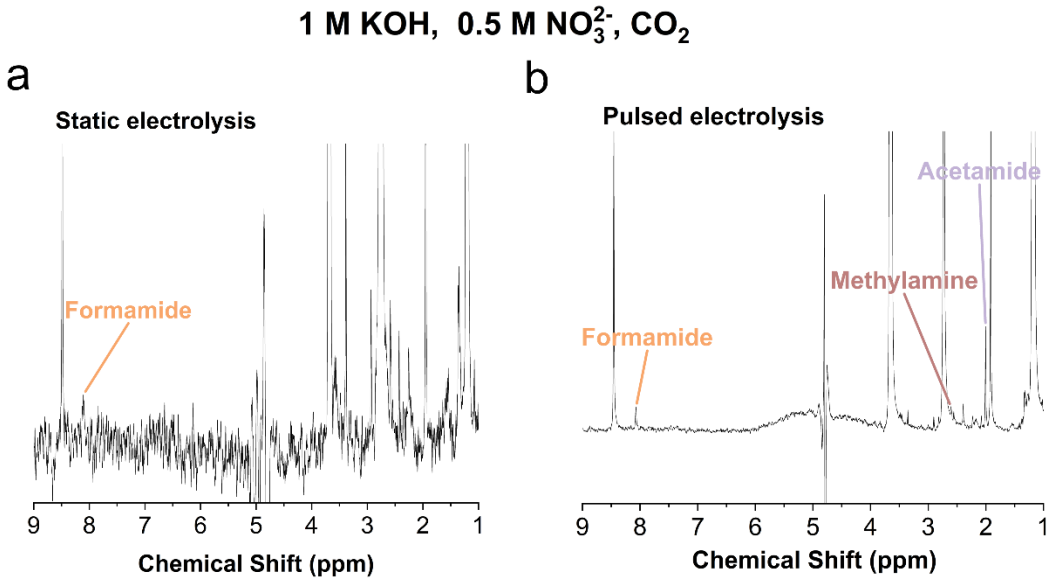

Figure 5-S30. NMR spectra of 0.5 M NO_3^{2-} as N-source to replace NH_4OH. Only Formamide can be observed in the static electrolysis condition, while both formamide, acetamide and methylamine are present in the electrolysis solution after pulsed electrolysis.

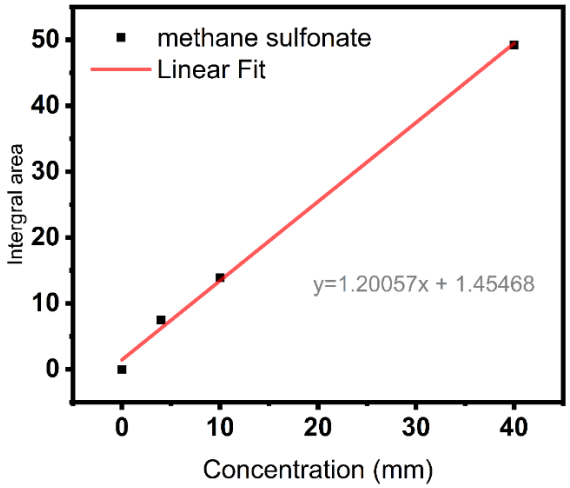

Figure 5-S31. The calibration curve of methane sulfonate obtained from different concentrations of standard methane sulfonate solutions in the employed 1.0 M KOH electrolyte using DMSO as an internal standard.

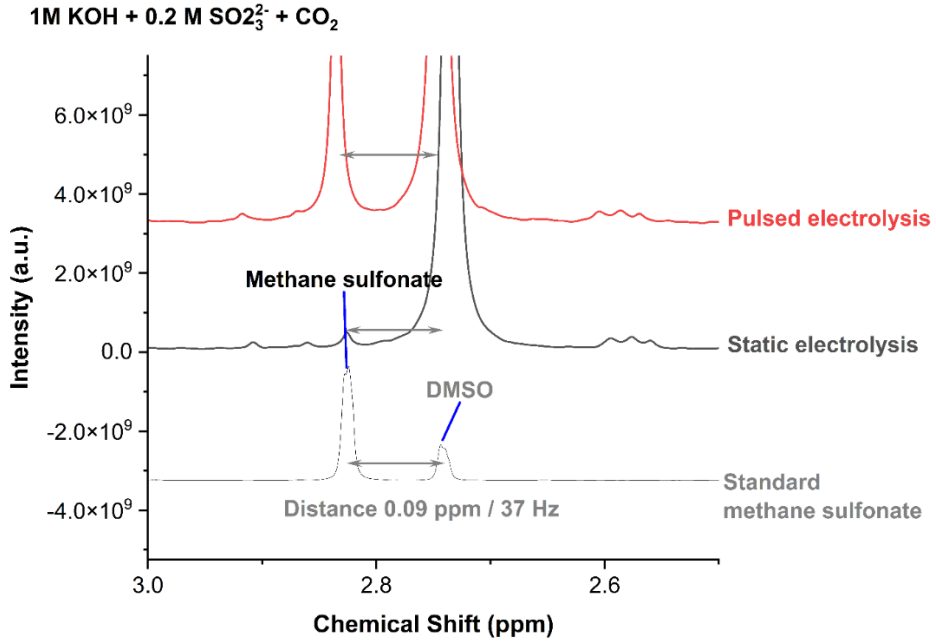

Figure 5-S32. NMR spectra of standard methane sulfonate, static electrolysis, and pulsing electrolysis (from bottom to top). The scale of NMR spectra of static electrolysis and pulsing electrolysis remains the same to illustrate the change in product concentration. The chemical shift is a bit of different likely due to the pH being different in these two electrolysis conditions. However, the distance of chemical shift between DMSO and methane sulfonate remains the same.

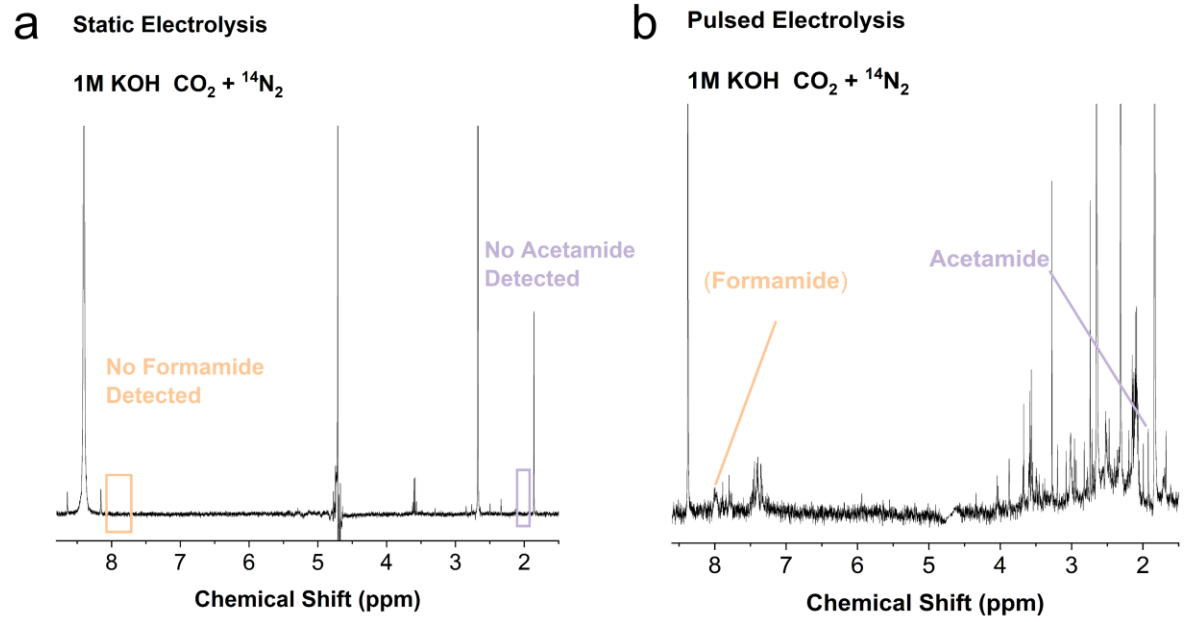

Figure 5-S33. Expanding Scope. NMR spectra of co-electrolysis CO_2 and N_2. The calculated Faradaic efficiency for formamide and acetamide is 0.39% and 0.4%. It should be noted that the current Faradaic efficiency is not high enough to prove the N-source is directly from N_2.

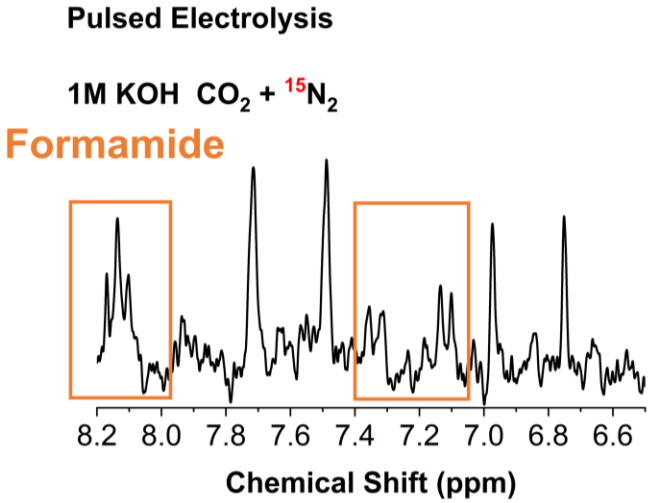

Figure 5-S34. $^{15}N_2$ Isotope experiment was conducted to verify the formation of formamide and acetamide. $^{15}N_2$ flowed into the GDE cell for 1h.

Table 5-S3. Raman and IR Peak assignment.

Band Position (cm^{-1})	**Infrared/Raman (Figure)**	**Potential Assignment**
209-220	Raman (4b)	Cu_2O
320	Raman (4b)	Cu-C_x
518, 619	Raman (4b)	CuO_x
635, 675	Raman (4b)	Cu-OH
983	Raman (4b)	HCO_3^-
1018	Raman (4b)	
1033	Raman (4b)	HCO_3^-
1067	Raman (4b)	CO_3^{2-}
1129	Raman (4b)	
1341	Raman (4c)	HCO_3^-
1363	Raman (4c)	$*CO_2^-$
1454	Raman (4c)	COOH
1547	Raman (4c)	C-N
1584	Raman (4c)	$*CO_2^-$
3564-3059	Infrared (4d)	N-H
2887	Infrared (4d)	C-H
1616	Infrared (4e)	C-N/HCO_3^-
1639	Infrared (4e)	H_2O
1450	Infrared (4e)	
1389	Infrared (4e)	NO_3^-
1232	Infrared (4e)	NO_2^-
666	Infrared (4e)	Cu-OH

5.8.9. Supplemental note 9: Density Functional Theory (DFT) information

DFT parameters: The DFT simulations were performed on a Cu(100) surface that was created using Atomic Simulation Environment (ASE)[22] and consisted of $5 \times 5 \times 4$ atoms, or 4 layers of 25 atoms. The bottom two layers were fixed to simulate the bulk and the top two layers were free to relax to resemble the surface. 15 Å of vacuum is added in the z direction (perpendicular to the surface) to avoid interaction between periodic images. The Monkhorst-Pack scheme was used for K-points of $4 \times 4 \times 1$. The energy cut-off and the relative cut-off used were 550 and 50 Rydberg, respectively. The force convergence was taken to be 3×10^{-4} $Bohr^{-1}$ Hartree. The exchange correlation functional of Perdew, Burke, and Ernzerhof (PBE)[23] was used. All these parameters were chosen after running convergence and sensitivity tests. DFT calculations are all performed using CP2K code[24] and further computational details are given elsewhere[25].

Computational methods: To compute energy differences of elementary proton coupled electron transfer (PCET) steps, the computational hydrogen electrode (CHE) model[26] was used. In this model we assume hydrogen gas is at equilibrium with proton and electron and the corresponding potential is 0 V vs. RHE, thus the energy of proton coupled with electron is estimated by half of the energy of hydrogen gas:

$$H^+ + e^- \leftrightarrow \frac{H_{2(g)}}{2} \quad \text{(Eq. 1)}$$

$$E_{H^+ + e^-} = \frac{E_{H_2(g)}}{2}, \text{ @ pH=0 and 1 atm} \quad \text{(Eq. 2)}$$

DFT raw data:

Table 5-S4. DFT raw data: Adsorbates on Cu(100). All intermediates of the first column are adsorbed species.

Intermediates	Energy [Hartree]	Energy [eV]	Position and Comments
CO*, hollow	-4834.418973	-131549.37	Hollow
CCO	-4840.103543	-131704.05	Top C*, vertical
NH_3	-4824.453163	-131278.19	Van Der Walls (Vdw), 4.5 A
NH_2	-4823.869376	-131262.30	Bridge
NH_2 + CO	-4845.586642	-131853.25	
NH_2 + CCO	-4851.271088	-132007.93	
$CONH_2$	-4845.580557	-131853.09	See photo
$CCONH_2$	-4851.246795	-132007.27	See photo
NH_2 + H*	-4824.459594	-131278.37	
NH_2 + CO, close	-4845.58733	-131853.27	Bridge CO
CO, bridge	-4834.419887	-131549.39	
$CONH_2$ + H	-4846.170948	-131869.15	
NH_2 + H_2O	-4841.108378	-131731.40	H_2O slight adsorption (abs) top

$NH_2 + H_2O$, far	-4841.099515	-131731.15	
$NH_3 + OH$	-4841.103413	-131731.26	
NH_3 + OH from Nudged Elastic Band (NEB)	-4841.119145	-131731.69	
$NH_3 + CO$	-4846.173935	-131869.23	
$NH_3 + CO + OH$	-4862.821075	-132322.22	
$CCO+NH_2$, close	-4851.263995	-132007.74	
CHO	-4834.989613	-131564.90	
$CHO + NH_2$	-4846.154416	-131868.70	
$CHONH_2$, Formamide	-4846.184478	-131869.52	
$CONH_2NH_2$, urea	-4856.75689	-132157.21	
$CO+NH_2+NH_2$	-4856.754545	-132157.14	
H	-4813.292211	-130974.49	
2H	-4813.882068	-130990.54	
H_2O	-4829.939542	-131427.48	top
OH, hollow	-4829.349417	-131411.42	
OH, bridge	-4829.346599	-131411.35	
OH, top	-4829.345777	-131411.32	moves to bridge/hollow, ignore
$CONH_2 + CH_2$	-4852.428023	-132039.41	
$CONH_2 + CH_3$	-4853.048074	-132056.29	
$CONH_2CH_2$	-4852.486287	-132041.00	

DFT results:

Table 5-S5. Reaction Energy differences from DFT raw data. Adsorption denoted as Ads, and desorption (denote as des).

Reaction	**dE**
NH_3 ads	-0.367
NH_3 => NH_2	2.572
NH_3 => *NH_2	-0.290
NH_3* => NH_2*+H*	-0.174
NH3* => NH_2*	0.076
NH_2 ads	-2.86
NH_2 + CO => $CONH_2$	0.184
NH_2 + CCO => $CCONH_2$	0.661
NH_3(des) + *CO => *$CONH_2$	-0.110
NH_3(des) + *CCO => *$CCONH_2$	0.36
NH_3 + CO => $CONH_2$ + H	0.337
NH_3 + CO + OH => CO + NH_2 + H_2O(des)	0.386
NH_3 + CO + OH => $CONH_2$+ H_2O(des)	0.571
NH_3 + OH => NH_2 + H_2O(des)	0.394
NH_3 + OH => NH_2 + H_2O(ads)	-0.135
NH_3 + OH => NH_2 + H_2O, far	0.106
CO => CHO	0.305
CHO + NH_2 => formamide(des)	0.039
$CONH_2$ + NH_2 => urea(des)	0.978
$CONH_2$ + NH_2 => urea(ads)	-0.063
urea(ads) => urea(des)	1.042
$CONH_2$ + H + e => Formamide(des)	0.232
$CONH_2$ + H + e => Formamide(ads)	-0.624
formamide (ads) => formamide(des)	0.857
HER ($2H^+$)	-0.249
HER (2H*)	0.491
OH ads	-0.695
H_2O ads	-0.487
$CONH_2$ + CH_2 => CH_2CONH_2	-1.585
$CONH_2$ + CH_3 => CH_3CONH_2 (des)	0.047
$CH2CONH_2$ => CH_3CONH_2 (des)	0.569

5.9. Supporting References

1 Chen, L., Ma, J., Huang, Y., Dai, M. H. & Li, X. L. Optimization of a colorimetric method to determine trace urea in seawater. *Limnol Oceanogr-Meth* **13**, 303-311 (2015).

2 Lv, C. D. *et al.* A Defect Engineered Electrocatalyst that Promotes High-Efficiency Urea Synthesis under Ambient Conditions. *Acs Nano* **16**, 8213-8222 (2022).

3 Feng, Y. G. *et al.* Te-Doped Pd Nanocrystal for Electrochemical Urea Production by Efficiently Coupling Carbon Dioxide Reduction with Nitrite Reduction. *Nano Letters* **20**, 8282-8289 (2020).

4 O'Keeffe, M. & Sherington, J. Comparison of three methods for the determination of urea in compound feed and silage. *Analyst* **108**, 1374-1379 (1983).

5 Zawada, R. J., Kwan, P., Olszewski, K. L., Llinas, M. & Huang, S. G. Quantitative determination of urea concentrations in cell culture medium. *Biochem Cell Biol* **87**, 541-544 (2009).

6 Wei, X. X. *et al.* Oxygen Vacancy-Mediated Selective C-N Coupling toward Electrocatalytic Urea Synthesis. *J Am Chem Soc* (2022).

7 Jiang, H. P., Zhang, Y. H., Yang, K. L. & Zou, J. Validation of a LC-MS Method for the Determination of Urea Contamination in Market Teas. *Food Anal Method* **7**, 13-20 (2014).

8 Wu, Y. S., Jiang, Z., Lin, Z. C., Liang, Y. Y. & Wang, H. L. Direct electrosynthesis of methylamine from carbon dioxide and nitrate. *Nat Sustain* **4**, 725-+ (2021).

9 Liler, M. Nuclear Magnetic Resonance Spectra of Acetamide N-15 - Solvent and Temperature Effects. *J Magn Reson* **5**, 333-& (1971).

10 Chen, C. *et al.* Coupling N2 and CO2 in H2O to synthesize urea under ambient conditions. *Nat. Chem.* **12**, 717-724 (2020).

11 Jouny, M. *et al.* Formation of carbon-nitrogen bonds in carbon monoxide electrolysis. *Nat Chem* **11**, 846-851 (2019).

12 Guo, C. Y. *et al.* Electrochemical Upgrading of Formic Acid to Formamide via Coupling Nitrite Co-Reduction. *J Am Chem Soc* (2022).

13 Hodgetts, R. Y. *et al.* Refining Universal Procedures for Ammonium Quantification via Rapid H-1 NMR Analysis for Dinitrogen Reduction Studies. *Acs Energy Letters* **5**, 736-741 (2020).

14 Liu, L. Y., Mo, H. P., Wei, S. W. & Raftery, D. Quantitative analysis of urea in human urine and serum by H-1 nuclear magnetic resonance. *Analyst* **137**, 595-600 (2012).

15 Timoshenko, J. *et al.* Steering the structure and selectivity of CO2 electroreduction catalysts by potential pulses. *Nature Catalysis* **5**, 259-267 (2022).

16 Matsui, T. *et al.* In Situ Attenuated Total Reflection Infrared Spectroscopy on Electrochemical Ammonia Oxidation over Pt Electrode in Alkaline Aqueous Solutions. *Langmuir* **31**, 11717-11723 (2015).

17 Liu, Q. *et al.* High-Performance Electrochemical Nitrate Reduction to Ammonia under Ambient Conditions Using a FeOOH Nanorod Catalyst. *Acs Appl Mater Inter* **14**, 17312-17318 (2022).

18 Daiyan, R. *et al.* Nitrate reduction to ammonium: from CuO defect engineering to waste NOx-to-NH3 economic feasibility. *Energ Environ Sci* **14**, 3588-3598 (2021).

19 Lu, X. *et al.* In Situ Observation of the pH Gradient near the Gas Diffusion Electrode of CO2 Reduction in Alkaline Electrolyte. *J Am Chem Soc* **142**, 15438-15444 (2020).

20 Gupta, N., Gattrell, M. & MacDougall, B. Calculation for the cathode surface concentrations in the electrochemical reduction of CO2 in KHCO3 solutions. *J Appl Electrochem* **36**, 161-172 (2006).
21 Jeon, H. S. *et al.* Selectivity Control of Cu Nanocrystals in a Gas-Fed Flow Cell through CO2 Pulsed Electroreduction. *J Am Chem Soc* **143**, 7578-7587 (2021).
22 Hjorth Larsen, A. *et al.* The atomic simulation environment-a Python library for working with atoms. *J Phys Condens Matter* **29**, 273002 (2017).
23 Perdew, J. P., Burke, K. & Ernzerhof, M. Generalized Gradient Approximation Made Simple. *Physical Review Letters* **77**, 3865-3868 (1996).
24 Kühne, T. D. *et al.* CP2K: An electronic structure and molecular dynamics software package - Quickstep: Efficient and accurate electronic structure calculations. *The Journal of Chemical Physics* **152**, 194103 (2020).
25 Al-Mahayni, H., Wang, X., Harvey, J.-P., Patience, G. S. & Seifitokaldani, A. Experimental methods in chemical engineering: Density functional theory. *The Canadian Journal of Chemical Engineering* **99**, 1885-1911 (2021).
26 Nørskov, J. K. *et al.* Origin of the Overpotential for Oxygen Reduction at a Fuel-Cell Cathode. *The Journal of Physical Chemistry B* **108**, 17886-17892 (2004).

Conclusion & Outlook

In this thesis, we put our focus on emerging areas in electrosynthesis instead of concentrating on mature directions in investigating electrochemical CO_2RR and HER. The general focus of the research is use simple abundant building blocks (e.g., H_2O, CO_2, N_2) or readily available small molecules (CH_4, NO_3^-, CH_3CN) that can be electrocatalytically transformed to fuels and commodity chemicals in the larger context of sustainability.

In **Chapter 3**, we successfully developed a modular electrocatalyst model system (M-CAT) that features well-defined $M-O_4$ active sites. Co-CAT exhibits a record performance with an ultralow onset potential and Ni-CAT features intrinsically faster reaction kinetics. Through the application in *operando* infrared spectroscopy, we show that the HMFOR reaction is initiated by the generation of the M(III) species and subsequent adsorption of HMF via its aldehyde group. The rate-limiting step is reactant adsorption in the case of Co-CAT and intermediate desorption for Ni-CAT.

For future work, we are planning to make use of this model system and modify its structure by substituting motifs into the structure such as hydroxyl-, amino, and thiol ligating groups to maximize its reactivity. Further, since our catalysts have capacity to oxidize -OH and -CHO groups, we are wondering it can extend the scope of the system to other reactants that contain those functional groups.

The **Chapter 4** describe that we develop and investigate a Pd-membrane based reactor. This system selectively adsorbs and permeates hydrogen from an aqueous electrolyte through to a nitrile-containing organic compartment to completely cleave the nitrile's C≡N triple bond. Through the state-of-the-art spectroscopic techniques, we provide a molecular picture of the newly discovered reaction process. The rate determining step is the hydrogenation of *NHx species. In the future, we are planning to develop an oxygen membrane reactor to fully utilize the water oxidation half-reaction. Also, this strategy also might work for nitrogen reduction. We wish to push this configuration into a gas capture, gas transformation cell by engineering molecular catalysts with the Pd-membrane reactor.

In **Chapter 5**, we highlight the potential of using pulsed electrolysis in CO_2 co-electrolysis to form heteroatom chemical bond such as C-N bond and C-S bonds. This advance in pulsed electrochemistry could open access for CO_2RR to more valuable chemicals than the currently pursued CO, ethylene, and alcohol products. Although the selectivity towards specific products should still be increased, we believe that one promising route to do so is through the incorporation of bifunctional active sites on the catalyst. Beyond this additional strategy include facet effect, bimetallic catalysts, and defect engineering. Furthermore, combining complementary analytical techniques serve as a powerful tool to understand then control multi-step pathways for selective catalytic processes.